Photoionization of the Helium Hydride Ions and Helium Atoms

Jinzhen Zhu

Munich 2020

Photoionization of the Helium Hydride Ions and Helium Atoms

Jinzhen Zhu

PhD Thesis
Faculty of Physics
Ludwig–Maximilians–University
Munich

Presented by
Jinzhen Zhu
from Dongtai city, Jiangsu province, China

Munich, 19.09.2020

Supervisor: Prof. Dr. Armin Scrinzi
Second referee: Prof. Dr. Dieter Bauer
Date of defense: 17.11.2020

Contents

Zusammenfassung

Das Ziel der ultraschnellen Wissenschaft ist es, die Elektronendynamik in den Atomen und Molekülen im Attosekundenbereich zu verstehen. Die Verwendung eines intensiven Laserpulses zur Messung der Attosekunden-Bewegung ist eine ideale Wahl. Es stehen verschiedene experimentelle Messungen zur Verfügung, um die Bewegungen von Partikeln in Materialien zu initiieren, zu steuern und zu beobachten. Die schwierige theoretische Arbeit folgt jedoch danach. Es sind verschiedene qualitative Erklärungen verfügbar, quantitative Ergebnisse für komplexe Systeme sind jedoch schwer zu erhalten. In dieser Arbeit konzentrieren wir uns auf die numerischen Berechnungen zur Photoionisierung eines Heliumatoms und eines Heliumhydridions und präsentieren theoretische Beschreibungen der Elektronendynamik im Attosekundenbereich.

Eine genaue Beschreibung des Attosekundenprozesses von Elektronen, die einem intensiven Laserfeld ausgesetzt sind, erfordert die Lösung der zeitabhängigen Schrödinger- Gleichung (TDSE). Das Photoelektronenspektrum ist eines der am leichtesten beobachtbaren Phänomene in Attosekundenversuchen, deren Berechnung mit Standardmethoden jedoch unter einer schlechten Skalierung zur Beschreibung des mit der Zeit expandierenden Simulationsraums leidet. Mit der zeitabhängigen Oberflächen- Flux-Methode (tSurff) kann man das Photoelektronenspektrum in einem begrenzten Raum mit hoher numerischer Effizienz erhalten. Die Erweiterungen von tSurff umfassen die Photoionisierung von Polyelektronensystemen mit der Methode der hybriden antisymmetrisierten gekoppelten Kanäle (haCC) und die Doppelionisierung des Heliumatoms. Die numerischen Methoden zur Lösung von TDSE werden demonstriert und bestehen aus der Diskretisierung, die den Winkelteil durch sphärische Ober- und Unterwellen und radiale Funktionen durch die Finite-Element-Methode (FEM) oder die Finite-Element-Discrete-Variable-Darstellung (FE-DVR) darstellt. Die durch die oben genannten Diskretisierungsstrategien dargestellte Elektronen-Elektronen- Wechselwirkungsformel wird vorgestellt. Ebenso werden der effiziente Absorber mit Infinite Rage Exterior Complex Scaling (irECS) und Mixed Gauge vorgestellt. Wir zeigen auch die numerischen Methoden zum zeitlichen Fortschreiten der Wellenfunktion sowie deren Parallelisierungsstrategie und -leistung. Bevor die Hauptergebnisse vorgestellt werden, wird die numerischen Verhaltensweisen der Diskretisierungsparameter in Simulationen der Doppelionisation eines Heliumatoms beschrieben, das einem 400-nm-Laserpuls ausgesetzt ist.

Wir berechnen die statischen Feldionisationsraten von HeH^+ nach der haCC-Methode zusammen mit einem Konvergenztest für Diskretisierungsparameter. Die Ergebnisse können

als Inputs für CTMC-Berechnungen verwendet werden, bei denen eine ineinander verschlungene Bewegung des Elektronenkerns beobachtet wird. Das Einzelionisations- Photoelektronenspektrum eines Heliumatoms wird bei verschiedenen Flat-Top-Impulsen mit Intensitäten von $1 \times 10^{13} - 1 \times 10^{15}\,\mathrm{W/cm^2}$ und Wellenlängen von $300 - 400$ nm berechnet, die durch Freeman-Resonanz verstärkt werden, wenn eine angeregte Eigenenergie E_x und die Gleichung $E_0 - E_0 + E_x + U_p = n\omega$ erfüllen, wobei U_p die ponderomotorische Energie ist. Die AC Stark-Verschiebung der Eigenenergien E_0, E_x mit Intensität werden durch Floquet-Analyse weiter bestätigt. Wir sehen, dass die Eigenenergie E 0 unveränderlich ist und die angeregten Eigenenergien E_x vor allem für 3p-Orbitale sich um U p nach oben verschieben. Die Populationsanalyse zeigt, dass die benachbarten 3s- and 3d- der 3p-Orbitale die höchsten Populationen aufweisen, wenn die Freeman- Resonanzbedingungen der Gleichtung $-E_0 + E_x + U_p = n\omega$ erfüllt werden. Dann werden die Resonanzkriterien durch den Gaußschen Hüllkurvenpuls und verschiedene andere Intensitäten und Wellenlängen verifiziert.

Die doppelte Photoelektronenemission von He-Atomen durch intensive Laserpulse mit einer Wellenlänge von 394,5 nm wird für Intensitäten von $3,5 - 9,2 \times 10^{14} W/cm^2$ berechnet. Gemeinsame Impulsverteilungen bestätigen die Eigenschaften klassischer Flugbahnberechnungen. Der ausgeprägte Übergang von einer Back-to-Back- zu einer Side-by-Side-Emission mit zunehmender Intensität, die He^{2+}/He^{+} -Verhältnisse und eine Modulation der gemeinsamen Energiespektren stimmen gut mit einem kürzlich durchgeführten Experiment überein [Henrichs et al., PRA 98, 43405 (2018)], wenn man eine Zunahme der experimentellen Intensitäten um den Faktor ~ 2 annimmt. Wir stellen fest, dass Freeman-Resonanzen die Back-to-Back-Emission verbessern, wir identifizieren die Signatur der Elektronenabstoßung in gemeinsamen Winkelverteilungen und wir interpretieren die Modulation gemeinsamer Energiespektren als Signatur mehrerer Rekollisionen.

Abstract

The goal of ultrafast science is to understand the electron dynamics in the atoms and molecules in attosecond timescale. Using an intense laser pulse for measuring attosecond motion is an ideal choice. Various experimental measurements are available to initiate, control and observe the motions of particles in materials. But the theoretical work follows painfully, where various qualitative explanations are available but quantitative results for complex systems are hard to obtain. In this thesis, we focus on the numerical calculations on photoionization of a Helium atom and Helium Hydride ion, and present theoretical descriptions of the electron dynamics in attosecond timescale.

A precise description of the attosecond process of electrons that are exposed to an intense laser field requires solving the time-dependent Schrödinger equation (TDSE). The photoelectron spectrum is one of the most easily accessible observables in attosecond experiments, whose computation with standard methods, however, suffers from poor scaling for describing the simulation space which expands with time. With the time dependent surface flux (tSurff) method, one may obtain the photoelectron spectrum in a limited space with high numerical efficiency. The extensions of tSurff include photoionization of polyelectron systems with hybrid anti-symmetrized coupled channels (haCC) method and double ionization of Helium atom. The numerical methods for solving TDSE are demonstrated, consisting the discretization that represents angular part by spherical harmonics and radial functions by finite element method (FEM) or finite element discrete variable representation (FE-DVR). The electron-electron interaction formula represented by the above-mentioned discretization strategies is introduced. The efficient absorber by infinite-range exterior complex scaling (irECS) and mixed gauge is also presented. We also demonstrate the numerical methods for advancing the wavefunction with time as well as its parallelization strategy and performance. Before presenting the main results, the numerical behaviors of the discretization parameters in simulations of the double ionization of a Helium atom that is exposed to a 400 nm laser pulse.

We compute the static field ionization rates of HeH^+ by haCC method, together with a convergence test on discretization parameters. The results can be used as the inputs for CTMC computations, where intertwined electron nuclear motion is observed. The single ionization photoelectron spectrum of a Helium atom is computed at various flat-top shape pulses with intensities $1 \times 10^{13} - 1 \times 10^{15}\,\mathrm{W/cm^2}$ and wavelengths $300 - 400$ nm, which are enhanced by Freeman resonance when an exited eigenenergy E_x and ground eigenenergy E_0 satisfy $-E_0 + E_x + U_p = n\omega$, with U_p being the ponderomotive energy. The AC Stark

shift of eigenenergies E_0, E_x with intensity are further confirmed by Floquet analysis; we find the ground energy E_0 is invariant and the excited eigenenergies E_x, especially for $3p$ orbitals, up-shift by U_p. The population analysis shows the adjacent $3s$ and $3d$ of $3p$ orbitals have the highest populations when the Freeman resonance conditions $-E_0 + E_x + U_p = n\omega$ are satisfied. Then resonance criteria is verified by the Gaussian-like envelope pulse and various other intensities and wavelengths.

Double photoelectron emission from He atoms by intense laser pulses with a wave length of 394.5 nm is computed for intensities $3.5 - 9.2 \times 10^{14}\,\mathrm{W/cm^2}$. Joint momentum distributions confirm the characteristics seen in classical trajectory calculations. The pronounced transition from back-to-back to side-by-side emission with increasing intensity, the He^{2+}/He^{+} ratios, and a modulation of joint energy spectra agree well with a recent experiment [Henrichs et al., PRA 98, 43405 (2018)], if one admits an increase of experimental intensities by a factor ~ 2. We find that Freeman resonances enhance back-to-back emission, we identify the signature of electron repulsion in joint angular distributions, and we interpret the modulation of joint energy spectra as a signature of multiple recollsions.

List of Publications

1 A. Vila, J.Zhu, A.Scrinzi and A.Emmanouilidou. Intertwined electron-nuclear motion in frustrated double ionization in driven heteronuclear molecules. *Journal of Physics B: Atomic, Molecular and Optical Physics*, 51(6):065602, 2018

2 J. Zhu, A.Scrinzi. Electron double-emission spectra for Helium atoms in intense 400 nm laser pulses. *Physical Review A*, 101(6):063407, 2020

Chapter 1

Introduction

1.1 Motivation and background

Attosecond physics

The motion of electrons in atoms, molecules, and solids is measured on the time scale of attoseconds (1 as = 10^{-18} s) [1]. The motion of electrons is fundamental to all chemical reactions, and its time scale is minuscule compared to that of vibrational dynamics in molecules of tens to hundreds of femtosecond (1 fs = 10^{-15} s) [2] and of rotational dynamics of molecules in picosecond (ps) time scale (1 ps = 10^{-12} s).

Typical candicates for measuring the electron dynamics are electrons, ions and light. Due to the repulsion among the charged particles, it is difficult to form very short duration pulses with electrons and ions. Thus, for many applications of femtosecond and attosecond time domain, the light probes are preferred choices. The first measurement of an attosecond trace by laser pulse was reported in Ref. [3]. With the development of strong laser fields with precisely controlled sub-cycle temporal evolution [4–6], the attosecond metrology, such as the attosecond streaking, is widely used not only for characterization of the key attosecond tools-ultrashort laser pulses, but also for probing electron dynamics with these tools on the attosecond-to-femtosecond time scale [7–9]. Apart from probing electron dynamics, the strong-field laser can also serve as a "pump" for ionizing the electrons, and the motion of electrons in time can be measured from the high-order harmonic emission [10–12] and electron diffraction [13] or isolated XUV pulses [14–18]. This newly emerging field is termed as "attosecond physics", the science of collective and individual motions of electrons in atomic, molecular, and high-density mesoscopic systems in an intense laser pulse.

Experimental progress

The developments in attosecond physics depend on the development of techniques to control laser pulses. With the generation and control of ultra-short pulses, advanced techniques such as the so-called light-wave electronics were developed to steer electrons inside and around atoms in attosecond resolution [19]. Ref. [4] reported few-cycle laser pulses

with a stable carrier envelope phase at a wavelength of 750 nm. In 2004, the first completely characterized light wave was reported [6] and two years later, the production of characterized short wavelength single pulse with a width of 1.6 fs [20] and long wavelength few-cycle phase-stable pulses at 21 μm [21] was published. Recently, isolated short soft X-ray with extreme peak power exceeding 100 GW was reported in Ref. [22].

Various well-known techniques have been developed to liberate, measure, or control the dynamics of electron wave packets, such as Attoclock [23–25], laser-induced electron diffraction (LIED) [13, 26], attosecond streak camera [27, 28], and transient absorption spectroscopy (TAS) [15, 29–31]. This thesis focuses on the electron dynamics of two-electron systems He and HeH^+ in a strong laser field, where the ionization and interaction of the two electrons is an important topic, and also opens an interest among experimental scientists where some recent breakthroughs are given in the following. Direct time-domain observation of the interaction of two electrons during liberation was possible because of the attosecond measurements [32]. Due to the two-electron correlation, photon-energy-dependent emission timing of electrons, released from the helium ground state by an extreme-ultraviolet photon was observed with attosecond streak camera [33]. The double emission spectrum can be measured by coincidence detection methods. The cold target recoil ion momentum spectroscopy (COLTRIMS) is a coincidence detection method that can detect with a single measurement the momenta of the ionized particles, including the ions and electrons [34–37]. The electron repulsion in multi-photon double ionization of argon, when exposed to a 780 nm pulse, was observed by COLTRIMS [38]. The two-electron momentum distributions, sequential and non-sequential double ionization, of argon were also investigated by another coincidence detection reaction microscope (REMI) in the few-cycle [39, 40] and single-cycle [40–43] regime. For double emission of Helium, apart from the ratios He^{2+}/He^+ reported in Ref. [44] for a 780-nm laser pulse and a 400-nm pulse used in Ref. [45], the correlated behavior of the two electrons in a 400 nm pulse was measured by COLTRIMS as reported by Ref. [46].

Theory lags behind

A clear conception of related theory is prerequisite to explain the experimental observables and to stimulate the development of technologies and systems. Good examples include the interpretation of diffraction images of diatomic molecules captured by the LIED [47] that can explain the interference effects with the high harmonic spectroscopy technique [48]. Some simple models such as the perturbation theory, ADK model, and above-threshold ionization (ATI) that facilitates qualitative analysis of the observed phenomena will be detailed later. However, a thorough understanding of the underlying mechanism requires accurate and quantitative analysis. A quantitative study of such ultrafast processes at the atomic scale requires solving the Schrödinger equation that has been used for single electron ionization by many groups to simulate the motion of two or more electrons; the equation consumes tremendous computational resources.

A. Computational resources

Thanks to the development of high-performance computers over the past ten years, numerical simulations of double ionization is possible. For example, an accurate prediction on the double-electron few-photons ionization of a Helium atom with photon energy ranging from 40-54 eV was reported in 2008 [49]. Although research on low dimensional simulations and full dimensional calculations at short wavelengths ($\sim$ 10 nm) has been reported, reports on quantum simulations on full dimensions at large wavelengths ($\lambda \geq 400$ nm) are very scarce [50–52] because of the poor scaling property of the equation. The calculation for a single optical cycle of 780 nm laser consumed computational resources of more than 4000 cores [53]. The **tSurff** method shown in chapter 2 facilitates the method that needs moderate consumption of computational resources for large-scale and full-dimensional quantum simulation for double ionization in a 780 nm pulse, where the convergence was hard to achieve, as reported by our group [54].

B. Classical and quantum models

The length scale of the electron dynamics is below a few nanometers, which is in the quantum regime. Although experimental observables can be extracted from wave-functions by solving the time-dependent Schrödinger equation (TDSE), this does not facilitate an intuitive description of the motions because of the uncertainty principle. However, an intuitive description is possible when using classical trajectory methods, wherein the movement of the wave packet is represented by the weighted average of various independent classical trajectories simulated by solving Newton's equation. Moreover, the classical simulations do not scale drastically with laser parameters and dimensions as they do for quantum methods. The classical trajectory simulations can also include the quantum effects by using data from quantum chemistry computations [55], which, however, are limited to describing the bound states of the molecules and fails to describe the free particles (unbound states). Thus, it fails to describe quantum properties such as multi-photon ionizations and precisely measuring static field ionization rates in HeH^+. The consistency of the quantum and classical methods are not fully investigated, especially in the double-emission problem where the comparisons between the classical description and quantum calculations are scarce.

C. Explaining the experiment

By approximations that neglect the minor effects, quantum computation by solving the Schrödinger equation simulates the electron dynamics in atoms and molecules in a simplified condition. Comparing the computational results with the experimental observables provides a better understanding of the physics and proves to be an exceptional way for scrutinizing the theoretical models. Adjusting theoretical computations to the experimental conditions requires extra treatment of computed results which is based on a thorough understanding of the parameters used in the experiment, such as the pulse shape, and intensity distribution. The comparison of the experiments and theoretical calculations in double ionization at 400 nm calculation was not fully investigated.

1.2 Scope of the thesis

In this thesis, the content is divided into the following pieces:

Efficient numerical method

We will illustrate the methods for the computations in chapter 2 and chapter 3. Chapter 2 introduces the efficient time-dependent surface flux (**tSurff**) method that reduces the computational cost. First, the tSurff method for producing the single emission photoelectron spectra is introduced. Then, we will demonstrate its extensions including the hybrid antsymmetrized coupled channels (haCC) method to efficiently deal with the single ionization of small molecules and double ionization method of He that is available for simulation of wavelength $\geq$ 400 nm with the commonly used computational hardware. The numerical strategies implemented in our code to solve the TDSE are demonstrated in chapter 3. In chapter 4, the effect of the discretization parameters on the numerical performance of the code is illustrated by the convergence study of double ionization on observables including the energy spectra, correlation ratios, and the joint angular distribution (JAD) spectra with a 400-nm laser pulse.

Single emission spectra

This part of the content is illustrated in chapter 5, consisting of the static field ionization by haCC in Sec. 5.1, Freeman resonance enhanced single ionization spectra in Sec. 5.2, and details for fitting the experimental data in Sec. 5.3.

We present the calculation of the static field ionization rates by our haCC method for HeH^+ as well as the convergence test of the parameters. The static field ionization rates serve as the weights for different trajectories of the classical calculations.

The single ionization photoelectron spectra of a Helium model with laser pulses of λ near 400 nm are calculated. The AC Stark shift of the excited eigenenergies of a Helium model with intensity is investigated using Floquet states by means of plotting the stable eigenenergies, recursive tracing of eigenstates by overlap of wavefunctions, and inverse iteration method for scanning the evolution of selected eigenenergies. The single ionization photoelectron spectrum is enhanced when a Floquet eigenenergy of an excited state $3p$ equals that of the ground state because of the AC Stark shift process, where the populations of the adjacent excited states of $3p$ are also enhanced. The resonance criteria is also presented based on the AC Stark shift of eigenenergies in the pulse.

Electron double-emission spectra for Helium atoms in intense 400 nm laser pulses

We perform double ionization calculations of He atoms with few-cycle pulses at 400 nm with intensities $3.5 - 9.2 \times 10^{14}\,\mathrm{W/cm^2}$. The goal is to mainly compare our theoretical calculations with experiments [Henrichs et al., PRA 98, 43405 (2018)]. We find a pronounced transition from back-to-back to side-by-side with increasing intensity, He^{2+}/He^+ ratios, and

a modulation of joint energy spectra that all agree well with the experiment, if one admits an increase of experimental intensities by a factor ~ 2. For single ionization spectra, the overall shape and cutoff supports our calculations. We find that Freeman resonances enhance anti-correlated emission. We identify the signature of electron repulsion in joint angular distributions and interpret the modulation of joint energy spectra as a signature of multiple recollsions.

1.3 Framework of Theory

The content of this thesis, as summarized above, is focused on simulating the motion of electrons in a strong laser field. The total wavefunction of an electron exposed to an intense laser field can be represented by a superposition of the ground and excited states. The electron may also get ionized by absorbing a sufficient number of photons and depart from the core under the acceleration of the external field. After the external field reverses its direction, the ionized electron slows down and returns to the parent ion, leading to complicated scatterings. The above-mentioned motion of the electrons is in the quantum regime and can be described by the time-dependent Schrödinger equation.

1.3.1 Time-dependent Schrödinger equation

In this thesis, the time-dependent Schrödinger equation (TDSE) can be simplified by the following approximations.

- Low-energy approximation: As the motion of the electrons is driven by the intense laser pulse, whose intensity may reach $1\times10^{18}\,\mathrm{W/cm^2}$ with wavelength 780 nm [56] in experiments, the ionized electron carries high kinetic energy whose motion may enter the relativistic regime. The thesis focuses on the laser with $\lambda \geq 10$ nm and intensities $I \leq 10^{15}\,\mathrm{W/cm^2}$. The energy of particles is always ≤ keV where the maximum energy of particles could be obtained from Sec. 1.3.7. The electron with kinetic energy ≤ keV travels ≤ 6% of speed of light and contributes ≤ 1% corrections to masses due to relativistic effect. Thus, we omit the relativistic effects and all negligible magnetic effects. The related spin effects such as spin-orbit coupling or Lamb shift are also neglected as the magnetic effect are magnitudes lower than the electric field. Also, the interaction of charges can also be described classically by the effective potential $V(r) \propto r^{-1}$ rather than the quantization of electromagnetic fields.

- High intensity limit: The bound electron absorbs a few photons and get ionized in the external laser field. The liberated charges in the laser field return to the parent ion and release photons, which could be observed in the experimental accessible high harmonic generation. The electron dynamics in atoms and molecules are in the quantum regime, implying that apart from the electron itself, the quantization of the external laser field may also be compulsory in principle. Luckily, the intensities used here are $I \sim 10^{14}\,\mathrm{W/cm^2}$, indicating $n \approx \frac{I\alpha_0^2\lambda}{hc/\lambda} \sim 10^{15}$ photons around the atom,

where $\alpha_0 = 0.052917$ nm is the Bohr radius, $c = 299792458$ m/s is the speed of light in vacuum, and $h = 6.626 \times 10^{-34}$ m^{2}kg/s is the Planck's constant. Thus, the creation and annihilation operators can be treated as commutable $a^\dagger a \left|n\right\rangle = n \left|n\right\rangle \approx (n+1) \left|n\right\rangle = aa^\dagger \left|n\right\rangle$, meaning the quantum effects of the laser field are negligible, and the external field can be treated as classical.

- Focal averaging. The electric field $\vec{E}(\vec{r}, t)$ can be factored into a product of envelope $\vec{E}_0(\vec{r}, t)$ and phase $\exp(\mathrm{i}(\omega t - \vec{k} \cdot \vec{r}))$, where the former represents the distribution of the intensity, ω is the frequency and $\vec{k}$ represents the momentum. The distribution of the pulse in space and time should also be taken into consideration in principle. However, in experiments, the induced laser is focused on the target atoms with a focal radius in the magnitudes of micrometers, implying the variation of the intensity is magnitudes smaller than the charges of the atoms and the envelope can be automatically simplified to $\vec{E}_0(\vec{r}, t) \approx \vec{E}_0(t)$.

- Dipole approximation. The phase can also be written as

$$\exp(\mathrm{i}(\omega t - \vec{k} \cdot \vec{r})) \approx \exp(\mathrm{i}\omega t), \tag{1.1}$$

  when $\vec{k} \cdot \vec{r} \ll 1, \lambda \geq 10$ nm, compared to $|\vec{r}|$ of few atomic units, which is called dipole approximation. Thereby, the magnetic field is neglected automatically, consistent with our previous statements. Thus, we have

$$\vec{E}(\vec{r}, t) \approx \vec{E}_0(t) \exp(\mathrm{i}\omega t). \tag{1.2}$$

- The motions of the nucleus can be neglected as the nucleus is much heavier than the electron, where the ratio of the mass is $\frac{m_{\text{nucleus}}}{m_{\text{electron}}} \approx 1836$ for the lightest nucleus of a Hydrogen atom.

With the approximations above, our task is simplified to solving the non-relativistic TDSE in a strong classical electric field for the wavefunction $\psi(t)$ as

$$\mathrm{i}\partial_t \psi(t) = H(t)\psi(t), \tag{1.3}$$

described by an N_e-electron Hamiltonian

$$H(t) = \sum_j^{N_e} (-\frac{\Delta_j}{2} + V(\vec{r}_j) + V_j^I) + \sum_{j<k} \frac{1}{|\vec{r}_j - \vec{r}_k|} \tag{1.4}$$

with V being the the external field. The Coulomb potential $V(\vec{r}_j)$ satisfies $V(\vec{r}_j) \propto r_j^{-1}$ for singles atoms, and the interaction with the electric field for the jth electron (V_j^I) is

$$V_{L,j}^I = \vec{r}_j \cdot \vec{E}(t) \tag{1.5}$$

represented by length gauge or

$$V_{V,j}^I = \mathrm{i}\vec{A}(t) \cdot \vec{\nabla}_j \tag{1.6}$$

represented by velocity gauge, where i is the imaginary number and $\vec{A(t)} = -\int_{-\infty}^{t} \vec{E(\tau)} d\tau$ is the vector potential. For the velocity gauge, $|\vec{A(t)}|^2/2$ is removed from the Hamiltonian, because it is independent of $\vec{r}$ and do not change the wave function. Atomic units $\hbar = e^2 = m_e = 4\pi\epsilon_0 \equiv 1$ are used throughout this thesis if not specified otherwise, whose values represented by the International System of Units (SI) can be found in Sec. A.1.

The general procedure to solve $\psi(t)$ is to firstly compute the field free ground state $\psi_0 = \psi(t_0)$ of corresponding Hamiltonian $H_0 = H(t_0)$ that satisfies $H_0\psi_0 = E_0\psi_0$ where E_0 is the ground state energy. Then the wavefunction at t can be obtained by advancing ψ_0 from t_0 to t by

$$\psi(t) = U(t, t_0)\psi_0 \tag{1.7}$$

with the propagation operator $U(t, t_0)$ written as

$$U(t, t_0) = \mathbb{T} \exp(-\mathrm{i} \int_{t_0}^{t} H(\tau) d\tau) \tag{1.8}$$

where $\mathbb{T}$ is the time ordering operator. A detailed description of time propagation can be found in Sec. 3.5.

The photoelectron spectra in the experiment $P(\vec{k_1}, \vec{k_2}, ..., C)$ with photoelectron momenta $\vec{k_1}, \vec{k_2}...$ and residual ionic configuration C can be calculated by projecting the final ansatz to the scattering states $\chi_{\vec{k_1},\vec{k_2},...,C}$ with respective outgoing boundary condition:

$$P(\vec{k_1}, \vec{k_2}, ..., C) = \left\langle \chi_{\vec{k_1},\vec{k_2},...,C} | \lim_{t\to\infty} \psi(t) \right\rangle . \tag{1.9}$$

A generalized and analytic solution of TDSE in Eq. (1.4) as well as its spectral analysis by Eq. (1.9) is hard to obtain; the numerical solutions are only feasible for specific examples by current computational power, whose details can be found in chapter 3. However, analytical solutions are accessible for describing the electron dynamics when the wavelength and the intensity of a laser pulse reach the limits (extremely low frequency and high intensity, extremely high frequency and low intensity, for example), where some well-known theoretical models that provide analytic solutions will be presented below.

1.3.2 Perturbation theory

When the incident pulse field is in an ultra violet (UV) regime ($\lambda \leq 20$ nm) and below excessive high intensity ($I \leq 10^{15}\,\mathrm{W/cm^2}$), the wave packet of the electron mainly occupies the ground state and the perturbation theory applies. Advancing the wavefunction with time can be approximated by the field free Hamiltonian H_0 and perturbative corrections with the interaction term $H_L = \vec{r} \cdot \vec{E(t)}$. The propagation operator $U(t, t_0)$ of the length gauge Hamiltonian in Eq. (1.4) can be written in nth order perturbation approximation where the formula is truncated after nth-order corrected term. The second order perturbation of $U(t, t_0)$ can be expanded by Dyson series [57] as

$$U(t, t_0) = U_0(t, t_0) + U_1(t, t_0) + U_2(t, t_0) + \mathcal{O}(H_L^3) \tag{1.10}$$

holds the zero order term as $U_0(t,t_0) = e^{-\mathrm{i}(t-t_0)H_0}$,the first order term

$$U_1(t,t_0) = -\mathrm{i}\int_{t0}^{t} U_0(t,t')H_L(t')U_0(t',t_0), \tag{1.11}$$

the second-order term as

$$U_2(t,t_0) = (-\mathrm{i})^2\int_{t_0}^{t} dt'\int_{t_0}^{t'} dt''U_0(t,t')H_L(t,t')U_0(t',t'')H_L(t',t'')U_0(t'',t_0), \tag{1.12}$$

and the higher order residuals $\mathcal{O}(H_L^3)$. With only keeping the first-order term, the spectrum is

$$\begin{aligned}\left\langle\chi_k\left|\lim_{t\to\infty}U(t,t_0)\right|\psi_0\right\rangle &\approx \left\langle\chi_k\left|\lim_{t\to\infty}\int_{t_0}^{t}dt'U_0(t,t')H_L(t')U_0(t',t_0)\right|\psi_0\right\rangle \\ &= \left\langle\chi_k\left|\vec{r}\cdot\hat{e_1}\right|\psi_0\right\rangle\int_{-\infty}^{+\infty}dt'\mathcal{E}(t')e^{-\mathrm{i}(E_0-E_k)t'}\end{aligned} \tag{1.13}$$

where $\vec{E}(t) = \mathcal{E}(t)\hat{e_1}$ is the electric field with $\hat{e_1}$ denoting the polarization direction. With the Gaussian-shape pulse that well approximates the experimental pulse envelope, where $\mathcal{E}(t) = \mathcal{E}_0 e^{-\frac{t^2}{\alpha}}e^{-\mathrm{i}\omega t}$, the spectrum is proportional to

$$\begin{aligned}\int dt'\mathcal{E}(t')e^{-\mathrm{i}(E_0-E_k)t'} &= \int dt'\exp(-\frac{t'^2}{\alpha}-\mathrm{i}\omega t'-\mathrm{i}(E_0-E_k)t') \\ &= \int dt'\exp(-\frac{1}{\alpha}(t'+\frac{\mathrm{i}\alpha}{2}(\omega+E_0-E_k))^2)\exp(-\alpha\frac{(\omega+E_0-E_k)^2}{4}) \\ &= \mathcal{E}_0 e^{-\alpha(E_0-E_k+\omega)^2/4}\sqrt{\alpha\pi},\end{aligned} \tag{1.14}$$

where E_0 and E_k are energies of the ground state ψ_0 and scattering state χ_k. When the width α of the Gaussian pulse approaches infinity, the spectrum is proportional to $\delta(E_0 - E_k + \omega)$. In other words, in the first-order approximation, the spectrum is a peak with a width $1/\alpha$ and a height proportional to $\mathcal{E}_0^2$ at the position $E_k = E_0 + \omega$. Similarly, the second perturbation term locates at position $E_k = E_0 + 2\omega$ [58, 59]. In general, the nth order term consists of n transition dipole moments, and up shifts the energy level by $n\omega$, where $E_k = E_0 + n\omega$ is obtained [60]. The analytic solution for a higher order term ($n > 1$) is unavailable, and high-order perturbation terms may also diverge. If a nth peak is first above the ionization threshold, this process is known as the multi photon ionization (MPI) process, with the higher peaks $(n+1, n+2, \cdots)$ named above threshold ionization (ATI) peaks [61].

The perturbation theory applies when the laser field is at high-frequency limit. On the contrary, when the laser pulse is at low-frequency limit, the ADK formula is a good approximation.

1.3.3 ADK formula

The ADK formula reported by Ammosov, Delone, and Krainov [62] shows the photoionization yield is

$$\Gamma = \left(\frac{3\mathcal{E}n^{*3}}{\pi Z^3}\right)^{1/2} \frac{Z^2}{2n^{*2}} \left(\frac{2e}{n^*}\right)^{2n^*} \frac{1}{2\pi n^*} \frac{(2l+1)(l+|m|)!}{2^{|m|}(|m|)!(l-|m|)!} \left(\frac{2Z^3}{\mathcal{E}n^{*3}}\right)^{2n^*-|m|-1} \exp\left(-\frac{2Z^3}{3n^{*3}\mathcal{E}}\right) \tag{1.15}$$

for a constant electric field $\mathcal{E}$ is the electric field strength, Z is the charge of the atomic residue, $n^* = Z(2E)^{1/2}$, E is the energy of the considered state of the electron in the atom, l, m are the orbital quantum number and its projection. This formula well applies to the ionization process using a pulse at its low-frequency limit. It can be deduced that when exposed to a constant field $\mathcal{E}$, the probability that the electron penetrates the barrier remains, which process is called tunneling ionization. And the ionization rate decays exponentially with the power of ionization energy.

ADK model is a quasi-static limit of PPT model, which includes the long range Coulomb potential that the ADK model neglects [63]. The ADK model is extended to MO-ADK when the asymptotic behavior, the symmetric property of wavefunction and empirical correction by an extension to a barrier-suppression regime are considered [64]. Being a single-electron model, (MO-) ADK does not include the exchange effect in angle dependent molecules [65, 66] and multi-electron effects of transition metal atoms [67].

1.3.4 The Keldysh parameter

The Keldysh parameter [68] is a ratio of two time parameters for describing the competing effect of tunneling to multi-photon ionization. One is the classical time of flight of the tunneling ionization through the barrier which is built by the external electric field and the Coulomb potential τ_T. The other is the period of the laser field oscillation τ_L describing how often the electric field changes its direction. The Keldysh parameter is defined as $\gamma = 2\frac{\tau_T}{\tau_L}$. With very strong fields and low frequencies ($\omega \to 0$) where $\gamma \ll 1$, the formula for ionization rate coincides with that for the tunneling ionization, which condition is named as tunneling regime. On the opposite limit of not very strong fields and high frequencies where $\gamma \gg 1$, the ionization rate could be described by absorbing many photons simultaneously. Thus, this condition is called multi-photon regime.

The Keldysh parameter may also be rewritten in the form of energies as following. As the tunneling time in Keldysh parameter is defined by the mean free time an electron passing thorough a barrier of width $l = \frac{I_p}{e\mathcal{E}}$, where I_p is the ionization potential and $\mathcal{E}$ is the electric field intensity, the Keldysh parameter can also be written as the ratio of I_p and the ponderomotive energy U_p (see below) as

$$\gamma = \sqrt{\frac{I_p}{2U_p}}. \tag{1.16}$$

The tunneling delay time is controversial where both instant tunneling [69] and long tunneling delay time around hundreds of attoseconds [70] with the same laser pulse were

reported and the Keldysh parameter is always represented by Eq. (1.16). Usually, the experimental parameters are selected around $\gamma \approx 1$ where both the tunneling ionization and the multi-photon ionization exist. In this thesis, a pulse with $\lambda \approx 400\,\mathrm{nm}, I \approx 5\times10^{14}\,\mathrm{W/cm^2}$ is applied in He atom whose single ionization potential is $I_p = 0.903\,\mathrm{a.u.}$ The Keldysh parameter is 1.28 where tunneling and multi-photon ionizations co-exist.

1.3.5 Strong Field Approximation

It may need considerable work to solve TDSE for describing electron dynamics in the potential combined by the Coulomb interactions from charges and the interaction from the laser field. With strong field approximation (SFA) [68] the Coulomb interaction is neglected and the motion of the electron is solely driven by the laser field, the solutions of TDSE are easy to obtain. SFA applies when the force an electron experiences from the ion is tiny compared to that from the external field. The particles that are far from the parent ion and exposed to the high intensity, large wavelength laser field are well described by SFA. The corresponding ansatz can be represented by the well known Volkov solutions (see Eq. (2.23)), which serve as the asymptotic scattering states for computation of the photoelectron spectra, and will be detailed in the introductions of tSurff methods in Sec. 2.2.

1.3.6 Three Step Model

Although the electrons can not be treated as classical particles and their motions are not definable due to the uncertainty principle, the photoionization, high harmonic generation (HHG) can be approximated by the trajectories of particles in the tunneling ionization regime $\gamma \ll 1$ with the intuitive three step model [72, 73]. As can be seen in Fig. 1.1, the electron is firstly driven outside the parent system in the intense laser field by tunneling ionization (step 1). Then it is accelerated in the external field (step 2). When the applied electric force reverses, e_1 slows down. As the reversed driven force aggravates, e_1 stops and is back scattered to the parent ion (step 3), leading to complicated recollision processes. The returned particle may combine with the ion and stay on a bound (ground or excited) state and release photons, which is a principle mechanism for high harmonic generation (HHG) [74] (another is Bremsstrahlung [75]). The returned particle may knock out a second electron with itself scattered away, which process exits in non-sequential double ionization, or remain on a bound state after knocking the other electron.

More sophisticated models were reported for refining the three step model. For example, Ref. [76] uses a semi-analytic version of SFA for the first step, Ref. [77] employs a classical ensemble model for the second step. For the third step, Ref. [78] introduces the the electron impact cross sections and Ref. [79] uses a full quantum-mechanical recollision model. Apart from the realistic full dimensional simulations, low dimensional models were also reported [80, 81].

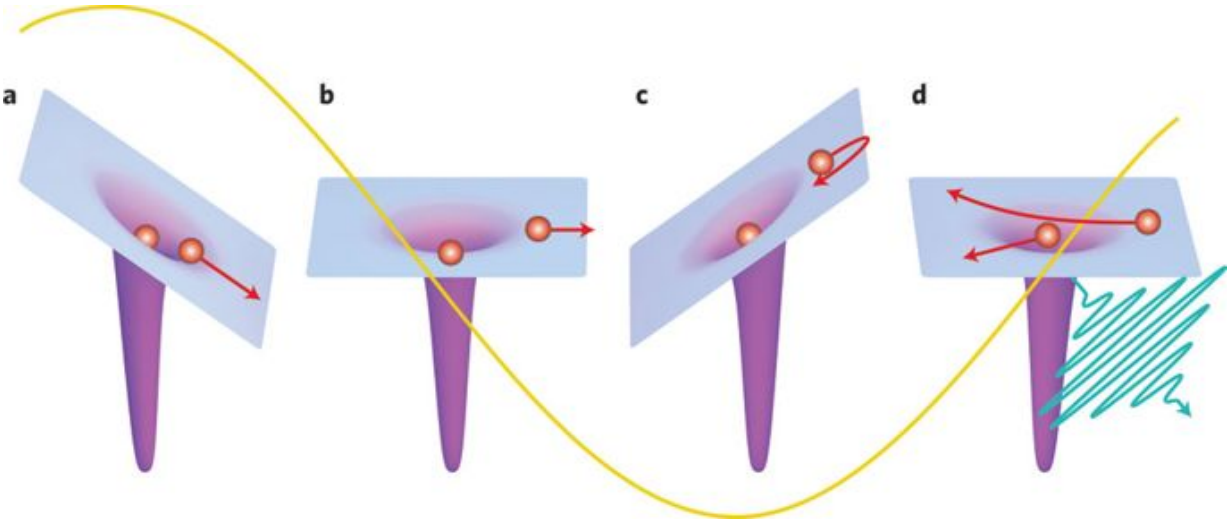

Figure 1.1: The illustration of the three-step model. The yellow curve depcits the external electric field. Firstly an electron e_1 (a) gets ionized in the external electric field (b) and leaves parent system. When (c) the external field reverses its direction and increases its strength, the liberated electron slows down and is drifted back, and (d) re-collides to the parent system where the possible recombination (emitting radiation) or further ionization of the system can happen. The figure is from Ref. [71].

1.3.7 Typical parameters

Typical energies are obtained from classical description of electrons in the laser field, which can also be observed in the photoelectron spectra from quantum simulations, examples can be found in the single electron spectrum in Ref. [82]. Suppose the electron is exposed to the laser field with frequency ω, peak electric field E_0 and peak vector potential $A_0 = \frac{E_0}{\omega}$. The average energy a free motion electron in the external field is $U_p = \frac{A_0^2}{4}$, and the maximal energy an electron asymptotically is $2U_p$. The maximum instant kinetic energy before the re-collision is $3.17U_p$ for satisfying the re-collision condition. And the kinetic energy of an electron after one elastic re-collision reaches up to $10U_p$. The $2U_p$ and $10U_p$ cutoff could be observed in single ionization photoelectron spectra, see Ref. [82]. The derivations of the above parameters can be found in Sec. A.2.

And the excursion amplitude of a free electron in the laser field is $r_q = \frac{E_0}{\omega^2}$, which is also named as quiver radius.

Chapter 2

The computational methods

Photoelectron spectrum is one of the most accessible observables from the experiment, which reflects the dynamics of the electrons in an oscillating external electric field. Obtaining photoelectron spectra requires solving the time-dependent Schrödinger equation using numerical techniques, which leads to tremendous computational consumption (see below). In this chapter, we present the tSurff method to effectively reduce computational effort as well as its extensions for modeling the single ionization of a few-electron system and double ionization. We focus on the linearly polarized pulse along z direction with the vector potential of electric field being

$$\vec{A}(t) = A_0(t)\sin(\omega t + \phi_{CEP})\hat{z}, \tag{2.1}$$

where ω is the photon energy, ϕ_{CEP} is the phase, and $A_0(t)$ represents the shape of the laser pulse.

2.1 Poor scaling problem

2.1.1 Single ionization

Suppose the Hamiltonian of the Schrödinger equation $\mathrm{i}\frac{\partial}{\partial_t}\psi(\vec{r},t) = H\psi(\vec{r},t)$ in velocity gauge is

$$H = -\frac{\Delta}{2} - \mathrm{i}\vec{A}(t)\cdot\vec{\nabla} + V(\vec{r}), \tag{2.2}$$

and the field-free scattering states are $\chi_{\vec{k}}$ with outgoing momenta $\vec{k}$ that satisfy $H\chi_{\vec{k}} = \frac{k^2}{2}\chi_{\vec{k}}$ and $\langle\chi_{\vec{k}'}|\chi_{\vec{k}}\rangle = \delta(\vec{k}' - \vec{k})$. The photoelectron spectrum is given by

$$P(\vec{k}) = \left|\langle\chi_{\vec{k}}|\lim_{t\to\infty}\psi(\vec{r},t)\rangle\right|^2, \tag{2.3}$$

which requires the propagation of the wavefunction from its initial state before the incoming of the pulse to some time after the end of the pulse, and its subsequent projection to the scattering states. The ionization and acceleration of particles in the external electric

field transform the ground state into bound and unbound states, of which the latter keeps spreading and renders nonzero overlap with the scattering states. Calculation of Eq. (2.3) necessitates a complete description of the outspreading wavefunction. For numerical computations, a general estimation of the scaling goes as follows. Suppose we have a n cycle pulse with intensity I, wavelength λ, and the time of one cycle is $\tau = \lambda/c$. Then, the maximum momentum of the electron can be approximated by

$$p_{\max} = \sqrt{2E_{\max}} \approx \sqrt{2 \cdot 10U_p} \propto \lambda\sqrt{I} \tag{2.4}$$

where we use the conclusion in Sec. 1.3.7 of the maximum energy $10U_p$. The maximum spreading of wavefunction in phase space by the product of momentum and distance is

$$V_r \sim r_{\max} \cdot p_{\max} \sim n\tau \cdot p_{\max} \cdot p_{\max} \propto n\lambda^3 I. \tag{2.5}$$

As the plane wave can be expanded by spherical harmonics $Y_l^m(\theta, \phi)$ and spherical Bessel functions $j_l(x)$

$$e^{\mathrm{i}\vec{k}\cdot\vec{r}} = 4\pi \sum_{l=0}^{\infty} \sum_{m=-l}^{l} \mathrm{i}^l j_l(kr) Y_l^m(\Omega_r) Y_l^{m*}(\Omega_k), \tag{2.6}$$

where l, m are always referred to as azimuthal quantum number and magnetic quantum number, in numerical discretization we set $0 \le l \le L_{\max}$ and $-M_{\max} \le m \le M_{\max}$ and $\Omega_{k/r} = (\theta_{k/r}, \phi_{k/r})$ represent the angles for momentum or position vectors. The expansion exponentially decays beyond a certain value controlled by l quantum number. In other words, the $L_{\max}$ is controlled by the free motion property, including the maximum momentum $k_{\max}$ and the maximum length $r_{\max}$. With large $k_{\max}$ and $r_{\max}$, we have the nearly linear dependence on density as follows:

$$L_{\max} \propto k_{\max} r_{\max} \propto \lambda^3 I, \tag{2.7}$$

similar to Eq. (2.5), where $k_{\max} \propto \sqrt{I}\lambda$ from Eq. (2.4) and $r_{\max} \sim r_q \propto \sqrt{I}\lambda^2$ is used to include the potential electrons returning to the core that deviates from the free motion. In linear polarization, there exists $m \equiv 0$ for symmetry. But for any arbitrary pulses, the similar scaling property

$$M_{\max} \propto \lambda^3 I \tag{2.8}$$

exits. Thus, the total scaling is the product of the three

$$V_r \cdot V_\theta \cdot V_\phi \cdot n\tau \propto n^2 \lambda^{10} I^3. \tag{2.9}$$

This indicates the total computational resource scales with 10th order of the wavelength and 3rd order of the intensity. The unfavorable scaling property makes the computation with long cycle infrared (IR) pulse at high intensity a challenging task.

2.1.2 Double ionization

The Hamiltonian of double ionization encompasses the tensor product of ionic Hamiltonian and unity operator $\mathbb{1}$, as well as the electron-electron (E-E) interaction term

$$H(t) = H_{\text{ion}}(\vec{r}_1, t) \otimes \mathbb{1} + \mathbb{1} \otimes H_{\text{ion}}(\vec{r}_2, t) + \frac{1}{|\vec{r}_1 - \vec{r}_2|}, \tag{2.10}$$

with the ionic Hamiltonian being

$$H_{\text{ion}}(\vec{r}, t) = -\frac{\Delta}{2} - \mathrm{i}\vec{A}(t) \cdot \vec{\nabla} + V(\vec{r}), \tag{2.11}$$

where $V(\vec{r}) = -\frac{2}{r}$ for the Helium atom. We denote the double ionized wavefunction as $\psi(\vec{r}_1, \vec{r}_2, t)$. The photoelectron spectra of the two liberated particles are

$$P(\vec{k}_1, \vec{k}_1) = \left| \langle\!\langle \chi_{\vec{k}_1, \vec{k}_2} | \lim_{t\to\infty} \psi(\vec{r}_1, \vec{r}_2, t) \rangle\!\rangle \right|^2, \tag{2.12}$$

where $\chi_{\vec{k}_1, \vec{k}_2}$ are the coupled two-electron scattering solutions that satisfy $H\chi_{\vec{k}_1, \vec{k}_2} = \frac{k_1^2 + k_2^2}{2}\chi_{\vec{k}_1, \vec{k}_2}$, double brackets $\langle\!\langle \cdots \rangle\!\rangle$ denote the overlap by integration over $\vec{r}_1, \vec{r}_2$ coordinates of the two-particle wavefunction. The single ionization photoelectron spectrum by double ionization is

$$P^I(\vec{k}) = \left| \langle\!\langle \chi^I_{\vec{k}} | \lim_{t\to\infty} \psi(\vec{r}_1, \vec{r}_2, t) \rangle\!\rangle \right|^2, \tag{2.13}$$

and $\chi^I_{\vec{k}}$ are the scattering solutions, with one electron occupying the ionic channel I that satisfy $H\chi^I_{\vec{k}} = \frac{k^2}{2}\chi^I_{\vec{k}}$. Similar to single ionization, the multi-channel out-spreading wavefunction $\psi(\vec{r}_1, \vec{r}_2, t)$ at the end of the pulse needs to be computed, with a complexity highly dependent on the laser parameters. The radial parts of the two coordinates r_1, r_2 are computed independently; thus, the phase space scales as $V_r^{DI} \propto n^2\lambda^6 I^2$. As we only focus on the linear polarization for double emissions in this thesis, with constraints on angular momenta (see Sec. 3.1.3), the scaling of angular space is identical to that of single ionization. Consequently, the simulated phase space expands as

$$V_r^{DI} \cdot V_\phi^{DI} \cdot V_\theta^{DI} \cdot n\tau \propto n^3\lambda^{13} I^4, \tag{2.14}$$

implying that the computation scales with the 13th order of the wavelength, 3rd order of the pulse duration, and 4th order of the intensity. A scaling property inferior to single ionization makes the double ionization calculation at a large wavelength very scarce.

Another inconvenience in calculating double ionization photoelectron spectra is extracting the double emission scattering amplitudes, which represent the total scattering solutions by the asymptotic momenta of the two particles. The most widely used strategy is to propagate the wavefunction long enough after the pulse and extract the wave packets in the asymptotic region where the various channels disentangle [54]. This requires an even larger simulation box than what is given above, and one may find examples from literature as listed below.

2.1.3 Discussion

As the photoelectron spectrum is not well defined in the presence of the field, one can only obtain the spectrum by collecting all the electrons after the end of the laser pulse. When one tries to precisely describe the out-spreading wavefunction in the whole phase space, including the parts far from the nucleus, the simulation box expands until the end of the time propagation, implying that large amounts of data are stored to describe the whole phase space in the memory and manipulate huge matrices, leading to high computational consumption.

The poor scaling problem is a challenge, especially for the 6D double ionization by laser pulses with large wavelength where the space is the tensor product of two 3D spaces. The double-ionization simulation was performed by various research groups, and many of them created a large simulation box with an extreme ultraviolet (XUV) pulse. In Ref. [49], a time-dependent close-coupling scheme (TDCC) [83] together with FE-DVR ([84, 85]) method are applied for two-electron ionization in a XUV pulse, and the wavefunction propagates for 21 fs after the pulse to project the ansatz into the energy-normalized coulomb waves for accuracy with the convergent radial size up to **800** a.u. The same method was applied by other groups to study ionization with a few photons [86–88] as well as the effects of an assisting IR streaking field [89]. Different discretization methods were applied. B-splines in the radial part for approximating the wavefunction and projection of wavefunction into products of uncorrelated numerical single-particle continuum states for spectrum analysis were reported in Ref. [90]; computation was applied in a XUV pulse, and the box size increased to **250** a.u. Ref. [51] reported finite difference methods, where doubly ionized wave packets were extracted from wavefunctions using masks. The method was also applied to a calculation with 390 nm pulse for various DI pathways with an extension of the box size to **1200** a.u. [52]. The box size reached **130** a.u. for simulating double emission at XUV pulse by surface integral with asymptotic form of wavefunction and Coulomb functions [91]. Despite some of the calculations on double ionization using different methods by other groups [51, 73, 92], the 6D, fully quantum calculations for wavelengths larger than 400 nm are scarce.

The time-dependent surface flux (tSurff) method computes the spectra only with information about a specific surface and largely increases the computational efficiency. In the following contents, the details of tSurff method are presented, and its scaling property is compared with Eq. (2.9).

2.2 Single electron tSurff

2.2.1 Methods

We suppress the Coulomb attraction that decays with r^{-1} from the nuclei by multiplying a function $f_{\alpha,\beta}(r)$ as

$$V(\vec{r}) \mapsto f_{\alpha,\beta}(|\vec{r}|)V(\vec{r}) \tag{2.15}$$

where $f_{\alpha,\beta}(r)$ satisfies

$$f_{\alpha,\beta}(r) := \begin{cases} 1 & r < \alpha \\ \frac{2}{(\alpha-\beta)^3}(r-\beta)^2(r-\frac{3\alpha-\beta}{2}) & \alpha \le r < \beta \\ 0 & r \ge \beta \end{cases} \tag{2.16}$$

to ensure the continuity of values and derivatives at $r = \alpha, r = \beta$. The truncation with $[\alpha, \beta]$ parameters are always checked carefully for convergence. We always choose $\beta = R_c$, which is the tSurff radius and will be explained later. The Hamiltonian is

$$H(t) = H_V(t),\ |\vec{r}| > R_c,\ \forall t. \tag{2.17}$$

where

$$H_V(t) = -\frac{\Delta}{2} - \mathrm{i}\vec{A}(t)\cdot\vec{\nabla} \tag{2.18}$$

when there is external electric field and

$$H_V(t) = -\frac{1}{2}\Delta \tag{2.19}$$

after the pulse is over. As the bound states remain localized and the continuous wave keeps moving after the pulse, at time T, which is long enough after the pulse, the wavefunction can be decomposed into bound and continuous spectra content by a box with the predefined radius R_c, wherein the bound state remains inside and the continuous wave outside

$$\psi(\vec{r}, T) = \psi_b(\vec{r}, T) + \psi_s(\vec{r}, T) \tag{2.20}$$

with the

$$\psi_b(\vec{r}, T) \approx 0, |\vec{r}| \ge R_c \tag{2.21}$$

being the bound part and

$$\psi_s(\vec{r}, T) \approx 0, |\vec{r}| \le R_c \tag{2.22}$$

being the scattering part. The approximation sign applies here because the exponential tail of the bound states extends to infinite distances beyond R_c, and there exists the low-momentum contribution of $\psi(\vec{r}, T)$ that remains in the simulation box at T. With the approximation, only $\psi_s(\vec{r}, t)$ contributes to the photoelectron spectrum $P(\vec{k})$.

The scattering solution of the TDSE with desired asymptotics is the delta normalized Volkov solution

$$\chi_{\vec{k}}(\vec{r}, t) = (2\pi)^{-3/2} e^{-\mathrm{i}\Phi(\vec{k},t)} e^{\mathrm{i}\vec{k}\cdot\vec{r}} \tag{2.23}$$

where

$$\Phi(\vec{k}, t) = \int_{-\infty}^{t} dt' \frac{\vec{k}^2}{2} + \vec{k}\cdot\vec{A}(t) \tag{2.24}$$

is called the Volkov phase. To compute the overlap, a step function with R_c is defined as

$$\Theta(R_c) = \begin{cases} 0, |\vec{r}| < R_c \\ 1, |\vec{r}| \ge R_c. \end{cases} \tag{2.25}$$

Thus, the scattering amplitudes $b(\vec{k},T)$ that contributes to the photoelectron spectrum

$$P(\vec{k}) = |b(\vec{k},T)|^2 \tag{2.26}$$

can be approximated by projection of unbound parts $\psi_s(\vec{r},T)$ on the scattering solutions $\chi_{\vec{k}}(\vec{r},t)$ at T as

$$\begin{aligned} b(\vec{k},T) =& \langle \chi_{\vec{k}}(T) \left| \Theta(R_c) \right| \psi(T) \rangle = \int_{-\infty}^{T} \frac{d(\langle \chi_{\vec{k}}(t) \left| \Theta(R_c) \right| \psi(t) \rangle)}{dt} dt \\ =& \int_{-\infty}^{T} \langle \frac{d\chi_{\vec{k}}(t)}{dt} \left| \Theta(R_c) \right| \psi(t) \rangle + \langle \chi_{\vec{k}}(t) \left| \Theta(R_c) \right| \frac{d\psi(t)}{dt} \rangle dt \\ =& \int_{-\infty}^{T} \mathrm{i} \langle \chi_{\vec{k}}(t) \left| H_V(t) \Theta(R_c) \right| \psi(t) \rangle - \mathrm{i} \langle \chi_{\vec{k}}(t) \left| \Theta(R_c) H_V(R_c) \right| \psi(t) \rangle dt \\ =& \mathrm{i} \int_{-\infty}^{T} dt \langle \chi_{\vec{k}}(t) \left| [H_V(t), \Theta(R_c)] \right| \psi(t) \rangle, \end{aligned} \tag{2.27}$$

where the assumption Eq. (2.17) is used and

$$F(\vec{k},t) = \langle \chi_{\vec{k}}(t) \left| [H_V(t), \Theta(R_c)] \right| \psi(t) \rangle \tag{2.28}$$

is called the flux. The commutator operator $[H_V(t), \Theta(R_c)]$ on a spherical coordinate can be written as

$$[H_V(t), \Theta(R_c)](r,\phi,\eta) = -\frac{1}{2}\frac{1}{r^2}\partial_r r^2 \delta(r-R_c) - \frac{1}{2}\delta(r-R_c)\partial_r - \mathrm{i}A_z \eta \delta(r-R_c), \tag{2.29}$$

where $\eta = \cos\theta \in [-1,1]$ if not specified otherwise in this thesis. The Volkov solution in Eq. (2.23) with the expansion of plane wave from Eq. (3.5) is

$$\chi_{\vec{k}}(\vec{r},t) = \frac{e^{\mathrm{i}\Phi(\vec{k},t)}}{\sqrt{\pi/2}} \sum_{l,m} \mathrm{i}^l j_l(kr) Y_l^m(\Omega_r) Y_l^{m*}(\Omega_k). \tag{2.30}$$

With the Volkov solution in Eq. (2.30), the matrix element of the commutator operator is

$$\langle \chi_{\vec{k}}(t) \left| [H_V(t), \Theta(R_c)] \right| \psi(t) \rangle = \frac{e^{\mathrm{i}\Phi(\vec{k},t)}}{\sqrt{\pi/2}} R_c^2 \sum_{l,m} (-\mathrm{i})^l Y_l^m(\Omega_k) (J_{lm} - \mathrm{i}A_z K_{lm}), \tag{2.31}$$

where

$$J_{lm} \coloneqq \frac{1}{2} j_l'(kR_c) R_{lm}(R_c,t) - \frac{1}{2} j_l(kR_c) R_{lm}'(R_c,t) \tag{2.32}$$

is the flux from lm partial wave,

$$K_{lm} \coloneqq \sum_{s=\pm 1} \langle Y_l^m(\Omega_r) | \cos\theta_r | Y_{l+s}^m(\Omega_r) \rangle j_l(kR_c) R_{l+s,m}(R_c,t) \tag{2.33}$$

is the correction term for the dipole field and $R_{lm}(r,t)$ is the radial function, see Eq. (3.30) in Sec. 3.1.1. Here, we only keep A_z term as we will mainly focus on the linear polarization

along z-direction in this thesis. The $j_l(x)$ is the spherical Bessel function. Detailed derivation of Eq. (2.31) can be found in the supplementary information in Sec. A.5.1. The matrix element of the commutator operator calculation only requires the values and derivatives of the wavefunction on the boundary R_c, rather than the values in full space. Moreover, one only needs an accurate approximation of wavefunction inside R_c, no matter how broadly the wavefunction spreads in space. This method largely reduces the computational cost for matrix operation and memory usage of coefficients for describing the wavefunction. With this method, one needs to store the **t**ime-dependent **Surf**ace **f**lux information for the spectrum. This is where the name **tSurff** comes from. The method was originally reported in Ref. [93], and has been successfully applied to single-electron systems such as Hydrogen atom [94] and single ionization of Helium model [95].

2.2.2 Scaling property

The tSurff method calculation only requires the surface values and derivatives of the wavefunction at R_c, instead of its information on the whole phase space. One only needs the simulation box size R_0 large enough that the absorber beyond R_0 does not affect the motions of electrons in the box, which can be approximated by $r_q = \frac{E}{\omega^2}$, see Sec. 1.3.7, where E, ω are the peak electric field and frequency. The single emission spectrum of a hydrogen atom in a 1600 nm laser pulse [82] also shows the converged simulation box size satisfies $R_0 \sim r_q$ and $R_0 \geq r_q$. The scaling property of tSurff method differs from the above in

$$R_0 \sim r_q = \frac{E}{\omega^2} \propto \sqrt{I}\lambda^2, \tag{2.34}$$

which contributes to scaling in radial part as

$$V_r \sim r_q \cdot p_{\max} \sim \sqrt{I}\lambda^2 \cdot p_{\max} \propto \lambda^3\sqrt{I}. \tag{2.35}$$

Similarly, the scaling on phase space θ and ϕ are given by

$$V_\theta \propto \lambda^3 I, V_\phi \propto \lambda^3 I. \tag{2.36}$$

The total scaling from the product of the three is

$$V_r \cdot V_\theta \cdot V_\phi \cdot n\tau \propto n\lambda^{10} I^3, \tag{2.37}$$

with only n removed from the above Eq. (2.9). However, a careful examination shows tSurff of a 3D computation optimizes the scaling to a factor $(10n)^3$ for a long wavelength single ionization calculation [82] as is on $r_{\max}$

$$\frac{r_{\max}}{R_0} = \frac{n\tau\sqrt{2 \cdot 10U_p}}{R_0} = \frac{n\frac{2\pi}{\omega}\sqrt{10\frac{E^2}{4\omega^2}}}{\frac{4}{3}\frac{E}{\omega^2}} \approx 10n, \tag{2.38}$$

where the quiver radius is independent of the pulse length n and $R_0 \approx \frac{4}{3}r_q$ is the optimal choice from our convergence study.

2.2.3 Discussion

In this section, we add a short discussion of the radius R_0 and R_c. The tSurff radius R_c is chosen to distinguish the bound and unbound contributions of a specific electron. The solution of Hamiltonian beyond R_c can be written in the asymptotic form; for example, Volkov solutions, where the Coulomb interaction from the nucleus and electrons are truncated. R_0 defines the simulation box for precisely approximating the movement of electrons beyond which the emission is absorbed. In our tRecX code (see Sec. 3.6 or Ref. [96]), the absorber is constructed by the infinite-range complex scaling method (see Sec. 3.3), which starts at R_0 and R_0 is also named complex scaling radius. The recollision of the free electron with the ion would be suppressed if the electron is reverted from $r > R_0$, suggesting the electron dynamics must be kept before absorption. The problem can be solved by choosing R_0 above the quiver radius, the electrons beyond which hardly come back close to the parent ion for recollision. The particle, which is far from the nucleus $r \geq R_c$ within its huge quiver radius, can be approximated by Volkov solutions but needs to stay in the simulation box for convergence. Thus, $R_0 \geq R_c$ is required. To reduce the error introduced by the truncation of Coulomb potentials, we set $\beta = R_c = R_0$, where β is the truncation radius from Eq. (2.16).

The tSurff method has the following limitations. First, the long tail of the Coulomb potential is truncated at R_c, requiring scrutiny of R_0 and R_c parameters by convergence study. Second, the photoelectron spectrum is computed by fluxes passing through R_c. To include low-energy particles, the wavefunction needs to be propagated long enough after the pulse ends. It is worth to mention that with the iSurff method, the standard spectra analysis is made after the pulse is off [97]. Third, the highly excited Rydberg states reaching R_c that do not decrease with the increasing R_c also lead to artifacts in the photoelectron spectra. The artifacts can be reduced by the time average of the scattering amplitudes in the time propagation (see Ref. [54]).

The tSurff method has two successful extensions: for single ionization on small molecules (the haCC) and for double ionization on two-electron systems.

2.3 haCC-hybrid anti-symmetrized Coupled Channels

2.3.1 Fuse strong field methods and electronic structure

Solving the high-dimensional TDSE of the few-electron structures of molecules and atoms is a complex problem. Efforts have previously been made to analyze electron dynamics [98]. The key strategy in the methods was to discretize the wave packet with a subspace the full Hilbert space, which is sufficient for describing the electronic structure [99].

Here, we give a short summary of the well-known approaches. Time-dependent Hartree-Fock (TDHF) theory [100] creates an ansatz of all electrons with a single Slater determinant for all the (time-dependent) single-particle orbitals, and correlation is not included. The Hartree-Fock (HF) equation is solved by the self-consistent field (SCF) method [101]; thus, the names "SCF" and "HF" are used interchangeably in many quantum chemistry

methods. As an extension to TDHF, the multi-configuration time-dependent Hartree-Fock (MCTDHF) approach [100, 102] forms a complete basis, as apposed to single-particle orbital in TDHF, where the coefficients and orbitals are all time-dependent. MCTDHF gives a compact description of the wavefunction but has unfavorable scaling with the number of electrons. The variants of the MCTDHF approach include the complete active space self-consistent field method (TD-CASSCF) [103] and time-dependent restricted-active-space self-consistent field method (TD-RASSCF) [104, 105] for specific problems. The time-dependent configuration interaction (TDCI) method introduces the time-independent "occupied" and "virtual" orbitals (excited states) as the field-free Hartree-Fock orbitals, and only the coefficients vary with time. The wavefunction of TDCI is a linear combination of Hartree-Fock determinants, each representing a configuration of "occupied" and "virtual" orbitals. When the "virtual" orbitals only contain the single excitations, the TDCI is simplified to time-dependent interaction singles (TD-CIS) [106, 107]. The coupled channels formalism [108, 109] discretizes the ansatz into various neutral-bound and single-ionic states, whose size is free from the number of electrons, making it easily applicable to large systems. The R-matrix method is similar to coupled channel formalism except that it divides the physical space into two regions, treating the inner region exact but the outer region with approximations.

The correlated bound electron states and their relative transitions can be precisely described using existing quantum chemistry packages (QCP), but the simulation of correlated states in the electronic continuum is quite challenging. First, the local orbitals in QCP fail to describe the oscillating electronic wavefunction for large distances, and the orbitals for describing unbound states must have some asymptotic behaviors [110]. Second, calculating the bound states and continuous wave requires different algorithms—the eigenenergy of the former is unknown and degeneracy only exists for selected subsets, whereas the eigenenergy of the latter is always given and infinite degeneracy exists in a continuous wave [110]. Recently, Martin et al. [110] developed the XCHEM code to solve ionization of polyelectron molecules and atoms with close-coupling scattering methods implemented using a hybrid Gaussian B-spline basis that interfaces with the existing quantum chemistry package MOLPRO, which was successfully applied to describe the photoionization of He, N_2, Ne and O_2 [110–114]. Douguet et al. reported the simulation of the photoionization of He in the perturbative regime by complex Kohn variational method[115].

In this section, we present our hybrid anti-symmetrized coupled channels (haCC) method for simulating the photoionization of the polyelectron atoms and molecules, which successfully combines the tSurff method for dealing with ionization process and traditional quantum chemistry calculations. The haCC method unitizes both the approaches for precise ab initio calculations by creating anti-symmetrized coupled channels from the two methods. Rather than using Gaussian B-splines basis for approximating the continuous wave as in XCHEM code [110], we implement FE-DVR for numerical discretization in haCC, as it better describes the re-scattering process. We have successfully applied haCC for the simulations in photoionization of He, Be, H_2, Ar, Ne, O_2, CO_2 and N_2 [66, 109, 116, 117].

2.3.2 Multi-electron discretization

The haCC method solves the single ionization photoelectron spectra of the N electron system with the field-free Hamiltonian

$$\hat{H}_0 = \sum_i [-\frac{\Delta_i}{2} + V(\vec{r}) - \sum_p \frac{Z_p}{|\vec{r}_i - \vec{R}_p|}] + \sum_{i<j} \frac{1}{|\vec{r}_i - \vec{r}_j|}, \tag{2.39}$$

where Z_p is the charge of the pth nucleus, and the dipole interaction term is $D^L = \sum_j E(\vec{t})\cdot\vec{r}_j$ for length gauge and $D^L = \sum_j \mathrm{i}A(\vec{t})\cdot\vec{\nabla}_j$. We discretize the N-particle wavefunction using channel wavefunctions formed by the anti-symmetrized product of the one-electron base and the ionic states, to which we add the neutral ground state wavefunction. The formula is given below

$$|\Psi(t)\rangle \approx \sum_{\mathcal{I}} |\mathcal{I}\rangle C_{\mathcal{I}}(t) + \sum_{\mathcal{N}} |\mathcal{N}\rangle C_{\mathcal{N}}(t), |\mathcal{I}\rangle = \mathcal{A}|i\rangle|I\rangle \tag{2.40}$$

where $|i\rangle$ is an one-electron basis, $|I\rangle$ and $|\mathcal{N}\rangle$ are the ionic and neutral ground states that are obtained by COLUMBUS code with multi-reference configuration interaction singles doubles (MR-CISI) method [118], $\mathcal{A}[\ldots]$ is the anti-symmetrization operator and $C_{I,i}(t), C_{\mathcal{N}}(t)$ are the expansion coefficients. The first part $\sum_{I,i} \mathcal{A}|i\rangle|I\rangle C_{\mathcal{I}}(t)$ is the coupling term of the ionized and the unionized particles where the anti-symmetrization is satisfied for Pauli's exclusion principle. The second term $\sum_{\mathcal{N}} |\mathcal{N}\rangle C_{\mathcal{N}}(t)$ represents the ground state of the system. The hybrid one-electron basis is a combination of the atom-centered Gaussian and finite-element methods (see Sec. 3.1.2). The inter-channel electron-electron exchanges are all included. We include the explicit neutral ground state $\mathcal{N}$, to increase the computational efficiency because of a strong correlation of the ground state. The description of correlation behavior needs more active orbitals only for the ground state. Introducing it explicitly reduces the number of active orbitals and increases numerical efficiency.

The orbitals of wavefunction of Eq. (2.40) are independent of time; time dependency is in the coefficients. The propagation of the time-dependent coefficients can be constructed by multiplying the "bra" vector of $\mathcal{N}$ and $\mathcal{I}$ on the left, resulting in two ordinary differential equations below

$$\mathrm{i}\frac{dC_{\mathcal{I}}(t)}{dt}\langle\mathcal{I}|\mathcal{I}\rangle + \mathrm{i}\frac{dC_{\mathcal{N}}(t)}{dt}\langle\mathcal{I}|\mathcal{N}\rangle = \langle\mathcal{I}|\hat{H}|\mathcal{I}\rangle C_{\mathcal{I}}(t) + \langle\mathcal{I}|\hat{H}|\mathcal{N}\rangle C_{\mathcal{N}}(t) \tag{2.41}$$

$$\mathrm{i}\frac{dC_{\mathcal{I}}(t)}{dt}\langle\mathcal{N}|\mathcal{I}\rangle + \mathrm{i}\frac{dC_{\mathcal{N}}(t)}{dt}\langle\mathcal{N}|\mathcal{N}\rangle = \langle\mathcal{N}|\hat{H}|\mathcal{I}\rangle C_{\mathcal{I}}(t) + \langle\mathcal{N}|\hat{H}|\mathcal{N}\rangle C_{\mathcal{N}}(t). \tag{2.42}$$

The propagation of coefficients is explicitly performed with the 4th order Runge-Kutta method with an adaptive step size. This standard way of solving the TDSE is further illustrated in chapter 3. More details on the haCC method can be found in Ref. [109].

Anti-symmetrization effectively enlarges the accessible space. Apart from the tSurff method for the spectrum, other methods such as the infinite-range exterior complex scaling

are applied for the numerical calculations, as shown in Sec. 3.3. We also apply the mixed-gauge method for numerical efficiency and computational resource. The transformation from the length gauge to the mixed gauge is

$$\psi_{\text{mixed}}(\vec{r},t) = e^{\mathrm{i}A(\vec{t})\cdot\frac{\vec{r}}{r}(r-R_g)\Theta(R_g)}\psi_{\text{L}}(\vec{r},t). \tag{2.43}$$

where R_g is the gauge radius and is always chosen $R_g = R_c = R_0$. With the above transformation, the wavefunction at r_g remains continuous at all times [119]. Details of the mixed gauge can be found in Sec. 3.4.

2.3.3 Representation of states and orbitals

The haCC wavefunction from Eq. (2.40) has a similar form to that of ansatz created by quantum chemistry in that they are both linearly expanded, and their states are represented by products of single-particle orbitals, which are pure Hartree-Fock orbitals for CI and a mixture of a free-electron orbital and Hartree-Fock orbitals for haCC. These following contents about the wavefunctions and matrix elements are mainly taken from the previous works of our group from Ref. [117]. Suppose the single-electron Hartree-Fock orbitals of the "n" electrons are $\Phi_1, \Phi_2, ..., \Phi_n$, the ionic and neutral state wavefunctions of the system can be represented by

$$|I\rangle = \sum_{p_1,\cdots,p_{n-1}} d_{p_1,\cdots,p_{n-1}} |\mathcal{A}[\Phi_{p_1}\cdots\Phi_{p_{n-1}}]\rangle \tag{2.44}$$

$$|\mathcal{N}\rangle = \sum_{p_1,\cdots,p_n} d_{p_1,\cdots,p_n} |\mathcal{A}[\Phi_{p_1}\cdots\Phi_{p_n}]\rangle \tag{2.45}$$

where $d_{p_1,\ldots,p_{n-1}}$ and $d_{p_1,\ldots,p_n}$ are the coefficients and the indexes satisfy $1 \le (i,p_i) \le n$, which also applies to the formulas below. The corresponding multi-particle reduced density matrices of two ionic states I, J are

$$\rho^{IJ}_{k_1,\cdots,k_p,l_1,\cdots,l_p} = \langle I|a^\dagger_{k_1}\cdots a^\dagger_{k_p} a_{l_1}\cdots a_{l_p}|J\rangle \tag{2.46}$$

and the generalized Dyson coefficients of an ionic state and a neutral state can be represented by

$$\eta^{\mathcal{N}J}_{k_1,\cdots,k_p,l_1,\cdots l_{p-1}} = \langle\mathcal{N}|a^\dagger_{k_1}\cdots a^\dagger_{k_p} a_{l_1}\cdots a_{l_{p-1}}|J\rangle, \tag{2.47}$$

where $a^\dagger_{k_i}, 1 \le (i,k_i) \le n$ and $a_{l_j}, 1 \le (j,l_j) \le n$ are creation and annihilation operators on k_ith and l_jth orbitals. The overlap of the states are

$$\langle\mathcal{N}|\mathcal{N}\rangle = 1 \tag{2.48}$$

$$\langle\mathcal{N}|I,i\rangle = \eta^{\mathcal{N}I}_k \langle\Phi_k|i\rangle \tag{2.49}$$

$$\begin{aligned}\langle I,i|J,j\rangle =& \langle i|j\rangle\langle I|J\rangle - \langle i|\Phi_l\rangle\rho^{IJ}_{kl}\langle\Phi_k|j\rangle \\ =& \langle i|j\rangle\delta_{IJ} - \langle i|\Phi_l\rangle\rho^{IJ}_{kl}\langle\Phi_k|j\rangle\end{aligned} \tag{2.50}$$

2.3.4 Matrix elements

Any exchange-symmetric single-particle operator can be written as

$$\hat{T} = t(\hat{1}) + t(\hat{2}) + \cdots t(\hat{n}) = \sum_{i}^{n} t(\hat{i}). \tag{2.51}$$

The matrix elements for a single-particle operator, represented by two neutral channels are

$$\langle \mathcal{N} \left| \hat{t} \right| \mathcal{N} \rangle = \rho_{kl}^{\mathcal{N}\mathcal{N}} \langle \Phi_k \left| \hat{t} \right| \Phi_l \rangle, \tag{2.52}$$

for a neutral channel and an ionic channel are

$$\langle \mathcal{N} | \hat{T} | I, i \rangle = \eta_{k}^{\mathcal{N}I} \langle \Phi_k | \hat{t} | i \rangle + \eta_{klm}^{\mathcal{N}I} \langle \Phi_k | \hat{t} | \Phi_m \rangle \langle \Phi_l | i \rangle, \tag{2.53}$$

and for two ionic channels are

$$\begin{aligned} \langle I, i | \hat{T} | J, j \rangle = & \underbrace{\langle i|j\rangle\langle I|\hat{t}|J\rangle + \langle i|\hat{t}|j\rangle\langle I|J\rangle}_{\text{direct}} + \underbrace{-\langle i|\hat{t}|\Phi_l\rangle\rho_{kl}^{IJ}\langle\Phi_k|j\rangle - \langle i|\Phi_l\rangle\rho_{kl}^{IJ}\langle\Phi_k|\hat{t}|j\rangle}_{\text{exchange}} \\ & \underbrace{- \langle i|\Phi_c\rangle\langle\Phi_a|j\rangle\langle\Phi_b|\hat{t}|\Phi_d\rangle\rho_{abcd}^{IJ}}_{\text{non-orthogonality } \langle\Phi_k|i\rangle \neq 0}. \end{aligned} \tag{2.54}$$

The two-particle operators

$$\hat{V} = \sum_{i<j}^{n} v_{\hat{ij}} \tag{2.55}$$

have matrix elements

$$\langle \mathcal{N} \left| \hat{V} \right| \mathcal{N} \rangle = \frac{1}{2} \rho_{abcd}^{\mathcal{N}\mathcal{N}} \langle \Phi_a \Phi_b \left| \hat{v} \right| \Phi_c \Phi_d \rangle \tag{2.56}$$

for two neutral channels,

$$\langle \mathcal{N} | \hat{V} | I, i \rangle = \eta_{klm}^{\mathcal{N}I} \langle \Phi_k \Phi_l | \hat{v} | \Phi_m i \rangle + \frac{1}{2} \eta_{abcde}^{\mathcal{N}I} \langle \Phi_a \Phi_b | \hat{v} | \Phi_d \Phi_e \rangle \langle \Phi_c | i \rangle \tag{2.57}$$

for one neutral and ionic channel,

$$\begin{aligned} \langle I, i | \hat{V}^{(2)} | J, j \rangle = & \frac{1}{2} \rho_{kl}^{IJ} \langle \Phi_a \Phi_b | \hat{v} | \Phi_c \Phi_d \rangle \langle i | j \rangle + \underbrace{\rho_{kl}^{IJ} \langle \Phi_k i | \hat{v} | \Phi_l j \rangle}_{\text{direct term}} \underbrace{- \rho_{kl}^{IJ} \langle \Phi_k i | \hat{v} | j \Phi_l \rangle}_{\text{standard exchange term}} \\ & \underbrace{- \rho_{abcd}^{IJ} \langle \Phi_a i | \hat{v} | \Phi_c \Phi_d \rangle \langle \Phi_b | j \rangle - \rho_{abcd}^{IJ} \langle \Phi_a \Phi_b | \hat{v} | \Phi_c j \rangle \langle i | \Phi_d \rangle}_{\text{extra terms due to non-orthogonality}} \\ & \underbrace{- \frac{1}{2} \rho_{abcdef}^{IJ} \langle \Phi_a \Phi_b | \hat{v} | \Phi_d \Phi_e \rangle \langle i | \Phi_f \rangle \langle \Phi_c | j \rangle}_{\text{extra terms due to non-orthogonality}}. \end{aligned} \tag{2.58}$$

and two ionic channels.

The overlap matrix of two ionic states in Eq. (2.50) is different from that of the standard finite elements, which may be banded and allows efficient numerical application for its inverse. However, the inverse overlap can still be efficiently computed with the Woodbury formula and using a low-rank update [120]

$$S^{-1} = (S_0 - U\Lambda U^\dagger)^{-1} = S_0^{-1} - S_0^{-1}U(U^\dagger S_0^{-1}U - \Lambda^{-1})^{-1}S_0^{-1}. \tag{2.59}$$

The overlap matrix of a two-channel example can be re-written in the form

$$S = \underbrace{\begin{pmatrix} s_0 & 0 & 0 \\ 0 & s_0 & 0 \\ 0 & 0 & 1 \end{pmatrix}}_{S_0} - \underbrace{\begin{pmatrix} u & 0 & 0 \\ 0 & u & 0 \\ 0 & 0 & 1 \end{pmatrix}}_{U} \underbrace{\begin{pmatrix} \rho^{11} & \rho^{12} & \eta^{\mathcal{N}1} \\ \rho^{21} & \rho^{22} & \eta^{\mathcal{N}2} \\ [\eta^{\mathcal{N}1}]^T & [\eta^{\mathcal{N}2}]^T & 0 \end{pmatrix}}_{\Lambda} U^\dagger \tag{2.60}$$

which satisfies the Woodbury formula, where

$$(s_0)_{ij} := \langle i|j\rangle, \qquad u_{ik} := \langle i|\Phi_k\rangle. \tag{2.61}$$

S_0 is banded for FEM and diagonal for FEM-DVR (see Sec. 3.1.2) and its inverse can be easily computed. The size of Λ is $(n_I n_{hf} + 1) \times (n_I n_{hf} + 1)$, much smaller than $(n_I n_a + 1) \times (n_I n_a + 1)$ of S, where n_I is the number of ionic states, n_{hf} is the number of Hartree-Fock orbitals and n_a is the number of active electron basis functions.

Another hurdle to overcome for the inverse of overlap matrix is singularity. Because we do not add orthogonal constraints to the active orbitals with respect to the Hatree-Fock orbitals, the near-linearity property of various $|i\rangle$ with respect to the Hartree-Fock states Ψ_k may render the anti-symmetrized haCC basis linearly dependent. This introduces near-zero eigenvalues of the overlap matrix, which makes its inversion numerically challenging. For numerical efficiency, the inverse operation of the overlap matrix is only applied on the subset spanned by non-singular eigenvectors, written as a pseudo-inverse $\tilde{S}^{-1}$ that satisfies $\tilde{S}^{-1}SQ = Q$, which could also be written with the Woodbury formula, where Q is a projector for removing the near singular eigenvectors. For the original reference of the above methods, refer to Ref. [66, 109].

2.3.5 Static field ionization

The ionization process under a laser field at its low-frequency limit is well modeled by quasi-static approximation, which means that ground-state depletion in the three-step model can be described by the static field ionization rates [116]. The interpretation of high harmonic spectroscopy (HHS) [121] and laser-induced electron diffraction (LIED) [122] depends on correct static field ionization rates from single-electron models.

For dealing with static field ionization problems, many analytic formulas with semi-classical approximations, such as WKB approximation [123] and saddle point approximation, have been proposed. One of the popular formulas is the ADK formula [62] (also detailed in Sec. 1.3.3), with its extension MO-ADK [64] formula, which considers the

asymptotic behavior and symmetric property of a wavefunction as well as its empirical correction by extension to a barrier suppression regime [124]. Being a simple analytic formula, the ADK formula has many disadvantages. First, it fails to describe the transition region where the effects of the Coulomb force and external field are comparable. Moreover, compared to the numerical calculations [125, 126] of Helium, the ADK formula overestimates ionization rates even in situations where one can give exact solutions [127]. Second, it fails to describe the ionization beyond single-electron models. Single-electron models such as MO-ADK fail due to the neglect of exchange effects in angle-dependent ionization of CO_2 [65, 66]. The neglect of the multi-electron effects of ADK might be responsible for its failure in describing the ionization of transition metal atoms [67]. For a detailed description of the background, readers are re-directed to Ref. [116].

In this section, we show the static field ionization described by the haCC method and infinite-range complex scaling method, which successfully produce the ionization rates for N_2, CO [116] and the angle-dependent ionization of CO_2 [66]. The content of the method is mainly from previous work in our lab published in Ref. [116].

The static field ionization Hamiltonian for an N-particle system is

$$H = \sum_{n=1}^{N} [T_n + V_n + \vec{r}_n \cdot \vec{E}] + V_{E-E}, \tag{2.62}$$

where T_n is the single-particle kinetic energy, V_n is the nuclear potential on the nth particle, $\vec{r}_n \cdot \vec{E}$ is the electric potential energy on the nth coordinate, and V_{E-E} is the electron-electron repulsion term. To avoid confusion of the notation for the active electron basis $|i\rangle$ and imaginary number i, we use n to denote the active electron basis of the liberated electron.

An ideal way to solve the decay rates is by transforming the Hamiltonian to non-hermitian via infinite-range exterior complex scaling method, which transforms the radial axis to

$$r \mapsto r_\theta = \begin{cases} r & r \le R_0 \\ R_0 + e^{\mathrm{i}\theta}(r - R_0) & r > R_0 \end{cases} \tag{2.63}$$

where θ is the scaling angle, and R_0 is the complex scaling radius, beyond which the electron is absorbed; for details refer to Sec. 3.3. As this thesis mainly focuses on single ionization, the ansatz for the static field ionization calculation can be created using the haCC method.

We choose a large enough R_c that the bound molecular orbitals represented by CI functions are negligible beyond R_c ($|\vec{r}_n| > R_c$). The Hartree potential is smoothly truncated, which starts at $a < R_c$ and ends at R_c.

With the above-mentioned approximations, we divide the space for simulation into the unscaled region with $|\vec{r}_n| \le R_0$, $n = 1, \ldots, N$ and N single-scaled region with $S_n : |\vec{r}_n| > R_0, |\vec{r}_m| \le R_0, m = 1, \ldots, N, m \ne n$. The Hamiltonian in the unscaled region is unchanged, as shown in Eq. (2.62), and that for the single-scaled region S_n is

$$H_n = H_{\text{ion}}^{(\check{n})} - e^{-2\mathrm{i}\theta}\frac{\Delta}{2} + [R_0 + e^{\mathrm{i}\theta}(r_n - R_0)]\hat{r_n} \cdot \vec{E}, \tag{2.64}$$

with a liberated electron n in the complex scaled region $\vec{r}_n > R_0$ and the others in bound states $\vec{r} \leq R_0$. The $\mathrm{H}_{\mathrm{ion}}^{(\check{n})}$ denotes the Hamiltonian of the other bound electrons.

A physical property of the eigenvalue is that it is independent of the types (Spherical, Cartesian and Cylindrical et.al), and scaling of the coordinates. This means that physically useful eigenvalues are independent of θ and the finite intervals (see Sec. 3.3 and Ref. [128]) with which one can distinguish true resonance states from accidental eigenvalues introduced by the finite discretization and complex scaling angles. The eigenvalues of the complex scaled Hamiltonian are complex values; their real parts represent energy and imaginary parts represent (twice) the decay width.

With the calculations performed on the different complex scaling angles (θ), we obtain the eigenvalue of the resonant state as $E_f = r_f - \mathrm{i}\frac{\Gamma_f}{2}$, and the Schrödinger equation is

$$\mathrm{i}\partial_t \psi_n(t) = E_f \psi_n(t), \tag{2.65}$$

where the subscript f refers to the "static field." The time-evolution of the field-ionization state is

$$\psi_n(t) = e^{-\mathrm{i}E_f t}\psi_n(t_0) = e^{-\mathrm{i}r_f t}e^{-\frac{\Gamma_f}{2}t}\psi_n(t_0) \tag{2.66}$$

with its norm decaying as

$$|\psi_n(t)|^2 = \langle\psi_n(t)|\psi_n(t)\rangle = e^{-\Gamma_f t}|\psi_n(t_0)|^2, \tag{2.67}$$

where Γ_f is the ionization rate.

2.3.6 Combination with Classical Trajectory Monte Carlo

Although experimental observables can be extracted from wavefunctions by solving the time-dependent Schrödinger equation (TDSE), an intuitive description of the motions is hard to obtain because of the uncertainty principle; however, it is possible with classical trajectory methods wherein the movement of the wave packet is represented by the weighted average of various independent classical trajectories simulated by solving Newton's equation [129]. With classical models, one can simulate the movement of electrons in a large system with a low computational resource, where the problem does not scale dramatically with laser parameters and dimensions. One of the famous classical trajectory Monte Carlo (CTMC) methods was reported in Ref. [55].

The CTMC method first runs a large number of semi-classical simulations with random initial values and then analyzes the statistic behavior of the results to obtain an averaged description of the particles. The external electric field strongly varies with time and considerably affects the ionization probability of the particles. We assume the particle ionizes at time t_0 with the phase $\phi_0 = t_0\omega$ and include the ionization rate as the weight for the averaged probability under consideration as

$$p^{\mathrm{proc}} = \frac{\sum_{\phi_0} p_{\phi_0}^{\mathrm{proc}}\Gamma(\phi_0)}{\sum_{\phi_0}\Gamma(\phi_0)}, \tag{2.68}$$

where $\Gamma(\phi_0)$ is the ionization rate at phase ϕ_0. p^{proc} and $p^{\text{proc}}_{\phi_0}$ describes the probabilities of the overall process and a single phase, respectively [55]. To include the quantum effects in the simulations, CTMC takes advantage of quantum chemistry methods for ionization rates [55, 130]. However, quantum chemistry computation is limited to describing the bound states of the molecules and fails in the free particles (unbound states). As shown above, haCC efficiently provides the static field ionization rates of a few-electron molecules, which serve as the valuable initial values for CTMC calculations.

2.4 Two electron tSurff

Many groups have solved the TDSE with two electrons at the XUV zone, as reported by various works [49, 89, 90, 131–134] because the computation favors small wavelength due to the scaling property in Eq. (2.14) and the perturbative method may apply [135, 136]. The famous two-photon ionization of XUV region was simulated by using the R-matrix Floquet theory [137, 138] and solving TDSE for the correlated behavior of two particles [87, 88]. The difficulties to overcome in a double-ionization simulation include the representation of the double continuum and scaling problem, as shown above [54]. Our two-electron calculation with tSurff in a 400 nm laser pulse only requires a radial extension to 40 a.u., which is much lower than those in the literature (see Sec. 2.1.3). In this section, we demonstrate the methods for extending tSurff to double-ionization simulations.

The Hamiltonian of the two-electron interacting system can be written as

$$H(t) = H_{\text{ion}}(t) \otimes \mathbb{1} + \mathbb{1} \otimes H_{\text{ion}}(t) + V_{\text{E-E}}, \tag{2.69}$$

which includes the tensor product of the ionic Hamiltonian

$$H_{\text{ion}}(t) = -\frac{\Delta}{2} - \mathrm{i}\vec{A}(t) \cdot \vec{\nabla} + V(\vec{r}), \tag{2.70}$$

and the unity operator $\mathbb{1}$ as well as the electron-electron interaction

$$V_{\text{E-E}} = \frac{1}{|\vec{r}_1 - \vec{r}_2|}, \tag{2.71}$$

where we have $V(\vec{r}) = -\frac{2}{|\vec{r}|}$ for Helium. The Coulomb attraction from the nuclei for the two particles as well as the repulsion of electrons are suppressed beyond a radial extension by multiplying a function $f_{\alpha,\beta}(r)$, which is also used in Sec. 2.2 as

$$\begin{aligned} V(\vec{r}) &\mapsto f_{\alpha,\beta}(|\vec{r}|)V(\vec{r}) \\ \frac{1}{|\vec{r}_1 - \vec{r}_2|} &\mapsto \frac{f_{\alpha,\beta}(|\vec{r}_1|)f_{\alpha,\beta}(|\vec{r}_2|)}{|\vec{r}_1 - \vec{r}_2|}. \end{aligned} \tag{2.72}$$

In tSurff for double ionization, we also choose $0 < \alpha \leq R_c, \beta = R_c$. This approximation is not specific to tSurff, as many asymptotic analysis show that the total scattering solution can be written as the product of two single scattering solutions, implying that the interaction of the two particles is neglected in the asymptotic region.

2.4.1 Double ionization photoelectron spectra

In our method, the two-electron scattering solution at T after time propagation can be written as $\chi_{\vec{k_1},\vec{k_2}}(\vec{r_1},\vec{r_2},T) \approx \chi_{\vec{k_1}}(\vec{r_1},T)\chi_{\vec{k_2}}(\vec{r_2},T)$ where $\chi_{\vec{k}_{1/2}}(\vec{r}_{1/2})$ can be Coulomb waves or even plane waves [54]. In this thesis, subscript "1/2" indicates "1 or 2" while "1,2" means "1 and 2" (used in the following chapters). The approximation is applied mainly because the Coulomb potentials are truncated beyond R_c. To avoid any built-in errors in the asymptotic range, spectra analysis is performed in the simplified model, and, again, Volkov solutions apply for $\chi_{\vec{k_{1/2}}}(\vec{r_{1/2}},T)$ [139]. Alternatively, the two-electron Coulomb potentials can also be represented by their center of mass and relative positions using a coordinate transformation $\vec{r_1'} = \vec{r_1} + \vec{r_2}$ and $\vec{r_2'} = \vec{r_1} - \vec{r_2}$ [140]. When they are far from the core, the Coulomb attraction from the nucleus can be neglected. However, the extraction of surface values is difficult, and this method has not yet been applied [139]. With the approximation of the full scattering solution, the scattering amplitude is

$$b(\vec{k_1},\vec{k_2},T) = \langle\!\langle \chi_{\vec{k_1}}(\vec{r_1},T) \otimes \chi_{\vec{k_2}}(\vec{r_1},T)\,|\Theta_1(R_c)\Theta_2(R_c)|\,\psi(\vec{r_1},\vec{r_2},T) \rangle\!\rangle, \tag{2.73}$$

with photoelectron energy spectra $P(\vec{k_1},\vec{k_2}) = |b(\vec{k_1},\vec{k_2},T)|^2$ similar to Eq. (2.26), where $\Theta_{1/2}(R_c)$ are step functions on $\vec{r_{1/2}}$ as

$$\Theta_{1/2}(R_c) = \begin{cases} 0\ , |\vec{r_{1/2}}| < R_c \\ 1\ , |\vec{r_{1/2}}| \geq R_c. \end{cases} \tag{2.74}$$

The whole radial space is split into four regions by tSurff radius, as shown in Fig. 2.1: bound region $\mathrm{supp}(\psi^B(t)) = B\ : [0,R_c) \otimes [0,R_c)$, the single ionized region $\mathrm{supp}(\psi^S(t)) = S\ : [R_c,\infty) \otimes [0,R_c)$, $\mathrm{supp}(\psi^{\bar{S}}(t)) = \bar{S}\ : [0,R_c) \otimes [R_c,\infty)$ and the double emission region $\mathrm{supp}(\psi^D(t)) = D\ : [R_c,\infty) \otimes [R_c,\infty)$, where the Hamiltonian in region B is unchanged and the rest Hamiltonians are

$$H^S(t) = H_V(t) \otimes \mathbb{1} + \mathbb{1} \otimes H_{\mathrm{ion}}(t) \qquad V(\vec{r_1}) = 0, V_{\text{E-E}}(\vec{r_1},\vec{r_2}) = 0 \tag{2.75}$$

and

$$H^{\bar{S}(t)} = H_{\mathrm{ion}}(t) \otimes \mathbb{1} + \mathbb{1} \otimes H_V(t) \qquad V(\vec{r_2}) = 0, V_{\text{E-E}}(\vec{r_1},\vec{r_2}) = 0 \tag{2.76}$$

for the single ionization region and

$$H^D(t) = H_V(t) \otimes \mathbb{1} + \mathbb{1} \otimes H_V(t) \qquad V(\vec{r_1}) = 0, V(\vec{r_2}) = 0, V_{\text{E-E}}(\vec{r_1},\vec{r_2}) = 0 \tag{2.77}$$

for double ionization region, followed by the constraints of potentials in Eq. (2.69). The Coulomb repulsion of the two electrons only exists in region B. Only region D contributes the emission to the double ionization spectrum. As the Hamiltonian in D can be factored into the tensor product form in Eq.(2.77), the scattering solutions on D can be automatically factored into the tensor product of single scattering solutions of $H_V(t)$, which is the single-particle Volkov solution.

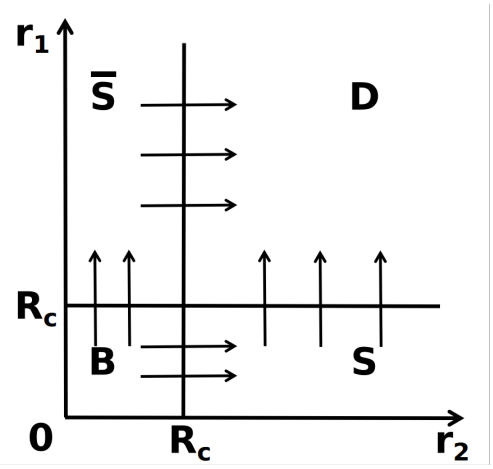

Figure 2.1: The regions of double ionization time propagation. The B stands for bound region, S stands for single ionization region, and D stands for the double emission region. R_c is the tSurff radius and $r_1 = |\vec{r}_1|, r_2 = |\vec{r}_2$. The figure is taken from Ref. [139]

Derivation

The two-particle unbound states in the D region for computing $b(\vec{k}_1, \vec{k}_2, T)$ in Eq. (2.73) are contributed by $\psi_S^D(T)$ from S subregion and $\psi_{\bar{S}}^D(T)$ from $\bar{S}$ subregion. As derived above using the single ionization tSurff, the projection of the unbound states to the scattering states can be computed by the time integration of fluxes, for double ionization problem here, scattering amplitudes can be computed by time integrating the flux $F(\vec{k}_1, \vec{k}_2, t)$ from S and flux $\bar{F}(\vec{k}_1, \vec{k}_2, t)$ from $\bar{S}$ subregions as

$$\begin{aligned} b(\vec{k}_1, \vec{k}_2, T) =& \langle \chi_{\vec{k}_1}(\vec{r}_1, T) \left|\Theta_1(R_c)\right| \psi_{\bar{S}}^D(T) \rangle + \langle \chi_{\vec{k}_2}(\vec{r}_1, T) \left|\Theta_2(R_c)\right| \psi_S^D(T) \rangle \\ =& \mathrm{i} \int_{-\infty}^{T} [F(\vec{k}_1, \vec{k}_2, t) + \bar{F}(\vec{k}_1, \vec{k}_2, t)] dt, \end{aligned} \tag{2.78}$$

According to the exchange asymmetry, $F(\vec{k}_1, \vec{k}_2, t) = \bar{F}(\vec{k}_2, \vec{k}_1, t)$ is satisfied and can be used to check for numerical consistency in the calculation. The contribution from $F(\vec{k}_1, \vec{k}_2, t)$ can be calculated by

$$F(\vec{k}_1, \vec{k}_2, t) = \langle \chi_{\vec{k}_1}(\vec{r}_1, t) \Theta_1(R_c)| \otimes \langle \chi_{\vec{k}_2}(\vec{r}_2, t)| [H_V(t), \Theta_2(R_c)] |\psi^S(\vec{r}_1, \vec{r}_2, t)\rangle\!\rangle, \tag{2.79}$$

with $\psi^S(\vec{r}_1, \vec{r}_2, t)$ being the wavefunction in S region. As the overlap of single-particle Volkov solutions slightly violates the orthogonal property $\langle \chi_{\vec{k}} | \Theta_{R_c} | \chi_{\vec{k}'} \rangle = S_{\vec{k}\vec{k}'} \neq \delta(\vec{k} - \vec{k}')$ because the integration starts from non-zero radial values; however, the property that integration is non-zero and goes to infinity only at $\vec{k} = \vec{k}'$ is still satisfied. To create an identity operator with Volkov states for derivation, we assume $S^{-1}_{\vec{k}'\vec{k}''}$ exists and

$$\int d\vec{k}' S_{\vec{k}\vec{k}'} S^{-1}_{\vec{k}'\vec{k}''} = \delta(\vec{k} - \vec{k}''), \tag{2.80}$$

can be obtained. Thus, we may expand the ansatz in the S region with the single-particle scattering solution and the single ionization channels as

$$\psi^S(\vec{r}_1,\vec{r}_2,t) = \int d\vec{k}_1' \int d\vec{k}_1'' \varphi_{\vec{k}_1'}(\vec{r}_2,t)\chi_{\vec{k}_1''}(\vec{r}_1,t)S^{-1}_{\vec{k}_1''\vec{k}_1'}, \tag{2.81}$$

and take it into Eq. (2.79). The contribution can be written as

$$\begin{aligned}
F(\vec{k}_1,\vec{k}_2,t) = &\int d\vec{k}_1' \int d\vec{k}_1'' \langle \chi_{\vec{k}_1}(\vec{r}_1,t)|\Theta_1(R_c)| \\
&\otimes \langle \chi_{\vec{k}_2}(\vec{r}_2,t)|[H_V(\vec{r}_2,t),\Theta_2(R_c)]|\varphi_{\vec{k}_1'}(\vec{r}_2,t)\chi_{\vec{k}_1''}(\vec{r}_1,t)S^{-1}_{\vec{k}_1''\vec{k}_1'}\rangle \\
= &\int d\vec{k}_1' \int d\vec{k}_1'' \underbrace{\langle \chi_{\vec{k}_1}(\vec{r}_1,t)|\Theta_1(R_c)|\chi_{\vec{k}_1''}(\vec{r}_1,t)\rangle S^{-1}_{\vec{k}_1''\vec{k}_1'}}_{S_{\vec{k}_1\vec{k}_1''}S^{-1}_{\vec{k}_1''\vec{k}_1'},\int d\vec{k}_1'' S_{\vec{k}_1\vec{k}_1''}S^{-1}_{\vec{k}_1''\vec{k}_1'}=\delta(\vec{k}_1-\vec{k}_1')} \\
&\langle \chi_{\vec{k}_2}(\vec{r}_2,t)|[H_V(\vec{r}_2,t),\Theta_2(R_c)]\varphi_{\vec{k}_1'}(t)\rangle \\
=&\langle \chi_{\vec{k}_2}(\vec{r}_2,t)|[H_V(\vec{r}_2,t),\Theta_2(R_c)]|\varphi_{\vec{k}_1}(\vec{r}_2,t)\rangle,
\end{aligned} \tag{2.82}$$

where the single emission channel $|\varphi_{\vec{k}_1}(\vec{r}_2,t)\rangle$ satisfies

$$\begin{aligned}
\mathrm{i}\partial_t|\varphi_{\vec{k}_1}(\vec{r}_2,t)\rangle =&\mathrm{i}\partial_t\langle \chi_{\vec{k}_1}(\vec{r}_1,t)|\psi^S(\vec{r}_1,\vec{r}_2,t)\rangle\rangle \\
=&\langle -\mathrm{i}\partial_t\chi_{\vec{k}_1}(\vec{r}_1,t)|\psi^S(\vec{r}_1,\vec{r}_2,t)\rangle\rangle + \langle \chi_{\vec{k}_1}(\vec{r}_1,t)|\mathrm{i}\partial_t\psi^S(\vec{r}_1,\vec{r}_2,t)\rangle\rangle \\
=&\langle -H_V(\vec{r}_1,t)\chi_{\vec{k}_1}(\vec{r}_1,t)|\psi^S(\vec{r}_1,\vec{r}_2,t)\rangle\rangle \\
&+\langle \chi_{\vec{k}_1}(\vec{r}_1,t)|[\mathbb{1}\otimes H_{\mathrm{ion}}(\vec{r}_2,t) + H_V(\vec{r}_1,t)\otimes\mathbb{1}]|\psi^S(\vec{r}_1,\vec{r}_2,t)\rangle\rangle \\
=&H_{\mathrm{ion}}(\vec{r}_2,t)|\varphi_{\vec{k}_1}(\vec{r}_2,t)\rangle - \langle \chi_{\vec{k}_1}(\vec{r}_1,t)|[H_V(\vec{r}_1,t),\Theta_1(R_c)]|\psi(\vec{r}_1,\vec{r}_2,t)\rangle\rangle,
\end{aligned} \tag{2.83}$$

and we write the coordinate into the Hamiltonian as $H_V(t) = H_V(\vec{r}_{1/2},t)$ for clarity. The formula $\bar{F}(\vec{k}_1,\vec{k}_2,t)$ can be derived in the identical way by changing $\vec{r}_1 \to \vec{r}_2, \quad \vec{k}_1 \to \vec{k}_2$.

Summary

To sum up, the solution is the projection of a single-electron wavefunction of the ionic Hamiltonian on the Volkov solution with the formula

$$F(\vec{k}_1,\vec{k}_2,t) = \langle \chi_{\vec{k}_2}(\vec{r}_2,t)\,|[H_V(\vec{r}_2,t),\Theta_2(R_c)]|\,\varphi_{\vec{k}_1}(\vec{r}_2,t)\rangle \tag{2.84}$$

and

$$\bar{F}(\vec{k}_1,\vec{k}_2,t) = \langle \chi_{\vec{k}_1}(\vec{r}_1,t)\,|[H_V(\vec{r}_1,t),\Theta_1(R_c)]|\,\varphi_{\vec{k}_2}(\vec{r}_1,t)\rangle. \tag{2.85}$$

The single-electron wavefunction $\varphi_{\vec{k}_{1/2}}$ represents the correlated single emission, which is correlated with the momenta of the other particle as

$$\mathrm{i}\partial_t\varphi_{\vec{k}_1}(\vec{r}_2,t) = H_{\mathrm{ion}}\varphi_{\vec{k}_1}(\vec{r}_2,t) - C_{\vec{k}_1}(\vec{r}_2,t) \tag{2.86}$$

and

$$\mathrm{i}\partial_t\varphi_{\vec{k}_2}(\vec{r}_1,t) = H_{\mathrm{ion}}\varphi_{\vec{k}_2}(\vec{r}_1,t) - C_{\vec{k}_2}(\vec{r}_1,t). \tag{2.87}$$

The sources are the overlaps of the two-electron wavefunction on the Volkov solutions, shown by

$$C_{\vec{k}_1}(\vec{r}_2,t) = \int d\vec{r}_1 \overline{\chi_{\vec{k}_1}(\vec{r}_1,t)}[H_V(\vec{r}_1),\Theta_1(R_c)]\psi(\vec{k}_1,\vec{k}_2,t) \tag{2.88}$$

and

$$C_{\vec{k}_2}(\vec{r}_1,t) = \int d\vec{r}_2 \overline{\chi_{\vec{k}_2}(\vec{r}_2,t)}[H_V(\vec{r}_2),\Theta_2(R_c)]\psi(\vec{k}_1,\vec{k}_2,t), \tag{2.89}$$

with the initial states 0 shown as

$$\varphi_{\vec{k}_1}(\vec{r}_2,t=-\infty)=0, \quad \varphi_{\vec{k}_2}(\vec{r}_1,t=-\infty)=0. \tag{2.90}$$

It should be noted that the advancement of the single-particle wavefunction $\varphi_{\vec{k}_1}(\vec{r}_2,t)$ is dependent on the momentum $\vec{k}_1$ of the other electron, indicating that each momentum $\vec{k}_1$ differently contributes to the propagation of the other, and coupling is contributed by the source term $C_{\vec{k}_1}(\vec{r}_2,t)$ of the inhomogeneous TDSE in Eq. (2.86).

For evaluating Eq. (2.88) or (2.89), one needs the surface values and derivatives on $|\vec{r}_1| = R_c$ ($|\vec{r}_2| = R_c$) with coefficients values on coordinate $\vec{r}_2(\vec{r}_1)$, which are provided by solving of a 6D TDSE on region B and the corresponding derivation could be found on Sec. A.5.1. Beyond the region B, the electrons are absorbed by the complex scaling, see Sec. 3.3. Thus, the computation of the photoelectron spectrum includes sequential time-propagating calculations for regions $B \to S(\bar{S}) \to D$.

2.4.2 Non-interacting system

In the non-interacting system of double emission, the E-E interaction term is neglected, the motions of the two particles are independent. The wavefunction of two non-interacting particles is written as the tensor product of two single-particle ansatz as

$$\psi(\vec{r}_1,\vec{r}_2,t) = \psi_1(\vec{r}_1,t)\otimes\psi_2(\vec{r}_2,t) \tag{2.91}$$

whose Hamiltonian is created by simply removing the E-E interaction term from Eq. (2.69). The scattering amplitude Eq. (2.73) of the two electrons

$$\begin{aligned} b(\vec{k}_1,\vec{k}_2,T) =& \langle\!\langle \chi_{\vec{k}_1}(\vec{r}_1,T)\otimes\chi_{\vec{k}_2}(\vec{r}_2,T)\,|\Theta_1(R_c)\Theta_2(R_c)|\,\psi_1(\vec{r}_1,t)\otimes\psi_2(\vec{r}_2,t)\rangle\!\rangle \\ =& \langle\chi_{\vec{k}_1}(\vec{r}_1,T)\,|\Theta_1(R_c)|\,\psi_1(\vec{r}_1,t)\rangle\langle\chi_{\vec{k}_2}(\vec{r}_2,T)\,|\Theta_2(R_c)|\,\psi_2(\vec{r}_2,t)\rangle \\ =& b_1(\vec{k}_1,T)b_2(\vec{k}_2,T) \end{aligned} \tag{2.92}$$

is the product of scattering amplitude of electron 1 $b_1(\vec{k}_1,T)$ and electron 2 $b_2(\vec{k}_2,T)$.

2.4.3 Single ionization photoelectron spectra

For completeness, we show the computational details here for single emission spectra. The asymptotic solution of single emission wave function can be written as

$$\chi^I_{\vec{k}_1}(\vec{r}_1,\vec{r}_2,t) = \chi_{\vec{k}_1}(\vec{r}_1)\otimes\varphi^I(\vec{r}_2,t), \tag{2.93}$$

with the corresponding TDSE constructed by Hamiltonian $H^S(t)$ (see Eq. (2.75)) written as

$$\mathrm{i}\partial_t \chi^I_{\vec{k}_1}(\vec{r}_1,\vec{r}_2,t) = H^S(t)\chi^I_{\vec{k}_1}(\vec{r}_1,\vec{r}_2,t), \tag{2.94}$$

where the ionic channel satisfies

$$\mathrm{i}\partial_t \varphi^I(\vec{r}_2,t) = H_{\mathrm{ion}}(t)\varphi^I(\vec{r}_2,t), \tag{2.95}$$

and normalization constraint $\|\varphi^I(\vec{r}_2,t)\|^2 = 1$. We only consider the ionic channels that remain in the box as

$$\varphi^I(\vec{r}_2,t) \approx 0,\ r_2 > R_c. \tag{2.96}$$

Similar to the single electron tSurff, here $\approx$ means we neglect the long, exponential tails as well as their interaction with pulse that contributes to tiny ionization signals [139]. With this approximation, the DI yields at all times computed from subregions S, $\bar{S}$ to D are neglected. Rather than the standard time propagation that starts before the laser pulse, we obtain the ionic channels by backward propagation from the final condition at $t = T$ with desired final state.

The single emission scattering amplitude from DI simulation is calculated by the projection of the wavefunction ψ^S on $\chi^I_{\vec{k}_1}$ at the end of the propagation T as

$$\begin{aligned} b^I(\vec{k}_1,T) &\approx \langle \chi^I_{\vec{k}_1}(\vec{r}_1,\vec{r}_2,T)|\Theta_1(R_c)(1-\Theta_2(R_c))|\psi^S(T)\rangle \\ &= \mathrm{i}\int_{-\infty}^{T} \langle \varphi^I(\vec{r}_2,t)(1-\Theta_2(R_c))|\langle \chi_{\vec{k}_1}(\vec{r}_1,t)|[H_V,\Theta_1(R_c)]|\psi^S(\vec{r}_1,\vec{r}_2,t)\rangle\rangle dt \\ &= \mathrm{i}\int_{-\infty}^{T} \langle \varphi^I(\vec{r}_2,t)|C_{\vec{k}_1}(\vec{r}_2,t)\rangle \end{aligned} \tag{2.97}$$

with the photoelectron spectra

$$P^I(\vec{k}_1,T) = 2|b^I(\vec{k}_1,T)|^2, \tag{2.98}$$

by taking both contributions from S and $\bar{S}$. Thus computation of the single emission spectrum only requires the sources in the sub region time propagation (see Eq. (2.88) and (2.89)), and the wavefunction of ionic channels, which is from the back propagation of a single particle Hamiltonian, as indicated above.

In this method, the ionic solution is independent of momenta $\vec{k}_1$ and only needs to be calculated once; however, it must be confined in $[0, R_c]$ in the back propagation. Otherwise it would lead to exponential divergence in the presence of an absorber [54], or extra reflections are introduced.

2.4.4 Computational remarks and performance

Photoionization spectra calculation by solving the TDSE in a strong electric field includes four major steps, namely set up, time propagation, surface flux integration, and post-processing, which are detailed below:

1. Set-up process: Create the simulation box as well as the absorber and sets the initial values for the time propagation.

2. Time propagation (1): Calculate the 6D field-free ground ansatz of Hamiltonian of region B in Eq. (2.69) and evolve $\psi(\vec{r}_1,\vec{r}_2,t)$ to T, whose surface values are written to disk at each time step.

3. Time propagation (2): Create the desired momenta grid $\vec{k}_1,\vec{k}_2$, evolve the 3D wavefunction $\varphi_{\vec{k}_1}(\vec{r}_2,t)$ and (or) $\varphi_{\vec{k}_2}(\vec{r}_1,t)$ in a single ionization region S and (or) $\bar{S}$ by Eq. (2.86) and (or) (2.87) with initial value given in Eq. (2.90). The sources of each time step are calculated by Eq. (2.88) and (or) (2.89) from previously stored surface values of $\psi(\vec{r}_1,\vec{r}_2,t)$. Afterwards, the corresponding surface values of $\varphi_{\vec{k}_1}(\vec{r}_2,t)$ and (or) $\varphi_{\vec{k}_2}(\vec{r}_1,t)$ are written to disk.

4. Surface flux integration: Calculate fluxes $F(\vec{k}_1,\vec{k}_2,t)$ and (or) $\bar{F}(\vec{k}_1,\vec{k}_2,t)$ by Eq. (2.82) from surface values of $\varphi_{\vec{k}_1}(\vec{r}_2,t)$ and (or) $\varphi_{\vec{k}_2}(\vec{r}_1,t)$. Then, integrate the flux $f(\vec{k}_1,\vec{k}_2,T) = \mathrm{i}\int_{-\infty}^{T} F(\vec{k}_1,\vec{k}_2,t)dt$ and (or) $\bar{f}(\vec{k}_1,\vec{k}_2,T) = \mathrm{i}\int_{-\infty}^{T} \bar{F}(\vec{k}_1,\vec{k}_2,t)dt$ and combine both into the scattering amplitude $b(\vec{k}_1,\vec{k}_2,T) = f(\vec{k}_1,\vec{k}_2,T) + \bar{f}(\vec{k}_1,\vec{k}_2,T)$. If only one source of flux is integrated, the exchange asymmetric property $f(\vec{k}_1,\vec{k}_2,T) = \bar{f}(\vec{k}_2,\vec{k}_1,T)$ is applied for calculating scattering amplitudes.

5. Post-processing: Obtain the energy photoelectron spectra by $P(\vec{k}_1,\vec{k}_2) = |b(\vec{k}_1,\vec{k}_2,T)|^2$.

The final scattering amplitude is symmetric as

$$\begin{aligned} b(\vec{k}_1,\vec{k}_2,T) =& f(\vec{k}_1,\vec{k}_2,T) + \bar{f}(\vec{k}_1,\vec{k}_2,T) \\ =& \bar{f}(\vec{k}_2,\vec{k}_1,T) + f(\vec{k}_2,\vec{k}_1,T) = b(\vec{k}_2,\vec{k}_1,T) \end{aligned} \tag{2.99}$$

is theoretically satisfied. The old version of our tRecX code (see Sec. 3.6 or Ref. [96]) by Dr. Zielinski calculates $b(\vec{k}_1,\vec{k}_2,T)$ integrated from flux in one subregion. In the new version, an extra option is available where $b(\vec{k}_1,\vec{k}_2,T)$ is integrated by flux from both subregions. A symmetric check of the photoelectron energy spectra for two particles $E_{1/2}$

$$\sigma(E_1,E_2) = \int d\theta_1 \int d\theta_2 \int d\phi_1 \int d\phi_2 P(\vec{k}_1,\vec{k}_2) k_1 k_2, \frac{k_{1/2}^2}{2} = E_{1/2} \tag{2.100}$$

calculated by flux from both subregions helps avoid systematic errors in the calculation. We introduce the error $\mathrm{err}(E_1,E_2)$ with the formula

$$\mathrm{err}(E_1,E_2) = \frac{2|\sigma(E_1,E_2) - \sigma(E_2,E_1)|}{\sigma(E_1,E_2) + \sigma(E_2,E_1)} \tag{2.101}$$

for measuring the symmetric property of the DI spectrum, and the tiny error given in Fig. 2.2 shows that the exchange asymmetry is well preserved.

A big advantage of the two-electron tSurff method is that the 6D wavefunction $\psi(\vec{r}_1,\vec{r}_2,t)$ only needs to be precisely approximated in region B, where the radial extension is mainly

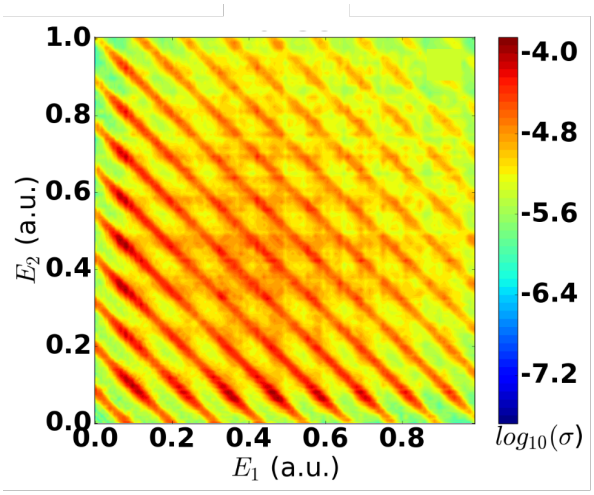

(a)

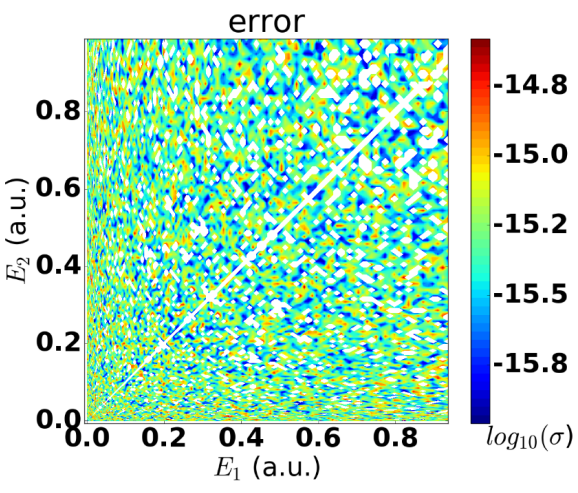

(b)

Figure 2.2: The (a) energy spectrum $\sigma(E_1, E_2)$ and (b) its error $\mathrm{err}(E_1, E_2)$. The laser is a FWHM=9 opt.cyc., 394.5 nm at $5.7 \times 10^{14}\,\mathrm{W/cm^2}$ and flat-top pulse.

controlled by the quiver radius r_q, instead of propagating the wavefunction to the asymptotic region, which requires a huge radius, as described in the single-electron tSurff. The single-electron tSurff method scales the phase space by $10n^3$ for large wavelength calculation. Thus, the double ionization tSurff scales the phase space by $\approx (10n)^6$ for the bound region calculation (time propagation in region B). Although computation on region S and $\bar{S}$ may take moderate time if one needs a fine $k_{1/2}$ grid, it scales the single emission problem by $\lambda^7 I^2$ rather than the $\lambda^{13} I^4$ of the DI calculation. Moreover, the simulations of different k grids are uncorrelated and can be perfectly parallelized.

The two-electron tSurff, however, has its own limitations. The numerical error mainly comes from our approximation of the total scattering solution by the product of two single-particle scattering solutions as $\chi_{\vec{k_1},\vec{k_2}}(\vec{r}_1, \vec{r}_2) \approx \chi_{\vec{k_1}}(\vec{r}_1)\chi_{\vec{k_2}}(\vec{r}_2)$, suggesting the two electrons disentangle at $|\vec{r}| \geq R_c$, which does not happen until the radial extension $|\vec{r}| > 100\,\mathrm{a.u.}$ according to Ref. [91], whereas the essence of tSurff method is to compute the smallest possible radial extension. The observable "post-collision" interactions, such as the repulsion between electrons far from the nucleus, cannot be described well. In our convergence test, which is presented in the following chapters, the performance of convergence in the double-electron calculation strongly varies with the target observable. The converged energy photoelectron spectra as well as the overall back-to-back emission and side-by-side emission properties are relatively easy to obtain. However, the joint angular distribution (JAD) at selected energy points is hard to converge, and we can only give an overall shape of the JAD for the comparison with the experiments. A possible solution is to include the electron-electron repulsion beyond tSurff radius, which is yet not available [139].

2.5 Generalized formula for TDSE

The TDSE for the above discussion can be abstracted to

$$\mathrm{i}\partial_t \Psi(t) = H(t)\Psi(t) + C_s(t) \tag{2.102}$$

where $\Psi(t)$ is a generalized wavefunction (wavefunction of any dimensions or scattering amplitudes), $C_s(t)$ is a generalized source, $H(t)$ is a specific Hamiltonian depending on the type of ionization processes, as follows

1. Single ionization, time propagation: $\Psi(t) \coloneqq \psi(\vec{r}, t)$, $C_s(t) = 0$, $H(t) \neq 0$
2. Single ionization, spectrum integration: $\Psi(t) \coloneqq b(\vec{k}, t)$, $H(t) = 0$, $C_s(t) =: -F(\vec{k}, t)$
3. The haCC method, time propagation: $\Psi(t) \coloneqq \sum_{\mathcal{I}} |\mathcal{I}\rangle C_{\mathcal{I}}(t)$, $H(t) \neq 0$, $C_s(t) \coloneqq H(t) \sum_{\mathcal{N}} |\mathcal{N}\rangle C_{\mathcal{N}}(t)$
4. Double ionization, time propagation in B region: $\Psi(t) \coloneqq \psi(\vec{r}_1, \vec{r}_2, t)$, $H(t) \neq 0$, $C_s(t) = 0$
5. Double ionization, time propagation in S region: $\Psi(t) \coloneqq \varphi_{\vec{k}_1}(\vec{r}_2, t)$, $H(t) \neq 0$, $C_s(t) \coloneqq -C_{\vec{k}_1}(\vec{r}_2, t)$
6. Double ionization, time propagation in $\bar{S}$ region: $\Psi(t) \coloneqq \varphi_{\vec{k}_2}(\vec{r}_1, t)$, $H(t) \neq 0$, $C_s(t) \coloneqq -C_{\vec{k}_2}(\vec{r}_1, t)$
7. Double ionization, spectrum integration in D region: $\Psi(t) \coloneqq b(\vec{k}_1, \vec{k}_2, t)$, $H(t) = 0$, $C_s(t) \coloneqq -F(\vec{k}_1, \vec{k}_2, t) - \bar{F}(\vec{k}_1, \vec{k}_2, t)$.

(2.103)

The formula in Eq. (2.102) provides a unified framework for implementing the tSurff method and its extensions in the form of code for a simple and clean design.

Chapter 3

Numerical Methods and Discretization

We have presented the existing analytic models for describing the attosecond dynamics of electrons when exposed to a short, intense laser in Sec. 1.3. The intuitive analytic models offer qualitative explanations of various phenomenons in experiments, however, fail to produce a quantitative explanation with the required precision. A universal and quantitative description of the electron dynamics in the pulse field can only be achieved by solving TDSE for theoretical investigations.

The TDSE is a time-dependent differential equation whose solution can be obtained from "method of lines" [141] for numerical simulations: expand the TDSE by discrete coefficients and solve an ordinary differential equation (ODE). The method can be detailed as the following:

1. Find a set of suitable basis functions to approximate the wavefunction with a finite number of coefficients. Theoretically, infinitely many basis functions are needed for an exact expansion of the wavefunction. In numerical simulations, a basis set by N_{coef} rather than infinitely many basis functions $\{f_n\}$ with corresponding time-dependent coefficients $c_n(t)$ is included to give an approximation of the ansatz depending on the required precision as

$$|\psi(t)\rangle = \sum_{n=1}^{\infty} |f_n\rangle c_n(t) \approx \sum_{n=1}^{N_{\text{coef}}} |f_n\rangle c_n(t). \tag{3.1}$$

   Choosing $\{f_n\}$ can be a difficult task which requires a clear understanding of the form of the solutions. The subspace span $(\{f_n\}_{n\leq N_{\text{coef}}}) \subset \mathcal{H}$ should not only cover all the necessary excited states to give an acceptable precision but also be as small as possible to reduce the computational resources [82]. One may also use a time-dependent basis [142], but it is not considered here.

2. Rewrite the differential equation in space spanned by basis functions. Occasionally this converts the "strong form" into a "weak form", which relaxes the continuity

and differentiability requirements on the potential solutions to the equation, whose influences will be discussed later. The overlap of the basis are calculated on both sides of the TDSE as

$$\langle f_m|\mathrm{i}\partial_t|\psi(t)\rangle = \langle f_m|H(t)|\psi(t)\rangle. \tag{3.2}$$

With a finite number of basis functions, one has

$$\begin{aligned} \partial_t \sum_{n=1}^{N_{\mathrm{coef}}} \underbrace{\langle f_m|f_n\rangle}_{=:S_{mn}} c_n(t) &= -\mathrm{i} \sum_{n=1}^{N_{\mathrm{coef}}} \underbrace{\langle f_m|H(t)|f_n\rangle}_{=:H_{mn}} c_n(t) \\ \partial_t \vec{c}(t) &= -\mathrm{i}\hat{S}^{-1}\hat{H}(t)\vec{c}(t) \end{aligned} \tag{3.3}$$

which is an ordinary differential equation depending on time, and is contributed by overlap matrix $\hat{S}$ and Hamiltonian matrix $\hat{H}$.

3. Solve the ordinary differential equation. The ODE converted from TDSE is solved by advancing the initial wavefunction given by the ground eigenstate of the field-free Hamiltonian. The time propagation is numerically approximated by the explicit 4th order Runge-Kutta method, as detailed in Sec. 3.5.

It is efficient to program the above standard routines including choosing suitable basis functions in step 1, constructing matrices in step 2, and matrix-vector multiplications in step 3 into code, mainly represented by abstract classes in object-oriented programming for further implementations. Matrix-vector multiplications in step 3 is the major computational task and consumes the most of computational time and memory. A judicious choice of basis functions in step 1 helps a smooth construction of computational efficient matrices in step 2, reducing the computational resources in step 3.

This chapter focuses on the computational strategies for numerically solving the TDSE with the arrangement of contents based on the above three steps, where the basis function (step 1) and corresponding matrix construction (step 2) are usually put together and collectively referred to as discretization strategy.

We will firstly present the general formula for discretizing the wavefunction into angular and radial parts. The numerical discretization of radial functions in the inner region ($r \leq R_0$) of the simulation box differs from that of the outer region ($r \geq R_0$). The finite element method (FEM) as well as finite element discrete variable representation (FE-DVR) method will be illustrated for approximating the radial functions of the inner region. Then we will demonstrate the constraints of the angular momenta basis sets of two particles for solving a 6D TDSE. With the mentioned basis functions, the data structure of the corresponding coefficients in programming will also be illustrated. Thereafter, computational strategies for electron-electron interactions will be introduced which include multipole expansion, and implementation by FEM and FE-DVR on radial coordinates. For numerical discretization in the outer region ($r \leq R_0$), we will present the infinite-range exterior complex scaling method (irECS) as the absorber, as well as the mixed gauge method for describing the ansatz in the outer and inner region with different gauges.

For the time propagation in step 3, we will demonstrate the 4th order Runge-Kutta methods with adaptive step size and the high energy projection treatment where the high

energy eigenstates of the wavefunction are removed for numerical efficiency. At last, we will present the tRecX code which implements the listed numerical recipes, as well as its parallelization strategy and scaling performance.

3.1 Discretization

We focus on the discretization strategy of the wavefunction in this section, which includes the FEM, FE-DVR methods for radial functions, and angular representations of one and two-particle wavefunctions.

3.1.1 General Form

The discussion begins with a representation of the few-electron wavefunctions with the simplest system, using the hydrogen atom as an example. The field-free ground state wavefunction describing the near-nucleus electron is spherically symmetric and is represented by a product of spherical harmonics for the angular part and the exponentially decaying function for the radial part [98]. When the electron is exposed in a laser field, the spherical symmetry of the wavefunction is broken. However, the new wavefunction formed by the combination of ground and excited states is still suitable for representation by the spherical harmonics [82], with the formula

$$\psi(r,\theta,\phi,t) = \psi(r,\Omega,t) \approx \sum_{m=-M_{\max}}^{M_{\max}} \sum_{l=|m|}^{L_{\max}} Y_l^m(\Omega) R_{lm}(r,t), \tag{3.4}$$

where $\Omega = (\theta,\phi)$ is the angle, $L_{\max}$ and $M_{\max}$ are the maximum quantum numbers, and $Y_l^m(\Omega)$ are the spherical harmonics. We chose the spherical harmonics to represent the angular parts for the following reasons. First, the ansatz of few-electron molecules is atom-centered and the spherical harmonics ideally suited for representing the bound states of hydrogenic atoms. Second, with the linearly polarized pulses along the z direction, the cylindrical symmetry can be easily satisfied by $m \equiv 0$. Furthermore, local representations already suffice for the dipole operator by connecting the neighbor functions with $l \pm 1$ and $m \pm 1$. We integrate the time-dependent property of the coefficients (shown in Eq. (3.3)) in the radial part, which puts a difference among various methods.

$L_{\max}$ and $M_{\max}$ in Eq. (3.4) control the accuracy for approximating the angular momenta of the wavefunction. Their minimum requirements that vary with the gauges can be predicted by the free particles in the field, because velocity gauge absorbs part of the quiver motion into the momentum part $[\mathrm{i}\vec{\nabla} - \vec{A}(t)]$ and is numerically more efficient than the length gauge; a detailed description can be found in Sec. 3.3 and Sec. 3.4. The free motion of the velocity gauge is given by the Volkov solution $\chi_{\vec{k}}(\vec{r},t)$ shown in Eq. (2.23), which involves a plane-wave factor. The expansion of the plane wave shows a strong radial dependence via spherical Bessel functions j_l and angles of $\vec{r}$ and $\vec{k}$: Ω_r and Ω_k as

$$e^{\mathrm{i}\vec{k}\cdot\vec{r}} = 4\pi \sum_{l=0}^{\infty} \sum_{m=-l}^{l} \mathrm{i}^l j_l(kr) Y_l^m(\Omega_r) Y_l^{m*}(\Omega_k), \tag{3.5}$$

We find that the scaling of $L_{\max}$ and $M_{\max}$ satisfies $\sim \lambda^3 I$, where λ is the wavelength and I is the intensity.

Multiple other possible basis functions can be applied, depending on the system of interest. The spherical harmonics are suitable for describing the single-centered wavefunction. For other multiple-centered systems, for example H^{2+}, the prolate spheroidal coordinates have better numerical efficiency [143].

3.1.2 FE-DVR of radial part

We demonstrate the FE and FE-DVR techniques for representing the radial function in this subsection. Apart from FE-DVR and FE, the radial functions can also be expanded by B-splines [90, 111] and finite difference methods [51, 144].

Finite element

The finite element method (FEM) subdivides a large space into smaller parts called finite elements (FE). It is widely applied to solve engineering and mathematical problems, including structural analysis, fluid dynamics, heat transfer, and electrodynamics. We subdivide the radial axis into several intervals, each independently represented except for boundary conditions, by a set of polynomials called basis functions, collectively referred to as a basis set. We approximate the radial function $R_{lm}(r,t)$ in Eq. (3.4) with different types of basis sets for $r < R_0$ and $r \geq R_0$.

The inner region $[0, R_0]$ is split into N intervals with $N+1$ equidistant points at r_n ($0 \leq n \leq N$, where $r_0 = 0, r_N = R_0$) with $[r_{n-1}, r_n]$ ($r \geq 1$) being the nth interval, simulated by P_n basis functions $f_p^{(n)}(r)$. We approximate the radial on separate intervals, and r_n is shared by the nth and $(n+1)$th intervals. $R_{lm}(r_n^-, t) = R_{lm}(r_n^+, t)$ should be fulfilled to ensure the continuity of the wavefunction. Assume $rR_{lm}(r,t) = \sum_{n,p} c_{m,l}^{n,p}(t) f_p^{(n)}(r)$, constraints on all the coefficients $c_{m,l}^{n,p}(t)$ represented by $\sum_p c_{m,l}^{n,p}(t) f_p^{(n)}(r_n) = \sum_p c_{m,l}^{n-1,p}(t) f_p^{(n-1)}(r_n)$ need to be implemented. To reduce the number of continuity constraints, the polynomials satisfy

$$\begin{aligned} f_p^{(n)}(r_{n-1}) = f_p^{(n)}(r_n) \equiv 0, \quad p = 0, 1, \cdots, P_n - 1 \\ f_0^{(n)}(r_{n-1}) = f_{P_n-1}^{(n)}(r_n) \equiv 1, \quad n > 1 \end{aligned} \tag{3.6}$$

for boundary conditions and

$$f_p^{(1)}(0) = 0, \quad f_{P_1-1}^{(1)}(r_1) = 1, \tag{3.7}$$

where the basis functions at $0 < p < P_n - 1$ are denoted by ascending order polynomials and $f_0^{(n)}(r), f_{P_n-1}^{(n)}(r)$ can be represented by linear functions in the old version of our code. For the intervals with $n > 1$, the local overlap matrix elements are

$$\begin{aligned} S_{pq}^{(n)} = \langle f_p^{(n)} | f_q^{(n)} \rangle = \delta_{pq}, \quad (p,q) \neq (0, P_n - 1), \quad (P_n - 1, 0) \\ S_{0,P_n-1}^{(n)} = S_{P_n-1,0}^{*(n)} \neq 0, \end{aligned} \tag{3.8}$$

being diagonal, except two non-zero off-diagonal elements with suitable transformations, if we let suitable basis functions $f_0^{(n)}, f_{P_n-1}^{(n)}$ be linear and others be modified Legendre polynomials that are orthogonal with $f_0^{(n)}$. Considering the orthogonality of spherical harmonics and assuming every finite element does not overlap, the overall overlap matrix with the FEM basis set above is narrow-banded and near diagonal.

It is known that the radial function in single-centered systems satisfies the asymptotic behavior $R_{lm}(r,t) \propto r^l$ when $r \to 0$. In the old version of our code that does not implement DVR method, we approximated the first interval near the core by implementing a tailored discretization, with the basis functions multiplied by r^l as

$$f_k^{(n),l}(r) := r^l f_k^{(n)}(r) \tag{3.9}$$

to automatically include the asymptotic behavior, which reduces the polynomial order of the first interval by l, thereby increasing computational efficiency. This operation is expected to remove the number of unphysical and large eigenvalues of the Hamiltonian. The tailored discretization is not implemented in the FE-DVR (shown below) where we only remove one polynomial in the first interval.

The outer region $[R_0, \infty)$ is approximated by the product of the shifted and scaled Laguerre polynomials and a decaying part

$$f_p^{N+1}(r) = [L_p(2\alpha(r - R_0)) - 1]e^{-\alpha(r-R_0)}, \tag{3.10}$$

where α is the decay factor and $N+1$ means the outer region is the $N+1$th interval. For details, refer to Sec. 3.3.3.

As shown in Eq. (3.8), the overlap matrix of each interval is diagonal except for the two off-diagonal elements. The disadvantage of FEM is that the inverse of the overlap matrix can be complicated and hard to parallelize; for more details, refer to Ref. [54]. The problem can be avoided by FE-DVR, wherein a diagonal overlap matrix is available.

Discrete variable representation

Similar to the FEM, the finite-element discrete variable representation (FE-DVR) method splits the whole radial axis into several simple and small elements; however, it approximates each element by a few Lagrange polynomials, contributing to a full overlap matrix, which may be diagonal at specific conditions and will be shown later. Compared to the FEM basis with an increasing order in the old tRecX code, as stated above, discrete variable representation (DVR) basis possesses an identical polynomial order. The Lagrange polynomials are created based on P_{n-1} discrete points $r_p^{(n)}, r_q^{(n)}$ denoted by subindex $p, q : r_0^{(n)} < r_1^{(n)} < \cdots < r_p^{(n)} < \cdots < r_{P_{n-1}}^{(n)}$ by

$$f_p^{(n)}(r) = \prod_{q=0, p\neq q}^{P_n-1} \frac{r - r_q^{(n)}}{r_p^{(n)} - r_q^{(n)}} \mathbb{1}_{[r_{n-1}, r_n]} \quad p, q \in \{0, 1\cdots, P_n - 1\} \tag{3.11}$$

whose values at qth point automatically satisfying

$$f_p^{(n)}(r_q^{(m)}) = \delta_{mn}\delta_{pq}, \tag{3.12}$$

where $[r_{n-1}, r_n], n \in [1, N]$ is the nth interval range with left boundary r_{n-1} and right boundary r_n, similar to what is used in FEM and $\mathbb{1}_{[r_{n-1},r_n]}$ returns 1 for $r \in [r_{n-1}, r_n]$ otherwise 0. To create orthogonal basis functions, the arbitrary discrete points $\{r_0^{(n)}, r_1^{(n)}, \cdots, r_{P_n-1}^{(n)}\}$ are chosen to be quadrature points. Assume the quadrature points of interval $[-1, 1]$ are $\{x_0, x_1, \cdots, x_{P_n-1}\}$ with weights $\{\omega_0, \omega_1, \cdots, \omega_{P_n-1}\}$, the quadrature points on interval $[r_{n-1}, r_n], n \in [1, N]$ are given by

$$r_p^{(n)} = \frac{r_n - r_{n-1}}{2} x_p + \frac{r_n + r_{n-1}}{2} \tag{3.13}$$

with corresponding weights

$$\omega_p^{(n)} = \frac{r_n - r_{n-1}}{2} \omega_p. \tag{3.14}$$

Thus, the integration satisfies

$$\langle f_p^{(n)} | f_q^{(m)} \rangle = \int f_p^{(n)}(x) f_q^{(m)}(x) dx = \delta_{mn} \sum_{k=0}^{P_n-1} f_p^{(n)}(r_k^{(n)}) f_q^{(n)}(r_k^{(n)}) \omega_k^{(n)} = \omega_p \delta_{mn} \delta_{pq}. \tag{3.15}$$

With a reduction in the number of continuity operations, we chose the Gauss-Lobatto quadratures, where the two end points are included as $r_0^{(n)} = r_{n-1}, r_{P_n-1}^{(n)} = r_n$. The boundary value condition similar to FEM polynomials in Eq. (3.6)

$$\begin{aligned} f_{P_n-1}^{(n)}(r_n) = f_0^{(n+1)}(r_n) = 1 \\ f_p^{(n)}(r_{n-1}) = f_p^{(n)}(r_n) = 0, \quad p = 1, \cdots, P_n - 2 \end{aligned} \tag{3.16}$$

is automatically satisfied. The DVR method implemented in Ref. [145] solves the TDSE, where the derivatives and values are only needed on different DVR grids, even if the philosophy is different, which we never did while programming the code. However, for completeness, we have presented the related results here. The derivatives of the basis function given in Ref. [145] for the quadrature points are

$$\frac{\partial f_p^{(n)}}{\partial r}\Big|_{r=r_q^{(n)}} = \frac{1}{r_p^{(n)} - r_q^{(n)}} \prod_{k \neq q, k \neq p} \frac{r_q^{(n)} - r_k^{(n)}}{r_p^{(n)} - r_k^{(n)}}, \quad p \neq q. \tag{3.17}$$

With the Lobatto quadrature and based on the approximate integration

$$\int_{r_{n-1}}^{r_n} f_p^{(n)}(r) dr \approx \sum_{k=0}^{P_n-1} \omega_k^{(n)} f_p^{(n)}(r_k), \tag{3.18}$$

we have

$$\begin{aligned} \int_{r_{n-1}}^{r_n} f_p^{(n)} \partial_r f_q^{(n)} + f_q^{(n)} \partial_r f_p^{(n)} dr =& f_p^{(n)}(r_{P_n-1}^{(n)}) f_q^{(n)}(r_{P_n-1}^{(n)}) - f_p^{(n)}(r_0^{(n)}) f_q^{(n)}(r_0^{(n)}) \\ \approx& \sum_{k=0}^{P_n-1} \omega_k^{(n)} \left[f_p^{(n)}(r_k^{(n)}) \partial_r f_q^{(n)}(r_k^{(n)}) + f_q^{(n)}(r_k^{(n)}) \partial_r f_p^{(n)}(r_k^{(n)}) \right]. \end{aligned} \tag{3.19}$$

Eq. (3.19) is useful when $p = q$ and we get

$$\frac{\partial f_p^{(n)}}{\partial r}\Big|_{r=r_q^{(n)}} = \frac{1}{2\omega_p^{(n)}}(\delta_{p,P_n-1} - \delta_{p,0}). \tag{3.20}$$

To a sum up, the relative derivatives at the quadrature points are

$$\frac{\partial f_p^{(n)}}{\partial r}\Big|_{r=r_q^{(n)}} = \begin{cases} \frac{1}{r_p^{(n)} - r_q^{(n)}} \prod_{k\neq q, k\neq p} \frac{r_q^{(n)} - r_k^{(n)}}{r_p^{(n)} - r_k^{(n)}}, & p \neq q \\ \frac{1}{2\omega_p^{(n)}}(\delta_{p,P_n-1} - \delta_{p,0}), & p = q. \end{cases} \tag{3.21}$$

At boundary $r = r_n$, $f_{P_{n-1}-1}^{(n-1)}(r_n) = f_0^{(n)}(r_n) = 1$ but derivative from the left

$$\frac{\partial f_{P_{n-1}-1}^{(n-1)}}{\partial r}\Big|_{r=r_n} = \frac{1}{2\omega_{P_{n-1}-1}^{(n-1)}} \tag{3.22}$$

does not equal to that from the right

$$\frac{\partial f_0^{(n)}}{\partial r}\Big|_{r=r_n} = -\frac{1}{2\omega_{P_0}^{(n)}}. \tag{3.23}$$

According to the previous work in our lab and as mentioned in Ref. [128], the derivative does not need to be continuous to solve the TDSE.

As the tSurff radius R_c does not fall on a quadrature point where derivatives are needed, it cannot be obtained by Eq. (3.21). Directly computing multiple products is expensive and scales as $\sim P_n^2$. For numerical efficiency, we introduce a new function $g_{p,k}^{(n)}(r)$ that goes as

$$g_{p,k}^{(n)}(r) = \prod_{q=0,q\neq p}^{k} \frac{r - r_q^{(n)}}{r_p^{(n)} - r_q^{(n)}} \mathbb{1}_{[r_{n-1}, r_n]} \quad p = 0, 1, \cdots, P_n - 1, \tag{3.24}$$

and satisfies $g_{p,P_n-1}^{(n)}(r) = f_p^{(n)}(r), g_{0,0}^{(n)}(r) = 1$ by definition. A recursive formula

$$\begin{aligned} g_{p,k}^{(n)}(r) &= \frac{r - r_k^{(n)}}{r_p^{(n)} - r_k^{(n)}} g_{p,k-1}^{(n)}(r), \quad p \neq k \\ \partial_r g_{p,k}^{(n)} &= \frac{g_{p,k-1}^{(n)}(r) + \partial_r g_{p,k-1}^{(n)}(r - r_k^{(n)})}{r_p^{(n)} - r_k^{(n)}}, \quad p \neq k \\ g_{p,p}^{(n)}(r) &= g_{p,p-1}^{(n)}(r), \quad \partial_r g_{p,p}^{(n)} = \partial_r g_{p,p-1}^{(n)} \end{aligned} \tag{3.25}$$

is applied, where the computation of values and derivatives scales as $\sim P_n$.

With the finite element representation, the wavefunction represented by FEM and FE-DVR can be re-written as

$$\psi(r, \theta, \phi, t) \approx \sum_{m=-M_{\max}}^{M_{\max}} \sum_{l=|m|}^{L_{\max}} Y_l^m(\Omega) \sum_{n=1}^{N} \sum_{p=0}^{P_n-1} \chi_p^{(n)}(r) c_{n,p}^{m,l}(t) \frac{1}{r}, \tag{3.26}$$

with $c_{n,p}^{m,l}(t)$ being the elements of coefficients vector $\vec{c(t)}$ introduced in Eq. (3.3), where $\chi_p^{(n)}(r)$ is a modified basis set from $f_p^{(n)}(r)$ for better numerical behaviors such as orthogonality and continuity, as shown below.

Continuity

As stated above, the matrices are created locally in each element with the FEM and FE-DVR methods, implying that TDSE is solved locally. The operations for continuity of the wavefunction connect the individual elements, making the solution global. Here, as an example, we present two methods to ensure the continuity of FE-DVR methods. Both methods introduce a modified basis set $\chi_p^{(n)}(r)$, as shown below.

The first is to include a "bridge" function to form a new basis set as

$$\chi_p^{(n)} = \begin{cases} f_p^{(n)}/\sqrt{\omega_p^{(n)}}, & r \in [r_{n-1}, r_n] \text{ if } 0 < p < P_n - 1 \\ (f_{P_n-1}^{(n)} + f_0^{(n+1)})/\sqrt{(\omega_{P_n-1}^{(n)} + \omega_0^{(n+1)})}, & r \in [r_{n-1}, r_{n+1}] \text{ if } p = P_{n-1} \end{cases} \tag{3.27}$$

with the first basis function crossing two intervals. With the new basis, the overlap matrix $\hat{S}$ is identity with

$$\hat{S}_{pq}^{mn} = \langle \chi_p^{(m)} | \chi_q^{(n)} \rangle = \delta_{mn}\delta_{pq} \tag{3.28}$$

and the local operators $\hat{V}$ are diagonal by

$$\hat{V}_{pq}^{mn} = \langle \chi_p^{(m)} | \hat{V} | \chi_q^{(n)} \rangle = \delta_{mn}\delta_{pq} V(r_p^{(n)}) \tag{3.29}$$

The radial function $R_{ml}(r,t)$ (in Eq. (3.4)) spanned in new basis is

$$R_{ml}(r,t) = \sum_{n=1}^{N} \sum_{p=0}^{P_n-1} \chi_p^{(n)}(r) c_{n,p}^{m,l}(t) \frac{1}{r}, \tag{3.30}$$

where the each coefficient depends on only one discrete value

$$c_{n,p}^{m,l}(t)(t) = r_p^{(n)} R_{lm}(r_p^{(n)}, t)[\sqrt{\omega_p^{(n)}} + \delta_{p,0}(\frac{\sqrt{\omega_{P_n}^{(n)}} + \sqrt{\omega_0^{(n+1)}}}{2} - \sqrt{\omega_p^{(n)}})]. \tag{3.31}$$

The second method involves keeping every interval independent by choosing a new basis

$$\chi_p^{(n)}(r) = \begin{cases} f_p^{(n)}/\sqrt{\omega_p^{(n)}} \text{ if } r \in (r_{n-1}, r_n) \\ f_p^{(n)} \text{ if } p = 0, P_n - 1 \end{cases}, \tag{3.32}$$

by which the overlap matrix on each interval is diagonal with elements

$$\hat{S}_{pq}^{mn} = \langle \chi_p^{(m)} | \chi_q^{(m)} \rangle = \delta_{pq}\delta_{mn} \left[1 + (\delta_{p,0} + \delta_{p,P_n-1})(\omega_p^{(n)} - 1) \right] \tag{3.33}$$

as well as the local operator matrices V_r with matrix elements being

$$\hat{V}_{pq}^{mn} = \langle \chi_p^{(m)} | \hat{V} | \chi_q^{(n)} \rangle = \delta_{pq}\delta_{mn} V(r_p^{(n)}) \left[1 + (\delta_{p,0} + \delta_{p,P_n-1})(\omega_p^{(n)} - 1) \right]. \tag{3.34}$$

Each coefficient in radial function $R_{ml}(r,t)$ (in Eq. (3.4) with the basis shown in Eq. (3.30)) can be written as

$$c_{n,p}^{m,l}(t) = r_p^{(n)} R_{ml}(r_p^{(n)},t)\left[\sqrt{\omega_p^{(n)}} - (\delta_{p,0}+\delta_{p,P_n-1})(\sqrt{\omega_p^{(n)}}-1)\right], \tag{3.35}$$

described by the discrete variables of the radial functions; each property is also satisfied by the first method above (see Eq. (3.31)), explaining the reason for the name "discrete variable representation." The boundary values are the coefficients values. For continuity, the coefficients at the boundaries are averaged by

$$c_{n,P_{n-1}}^{m,l}(t) = c_{n+1,0}^{m,l}(t) = \frac{c_{n,P_{n-1}}^{m,l}(t) + c_{n+1,0}^{m,l}(t)}{2}. \tag{3.36}$$

Both the methods create the matrix element of the derivative operator as

$$\hat{\mathrm{Der}}_{pq}^{mn} = \langle \chi_p^{(m)} | \frac{d}{dr} | \chi_q^{(n)} \rangle = \delta_{mn} \sum_k \omega_k^{(n)} \chi_p^{(m)}(r_k^{(m)}) \frac{d\chi_q^{(n)}}{dr}|_{r=r_k^{(n)}}, \tag{3.37}$$

which is a set of non-diagonal blocks. Thus, the matrix elements for the second derivative operator are also non-diagonal.

When the wavefunction is discretized by FEM, the two above-mentioned methods also apply to ensure the continuity, and creating the new basis only requires forcing the weights in Eq. (3.27) and (3.32) to be 1. Apparently, the local overlap and potential operators are not diagonal, same as the FE-DVR method.

In the first method, continuity is automatically satisfied by the bridge basis function, and operations for continuity are not needed for time propagation. The disadvantage is that the introduction of the bridge function requires extra treatment and complicates the creation of operators, such as the electron-electron-interaction (E-E) operator. Despite additional operations for continuity with minor computational cost, the second method keeps a relatively simpler design. Currently, we use the second method in our code.

3.1.3 Constraints of two-particle basis set

The entangled ansatz, while considering the repulsion of the two particles, cannot be factored into the *tensor product* of two single-particle states but can still be represented by the *combined* two single-particle basis sets as

$$\begin{aligned}\psi(\vec{r}_1,\vec{r}_2,t) =& \psi(r_1,\Omega_1,r_2,\Omega_2,t) \\ =& \sum_{m_1,l_1} Y_{l_1}^{m_1}(\Omega_1) \sum_{m_2,l_2} Y_{l_2}^{m_2}(\Omega_2) R_{m_1,m_2,l_1,l_2}(r_1,r_2,t),\end{aligned} \tag{3.38}$$

where $\Omega_{1/2} = (\theta_{1/2},\phi_{1/2})$ are angles of electron 1/2, and we include the correlation of the two particles in the radial function $R_{m_1,m_2,l_1,l_2}(r_1,r_2,t)$. The angular momenta are represented by the coupled spherical harmonics in literature [146] as

$$\mathcal{Y}_{l_1,l_2}^{LM}(\Omega_1,\Omega_2) \coloneqq \sum_{m_1,m_2}^{M} \langle l_1 m_1 l_2 m_2 | l_1 l_2 L M \rangle Y_{l_1}^{m_1}(\Omega_1) Y_{l_2}^{m_2}(\Omega_2) \tag{3.39}$$

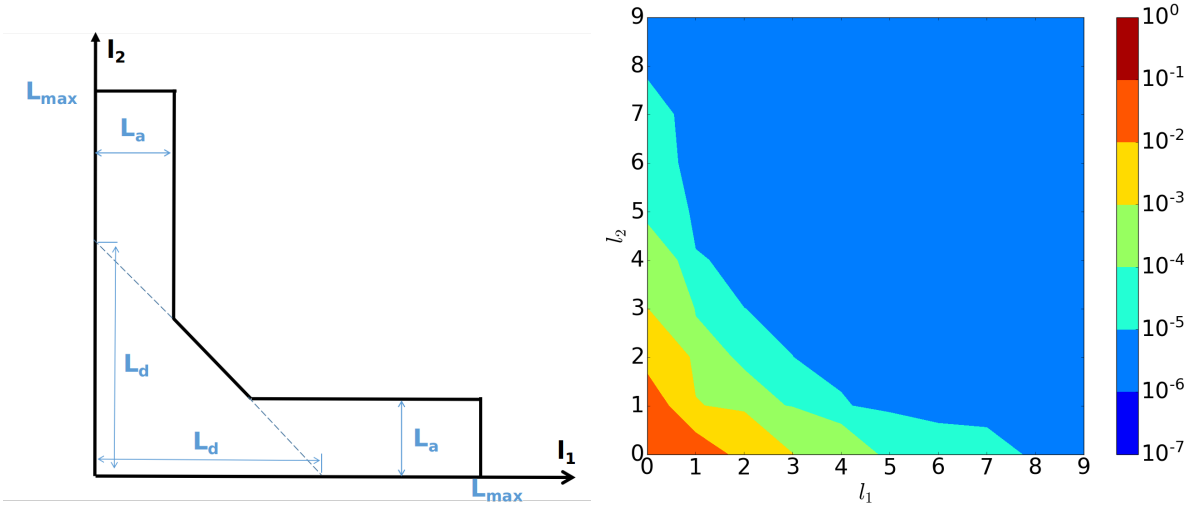

(a) (b)

Figure 3.1: (a) The l_1,l_2 constraint illustration. The $l_{1,2}$ are confined in the armchair shape which is defined by the diagonal part L_d and arm-width part L_a apart from $L_{\max}$. (b) The maximum populated yields of angular momentum l_1, l_2 during the propagation calculated by $\rho^{\max}_{l_1,l_2} = \max_{t,m_1,m_2}(\|\rho_{l_1,l_2}(t)\|^2)$, where $\|\cdots\|$ means the integration over $\vec{r}_1, \vec{r}_2$ coordinates, and $\rho_{l_1,l_2}(t) = \int\int d\Omega_1 d\Omega_2 Y^{m_1}_{l_1}(\Omega_1) Y^{m_2}_{l_2}(\Omega_2)\psi(t)$. The exemplary pulse has $\lambda = 394.5$ nm, $3.7 \times 10^{14}\,\mathrm{W/cm^2}$ with "flat-top" trapezoidal envelope whose definition can be found in Sec. A.4.

with $\langle l_1 m_1 l_2 m_2 | l_1 l_2 L M\rangle$ being the Clebsch-Gordan coefficients for representing the coupled state by the tensor product of individual spherical harmonics basis. Whereas this formula is not applied in our code and the $L_{\max}$ is the total angular momentum in our code and is different from L in the above equation. Theoretically, introducing the total angular momentum quantum number L, M enables an easy truncation of angular space. However, truncation of $M = m_1 + m_2$ is negligible in the z-direction, linearly polarized pulse, as $M = 0$ is automatically satisfied for symmetry. The $m_1 - m_2$ coupling for the Coulomb potential is weak and mostly from the initial state. If there are hard collisions between the electrons in laser dynamics, M number might increase while $m_1 - m_2$ is still conserved. Further, the truncation of L is only available for short wavelengths where the movement of particles is contributed by the absorption of only a few photons. In the perturbative regime (high-frequency limit), the simple square l_1, l_2 grid constrained by $L_{\max,1/2}$ already suffices, as the populated angular momentum l_1 is independent of l_2. For larger wavelengths, the constraint of l_1, l_2 grid forms an armchair-like shape, as shown in Fig. 3.1 from our previous study by analyzing the population of partial waves at the borders of grids [54]. The shape is constrained by two parameters, including the armchair width L_a and the diagonal L_d

with formula

$$\begin{aligned} l_1 + l_2 \leq L_d, l_{1,2} \in (L_a, L_d - L_a) \\ l_1 \leq L_a, l_2 \in [L_d - L_a, L_{\max}] \\ l_2 \leq L_a, l_1 \in [L_d - L_a, L_{\max}]. \end{aligned} \tag{3.40}$$

With the constraints mentioned above, the Eq. (3.38) can be re-written as

$$\psi(\vec{r}_1, \vec{r}_2, t) = \sum_{m=-M_{\max}}^{M_{\max}} \sum_{l_1=|m|}^{L_{\max}} \sum_{l_2=|m|}^{g(L_a,L_d,l_1)} Y_{l_1}^{m}(\Omega_1) Y_{l_2}^{-m}(\Omega_2) R_{m,-m,l_1,l_2}(r_1, r_2, t), \tag{3.41}$$

where $g(L_a, L_d, l_1) = \max(l_2)$ is depicted by Eq. (3.40) and we use $m_1 + m_2 = 0$ for cylindrical symmetry in z-direction, linear polarization.

The radial function $R_{m_1,m_2,l_1,l_2}(r_1, r_2, t)$ in Eq. (3.38) represented by the optimized basis functions χ in Eq. (3.32) or Eq. (3.27) for continuity goes as

$$R_{m_1,m_2,l_1,l_2,}(r_1, r_2, t) = \sum_{n_1=1}^{N_1} \sum_{p_1=0}^{P_{n_1}-1} \sum_{n_2=1}^{N_2} \sum_{p_2=0}^{P_{n_2}-1} \chi_{p_1}^{(n_1)}(r_1) \chi_{p_2}^{(n_2)}(r_2) c_{n_1,n_2,p_1,p_2}^{m_1,m_2,l_1,l_2}(t) \frac{1}{r_1 r_2}, \tag{3.42}$$

where $c_{n_1,n_2,p_1,p_2}^{m_1,m_2,l_1,l_2}(t)$ is the time-dependent coefficient, $N_{1/2}$ and $P_{n_{1/2}}$ are the number of intervals and polynomials order of radial axis $r_{1/2}$. $\chi_{p_{1/2}}^{(n_{1/2})}(r_{1/2})$ are the $p_{1/2}$th basis functions on $n_{1/2}$th interval of radial axis $r_{1/2}$, where we use $p_{1/2}$ to represent the basis function order for two correlated particles, compared to previous p, q for sub-indices of matrix; for example, in Eq. (3.33). Each coefficient is represented by the value of the radial function at one r_1, r_2 grid, similar to the single-particle situation in Eq. (3.31) as

$$\begin{aligned} c_{n_1,n_2,p_1,p_2}^{m_1,m_2,l_1,l_2}(t) =& r_{p_1}^{(n_1)} r_{p_2}^{(n_2)} R_{m_1,m_2,l_1,l_2}(r_{p_1}^{(n_1)}, r_{p_2}^{(n_2)}, t) \\ & \times \left[1 - (\delta_{p_1,0} + \delta_{p_1,P_{n_1}-1})(\sqrt{\omega_{p_1}^{(n_1)}} - 1)\right] \left[1 - (\delta_{p_2,0} + \delta_{p_2,P_{n_1}-1})(\sqrt{\omega_{p_2}^{(n_2)}} - 1)\right], \end{aligned} \tag{3.43}$$

with FE-DVR basis in Eq. (3.32), where $\omega_{p_{1/2}}^{(n_{1/2})}$ is the $p_{1/2}$th quadrature weight on $n_{1/2}$th interval of radial axis $r_{1/2}$.

Exchange asymmetry of ansatz

As the two electrons are indistinguishable and the ground symmetric state gives the lowest energy, the particles are in a singlet state without laser field. With the Hamiltonian that respects symmetry, the exchange asymmetry of the wavefunction

$$\psi(\vec{r}_1, \vec{r}_2, t) = \psi(\vec{r}_2, \vec{r}_1, t) \tag{3.44}$$

represented by coefficients as

$$c_{n_2,n_1,p_2,p_1}^{m_2,m_1,l_2,l_1}(t) = c_{n_1,n_2,p_1,p_2}^{m_1,m_2,l_1,l_2}(t) \tag{3.45}$$

is satisfied in theory for double ionization computation, which is also listed in Ref. [49], because we neglect the relativistic effect and magnetic field; see Sec. 1.3.1 where spin is conserved. Application of exchange asymmetry reduces the total number of coefficients by nearly a factor of two, except the diagonal elements. However, this does not dramatically increase the performance, and it destroys the locality of the operators in memory. The exchange asymmetry is not enforced in tRecX, but we always start from an exchange symmetric state for Helium to ensure an exchange symmetric result.

3.1.4 Recursive indexing code design

The recursive indexing code design is an implementation of the "composite pattern" [147] or partitioning design pattern that allows treating the individual objects and the compositions uniformly by "composing" the objects into tree structures to represent the part-whole hierarchies. By definition of the tree structure, every local structure resembles the total structure, and the whole structure can be reached from any node. The method provides the consistency required to represent the individual part as well as the overall structure. Moreover, it is easy to translate the mathematical representation of the wavefunctions and basis into code.

Here, we will show the composite pattern for representing a 3D single-particle wavefunction in Eq. (3.2), whose coefficient vector $\vec{c}(t)$ consists of elements $c_{m,l,n,p}(t)$ (see Eq. (3.26)) marked by a sequence of discretization parameters m, l, n, p with constraints $l \geq |m|$. The hierarchy structure of the coefficient can be represented by a tree structure, as shown in Fig. 3.2a, where the position of a node in the tree represents a typical discretization parameter, namely the depth of the type of parameter or queue number for the value of a discretization parameter among its siblings. Notably, here we only present one possible hierarchy m, l, n, p, where one may also choose l, m, n, p and n, l, m, p on different occasions, with suitable coordinate constraints.

The single emission hierarchy above can be extended to present the double-emission 6D wavefunction coefficient $c^{m_1,m_2,l_1,l_2}_{n_1,n_2,p_1,p_2}(t)$ (see Eq. (3.42) and (3.38)), as shown in Fig. 3.2b. The angular momentum constraints, including $l_{1/2} \geq |m_{1/2}|$, $m_1 + m_2 = 0$ and the armchair-shape constraint for l_1, l_2 should also be included on lower level nodes which is not displayed the figure as small $L_{\max}$ and $M_{\max}$ are used due to the limited space for displaying the figure. The modified sequence of quantum numbers $m_1, m_2, l_1, l_2, n_1, n_2$ can also be described using the tree structure with suitable constraints, similar to its use for single-particle representation.

3.2 Electron-electron interaction

Electron-electron (E-E) interaction, representing the entanglement of two particles, is the only term that could not be factored into a tensor product of two single-particle operators, see Eq. (2.69). Without E-E interaction, the total wavefunction can be written as a tensor product of two single-particle wavefunctions.

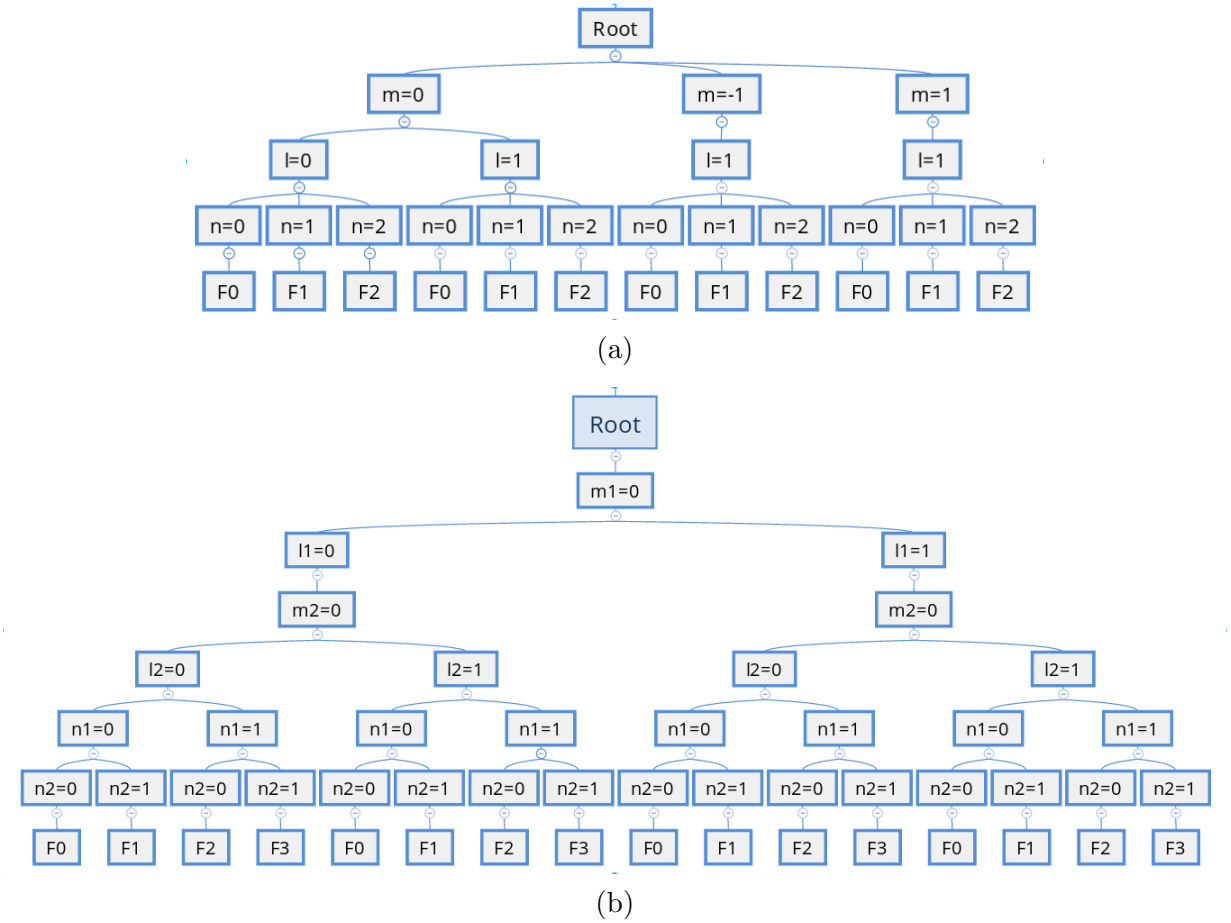

Figure 3.2: (a) The schematic illustration of the tree structure of a discretization for a single-particle hierarchy with parameters $M_{\max} = 1 : m = 0, \pm 1$ and $L_{\max} = 1 : l = 0, 1$ with angular constraint $l \geq |m|$, $N = 2 : n = 0, 1, 2$ represents the intervals, and F_0, F_1, F_2 are corresponding floors, representing the basis functions on $[0, \frac{R_0}{2}]$, $[\frac{R_0}{2}, R_0]$ and $[R_0, \infty)$, respectively. (b) The schematic illustration of the tree structure of a discretization for two particle wavefunction with parameters $M_{\max} = 0, L_{\max} = 1$ and only 1 interval in the simulation box. In the figure, $N1/2$ represent the index of interval on $r_{1/2}$ axis with $N1/2 = 0 : \Omega_0 = [0, R_0), N1/2 = 1 : \Omega_1 = [R_0, \infty)$. $F0, F1, F2, F3$ are the floors, representing basis functions on the corresponding intervals as: $\Omega_0 \otimes \Omega_0, \Omega_0 \otimes \Omega_1, \Omega_1 \otimes \Omega_0, \Omega_1 \otimes \Omega_1$.

3.2.1 Multipole expansion

The E-E interaction can be written in the multipole expansion form, which splits the E-E interaction into angular and radial functions $R^{n_1 n_2}_{m_1 l_1 m_2 l_2}$, $R^{n_1' n_2'}_{m_1' l_1' m_2' l_2'}$ as

$$\begin{aligned}
&\langle \psi^{(n_1' n_2')}_{m_1' m_2' l_1' l_2'} | \frac{1}{|\vec{r}_1 - \vec{r}_2|} | \psi^{(n_1 n_2)}_{m_1, m_2, l_1, l_2} \rangle \\
&= \sum_{\lambda\mu} \frac{4\pi}{2\lambda+1} \langle Y^{m_1'}_{l_1'} Y^{\mu}_{\lambda} | Y^{m_1}_{l_1} \rangle \langle Y^{m_2'}_{l_2'} | Y^{\mu}_{\lambda} Y^{m_2}_{l_2} \rangle \underbrace{\langle R^{n_1' n_2'}_{m_1' l_1' m_2' l_2'} | \frac{\min(r_1, r_2)^{\lambda}}{\max(r_1, r_2)^{\lambda+1}} | R^{n_1 n_2}_{m_1 l_1 m_2 l_2} \rangle}_{:= \hat{V}^{(\lambda)}}
\end{aligned} \tag{3.46}$$

where n_1, n_2, n_1', n_2' are the interval indexes, l_1, l_2, m_1, m_2 are the angular quantum numbers, as stated before, and $\psi^{(n_1' n_2')}_{m_1' m_2' l_1' l_2'}$, $\psi^{(n_1 n_2)}_{m_1, m_2, l_1, l_2}$ are fragments of wavefunctions with specific quantum numbers. With the orthogonality of the spherical harmonics, the matrix elements are non-zero only when $\mu = m_1 - m_1'$ and $\mu = m_2' - m_2$. This thesis focuses on the $z-$direction, linear polarization where the constraint $m_1 + m_2 = 0, m_1' + m_2' = 0$ is always satisfied. Thus, the two constraints are simplified to $\delta_{\mu, m_1 - m_1'}$. The angular contribution of all azimuthal quantum numbers is summed over all available quantum numbers λ, whose limit satisfies $\lambda_{\max} = 2L_{\max}$, which in practice is often not needed and $\lambda_{\max} = 8$ is already sufficient, even when $L_{\max}$ exceeds 20.

The main computational task is in the radial part $\hat{V}$, which can be written in a tensor product form as

$$\hat{V}^{(\lambda)} = \left(\hat{T}^{(n_1)} \otimes \hat{T}^{(n_1)} \right)^T \hat{D}^{(\lambda)} \left(\hat{T}^{(n_1)} \otimes \hat{T}^{(n_2)} \right) \tag{3.47}$$

to reduce the computational cost [82]. The details are in the next section.

3.2.2 Radial matrix diagonalization

With the FEM, radial part matrix element is

$$\hat{V}^{\lambda, n_1 n_2}_{p_1' p_2' p_1 p_2} = \int dr_1 \int dr_2 f^{(n_1)}_{p_1'}(r_1) f^{(n_2)}_{p_2'}(r_2) f^{(n_1)}_{p_1}(r_1) f^{(n_2)}_{p_2}(r_2) \frac{\min(r_1, r_2)^{\lambda}}{\max(r_1, r_2)^{\lambda+1}} \tag{3.48}$$

where we still use $f^{(n)}_{p_{1/2}}(r_{1/2})$ to represent the basis set rather than $\chi^{(n)}_{p_{1/2}}(r_{1/2})$ (see Eq. (3.26), for numerical efficiency) by convenience. Since we do not consider the bridge function for continuity where $\chi^{(n)}_{p_{1/2}}(r_{1/2})$ and $f^{(n)}_{p_{1/2}}(r_{1/2})$ only differ by a constant, multiplicative factor, the derivations given here for the E-E interaction do not change. The meaning of relevant discretization parameter is given in Sec. 3.1.3.

Coupled basis and DVR

If we group the basis functions represented by sub-indexes $(p_1' p_2', p_1 p_2)$ of Eq. (3.48) into to coupled basis functions $F^{(n_{1/2})}_{P_{1/2}} = f^{(n_{1/2})}_{p_{1/2}} f^{(n_{1/2})}_{p_{1/2}'}$ with sub-indexes $P_1 = (p_1' p_1)$ and $P_2 = (p_2' p_2)$

where $P_1 \le N_p^2$ and $P_2 \le N_p^2$, the radial part is written as a $N_p^2 \times N_p^2$ matrix

$$\hat{V}^{\lambda,n_1n_2}_{p_1'p_2'p_1p_2} = \hat{W}^{(\lambda)}_{P_1,P_2}. \tag{3.49}$$

Note that the maximum polynomial order for coupled basis functions is $2(N_p-1)$ and for matrix elements is $4(N_p-1)$. A set of $R := 2N_p-1$ Gaussian quadrature points that give the exact integration value for up to $2R-1 = 4N_p-3 > 4(N_p-1)$ order polynomials helps simplify the integration, and the coupled basis functions are evaluated on R grid points as

$$F^{(n_{1/2})}_{P_{1/2}}(r_{1/2,q}) := f^{(n_{1/2})}_{p'_{1/2}}(r_{1/2,q}) f^{(n_{1/2})}_{p_{1/2}}(r_{1/2,q}), 1 \le q \le R \tag{3.50}$$

where $r_{1/2,q}$ represents the qth quadrature points on r_1 or r_2. Assuming that there exist Gaussian quadrature grids $\{q^{(n_{1/2})}_{i/j}\}_{i,j=1,\cdots R}$ with quadrature weights $\omega^{(n_{1/2})}_{i/j}$ on interval $[r_{1/2,n_{1/2}-1}, r_{1/2,n_{1/2}}]$, matrix $\hat{W}^{(\lambda)}_{P_1,P_2}$ can be reduced to a $R \times R$ matrix $\hat{D}^{(\lambda)}_{ij}$ by

$$\hat{D}^{(\lambda)}_{ij} = \sum_{P_1,P_2} F^{(n_1)}_{P_1}(q^{(n_1)}_i) \hat{W}^{(\lambda)}_{P_1,P_2} F^{(n_2)}_{P_2}(q^{(n_2)}_j), \tag{3.51}$$

where $r_{1/2,n_{1/2}-1}, r_{1/2,n_{1/2}}$ are the boundaries of $n_{1/2}$th interval on $r_{1/2}$ axis, and i/j means i or j. The coupled basis are thus described by discrete variable representation (DVR). For the FEM, the information on the quadrature grids are obtained by a matrix which factors into a tensor product form of the two separate particles as $\hat{T}^{(n_1)} \otimes \hat{T}^{(n_2)}$ because the transformation of the polynomials to the grids can be separately performed. The separate transformation $R \times N_p$ matrix on each particle has its matrix element

$$\hat{T}^{(n_1)}_{i,p_1} = \sqrt{\omega^{(n_1)}_i} f^{(n_1)}_{p_1}(q^{(n_1)}_i), \quad \hat{T}^{(n_2)}_{j,p_2} = \sqrt{\omega^{(n_2)}_j} f^{(n_2)}_{p_2}(q^{(n_2)}_j), \tag{3.52}$$

where the square root of weight is introduced for convenience, same as Eq. (3.32).

Vectorization and Hadamard product

As the matrix transformation of tensor product satisfies

$$(B^T \otimes A)\mathrm{vec}(X) = \mathrm{vec}(AXB), \tag{3.53}$$

where A, B, X are matrices and $\mathrm{vec}(X)$ is the vectorization X by combining all its columns by order into a vector [148]. The coefficients C representing the ansatz by a tensor product basis can also be written in matrix form, denoted by $\mathrm{Mat}(C)$. The operation of a transformation matrix on the coefficients is given as

$$(\hat{T}^{(n_1)} \otimes \hat{T}^{(n_2)})C = \mathrm{vec}(\hat{T}^{(n_2),\tau} \mathrm{Mat}(C) \hat{T}^{(n_1)}), \tag{3.54}$$

wherein operation count is $RN_p(N_p+R) \sim N_p^3$, rather than $RN_pRN_p \sim N_p^4$, and the columns of matrix $\mathrm{Mat}(C)$ are fragments of the long coefficients vector C and $\hat{T}^{(n_2),\tau}$ is the transpose

of matrix $\hat{T}^{(n_1)}$. With the integration of quadrature grids, the radial part is the product of two transformation matrix with size $R^2 \times N_p^2$ and $R \times R$ matrix $\hat{D}_{i,j}^{(\lambda)}$ shown below

$$\hat{V}_{p_1' p_2', p_1 p_2}^{(\lambda, n_1 n_2)} = \left(\hat{T}_{i,p_1'}^{(n_1)} \otimes \hat{T}_{j,p_2'}^{(n_2)}\right)^T \hat{D}_{i,j}^{(\lambda)} \circ \left(\hat{T}_{i,p_1}^{(n_1)} \otimes \hat{T}_{j,p_2}^{(n_2)}\right), \tag{3.55}$$

where $\hat{D}_{i,j}^{(\lambda)} \circ (\hat{T}_{i,p_1}^{(n_1)} \otimes \hat{T}_{j,p_2}^{(n_2)})$ means the Hadamard product $\circ$ (also known as element-wise or Schur product) of the vectorized $\hat{D}_{i,j}^{(\lambda)}$ with the values on the grids on the right [148]. Then, the new evaluations on the grids are transformed back to the coefficients.

$\hat{D}_{ij}^{(\lambda)}$ matrix elements

The $\hat{D}_{ij}^{(\lambda)}$ matrix is calculated during the setup process. During its setup, the integration with $\frac{\min(r_1,r_2)^\lambda}{\max(r_1,r_2)^{\lambda+1}}$ cannot be computed like $\frac{\min(r_i,r_j)^\lambda}{\max(r_i,r_j)^{\lambda+1}}$ with quadrature points, as the Gaussian quadrature expands the derivative discontinuity of $\frac{\min(r_1,r_2)^\lambda}{\max(r_1,r_2)^{\lambda+1}}$ in a polynomial basis and gives poor numerical accuracy.

The tRecX code (see Sec. 3.6) uses the method reported in Ref. [84] to calculate $\hat{D}_{ij}^{(\lambda)}$ based on the discrete values on the grids (DVR method). As the integration of the matrix element covers the whole unscaled radial range, for notational brevity, we write the new basis functions (Lagrange polynomials) created by $NR, N = N_1 = N_2$ grid points of radial axes r_1, r_2 as $g_i(r), g_j(r) \quad i,j \in [0, NR)$ and $g_i(q_k) = \frac{\delta_{i,k}}{\sqrt{\omega_i}}$, a method similar to re-labeling the DVR points on all intervals into a general index as $i = (n_1, p_1)$ and $j = (n_2, p_2)$. The generic matrix element $\hat{V}_{p_1' p_2' p_1 p_2}^{\lambda, n_1 n_2}$ on the whole radial, except the complex scaled region, has the form

$$\hat{V}_{ijkl}^{\lambda} = \int_0^{R_0} dr_1 \int_0^{R_0} dr_2 \frac{r_<^\lambda}{r_>^{\lambda+1}} g_i(r_1) g_k(r_1) g_j(r_2) g_l(r_2) = \int_0^{R_0} dr_1 \int_0^{R_0} dr_2 \frac{r_<^\lambda}{r_>^{\lambda+1}} G_1(r_1) G_2(r_2), \tag{3.56}$$

where $r_< = \min(r_1, r_2), \quad r_> = \max(r_1, r_2)$ and $G_1(r) = g_i(r) g_k(r), G_2(r) = g_j(r) g_l(r)$ are the product of the basis functions similar to Eq. (3.50). A new function

$$y(r) = r \int_0^{R_0} G_1(r') \frac{r_<^\lambda}{r_>^{\lambda+1}} dr' = \int_0^r G_1(t) (\frac{t}{r})^\lambda dt + \int_r^{R_0} G_1(t) (\frac{r}{t})^{\lambda+1} dt \tag{3.57}$$

that satisfies the Poisson equation

$$\frac{d^2 y}{dr^2} - \frac{\lambda(\lambda+1)}{r^2} y = -\frac{2\lambda+1}{r} G_1(r) \tag{3.58}$$

is introduced. Thus, we can solve the integration of $\frac{r_<^\lambda}{r_>^{\lambda+1}}$ by solving $y(r)$, which can be well described by the quadrature points. Eq. (3.57) has boundary conditions at 0 and R_0 goes as

$$\begin{aligned} y(0) &= 0 \\ y(R_0) &= \frac{1}{R_0^\lambda} \int_0^{R_0} G_1(t) t^\lambda dt = \frac{1}{R_0^\lambda} \delta_{i,k} r_i^\lambda. \end{aligned} \tag{3.59}$$

The two boundary conditions can not be satisfied at the same time by the Lagrange polynomials of DVR method. However, from Ref. [84], the right boundary condition can be satisfied by adding an extra part to the solution. The solution satisfying the left boundary condition can be written as

$$y^{(0)}(r) = \sum_m C_m g(r). \tag{3.60}$$

Take Eq. (3.60) into Eq. (3.58), multiply $g_n(r)$ on the left and integrate and we have

$$\sum_m T^\lambda_{n,m} C_m = (2\lambda+1)\int_0^{R_0} g_n(r)\frac{1}{r}G_1(r)dr = (2\lambda+1)\frac{\delta_{n,i}\delta_{i,k}}{r_n\sqrt{\omega_n}}, \tag{3.61}$$

where the kinetic term is

$$T^\lambda_{n,m} = -\int_0^{R_0} g_n(r)\left(\frac{d^2}{dr^2} - \frac{l(l+1)}{r^2}\right)g_m(r)dr, \tag{3.62}$$

and the coefficients are

$$C_i = (2\lambda+1)\frac{[T^\lambda_{m,i}]^{-1}\delta_{i,k}}{r_i\sqrt{\omega_i}}. \tag{3.63}$$

Then, the solution becomes

$$y(r) = y^{(0)}(r) + \frac{r^{\lambda+1}}{R_0^{2\lambda+1}}\int_0^{R_0} G_1(r')r'^\lambda dr' = (2\lambda+1)\sum_m g_m(r)[T^\lambda_{m,i}]^{-1}\frac{\delta_{i,k}}{r_i\sqrt{\omega_i}} + \frac{r^{\lambda+1}}{R_0^{2\lambda+1}}\delta_{i,k}r_i^\lambda, \tag{3.64}$$

with the matrix element

$$\langle g_j g_l|\frac{r_<^\lambda}{r_>^{\lambda+1}}|g_i g_k\rangle = \delta_{i,k}\delta_{j,l}\left(\frac{2\lambda+1}{r_i r_j\sqrt{\omega_j\omega_k}}[T^\lambda_{i,j}]^{-1} + \frac{r_i^\lambda r_k^\lambda}{R_0^{2\lambda+1}}\right). \tag{3.65}$$

The matrix is diagonal by the indices corresponding to the grids on the FE-DVR unscaled region, and the computational expensive part is the inverse of the kinetic matrix $[T^\lambda_{i,j}]^{-1}$, which only needs to be calculated once in the setup process. It has R^4 values but only R^2 non-zero ones that correspond to $R\times R$ matrix $\hat{D}^{(\lambda)}_{ij}$

$$\hat{D}^{(\lambda)}_{ij} = \frac{2\lambda+1}{r_i r_j\sqrt{\omega_i\omega_j}}[T^\lambda_{i,j}]^{-1} + \frac{r_i^\lambda r_j^\lambda}{R_0^{2\lambda+1}}. \tag{3.66}$$

With FE-DVR, where i,j are split by N_1, N_2 intervals with indexes n_1, n_2, we have rewritten $\hat{D}^{(\lambda)}_{ij}$ as

$$\hat{D}^{(\lambda,n_1,n_2)}_{ij} = \frac{2\lambda+1}{r_i^{(n_1)}r_j^{(n_2)}\sqrt{\omega_i^{(n_1)}\omega_j^{(n_2)}}}[T^{(\lambda,n_1,n_2)}_{i,j}]^{-1} + \frac{(r_i^{(n_1)})^\lambda (r_j^{(n_2)})^\lambda}{R_0^{2\lambda+1}}, \tag{3.67}$$

where i,j are indexes on intervals n_1, n_2. In practice, we find the integration by quadrature grids does not need to be exact and that $R = N_p$ is enough for the required accuracy.

Further, for the FE-DVR method, the transformation matrix in Eq. (3.52) is not needed and

$$\hat{V}^{(\lambda,n_1,n_2)}_{p_1'p_2',p_1p_2} = \delta_{p_1,p_1'}\delta_{p_2,p_2'}\hat{D}^{(\lambda,n_1,n_2)}_{p_1,p_2}. \tag{3.68}$$

Its operation on the coefficient is the Hadamard product of $R \times R$ size matrix $\hat{D}^{(\lambda,n_1,n_2)}_{p_1,p_2}$, or matrix-vector multiplication by full matrix with size $R^2 \times R^2$, including all the zero value elements.

E-E interaction in haCC

Apart from double emission calculations, the electron-electron interaction also exists in haCC calculations. Rather than two liberated particles, haCC calculates the Coulomb interaction of an ionized particle and bound electrons represented by Hartree-Fock orbitals. For computing E-E integrals, the kth Hartree-Fock orbitals $\Phi_k(\vec{r})$ are evaluated on single center quadrature points $r_0, r_1, ..., r_Q$

$$\Phi_k(\vec{r}) = \sum_{q_k l_k m_k} c^{(k)}_{q_k l_k m_k} Y_{l_k m_k}(\theta, \phi). \tag{3.69}$$

For more details on haCC, refer to Sec. 2.3. With the free particle ansatz evaluated at the same quadrature points, the E-E interaction can be calculated based on the DVR values above.

The advantage of the above-mentioned method is that one can approximate the E-E term in the diagonal form after accurately computing the integrals once. The method can be generally applied to most two-dimensional multiplication potentials, even with the non-analytical potential, and it gives exact results with product polynomial basis functions. One can use this method to directly compute the potential that is convergent in the Taylor series.

3.3 Infinite-Range Exterior Complex Scaling

With the tSurff methods, one can solve the TDSE in a reduced space range. As the number of coefficients for approximating the radial function largely depends on R_0, one needs the smallest possible inner region ($r \leq R_0$) to precisely approximate the wavefunction. The outer region ($r \geq R_0$) has an absorber to avoid any reflections to the inner region of interest. As the reflections at the boundaries of the outer region affect the wavefunction near the nucleus and amplify quickly, especially when the space of interest is not large, the criteria of the absorber are stringent.

Infinite-range exterior complex scaling (irECS) is an ideal choice [149]. First, complex scaling is an analytical continuation method that is easy to implement. Second, the irECS preserves the dynamics of the particles in both scaled and unscaled regions, allowing the re-entry of electrons to the unscaled region, and it also keeps the small tails of the re-scattering wave packets, which moderately extend outside, undisturbed. This even allows

us to choose a region smaller than the quiver radius. The corresponding numerical evidence is given in Ref. [150]. Third, irECS promotes the suppression of reflection in comparison with the conventional masking function technique [151]. Moreover, the resonant states in the complex plane do not move with the complex angle. This allows to find the resonance energies, see Ref. [128] and Fig. 5.7 of Sec. 5.2.4.

3.3.1 Definition

Exterior complex scaling rotates the real axis r to a complex plane after a complex scaling radius R_0 by

$$r \mapsto r_\theta = \begin{cases} r & r \leq R_0 \\ R_0 + e^{\mathrm{i}\theta}(r - R_0) & r \geq R_0 \end{cases} \tag{3.70}$$

where $\theta > 0$ is the complex scaling angle. Plane waves serve as the asymptotic solutions of the wavefunction that are far from the nucleus when the Coulomb interaction is negligible. The irECS maps the asymptotic solution onto a decaying plane wave with the decaying factor $k \sin\theta$, see Eq. (3.71), where k is the momentum, suggesting that wave packets are "absorbed" at $r \geq R_0$.

$$e^{\mathrm{i}kr} \overset{r \geq R_0}{\mapsto} e^{\mathrm{i}kR_0} e^{\mathrm{i}k\cos\theta(r-R_0)} e^{-k\sin\theta(r-R_0)} \overset{r\to\infty}{\to} 0 \tag{3.71}$$

3.3.2 Operators

The operator

$$U_\lambda^R : L^2(\mathbb{R}^+) \mapsto L^2(\mathbb{R}^+), \tag{3.72}$$

denotes the operation of the irECS, which scales the analytical wavefunction ψ as

$$\psi \mapsto U_\lambda^R \psi \equiv \psi_\lambda, \tag{3.73}$$

with the scaled analytical wavefunction ψ_λ being

$$\psi_\lambda(r) \coloneqq \begin{cases} \psi(r) & r \leq R_0 \\ e^{\lambda/2}\psi(e^\lambda(r - R_0) + R_0) & r \geq R_0, \end{cases} \tag{3.74}$$

where $\lambda = \mathrm{i}\theta$.

The scaled operators are defined as $\boldsymbol{O}^\theta \coloneqq U_\theta \boldsymbol{O} U_\theta^\dagger$ where $\boldsymbol{U}_\theta \coloneqq U_{\mathrm{i}\theta}^{R_0}$. The Coulomb operator with r is scaled as

$$V^\theta(r) = (U_\theta V U_\theta^\dagger)(r) = V(e^{\mathrm{i}\theta}(r - R_0) + R_0) \coloneqq V(r_\theta). \tag{3.75}$$

We would like to point out that the transformation matrix U is not unitary for complex λ, and, even worse, the transformed operator is ill-defined if the domain is not defined. Thus, the corresponding spectrum is changed by irECS. However, the complex scaled Hamiltonian is well-defined when $\lambda = -\mathrm{i}\theta$ with $\theta > 0$ in a specific range on domains, where Δ is defined ($D(\Delta)$).

With the following formulas, which may work as the computational recipes, the derivative operator is scaled to

$$\begin{aligned}(\partial_r^{(\theta)}\psi)(r) =&(U_\theta \partial_r U_\theta^\dagger \psi)(r)\\ =&U_\theta \partial_r [e^{-\mathrm{i}\theta/2}\psi(e^{-\mathrm{i}\theta}(r-R_0)+R_0)]\\ =&U_\theta e^{-\mathrm{i}\theta/2} e^{-\mathrm{i}\theta}\psi'[e^{-\mathrm{i}\theta}(r-R_0)+R_0]\\ =&e^{-\mathrm{i}\theta}(\partial_r\psi)(r)\end{aligned} \tag{3.76}$$

where a multiplier by a rotational factor $e^{-\mathrm{i}\theta}$ is added. The Laplacian operator is a product of two derivative operators and can be scaled as

$$\Delta^{(\theta)} = e^{-2\mathrm{i}\theta}\Delta. \tag{3.77}$$

Thus, the scaled Hamiltonian of single particle ionization (see Eq. (2.2)) in the velocity gauge is

$$H_V^{(\theta)} = -e^{-2\mathrm{i}\theta}\frac{\Delta}{2} - \mathrm{i}e^{-\mathrm{i}\theta}\vec{A}(t)\cdot\vec{\nabla} + V(\vec{r}_\theta) \tag{3.78}$$

and in the length gauge is

$$H_L^{(\theta)} = -e^{-2\mathrm{i}\theta}\frac{\Delta}{2} + [R_0 + e^{\mathrm{i}\theta}(r-R_0)]\hat{r}\cdot\vec{E}(t) + V(\vec{r}_\theta). \tag{3.79}$$

We usually truncate the Coulomb interaction beyond $R_c \le R_0$ to keep the most of Coulomb long tails. The main contribution of the eigenvalue is the kinetic energy term, which is scaled by $e^{-2\mathrm{i}\theta}$. With the irECS, the continuous spectrum is rotated by 2θ while the discrete part remains unchanged. The resonant eigenenergies do not move in the complex plane when the complex angle changes, which is a property that can be used when searching for resonant states. We also find that for the dipole interaction term with an oscillating electric field, the length gauge $\vec{E}\cdot\vec{r}$ fails but the velocity gauge $\mathrm{i}\vec{A}\cdot\vec{\nabla}$ does not [150]. Thus, Eq. (3.78) is always applied for calculating photoelectron spectrum, and Eq. (3.79) is always used for static field ionization calculation in the tRecX code.

3.3.3 Implementation of irECS

The irECS is implemented in the radial functions in the tRecX code. The basis functions on the whole radial range are scaled by

$$f_p^{(\theta)}(r) = \begin{cases} f_p(r) & r \le R_0 \\ e^{\mathrm{i}\theta/2} f_p(r) & r \ge R_0, \end{cases} \tag{3.80}$$

and we temporarily remove the (n) in $f_p^{(n)}$ for notational brevity. The scaling of matrix elements depends on the operator type, which is defined as

$$\langle f_p^{(\theta)} | \boldsymbol{O}^\theta | f_q^{(\theta)} \rangle_\theta := \int_{R_0}^\infty dr\, f_p^{(\theta)}(r)(\boldsymbol{O}^\theta f_q^{(\theta)})(r), \tag{3.81}$$

analogous to the unscaled operator in which we assume f_i are purely real. For the overlap S and potential V operators, the scaled basis function applies an extra multiplier $e^{i\theta}$ to the matrix elements as

$$\langle f_p^{(\theta)}|f_q^{(\theta)}\rangle_\theta = S_{pq}^{(\theta)} = \int_{R_0}^{\infty} dr(e^{i\theta/2}f_p)(r)(e^{i\theta/2}f_q^{(\theta)})(r)dr = e^{i\theta}S_{pq} \tag{3.82}$$

and

$$\langle f_p^{(\theta)}|V^{(\theta)}|f_q^{(\theta)}\rangle_\theta = V_{pq}^{(\theta)} = e^{i\theta}\int_{R_0}^{\infty} dr f_p(r)V(r_\theta)f_q(r). \tag{3.83}$$

Further, the kinetic operator applies a multiplier $e^{-i\theta}$ to the matrix elements, see Eq. (3.84),

$$\langle \partial_r^\theta f_p^{(\theta)}|\partial_r^\theta f_q^{(\theta)}\rangle_\theta = \Delta_{pq}^{(\theta)} = e^{i\theta}\int_{R_0}^{\infty} dr(e^{-i\theta}\partial_r f_p)(r)(e^{-i\theta}\partial_r f_q)(r) = e^{-i\theta}\Delta_{pq}, \tag{3.84}$$

where $r_\theta = e^{i\theta}(r - R_0) + R_0$ is the scaled axis.

The irECS method has a scaled region that extends to $r \in [R_0, +\infty)$. With FEM in the old version of tRecX, the basis functions $f_p^{(N+1)}(r)$ are composed by the product of an exponentially decaying factor and Laguerre polynomials $L_p(r)$ [150] as

$$f_p^{(N+1)}(r) = [L_p(2\alpha(r - R_0)) - 1]\exp(-\alpha(r - R_0)), \tag{3.85}$$

where

$$L_p(r) = \frac{1}{p!}\exp(r)\partial_r^p(\exp(-r)r^p), \tag{3.86}$$

$\alpha = 2\theta > 0$ is the decay factor and N depicts the $N+1$th interval, compared to N intervals ($n = 1, \cdots, N$) in the unscaled region. We would like to mention that the shift -1 to the scaled Laguerre polynomials is introduced to force the values of basis functions at the left boundary R_0 is 0 to approximate the near zero wavefunction at the boundary of the simulation box. With FE-DVR method in the new version, the basis functions are

$$f_p^{(N+1),\mathrm{DVR}}(r) = L_p^{\mathrm{DVR}}(r)\exp(-\alpha(r - R_0)) \tag{3.87}$$

where $L_p^{(N),\mathrm{DVR}}(r)$ for DVR are Lagrange polynomials created from Gaussian Radau quadratures points for Laguerre polynomials, where the left point is fixed. It has been proven in our group's previous work [144] that irECS implemented by FE-DVR also allows for perfect absorption. For both FE-DVR and FEM, $\theta \in [0.2, 0.4]$ often results in the best numerical performance.

3.4 Gauges

3.4.1 Gauge transformation

The word "gauge" in mathematical physics refers to any specific mathematical formalism used to regulate redundant degrees of freedom in the Lagrangian [82]. In the quantum

mechanical problems of this thesis, the time- and space-dependent unitary gauge transformation both applies to the wavefunction and operators, and the transformed wavefunction does not need to be the solution for the untransformed one. The gauge transformation operator with the form

$$U_g = e^{\mathrm{i}g(\vec{r},t)} \tag{3.88}$$

maps a wavefunction ψ to ψ_g :

$$\psi \mapsto \psi_g := U_g\psi, \tag{3.89}$$

any operator $\mathcal{O}$ to $\mathcal{O}_g$:

$$\mathcal{O} \mapsto \mathcal{O}_g := U_g\mathcal{O}U_g^\dagger, \tag{3.90}$$

and maps the time derivative operator as

$$\partial_t \mapsto= \partial_t - \mathrm{i}\partial_t g(\vec{r},t). \tag{3.91}$$

An implementation of the transformation in our calculations is the length-to-velocity gauge transformation with

$$U_g = U_{L\to V} = e^{-\mathrm{i}\vec{A}(t)\cdot\vec{r} - \frac{\mathrm{i}}{2}\int_{-\infty}^{t} d\tau \vec{A}^2(\tau)} \tag{3.92}$$

and its inverse

$$U_g^{-1} = U_{L\to V} = e^{\mathrm{i}\vec{A}(t)\cdot\vec{r} + \frac{\mathrm{i}}{2}\int_{-\infty}^{t} d\tau \vec{A}^2(\tau)}. \tag{3.93}$$

The wavefunction in the length gauge ψ_L can be represented by that in the velocity gauge ψ_V with gauge transformation

$$\psi_L = U_g^{-1}\psi_V = e^{\mathrm{i}\vec{A}(t)\cdot\vec{r} + \frac{\mathrm{i}}{2}\int_{-\infty}^{t} d\tau \vec{A}^2(\tau)}\psi_V. \tag{3.94}$$

With the ansatz $\psi_L(\vec{r},t)$ in the TDSE of the length gauge

$$\mathrm{i}\partial_t\psi_L(\vec{r},t) = \left[-\frac{\Delta}{2} + \vec{E}(t)\cdot\vec{r} + V(\vec{r})\right]\psi_L(\vec{r},t) \tag{3.95}$$

replaced by Eq. (3.94), we have the TDSE of the velocity gauge

$$\mathrm{i}\partial_t\psi_V(\vec{r},t) = \left[-\frac{\Delta}{2} - \mathrm{i}\vec{A}(t)\cdot\vec{\nabla} + V(\vec{r})\right]\psi_V(\vec{r}) \tag{3.96}$$

where the formula $\vec{A}(t) := -\int_{-\infty}^{t} d\tau \vec{E}(\tau)$ is used.

3.4.2 Mixed gauge

The length gauge representation well describes bound states, such as the motions of bare atom eigenstates. It is also possible to perform computations with length gauge in the perturbative regime or describe low-energy photoionization peaks near the threshold. However, with length gauge, the description of properties at high momentum, such as the recollision plateau, requires a shorter range modulation of radial parts and more radial

coefficients [152]. With the length gauge, the pulse field accelerates the particle by $\vec{A}(t)$ to a significant momentum that requires a finer resolution on the radial discretization, especially when $\vec{A}(t)$ is comparable or above the momenta of electrons in the field-free system. However, with the velocity gauge representation, canonical momentum is conserved. Compared to the length gauge, the velocity gauge representation requires fewer radial coefficients and is numerically more efficient. Moreover, irECS can only be applied to systems with velocity gauge asymptotics, according to numerical study in Ref. [150]. Thus, the velocity gauge is applied by default in tRecX code unless specified differently.

An exception is the inner region ($r \leq R_0$) of haCC calculation with a restricted multi-electron basis, as mentioned above, where all particles but one are in the near-nucleus region and can only be described with a length gauge [119]. High-momentum particles, better described by a velocity gauge, are free electrons in the remote area from the nucleus. Thus, free electrons and particles at a moderate distance from the nucleus must be described separately. A "mixed gauge" representation of the ansatz by the transformation

$$U_{L\to M} := \begin{Bmatrix} 1 & r \leq R_0 \\ e^{-\mathrm{i}\vec{A}(t)\cdot\vec{r}\frac{r-R_0}{r}} e^{-\frac{\mathrm{i}}{2}\int_\infty^t d\tau \vec{A}^2(\tau)} & r \geq R_0 \end{Bmatrix} \tag{3.97}$$

is applied. Based on previous research in Ref. [119, 152], the mixed gauge representation is numerically efficient with moderate implementation work. A combination of the two gauges in the same computation couples the free electron motion and bound orbitals, thus, clear the air for the coupled channels computation for the polyelectron systems in laser-matter interactions.

3.5 Time propagation

The TDSE can be transformed into the ordinary differential equation in Eq. (3.3) with suitable discretization methods, which can be solved by the 4th order Runge-Kutta method in tRecX code. Apart from the 4th order Runge-Kutta method, there are other propagators reported in the literature, such as the real-space product algorithm [153] used in Ref. [53], the short iterative Lanczos method [154] used in Ref. [49], and the Crank-Nicolson method used in Ref. [80, 91, 155–160].

3.5.1 Initial state

Before the incoming of the pulse, electrons stay in a field-free state, which, for the single ionization propagation and B region time propagation of a double emission, is a ground state of the system ψ_0 with corresponding ground energy E_0 satisfying

$$E_0 = \langle\psi_0|H_0|\psi_0\rangle = \min_{\|\psi\|=1}\langle\psi|H_0|\psi\rangle \tag{3.98}$$

where H_0 is the field-free Hamiltonian of Eq. (3.3). For the single-particle time propagation in the $S(\bar{S})$ region of double ionization stated in Eq. (2.86) and Eq. (2.87), where another particle is ionized, the initial state is a zero vector, as no particles are ionized before the incoming pulse field.

3.5.2 4th order Runge-Kutta

By introducing $f(\psi,t) = -\mathrm{i}\hat{S}^{-1}\hat{H}(t)\psi$, Eq. (3.3) turns into

$$\partial_t\psi = f(\psi,t). \tag{3.99}$$

The propagation of ψ from $\psi_n(\psi \text{ at } t_n)$ to ψ_{n+1} (ψ at $t_{n+1} = t_n + h$, $n = 0,1,2,\cdots$) can be approximated by

$$\psi_{n+1} \doteq \psi_n + \frac{1}{6}(k_1 + 2k_2 + 2k_3 + k_4), \tag{3.100}$$

if the arbitrary time step h is small, where

$$\begin{aligned} k_1 &= hf(\psi_n, t_n) \\ k_2 &= hf(\psi_n + \frac{1}{2}k_1, t_n + \frac{h}{2}) \\ k_3 &= hf(\psi_n + \frac{1}{2}k_2, t_n + \frac{h}{2}) \\ k_4 &= hf(\psi_n + k_2, t_n + h) \end{aligned}. \tag{3.101}$$

This implies that the advancement of the coefficient vector with time can be approximated by a linear combination of vectors, with each obtained by matrix-vector multiplications from the present wavefunction, and numerically simulated on computers and parallelized. Computational accuracy can be ensured by a relatively short time step h. In tRecX code, an adaptive time step is utilized to balance the accuracy and efficiency of the computation.

3.5.3 Adaptive time step control

The longest possible time step for reducing computational time is preferred on the prerequisite that the evolution of the wave packet is accurately described in the oscillating external electric field. The evolution of wave packets is driven by the external field and is highly dependent on the external vector potential. An adaptive time step control is helpful to obtain better convergence properties for computations with long-wave-length laser pulse. Step doubling is implemented in tRecX [161] to compare results from two individual time propagations, with one directly obtained by propagating $\psi_n \to \psi_{n+1}$, and the other by two half steps $\psi_n \to \psi'_{n+1/2} \to \psi'_{n+1}$ ($\psi'_{n+1/2} = \psi'(t_n + 1/2h)$). The error represented by the l_∞−norm of the coefficients vector as

$$\epsilon(\psi_{n+1}, \psi'_{n+1}) := \max_{i=1\cdots N_{\text{coef}}} |C'_{n+1,i} - C_{n+1,i}| \tag{3.102}$$

is applied for controlling the accuracy of the propagation, where $C_{n+1,i}$ and $C'_{n+1,i}$ are the corresponding vector elements of coefficients (see Sec. 3.3). If the error exceeds the maximally admissible error ϵ_0, the step is discarded. The time step h is adjusted based on the error ϵ to ensure the accuracy with formula

$$h \to h(\frac{s\epsilon_0}{\epsilon})^{\frac{1}{5}}, \tag{3.103}$$

where $\frac{1}{5}$ is from $\frac{1}{1+N}$, N is the consistency order (4 for 4th order Runge-Kutta method), $s = 1.5$ is the safety factor in order not to discard too many steps.

The adaptive time step ensures the accuracy of time propagation but introduces a factor 1.5 to the propagation time by applying two extra propagations with half the step size. In a 400 nm pulse calculation with cutoff energy 100 a.u. (see the next subsection), we find that the rejected low-accuracy propagation steps are scarce and a fixed step size computation already suffices.

3.5.4 High energy projection

In FE-DVR, the basis function does not behave well near 0; one reason is that r^l is not included to describe the asymptotic behavior at $r \to 0$ of wavefunction as it is in FEM. This creates a very high contribution from $\frac{1}{r^2}$ term of kinetic energy. Thus, the wavefunction near the nucleus corresponds to the high-energy electrons, which should be removed during wavefunction evolution for numerical efficiency. On the other hand, the maximum energy of an electron in the laser field we consider is $10U_p$ (see Sec. 1.3.7), and high-energy contributions beyond this level do not change the physics but lead to extra computational consumption. Removing the high-energy eigenvectors speeds up the calculation without changing the physics. We find that the large energy eigenvalues in our calculations are contributed by the kinetic energies if the intensity is not too large. Considering that the eigenstate of the kinetic operator does not change with time and the two-particle kinetic operator can be decomposed into a tensor product of two single-particle kinetic operators, for a single-ionization time propagation, the whole Hamiltonian can be approximated by field-free high-energy eigenvectors before time propagation; and for a double emission computation, they can be approximated by a tensor product from two single-particle, field-free high-energy eigenvectors, see below for details. This implies that the projector operator can be constructed during the set-up, before the time propagation, largely reducing the computational resources.

The normalized field-free eigenstates below cutoff energy E_{cut} are denoted as $|E^{(i)}\rangle$ (or $\varphi_i(\vec{r})$) with eigenenergies E_i that satisfy

$$\hat{H}_0|E^{(i)}\rangle = E_i|E^{(i)}\rangle \qquad E_i \geq E_{\text{cut}}. \tag{3.104}$$

If represented by real basis functions, as in tRecX code, the eigenvectors are mutually orthogonal after complex scaling with the c-product formula

$$\langle E^{(i)*}|E^{(j)}\rangle = \int d\vec{r}\varphi^{(j)}(\vec{r})\varphi^{(i)}(\vec{r}) = \delta_{ij} \quad E_{i,j} \geq E_{\text{cut}}, \tag{3.105}$$

which satisfies both unscaled and complex scaled eigenstates, and the complex conjugate operation goes *before* the complex scaling, implying that we do NOT take the complex conjugate of the terms in the wavefunction which *become complex only due to the rotating of the coordinate into the complex plane* [162, 163]. One can remove the partial ansatz whose projection on the high eigenstates is non-zero by

$$\hat{Q} = \hat{\mathbb{1}} - \sum_i \hat{P}_i = \hat{\mathbb{1}} - \sum_i |E^{(i)}\rangle\langle E^{(i)*}|, \tag{3.106}$$

where $\hat{\mathbb{1}}$ is an identity operator. Computing various eigenvalues directly consumes acceptable and moderate resources for single ionization in most cases, but it requires huge computational resources for a 6D TDSE. Instead of calculating the eigenvalue problem for the two particles, we use the tensor product of a unit vector $|\vec{e_{i/j}}\rangle$ and the eigenstate of an individual particle of the ionic Hamiltonian for constructing the projector

$$\hat{Q} = \hat{\mathbb{1}} - \sum_{i,j}(|E^{(i)}\rangle \otimes |\vec{e_j}\rangle + |\vec{e_i}\rangle \otimes |E^{(j)}\rangle)(\langle \vec{e_i}| \otimes \langle E^{(j)*}| + \langle E^{(i)*}| \otimes \langle \vec{e_j}|). \tag{3.107}$$

That is, we perform high-energy projection for two individual particles separately. With the projection, an operator is added to modify the ordinary differential equation Eq. (3.3) to

$$\partial_t \vec{c} = -\mathrm{i}\hat{Q}\hat{S}^{-1}\hat{H}\vec{c}. \tag{3.108}$$

3.6 The tRecX code

The tRecX code [96], short for **t**ime-dependent **Rec**ursive inde**X**ing, is a general numerical PDE solver package that transforms PDE into ODEs by representing the solution with discretized basis functions, whose corresponding coefficients are stored in a recursive indexing data structure, as is demonstrated in Sec. 3.1.4. Numerically, the tRecX code implements FE-DVR for radial discretization and E-E interaction for computational efficiency. The main features of tRecX code are the tSurff method, irECS absorber, and mixed gauge, enabling the simulation of the ionization of few-electron molecules and double-emission problems by solving TDSE [54, 66, 109, 116, 117, 130, 139] and the simulation of surface plasmas by solving Maxwell equations [164, 165].

Apart from the representation of the wavefunction by the recursive indexing code design, efficient numerical packages are employed for computation. The code integrates EIGEN library [166] to do the matrix-vector multiplication, which is the best for small matrices (100×100). The general integrals of the code are calculated by ALGLIB [167]. The ARPACK package [168] is applied for the eigenvalue problem by Arnoldi iteration [169] method. The openMPI [170] interfaces are utilized for parallelization.

3.6.1 Recursive structure implementation

In the code, a core template named "Tree" is designed to represent the recursive data structure, and its implementation includes a tree-structured "Index" class and "Coefficients" class. The Index class represents the hierarchy of coordinates, wherein each node of the tree points to the corresponding basis function. The Coefficients class represents the coefficients vector $c(\vec{t})$ at a given time step t as is presented in Fig. 3.2.

3.6.2 Parallelization

The parallelization technique has been used for many years, especially in the field of supercomputing. Normally, the computer executes programs serially, and computational tasks

are executed sequentially. The parallelization is to make the code suitable for parallel computation where many calculations or executions are simultaneously carried out. The parallel computation splits the computational task into many similar sub-tasks, which can be simultaneously processed in different CPUs and their results combined afterwards. This method considerably reduces the computational time. For most of the computations, the CPU (also referred to as core) approaches its limit; thus parallelization is the predominant requirement for improving computational performance.

In practice, part of the data is passed through different sub-tasks among all the CPUs, a process called "communication." With a suitable parallelization strategy, computational consumption can be scaled by increasing the number of sub-tasks. In the following contents, a *process* refers to a sub-task or the thread unless specified differently. The total scaling performance of the tRecX code is influenced by two of the following factors

- Maximum single running time of all the sub-tasks. This factor can be optimized by load balancing or appropriately allocating the total computational task across all the CPUs to avoid any waiting time at the nodes; this requires considering the working condition of each CPU, i.e, the slower the CPU with less computational task, and vice versa. Usually, the working conditions of all cores are similar, and the computational task is equally distributed over all cores.

- Communication between each sub-task. The frequency and size of transferred data during a communication should be reduced, as communication of data through the network is much slower than its computation in a CPU.

We perform simulations using tRecX code on the servers of Leibniz Supercomputing Center (LRZ), where each computational node contains 16 or 24 cores (or CPUs).

This section focuses on the parallelization strategy and performance of the three computational steps in the 6D double ionization calculation: (1) time propagation in the B region, (2) time propagation in the S and $\bar{S}$ regions, and (3) spectrum integration (D region) and plot.

3.6.3 Time propagation in B region

Time propagation with the formula $\mathrm{i}\partial_t\psi = H\psi$ refers to advancing the full-dimensional wavefunction in the external field without any sources, and its Hamiltonian H corresponds to Eq. (2.2) for single-ionization and Eq. (6.1) (B region time propagation) for double-ionization problems; the main time-consuming calculations are wavefunction operations, as stated in Sec. 3.5, which, by numerical approximations in tRecX, are matrix-vector multiplications.

Parallelization of matrix-vector multiplications

The parallelization strategy involves distributing the data of the coefficients vector and operator matrix over different *processes* to scale the number of float operations in the matrix-vector multiplications.

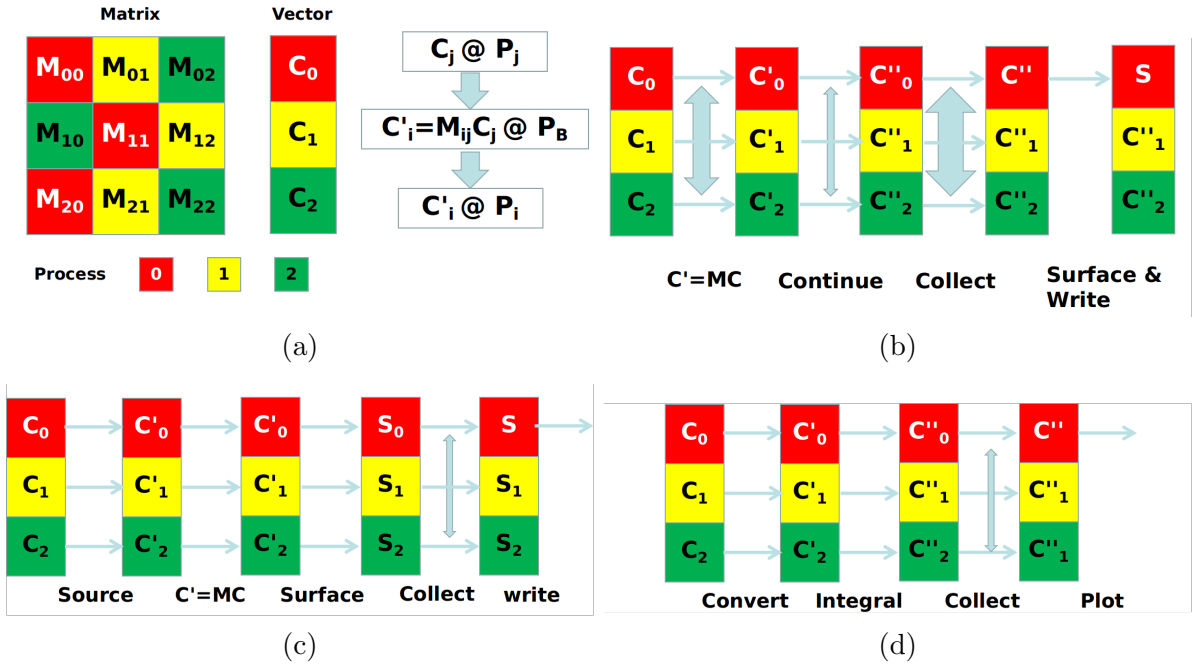

Figure 3.3: Computational details in tRecX code including (a) a general illustration of the allocations of sub matrices over *processes* for parallelizing matrix-vector multiplications, the illustrations of time propagation in (b) B regions, (c) S and $\bar{S}$ regions, as well as (d) time integration and creation of photoelectron spectra.

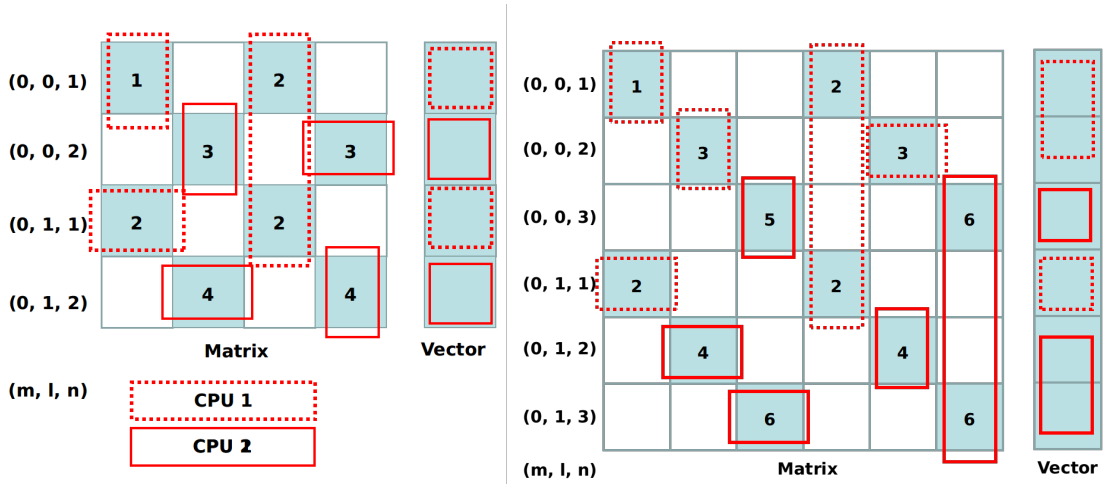

(a) (b)

Figure 3.4: The illustration of "ParallelCross" for evolution of a single-particle wavefunction with discretized parameters $M_{\max} = 0$, $L_{\max} = 1$ (a) $N = 1$ (unscaled radial intervals) or (b) $N = 2$. The definitions of the parameters can be found in Sec. 3.1. Vectors with $(M_{\max}+1)(L_{\max}+1)(N+1)$ (4 for (a) and 6 for (b)) sub-vectors on the right of each figure represent the "Coefficients". Matrices with 4×4 (a) and (b) 6×6 blocks on the left of each figure for matrices represent the time propagators, where each row or column is labeled by a m, l, n with $0 \le m \le M_{\max}$, $|m| \le l \le L_{\max}$ and $1 \le n \le N+1$. The unpainted blocks are zero matrices and will not be used. The painted blocks with the same number are put in the same "ParallelCross" object and the same CPU. Each "ParallelCross" contains a column and a row if it has more than one block. The red rectangle groups the blocks in a row or a column. Only two CPUs are applied for the illustration. The blocks or sub-vectors that are grouped by dashed red squares are in CPU 1 and the others are in CPU 2.

We illustrate such a standard strategy with computations running on three *processes*, as shown in Fig. 3.3a. The coefficients vector C is split into three sub-vectors named local coefficients $C_i, i = 0, 1, 2$ as well as coefficients after operation $C'_i, i = 0, 1, 2$. The matrix M is split into nine blocks named local operators as $M_{ij}, i, j \in \{0, 1, 2\}$ and distributed over three *processes*. We define the *process* rank for a specified local coefficient C_i, C'_i as $P_{C,i}, P_{C',i}$ and local operator M_{ij} as $P_{M,i,j}$. For simplicity, let i here be the *process* rank: $P_{C,i} = i = P_{C',i}$, which is marked in red (0), yellow (1), and green (2), respectively. A sub-vector on rank i of the coefficients after operation labeled by C'_i ($P_{C',i} = i$) is calculated by summing the local matrix-vector multiplications as $C'_i = \sum_{j=0}^{2} M_{ij} C_j$. Apart from the main computational cost $M_{ij} C_j$, there exists two possible communication events, depending on the location of M_{ij} and C_j compared to the *process* rank:

- A - Block M_{ij} is not in the same *process* as C_j ($P_{C,j} = j \neq P_{M,i,j}$), C_j is sent to the *process* $P_{M,i,j}$ that holds M_{ij}.

- B - After the multiplication, $M_{ij} C_j$ will be added to C'_i. M_{ij} is not in the same *process* as C'_i ($P_{C',i} = i \neq P_{M,i,j}$), we send $M_{ij} C_j$ to i.

In Fig. 3.3a, the blocks of the matrix are assigned different colors depending on their *process* rank and coefficients vector. From the sub-index of the blocks, neither A nor B exists in $M_{00}C_0, M_{22}C_2$, being the fastest computations (case 1). Only B exists in $M_{01}C_1, M_{02}C_2, M_{21}C_1, M_{20}C_0$, and only A exists in $M_{12}C_2$, introducing slower computations (case 2). A and B co-exist in $M_{10}C_0, M_{11}C_1$, indicating that these two operations are slowest (case 3).

The tRecX code generates the operator based on the discretized parameters with the recursive indexing structure, and only the non-zero sub-blocks are generated and used (see the painted blocks of Fig. 3.4a and 3.4b). Thus, the complete structure of the matrix is not needed, which saves time for construction, reduces memory consumption, and increases numerical efficiency of matrix-vector multiplications for sparse matrices.

In tRecX code, these blocks are distributed using a heuristic algorithm to minimize communication and balance the load on the CPUs. The strategy is illustrated by the example in Fig. 3.4. Each block is created from two "Index"es (see Sec. 3.6.1) with discretized parameters m, l, n that also define its positions. A set of blocks with the same row or column are saved in a "ParallelCross" object; each "ParallelCross" has a column and a row of blocks (if it has more than one block, see the blocks labeled "2" in Fig. 3.4a and blocks labeled "2" and "6" in Fig. 3.4b). The blocks of a "ParallelCross" are in the same CPU, and are as equally distributed as possible in the row and column to balance the "send" (for the columns, labeled "B" above) and "receive" (for the rows, labeled "A" above) communications. The identity of a "ParallelCross" is defined by the column "Index" of the block where the row and column crosses (see diagonal block "2" of Fig. 3.4a and diagonal blocks "2" and "6" of Fig. 3.4b). The CPU that holds this block also holds the local fragments of a vector, see the areas on the right of each sub-figure labeled by solid and dashed red rectangles in Fig. 3.4. Thus, case 3 (shown above in the standard

case) is avoided as much as possible to reduce the communications here. There is no communication for computations described in Fig. 3.4a and the communication only exists in two non-diagonal blocks labeled "3" and "4" for computations described in Fig. 3.4b. Before assigning a "ParallelCross" to a CPU, a "load" value is introduced by the sum of computational consumptions of its blocks. The load of a CPU is calculated by the sum of "load"s of its "ParallelCross"es. These loads of each CPU are balanced to optimize the computational performance.

Operations in time propagation

The main operations in time propagation, as illustrated in Fig. 3.3b, are repeatedly carried out over each time step. The computer performs matrix-vector multiplication, as is shown in the right side of Eq. (3.3) (step 1, $C' = MC$), after which boundary coefficients elements of each neighboring radial interval are averaged to ensure the continuity of the wavefunction (see Eq. (3.36) of Sec. 3.1.2) (Step 2, Continue). Then, all the coefficients are sent to the primary *process* (Step 3, Collect), and, finally, the surface values of the wavefunction are converted and written to disk (Step 4, Surface & Write) required by computation of S,$\bar{S}$ regions (see Sec. 2.4.1), or for photoelectron spectrum (see Sec. 2.2). Of the four steps, only Step 4 does not require communication between the *processes*. Moderate communication is needed for the matrix-vector multiplications in Step 1 as well as Step 2, wherein two neighboring intervals are in different *processes*. Apparently, collecting all the vector data of other *processes* requires the communication of relatively large data, which is unfavorable for scaling computational time.

Scaling performance

As can be seen in Fig. 3.5a, the computational time is scaled to $1/5 - 1/6$ of the single runs at maximum by parallelization. The primary computational consumption is in the time propagation. The communication is positively related to the number of *processes*, which, however, is tiny compared to the total computational time. A calculation with over 16 CPUs indicates a computation with multi-nodes which is unfavorable for the total scaling performance, see Fig. 3.5.

3.6.4 Time propagation in S and $\bar{S}$ regions

Strategy

The time evolution in S and $\bar{S}$ is a single-particle time propagation with sources subtracted to the time derivative of the wavefunction (formula shown in Eq. (2.86) and Eq. (2.87)), which are computed from surface values produced in calculations for B region. By recursive indexing representation of tRecX code, ansatz $\varphi_{\vec{k}_1}(\vec{r}_2, t), \forall \vec{k}_1$ is presented by a tree-structured class "Coefficients" with a level named "kRn1" containing all the information of $\vec{k}_1$ grids. Normally, advancing $\varphi_{\vec{k}_1}(\vec{r}_2, t)$ is performed in one *process* for all $\vec{k}_1$s sequentially.

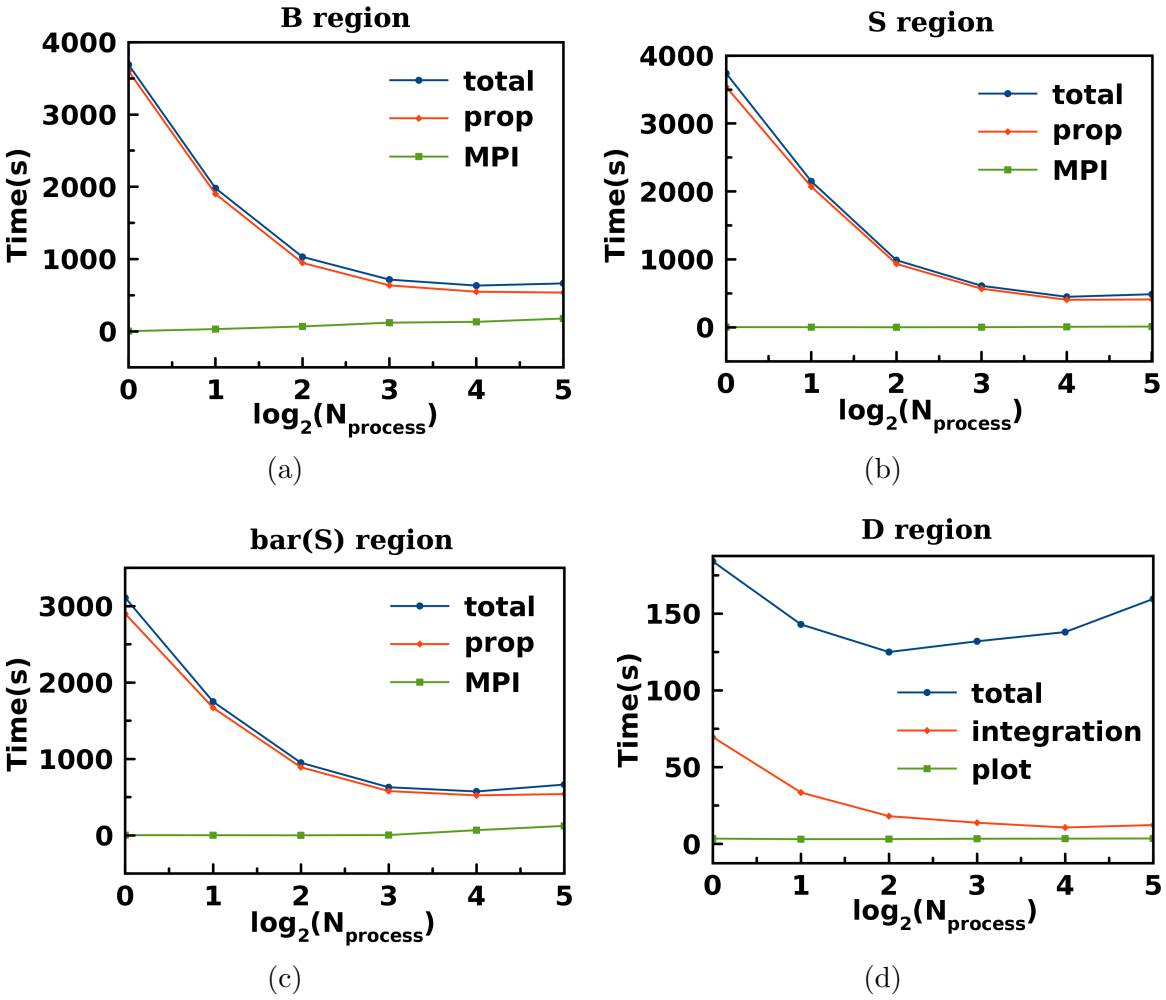

Figure 3.5: The parallelization performance of time propagation in (a) region B , (b) subregion S, (c) subregion $\bar{S}$ and (d) photoelectron spectrum creation in D region. The label "total" means total running time, "prop" indicates the propagation time and "MPI" indicates the time for communication between *processes*. A 20-nm, $3 \times 10^{15}\,\mathrm{W/cm^2}$, FWHM=5 opt.cyc. pulse is applied. The unscaled radial axis is split into four intervals with polynomials order 15, and $M_{\max} = 0$ and $L_{\max} = 3$. $\log_2(N_{process}) = 5$ indicates 2 nodes. We use $N_k = 128$ energy grid points for the computation that satisfies $k^2_{1/2,i} - k^2_{1/2,i-1} = k^2_{1/2,i+1} - k^2_{1/2,i}$, $1 \le i \le N_k - 2$ and $\frac{k^2_{1/2,N_k-1}}{2} = E_{\max} = 11.4\,\mathrm{a.u.}$.

As is mentioned previously in Sec. 2.4.4, the advancement of the single-particle wavefunction $\varphi_{\vec{k}_1}(\vec{r}_2,t)$ in subregion S, which is dependent on $\vec{k}_1$ of the other particle could be perfectly parallelized with respect to $\vec{k}_1$. For parallelization, the total wavefunction is distributed over several *processes*, with each local coefficient representing a subgroup of k_1 grids. A similar procedure is applied for the propagation of $\varphi_{\vec{k}_2}(\vec{r}_1,t)$.

For an ansatz with N_k momentum grid points $k_{1/2,0} < k_{1/2,1} < \cdots < k_{1/2,N_k-1}$ to be calculated on N_p *processes*, we split the global wavefunction into N_p local wavefunctions, with ith CPU evaluating momenta $k_{1/2,j}, j \in [\frac{N_k(i-1)}{N_p}, \frac{N_k i}{N_p})$ ($N_k \bmod N_p \quad = 0$ is required). There are two types of $k_{1/2}$ grids in tRecX, namely: the momentum grid with $k_{1/2,i} - k_{1/2,i-1} = k_{1/2,i+1} - k_{1/2,i}$, $1 \le i \le N_k - 2$ and the energy grid $k^2_{1/2,i} - k^2_{1/2,i-1} = k^2_{1/2,i+1} - k^2_{1/2,i}$, $1 \le i \le N_k - 2$. Here the $k_{1/2}$ means "k_1" or "k_2". For preserving the recursive structure of the wavefunction by only keeping one tree-structured coefficients, a new level called "subRn1(2)" is added to the top of the tree structure (see Sec. 3.1.4), with its ith child coefficients carrying grids $k_{1/2,j}, j \in [\frac{N_k(i-1)}{N_p}, \frac{N_k i}{N_p})$. This strategy perfectly scales the computation on momenta grids but does not reduce the recursion depth or scale the matrix-vector multiplications. Thus, the scaling performance is positively related to the relative cost of computations on the momenta grid level, such as generating sources for k-grids using surface information and multiplications of the Volkov phase.

Operations in time propagation

Fig. 3.3c shows the numerical procedure for time propagation in tRecX. The surface values and derivatives are converted to sources that will be subtracted from the time derivative of the wavefunction ($C_{\vec{k}_1}(\vec{r}_2,t)$ for Eq. (2.86) or $C_{\vec{k}_2}(\vec{r}_1,t)$ for Eq. (2.87)) (step 1, Source), and then the code performs separate matrix-vector multiplications for each *process* (step 2, $C' = MC$). The surface values and derivatives of each local coefficient (sub-vector) are separately calculated for each *process* in Step 3 (Surface), which are then collected and sent to the main *process* (Step 4, Collect) and written to the disk (step 5, write). Data communication only occurs in Step 4 and does not slow down the scaling much, as the surface data size is tiny compared to the wavefunction.

Scaling performance

A few time-propagations in S and $\bar{S}$ are computed with the surface values produced in B region time propagation in Sec. 3.6.3, shown in Fig. 3.5b and 3.5c. Scaling performance barely increases with over 8 CPUs because of the limited k-grids; computational consumption of k-grid generation does not dominate the total calculation.

3.6.5 Photoelectron spectrum creation

Photoelectron spectrum creation is a set of post-processing operations that includes the following:

1. Computing scattering amplitudes from time integrating the flux, which for single ionization is only contributed by one channel shown in Eq. (2.31) and for double ionizion is contributed by two channels $F(\vec{k_1}, \vec{k_2}, t)$ and $\bar{F}(\vec{k_1}, \vec{k_2}, t)$ (Eq. (2.84) and Eq. (2.85)) from computations in S and $\bar{S}$. The formulas for integration are given in Eq. (2.27) and Eq. (2.78) in chapter 2.

2. Creation of plots for a spectrum such as the energy spectrum or the joint angular spectrum from scattering amplitudes.

The integration of scattering amplitudes is the most time-consuming step in photoelectron spectrum creation, especially for long pulses. The flux for each k-grid is independently integrated, similar to the time propagation of $\varphi_{\vec{k_1}}(\vec{r_2})$, indicating that the parallelization strategy for time propagation in S and $\bar{S}$ regions also applies. For the double ionization in Eq. (2.78), the integration of fluxes $F(\vec{k}_1, \vec{k}_2, t)$ and $\bar{F}(\vec{k}_1, \vec{k}_2, t)$ is split into different *processes* by the k-grid sub-index, where the conversion from surface values to fluxes (Step 1, Convert) and integration (Step 2, Integral) are carried out independently. Then, all the scattering amplitudes are sent to the main *process* (Step 3, Collect). Finally, the plot from the scattering amplitudes is generated (Step 4, Plot). Communication only occurs in Step 3, and the time is negligible for our specific test here in Fig. 3.5d and Fig. 3.6, where N_k = 128 energy grid points with $k^2_{1/2,N_k-1}/2$ = 11.4 a.u. are used in Fig. 3.5d and N_k = 128 momentum grid points with $k^2_{1/2,N_k-1}/2$ = 2 a.u. are used in Fig. 3.6, but the communicational times are all below 5 s. The four steps are illustrated in Fig. 3.3d.

Scaling performance

Two individual computations with different inputs are tested for the scaling performance. The first starts from the surface values from the computations in Sec. 3.6.4 with relevant computational times plotted in Fig. 3.5d, which shows the integration time decreases with the increasing *process* number but the total time increases. The reason is that the set-up times for the Index and Coefficients objects are comparable to the integration time. A larger *process* number requires generating more local coefficients and a longer set-up time. The other is performed with a more substantial basis with longer pulses in Fig. 3.6. The central computational time is in the integration step, which becomes 6 times faster with 16 CPUs and scales the entire computation similarly.

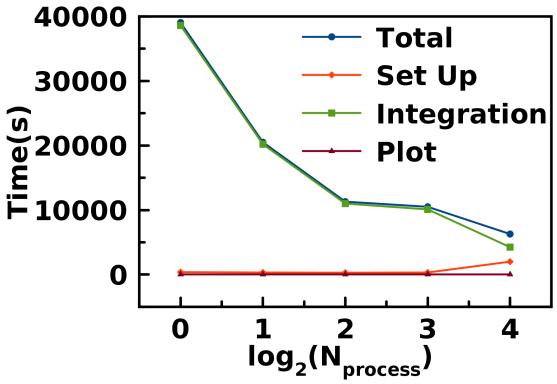

Figure 3.6: The parallelization of photoelectron spectrum creation in double ionization of Helium with parameters $L_{\max} = 20, L_{\mathrm{a}} = 3, L_{\mathrm{d}} = 21$, $M_{\max} = 1$ with constraint $m_1 + m_2 = 0$, $R_0 = 37.5$ a.u. and $N_k = 80$. The external field is a 6 fs, $\cos^8$ shape, 400-nm linearly polarized pulse along z direction. We use $N_k = 128$ momentum grids.

Chapter 4

Convergence study

As is stated in previous chapters, tRecX code implements the tSurff method and irECS as well as efficient numerical discretization techniques for solving the TDSE. The Coulomb attraction from the nucleus, the electron electron interaction and Hartree potential are truncated beyond the tSurff radius. In this chapter, we present the photoelectron spectra produced by tRecX code and discuss how they are influenced by parameters for numerical discretization and computational methods. The performance of tRecX code which is dependent on the these parameters is illustrated by a convergence study of double ionization of Helium in a 400 nm pulse. The convergence study is important especially for the double emission photoelectron spectra, see Sec. 2.1.2, where the long range electron electron interaction is truncated by the arbitrary tSurff radius R_c. For a single ionization convergence study, refer to the convergence study of hydrogen atom in Dr. Zielinski's thesis [82].

4.1 Convergence test of DI

Our computation of double emission spectra was motivated by an interesting work as the following. Katsoulis et al. (2018) reported the slingshot mechanism of two electrons for the double ionization of helium with classical trajectory Monte Carlo (CTMC) simulation, which strongly favors "back-to-back" (B2B) emission [171], but relevant quantum investigations have not yet been reported. The tRecX code developed in our laboratory implements the tSurff and irECS methods that can solve the two-electron ionization problem for a large wavelength ≥ 400 nm by solving TDSE. Our previous paper reported the full quantum-mechanical calculation for the double emission problem at IR wavelength [54], but the convergence was difficult to obtain.

The convergence of double emission behavior strongly varies with the investigated observables, as pointed out in Sec. 2.4.4. To compare our results with the CTMC simulations, we consider the convergence study based on observables that include the photoelectron energy spectra, and correlation ratio by the "back-to-back" (B2B) emission with respect to "side-by-side" (SBS) emission properties of the two particles integrated over all the energy range. Our simulation was performed with a FWHM = 2 fs, $5 \times 10^{14}\,\mathrm{W/cm^2}$, 400-nm

and Gaussian-like $\cos^8$ envelope pulse that is used in Ref. [171], whose formula can be described by Eq. (A.24) with $n = 2$; the pulse shape can be found in Fig. A.1 in the appendix. For completeness, we also present the convergence behavior of joint angular distributions (JAD) of the selected energy points. Finally, we present the calculated correlated behavior of the two particles with typical pulses.

4.1.1 Definition of Formulas

The two-electron tSurff introduced in Sec. 2.4.1 can be applied for computing the double-emission spectra of He.

Photoelectron spectra

The photoelectron energy spectrum is given as

$$\begin{aligned}\sigma_E(E_1, E_2) = \int_0^{2\pi} d\phi_1 \int_0^{2\pi} d\phi_2 \int_0^{\pi} d\theta_1 \sin\theta_1 \int_0^{\pi} d\theta_2 \sin\theta_2 \\ |b(\sqrt{2E_1}, \sqrt{2E_2}, \theta_1, \theta_2, \phi_1, \phi_2, T)|^2 \sqrt{E_1}\sqrt{E_2},\end{aligned} \tag{4.1}$$

where $b(k_1, k_2, \theta_1, \theta_2, \phi_1, \phi_2, T)$ is the scattering amplitude from Eq. (2.73). We also define two types of spectrum for describing the correlated behavior of the two particles:

$$\sigma_\eta(\theta_1, \theta_2) = \int_0^{\infty} \int_0^{\infty} k_1^2 k_2^2 dk_1 dk_2 \int_0^{2\pi} d\phi_1 \int_0^{2\pi} d\phi_2 |b(k_1, k_2, \theta_1, \theta_2, \phi_1, \phi_2, T)|^2, \quad \theta_{1,2} \in [0, \pi) \tag{4.2}$$

represented by the angle $\theta_{1/2}$ for the two particles and evaluated along the z coordinates

$$\sigma_z(k_{z,1}, k_{z,2}) = \int_{|k_{z,1}|}^{+\infty} \int_{|k_{z,2}|}^{+\infty} k_1 k_2 dk_1 dk_2 \int_0^{2\pi} d\phi_1 \int_0^{2\pi} d\phi_2 |b(k_1, k_2, \arccos\frac{k_{z,1}}{k_1}, \arccos\frac{k_{z,2}}{k_2}, \phi_1, \phi_2, T)|^2, \tag{4.3}$$

whose derivation can be found in Sec. A.6. The total yield of emission integration is calculated by

$$Y_E = \int_0^{\infty} \int_0^{\infty} \sigma_E(E_1, E_2) dE_1 dE_2, \tag{4.4}$$

for energy spectra and

$$Y_\eta = \int_0^{\pi} \int_0^{\pi} \sigma_\eta(\theta_1, \theta_2) \sin\theta_1 \sin\theta_2 d\theta_1 d\theta_2 \tag{4.5}$$

for spectra with $\theta_{1/2}$ coordinates, and

$$Y_z = \int_{-\infty}^{\infty} \int_{-\infty}^{\infty} \sigma_{k_z}(k_{z,1}, k_{z,2}) dk_{z,1} dk_{z,2} \tag{4.6}$$

for spectra with $z_{1/2}$ coordinates. Theoretically $Y_E = Y_\eta = Y_z$. Convergence behavior is obtained by measuring the error of spectra at two independent calculations

$$\epsilon_E = \max_{E_1, E_2} \left(2 \frac{|\sigma_E(E_1, E_2) - \sigma'_E(E_1, E_2))|}{|\sigma_E(E_1, E_2) + \sigma'_E(E_1, E_2))|} \right) \tag{4.7}$$

for subsequent calculations σ_E and σ'_E as we increase the parameters, as well as

$$\epsilon_\eta = \max_{\theta_1,\theta_2}\left(2\frac{|\sigma_\eta(\theta_1,\theta_2) - \sigma'_\eta(\theta_1,\theta_2))|}{|\sigma_\eta(\theta_1,\theta_2) + \sigma'_\eta(\theta_1,\theta_2))|}\right) \tag{4.8}$$

for subsequent calculations σ_η and σ'_η as we increase the parameters. A disadvantage of this measurement is that the error can be very small if the two subsequent parameters are very close, even if it is not converged. To avoid these arbitrary small errors in the convergence tests of this section, intervals between all subsequent parameters are similar and small intervals are avoided.

Correlation ratio

The correlation ratio is introduced to describe how "back-to-back" (B2B) emission compares with "side-by-side" (SBS) emission, defined by the ratio of B2B to SBS yield. From the above two representations of the photoelectron spectra in Eq. (4.2) and (4.3), one may obtain the correlation ratio by using the formula

$$\Gamma_\eta = \frac{\int_0^{\pi/2}\sin\theta_1 d\theta_1 \int_{\pi/2}^{\pi}\sin\theta_2 d\theta_2 \sigma_\eta(\theta_1,\theta_2) + \int_{\pi/2}^{\pi}\sin\theta_1 d\theta_1 \int_0^{\pi/2}\sin\theta_2 d\theta_2 \sigma_\eta(\theta_1,\theta_2)}{\int_0^{\pi/2}\sin\theta_1 d\theta_1 \int_0^{\pi/2}\sin\theta_2 d\theta_2 \sigma_\eta(\theta_1,\theta_2) + \int_{\pi/2}^{\pi}\sin\theta_1 d\theta_1 \int_{\pi/2}^{\pi}\sin\theta_2 d\theta_2 \sigma_\eta(\theta_1,\theta_2)} \tag{4.9}$$

for representation in $\theta_{1/2}$ coordinates or

$$\Gamma_z = \frac{\int_0^{+\infty}\int_{-\infty}^{0}\sigma(k_{z,1},k_{z,2})dk_{z,1}dk_{z,2} + \int_{-\infty}^{0}\int_0^{+\infty}\sigma(k_{z,1},k_{z,2})dk_{z,1}dk_{z,2}}{\int_0^{+\infty}\int_0^{+\infty}\sigma(k_{z,1},k_{z,2})dk_{z,1}dk_{z,2} + \int_{-\infty}^{0}\int_{-\infty}^{0}\sigma(k_{z,1},k_{z,2})dk_{z,1}dk_{z,2}}. \tag{4.10}$$

for representation in $k_{z,1/2}$ coordinates, where $\theta_{1,2} \in ([0,\pi/2]\otimes[0,\pi/2])\cup([\pi/2,\pi]\otimes[\pi/2,\pi])$, $z_{1,2} \in ([0,+\infty)\otimes[0,+\infty))\cup((-\infty,0]\otimes(-\infty,0])$ are called the SBS regime and $\theta_{1,2} \in ([0,\pi/2]\otimes[\pi/2,\pi]) \cup ([\pi/2,\pi]\otimes[0,\pi/2])$, $z_{1,2} \in ([0,+\infty)\otimes(-\infty,0]) \cup ((-\infty,0]\otimes[0,+\infty))$ are called the B2B regime. $\theta_{1,2}, z_{1,2}$ means particle "1" and "2" while $\theta_{1/2}, z_{1/2}$ means particle "1" or "2". Theoretically, the two ratios have an identical physical property, i.e., $\Gamma_\eta > 1$ (or $\Gamma_z > 1$) is B2B dominated and $\Gamma_\eta < 1$ (or $\Gamma_z < 1$) is SBS dominated. In practice, the numerical calculation approximates the phase space with finite grid points, leading to different quantities with the two representations, as presented in the next section.

4.1.2 Overview of the convergence study

The quiver radius of the 400-nm, $5\times10^{14}\,\mathrm{W/cm^2}$ pulse is 9.2 a.u., unlike the single emission wherein the convergent box size can be approximated with the huge quiver radius from the previous section, R_0 for a convergent double emission simulation not only depends on electrodynamics in the pulse but also the truncation of the Coulombic attraction from the nucleus and electron-electron interactions, which are non-negligible near the small quiver radius of 9.2 a.u. Further, approximating the asymptotic solution with the product of two

single-scattering solutions is only available beyond a larger simulation range where the wave packets disentangle, making the regulation of the box size a complex task. To reduce the error introduced by the Coulomb truncation, we set $\beta = R_c = R_0$ as default. In the following convergence study, we use R_c to represent the simulation box size.

The default parameters for the calculations are the polynomial order (18), cutoff energy E_{cut} (100 a.u., see high energy projection in Sec. 3.5.4) and number of k grids N_k (80). The numerical discretization parameters that are considered for convergence studies mainly focus on simulation box size and angular momenta, whose definitions can be found in Sec. 3.1.3.

η and z representation

Fig. 4.1 shows how the yields (Y_E, Y_η, Y_z) and the correlation ratio vary with the number of k grids (N_k). The yields integrated from photoelectron spectra by the three representations are theoretically equivalent. However, the values are distinctive due to numerical errors of different representations. Y_E and Y_η are identical with an error of approximately 10% and both alter below 10% with k grid number increasing from 80 to 120, while Y_z decreases to 26% with an error reaching 82%, compared to Y_E. The correlation ratios (Γ_η and Γ_z) are computed by divisions of the yields integrated from different quadrants, and their accuracies are expected to be similar to the total yield integrated from all quadrants. We found Γ_η is invariant of N_k, but Γ_z decreases from 1.14 to 1.08. As σ_E are computed directly from the scattering amplitude by Eq. 2.12 with the least approximations and numerical errors, Y_E serves as the most precise value. The similarity of Y_η with Y_E indicates σ_η is numerically more reliable than σ_z. The near-invariant ratio Γ_η and Y_η with N_k implies $N_k = 80$ is sufficient for our simulation.

The numerical error may arise from the plotting function in the code, which represents the scattering amplitudes by discrete variables on a finite number, equidistant k_z or η grids with identical weights. The error becomes non-negligible with small discretized grids and aggravates with operations on the plotted data sets. In this section, Γ refers to Γ_η if not specified.

As the yields from Y_E (integrated from $\sigma_E(E_1, E_2)$) and Y_η (integrated from $\sigma_\eta(\theta_1, \theta_2)$) calculations are close in our numerical calculations, and the overall B2B to SBS behavior that can be obtained by integrating $\sigma_\eta(\theta_1, \theta_2)$ over relevant quadrants is our main concern, we chose the ratio Γ (Γ_η) and ϵ_η as the criteria for the convergence study on angular and radial discretization parameters.

Angular discretization convergence

As mentioned in Sec. 3.1.3, the angular part of the 6D wavefunction is represented by spherical harmonics $Y_{l_1}^{m_1}(\theta_1, \phi_1), Y_{l_2}^{m_2}(\theta_2, \phi_2)$ with quantum numbers $l_1, l_2 \in [0, L_{\max}], m_1, m_2 \in [-M_{\max}, M_{\max}]$. For a linear polarization pulse in our calculation, $m_1 + m_2 = 0$ is satisfied for symmetric property, and the values of l_1, l_2 can be constrained into an "armchair" shape that is determined by the "arm-width" L_a and "diagonal" L_d parameters as shown

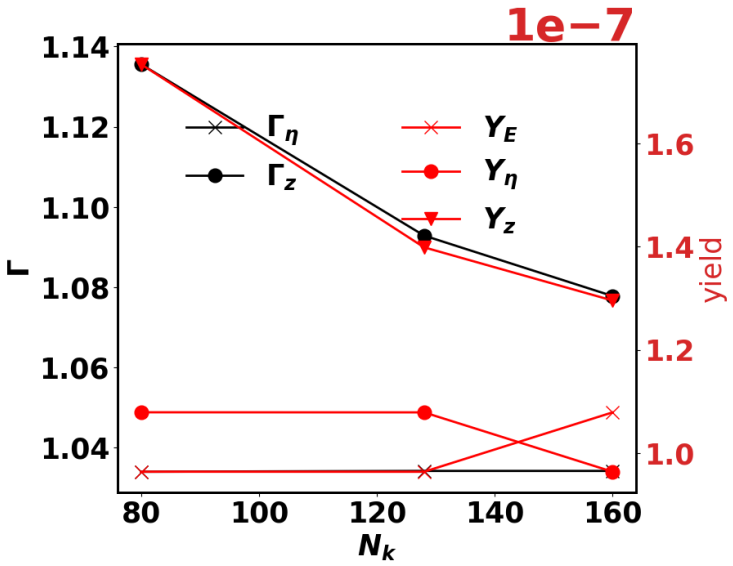

Figure 4.1: Convergence of total double-ionization yield and ratios with N_k k grid points. Yields and ratios are computed through different methods. The yield of Y_η is very close to Y_E and its ratio Γ_η does not change. But ratio Γ_{k_z} is modified substantially and Y_{k_z} approaching Y_E with the increased N_k. The ratio Γ_{k_z} is also approaching Γ_η. The $L_d = 9$, $L_a = 3$, $M_{\max} = 0$ and $R_c = 21$ a.u.

in Fig. 3.1. We mainly examine $L_{\max}, M_{\max}, L_a, L_d$ parameters for convergence of angular discretization. The constraints on angular momentum are correlated with radial discretization, theoretically illustrated in Sec. 2.1.1 and the corresponding numerical evidence will be given later.

We ensure that $M_{\max} = 1$ produces convergent results with equivalent Γ and $\epsilon_\eta < 9\%$ as compared to $M_{\max} = 2$. Further, $L_{\max} = 19$ calculation produces data with the same Γ and $\epsilon_\eta < 2\%$ as $L_{\max} = 29$. Fig. 4.2 shows $L_a = 3$ already produces the convergent $\sigma_\eta(\theta_1, \theta_2)$ and Γ ratios when $L_d \leq 18$, where σ_η shifts below 3% and Γ shifts below 1%. Fig. 4.3 shows $M_{\max}$=1, $L_d = 21$ and $L_a = 3$ gives convergent results for $R_c = 37.5$ a.u., where $\epsilon_\eta < 10\%$ and Γ shifts from 1.41 to 1.43 when L_d alters from 18 to 21.

Simulation box size

As radial extension and angular discretization are correlated, a systematic study is demonstrated in Fig. 4.4, which includes the analysis of L_d with $R_c = 37.5$ a.u. and of R_c with $L_d = 21$. In the figure for the R_c convergence test, although Γ stabilizes until $R_c = 45$ a.u., $R_c = 37.5$ a.u. already provides a correlation ratio with an error around 1%, which is negligible for the analysis of correlated behavior in this thesis. We also find that Y_E and Y_η are similar and yet different from Y_z and that Γ_η is more accurate and stable with the simulation box. Fig. 4.5 displays the convergence of σ_η with R_c where the angular discretization is converged; we find that σ_η also converges at $R_c = 37.5$ a.u., with an error of 10% for

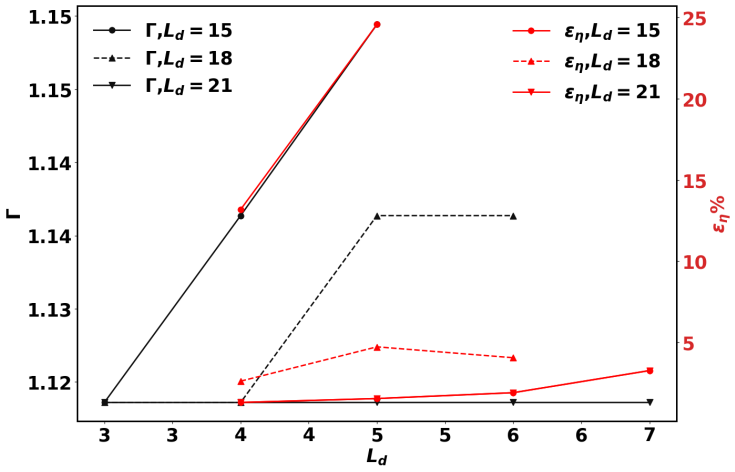

Figure 4.2: The convergence study of ϵ_η and Γ_η with L_a. In the figure, the black curve represents Γ_η and the red represents ϵ_η. The default parameters are $M_{\max}$=0, $L_{\max}$ = 19 and R_c = 21 a.u. The L_a = 3 gives convergent results with different L_d. One can neglect the increasing error of the latter two figures, as the values are very small.

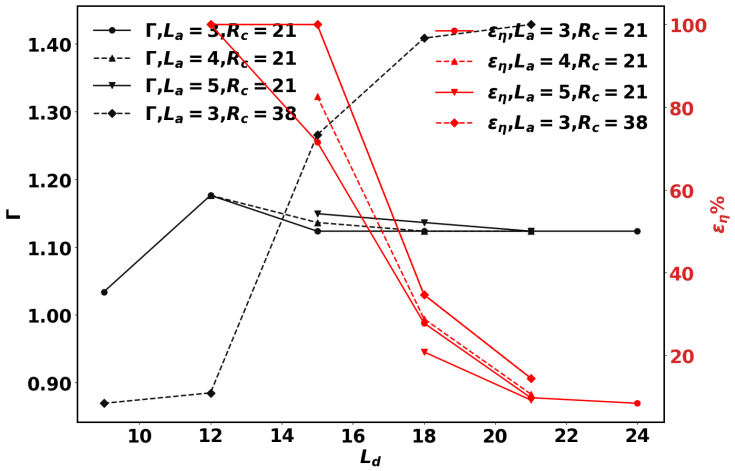

Figure 4.3: The convergence study ϵ_η and Γ_η with L_d. The L_d = 21 starts to give convergent results. The figure plots the variations in Γ_η (in black) and ϵ_η (in red) with diagonal constraints L_d when L_a = 3, R_c = 21 a.u., $L_{\max}$ = 19 (represented by solid line and circles), L_a = 4, R_c = 21 a.u., $L_{\max}$ = 19 (dashed line and up triangles) ,L_a = 5, R_c = 21 a.u., $L_{\max}$ = 19 (solid line and down triangles) and L_a = 3, R_c = 38 a.u., $L_{\max}$ = 29 (dashed line and diamonds). The default parameters are $M_{\max}$ = 0, and we omitted the difference of $L_{\max}$ in the labels because $L_{\max}$ = 19 is sufficient for the convergence.

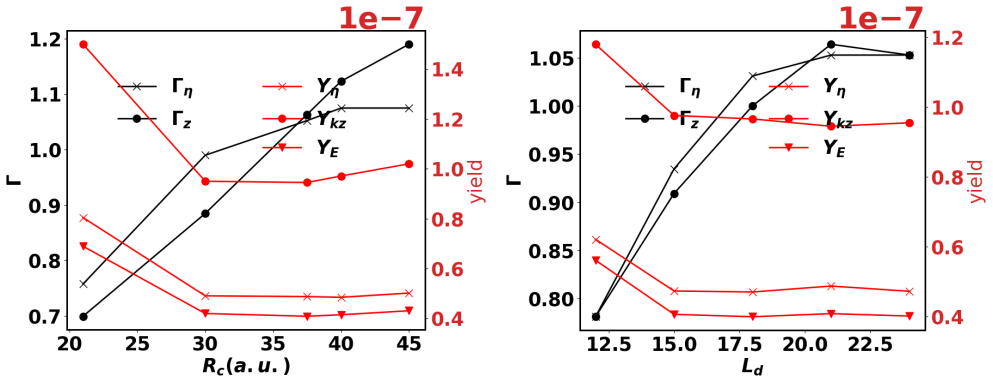

Figure 4.4: Convergence of total double-ionization yield and correlation ratios with box-size (left) and angular momentum expansion (right). At box size 45 the ratio stabilizes at 1.08. Yields and ratios are calculated through different methods. The discrepancy between Y_{k_z} and Y_η is due to the limited k grid number, so is the discrepancy in the ratios. The other parameters are $M_{\max} = 1$, $L_{\max} = 29$, $L_a = 3$. For the convergence test of R_c with $L_d = 21$. And for the convergence test of L_d with $R_c = 37.5$ a.u.

$R_c = 37.5$ a.u. and $R_c = 40$ a.u..

After the convergence test above, convergent parameters for calculation with $L_{\max} = 19, L_d = 21, M_{\max} = 1, R_c = R_0 = 37.5$ a.u. are obtained for correlated behavior calculations. We would like to point out that σ_E also converges with these parameters when we did not place the relevant data here.

Convergence study on JAD

Before the analysis of the convergence behavior of JAD, we would like to show a cheap calculation with a 20-nm, 4.5×10^{14} W/cm^2 pulse, as shown in Fig. 4.6, and select the spot around the peak in the energy spectrum. Emission of particle 2 is 0 around the

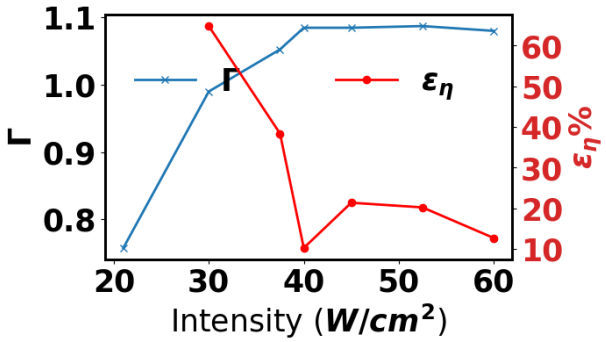

Figure 4.5: The convergence study of ϵ_η and Γ_η with R_c. Γ_η starts to converge at $R_c = 37.5$ a.u. and stabilizes at $R_c = 40$ a.u. In the figure, the black curve represents Γ_η and the red represents ϵ_{JAD}. The $M_{\max}$=1, $L_{\max} = 29$, $L_a = 3$ and $L_d = 21$.

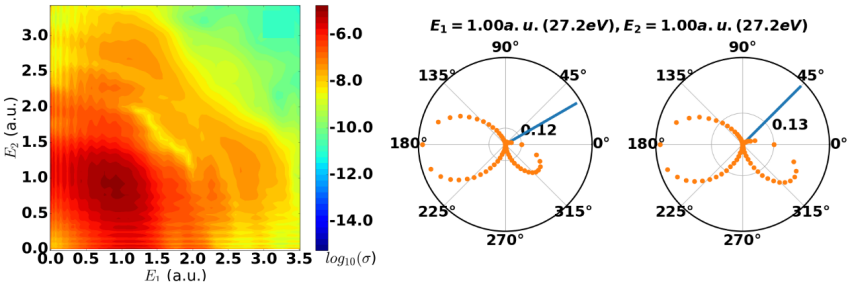

Figure 4.6: The (left) energy spectra $\sigma(E_1, E_2)$ and (right) JAD spectra $JAD(\theta_2) = \sigma(\sqrt{2E_1}, \theta_1, 0, \sqrt{2E_2}, \theta_2, \phi_2)$ with angles of $\theta_1 = \frac{1}{6}\pi, \frac{1}{4}\pi$ averaged in $E_1, E_2 \in [0.5, 1.5] \otimes [0.5, 1.5]$ a.u. to cover the peak in the energy spectra. $\phi_2 = 0$ for $\theta_2 \in [0, \pi]$ and $\phi_2 = \pi$ for $2\pi - \theta_2 \in [0, \pi]$. The blue line represents the emission angle θ_1 and orange dots represent the relative probability of particle 2 emitted at various θ_2s, whose ticks are labeled in the figure ("0.12" and "0.13"). The other parameters are $M = 1$. $L_{\max} = 2$. The laser field applied is 20-nm, 4.5×10^{14} W/cm^2, FWHM=4 and flat-top type pulse.

direction, particle 1 is ionized and reaches its maximum at $\theta_2 = \pi$ in the polarization direction, implying a clear signature of electron repulsion. Fig. 4.7 shows the importance of averaging over energies by plotting JADs selected at different energy points, and an active turbulence of the JAD plots with similar energy points is observed. To smoothen the turbulence, JAD points are averaged over a specific energy range of 0.03 a.u. around the points of interest in this thesis.

With the convergent parameters for the overall B2B and SBS scattering calculation, a convergence study on JAD behavior of two particles can be performed at selected energy points. As can be seen in Fig. 4.8, convergence of JAD plot is obtained with $M_{\max} = 1$ in both the shape and size at small box size, which is, however, not for the box size $R_c = 37.5$ a.u. from previous section. In Fig. 4.9, we find a relatively stable shape of JAD plots, but with an oscillating size. This means that the interaction between two particles at selected energy points is a long-range effect. A potential solution for this is to apply Eikonal-Volkov approximation [172], which includes the interaction beyond tSurff radius but is currently not available in tRecX code; therefore, we leave this up to future researchers. The computation with a larger box size also requires finer angular description, as angular and radial discretization are correlated, leading to enormous computational resources.

4.1.3 Results

After the systematic convergence study, the convergent parameters are applied for the computation of the correlation ratio:$L_{\max}$=19, $M_{\max}$=1, R_c=37.5 a.u., L_d=21, L_a=3 and the polynomial order is 18. As shown by the blue line-cross in Fig. 4.10, the overall correlation ratio shifts from 0.9 to 1.04, depending on the phase of the pulse ϕ_{CEP}, suggesting a near-equal contribution from B2B and SBS. The significant dependence on the phase,

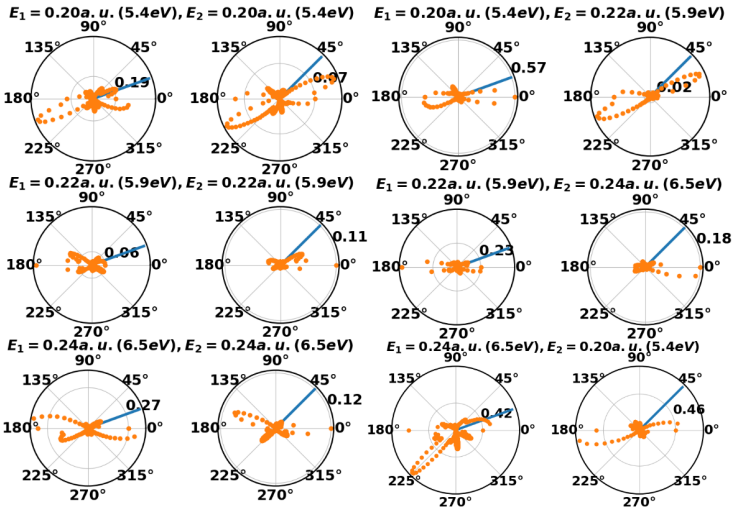

Figure 4.7: The JAD spectra $JAD(\theta_2) = \sigma(\sqrt{2E_1}, \theta_1, 0, \sqrt{2E_2}, \theta_2, \phi_2)$ with angles of $\theta_1 = \frac{1}{6}\pi, \frac{1}{4}\pi$ at $(E_1, E_2) = (0.22 \pm 0.02, 0.22 \pm 0.02)$ a.u.$\phi_2 = 0$ for $\theta_2 \in [0, \pi]$ and $\phi_2 = \pi$ for $2\pi - \theta_2 \in [0, \pi]$. The blue line represents the emission angle θ_1 and orange dots represent the relative probability of Particle 2 emitted at various θ_2s, whose ticks are labeled in the figure. The laser field applied is a 394.5-nm, $3.5 \times 10^{14}\,\mathrm{W/cm^2}$, FWHM = 5 and flat-top type pulse. $R_c = 37.5$ a.u., $L_{\max} = 20, L_{\mathrm{diag}} = 21, L_{\mathrm{armwidth}} = 3$.

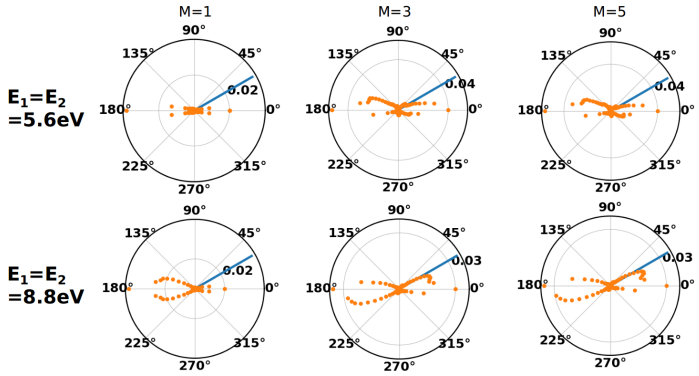

Figure 4.8: The convergence study of $JAD(\theta_2) = \sigma(\sqrt{2E_1}, \theta_1, 0, \sqrt{2E_2}, \theta_2, \phi_2)$ at $\theta_1 = \frac{1}{6}\pi$ with $M = 1, 3, 5$. $\phi_2 = 0$ for $\theta_2 \in [0, \pi]$ and $\phi_2 = \pi$ for $2\pi - \theta_2 \in [0, \pi]$. The blue line represents the emission angle θ_1 and orange dots represent the relative probability of particle 2 emitted at various θ_2s, whose ticks labeled in the figure. The default discretization parameters are $L_{\max} = 15, L_{\mathrm{diag}} = 15, L_{\mathrm{armwidth}} = 3$ and $R_c = 20$ a.u. The laser field applied is a 394.5-nm, $3.5 \times 10^{14}\,\mathrm{W/cm^2}$, FWHM=5 opt.cyc. and flat-top type pulse. The JAD is calculated at energy point $E_1 = E_2 = 5.6$ eV and $E_1 = E_2 = 8.8$ eV with a smooth range 0.8 eV.

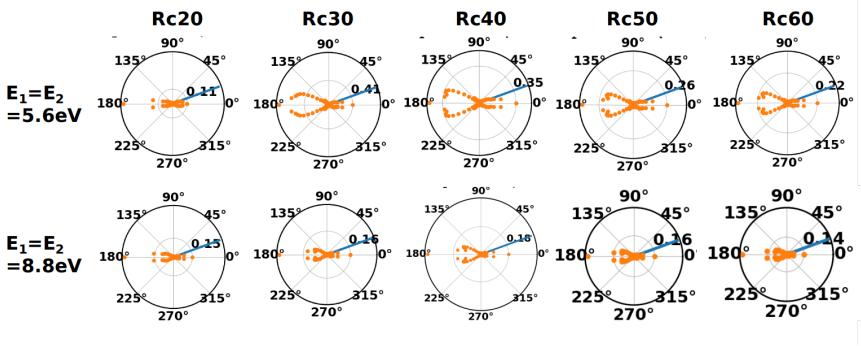

Figure 4.9: The convergence study of $JAD(\theta_2) = \sigma(\sqrt{2E_1}, \theta_1, 0, \sqrt{2E_2}, \theta_2, \phi_2)$ at $\theta_1 = \frac{1}{6}\pi$ with box size $R_c = 20, 30, 40, 50, 60$ a.u. $\phi_2 = 0$ for $\theta_2 \in [0, \pi]$ and $\phi_2 = \pi$ for $2\pi - \theta_2 \in [0, \pi]$. The blue line represents the emission angle θ_1 and orange dots represent the relative probability of particle 2 emitted at various θ_2s, whose ticks are labeled in the figure. The other parameters are $M = 1$, $L_{\max} = 15, L_{\text{diag}} = 15, L_{\text{armwidth}} = 3$. The laser field applied is a 394.5-nm, $3.5 \times 10^{14}\,\text{W/cm}^2$, FWHM=5 opt.cyc. and flat-top type pulse. The JAD is calculated at energy point $E_1 = E_2 = 5.6$ eV and $E_1 = E_2 = 8.8$ eV with a smooth range 0.8 eV.

however, disappears for a longer 6-fs pulse (see the green line-down triangles), which is also observed in a flat-top pulse with a constant intensity. The spectra obtained by the summation of those from calculations and a set of ϕ_{CEP}s with formula

$$\sigma(\theta_1, \theta_2)_{\text{total}} = \sum_{\phi_{CEP}} \sigma(\theta_1, \theta_2)_{\phi_{CEP}}, \tag{4.11}$$

where the corresponding correlation ratio is 0.96 for $I_1 = 5\times10^{14}\,\text{W/cm}^2$, indicates that B2B scattering is slightly overweight. Compared to $I_1 = 5 \times 10^{14}\,\text{W/cm}^2$, $I_2 = 3 \times 10^{14}\,\text{W/cm}^2$ in Fig. 4.10 produces more anti-correlation. For completeness, the $k_{z/2}$ spectra at $I_1 = 5\times10^{14}\,\text{W/cm}^2$ and $I_2 = 3\times10^{14}\,\text{W/cm}^2$ are also presented with FWHM=2 fs. We find that our calculation at $I_2 = 3\times10^{14}\,\text{W/cm}^2$ produces similar results to those in Ref. [171].

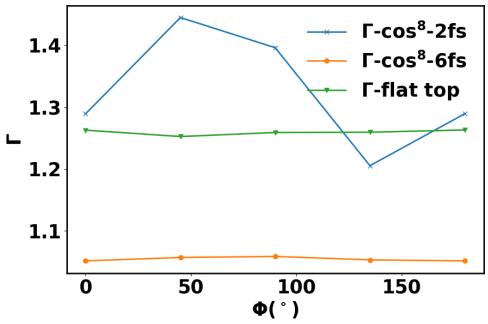

Figure 4.10: Γ calculations at $\phi_{CEP} = 0, 45, 90, 135, 180°$ with the following pulses: 400 nm, $\cos^8$ shape pulse (blue line-cross) FWHM=2 fs, $I_1 = 5 \times 10^{14}\,\mathrm{W/cm^2}$; (orange line-dot) FWHM=2 fs, $I_2 = 3 \times 10^{14}\,\mathrm{W/cm^2}$; (green line-down-triangle), FWHM=6 fs, $I_2 = 3 \times 10^{14}\,\mathrm{W/cm^2}$ (red line-diamond); as well as the 394.5-nm, FWHM=9 opt. cyc. flat-top pulse with intensity $I_1 = 5 \times 10^{14}\,\mathrm{W/cm^2}$.

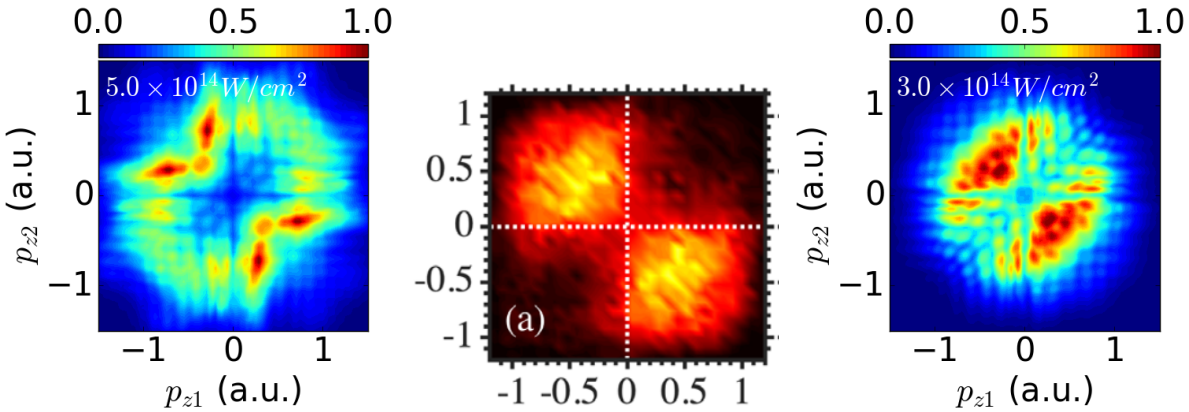

Figure 4.11: Joint momentum distributions at FWHM 2fs and intensity averaged over carrier-envelope phase. Center: classical trajectory calculation at $5 \times 10^{14}\,\mathrm{W/cm^2}$, reproduced from Ref. [171], Fig.1(a). Left: TDSE result for $5 \times 10^{14}\,\mathrm{W/cm^2}$, right: TDSE for $3 \times 10^{14}\,\mathrm{W/cm^2}$. Densities are normalized to to a maximal value of 1.

Chapter 5

Single Ionization

5.1 Static field ionization by haCC for frustrated double ionization of HeH^+

5.1.1 Background

Frustrated double ionization (FDI) takes place in a multi-electron system. It is a two-electron ionization process where one particle is liberated while the other is captured in a Rydberg state of the parent system at the end of the pulse, resulting in a single ionization spectrum [173]. FDI is a critical process for the non-linear response of a strong field of small molecules. It is reported to be a candidate for the inversion of N_2 in the free air lasing [174], where the population of excited ionic states grows increasingly. A number of experiments on FDI were performed on molecules such as H_2 [175], N_2 [176] and D_3^+ [177]. FDI accounts for a 10% share of all the ionization events [175, 177, 178].

Thus, FDI draws attention among the researchers in both experiments and theoretical calculations. A simple, few electron molecule acting as a candidate for theoretical calculations on the FDI process is required. An ideal candidate for simulating the FDI process has the fewest possible electrons to reduce the computational cost and is better to be an influential molecule in science. The helium hydride ion (HeH^+) is such a critical molecule as it is one of the first compounds in the early universe, along with He_2^+, and draws the interest of researchers [179, 180]. For theoretical calculations, it is the simplest heteronuclear molecule ion and isoelectronic with H_2. In this chapter, we present the calculations for the static field ionization rates of HeH^+ by haCC, which serves as a necessary input for the classical trajectory Monte Carlo calculations (see Sec. 2.3.6) for investigating the FDI process.

5.1.2 Methods

The hybrid anti-symmetrized coupled channels (haCC) method, introduced in Sec. 2.3, is applied to analyze the ionization process of HeH^+. The ground states of HeH^+ ($|\mathcal{N}\rangle$) and

HeH^{2+} ($|I\rangle$) are firstly computed by quantum chemistry packages and are then input into the haCC code. The details are listed below.

Within haCC, we calculate HeH^+ electronic ground state energy of -2.9756 a.u. at an internuclear distance of 1.46 (a.u.), which coincides with value given in the literature [180]. The results are presented in atomic units, whose relation to SI units can be found in Sec. A.1.

In haCC calculation, we split the total ansatz into coupled channels as

$$|\psi(t)\rangle \approx \sum_{I,i} \mathcal{A}|i\rangle|I\rangle C_{I,i}(t) + \sum_{\mathcal{N}} |\mathcal{N}\rangle C_{\mathcal{N}}(t) \tag{5.1}$$

where $\mathcal{A}$ is the anti-symmetrized operator and $|i\rangle$ is the single unrestricted basis from tRecX calculation. The ionic wavefunctions $|I\rangle$ and ground state wavefunction $|\mathcal{N}\rangle$ are in practice obtained from multireference configuration interaction singles doubles (MR-CISD) method [181] of quantum chemistry, computed by the COLUMBUS code [118]. Numerically dunning basis sets such as cc-pVDZ, cc-pVQZ, and cc-pVTZ are employed to approximate these two electronic wavefunctions.

The active electron basis $|i\rangle$ in the field written as

$$|i\rangle = \psi_i(r,\theta,\phi,t) = \sum_{m=-M_{\max}}^{M_{\max}} \sum_{l=|m|}^{L_{\max}} Y_l^m(\theta,\phi) R_{ml}(r) C_{ml}(t) \tag{5.2}$$

is simulated by the numerical discretization methods in the tRecX code (see Sec. 3.1.4). We use $M_{\max}$ and $L_{\max}$ to constrain the angular part, see Sec. 3.1.1. For the radial part ($R_{ml}(r)$), discretization parameters P_n and N are the order of polynomials and number of intervals in the inner region ($r \le R_0$), respectively, first introduced in Sec. 3.1.2. P_{N+1} and α are the order of polynomials and decay factor for the outer region ($r \ge R_0$), respectively, see Sec. 3.3.

The wavefunction of the fully effective electron $|i\rangle$ is then formulated into a coupled ansatz with the wavefunctions from COLUMBUS; a total of five orbitals are used, the ionic basis $|I\rangle$ of which creates a sophisticated time-dependent effective potential for the active electron. The resulting set of coupled ordinary differential equations can be solved with our tRecX code. For the details of the coupled ansatz from COLUMBUS calculation and the discretized single particle, refer to Sec. 2.3.

Static field ionization

The static field ionization rate Γ_f with various field strengths are calculated by haCC. A detailed description of the method can be found in Sec. 2.3.5 and Ref. [116]. Field-strength-($E(\phi_0)$) and angle-dependent Γ_f act as weights for the total probability of different trajectories from CTMC simulations, where $\phi_0 = t_0\omega$ and t_0 are the ionization times for e_1, see Sec. 2.3.6. Thus, the overall probability of a certain trajectory can be achieved by the ionization rate weighted average using Eq. (2.68).

Convergence study of haCC calculation

As stated above, the ionization rates obtained from the haCC calculation serve as the inputs for the CTMC calculations. Here, we only present the convergence study of haCC calculations for HeH^+, as the ionization rates for H_2^+ can be achieved by the classical method [55].

The internuclear distance of HeH^+ is fixed as 1.46 a.u. for all our calculations – a value taken from Ref. [179], which is reported to be the most reliable calculation [180] – by a variation calculation of the energy; in other words, a value that gives the lowest ground eigenenergy. The largest field strength 0.3 a.u. along z-axis (Angle = 0) is chosen for the convergence study to ensure convergence of all the other smaller values. We consider the calculations as converged when the ionization rate changes less than 0.1% under the increase of the specific test parameters.

The convergence study on angular quantum numbers is depicted in Fig. 5.1a and 5.1b, and one can see that the ionization rate changes by less than 0.1% with $L_{\max} \geq 8$ and $M_{\max} \geq 6$. The numerical behavior of the radial discretization parameters are illustrated in Fig. 5.1c and 5.1d. The convergence has been reached for the number of intervals $N \geq 4$. The ionization rate decreases when $12 \leq P_n \leq 16, 1 \leq n \leq N$ and slowly goes up after $P_n \geq 16$. Finally, the value shifts less than 0.1% after $P_n \geq 24$. A detailed description of the discretization parameters can be found in chapter 3. After the convergence study, we chose the parameters shown in Table 5.1 for haCC calculation.

P_n	P_{N+1}	$L_{\max}$	$M_{\max}$	N	α	basis set
24	24	8	6	4	1	Aug-cc-pvtz

Table 5.1: The convergent parameters achieved with field strength = 0.3 a.u. and angle = 0° except for $M_{\max}$ (tested at angle = 90°). The basis set "Aug-cc-pvtz" stands for augmented versions (Aug) of correlation-consistent (cc) polarized valence-only basis sets (pv) with triple zeta (tz). P_{N+1} is the polynomials order when $r \geq R_0$.

5.1.3 Results of static field ionization by haCC

The static field ionization rates calculated by haCC help produce the weighted performance of the various trajectories by CTMC simulations on the FDI processes of HeH^+. That is, CTMC calculation runs a large amount of simulations with the random distributions of the ionized particles and trajectories. The static field ionization rate provides the percentage of each trajectory, which depends on the instantaneous field strength when it starts to get ionized (in phase ϕ_0) and the angle of the liberated particle (see Sec. 2.3.6).

As can be seen in Fig. 5.2, the field-strength-sensitive ionization rate increases from 10^{-14} to 10^{-5} with the increasing field strength (from 0.1 a.u. to 0.24 a.u.). Note that the atomic coordinates are (0, 0, 0) (a.u.) of He^{2+} and (0, 0, 1.46) (a.u.) of H^+ in Cartesian coordinates. Thus, for each field strength, which corresponds to a certain t_0, the ionization

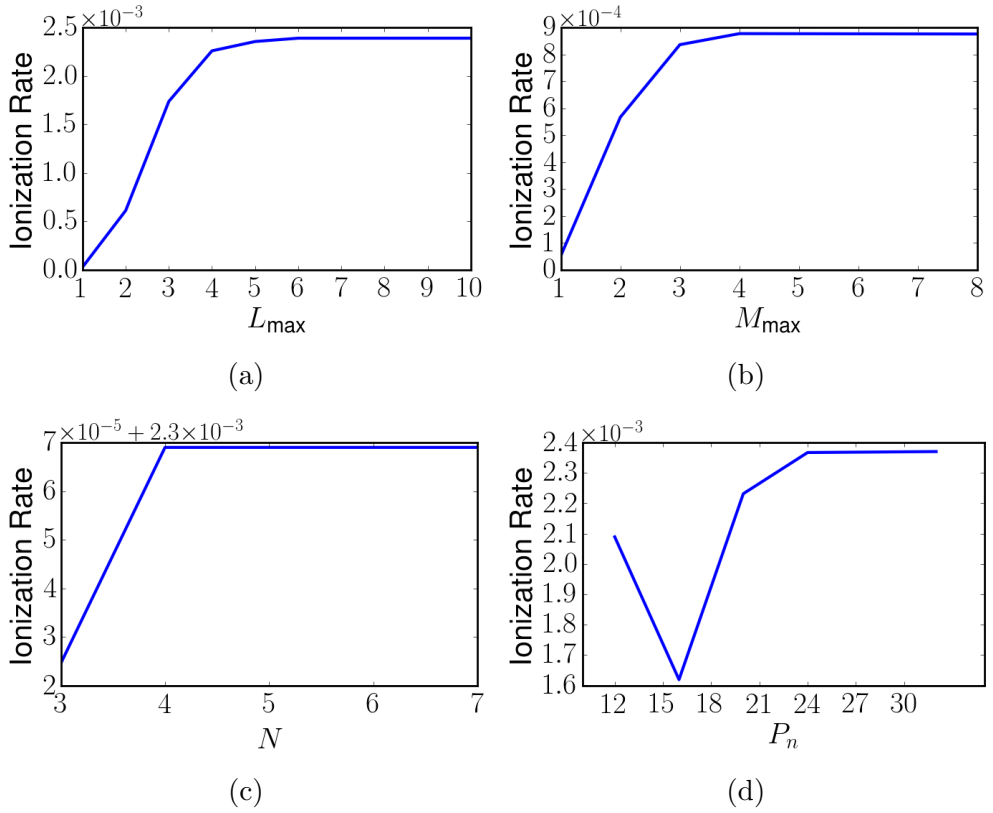

Figure 5.1: Convergence study for (a) $L_{\max}$, (b) $M_{\max}$, (c) number of intervals N, and (d) polynomials order P_n in unscaled region. The initial parameters for convergence test are P_n = 20, polynomials order in scaled region P_{N+1} = 24, $L_{\max}$ = 8, $M_{\max}$ = 8, N = 7, and decay factor α = 1. A detailed description of the discretization parameters can be found in Chapter 3.

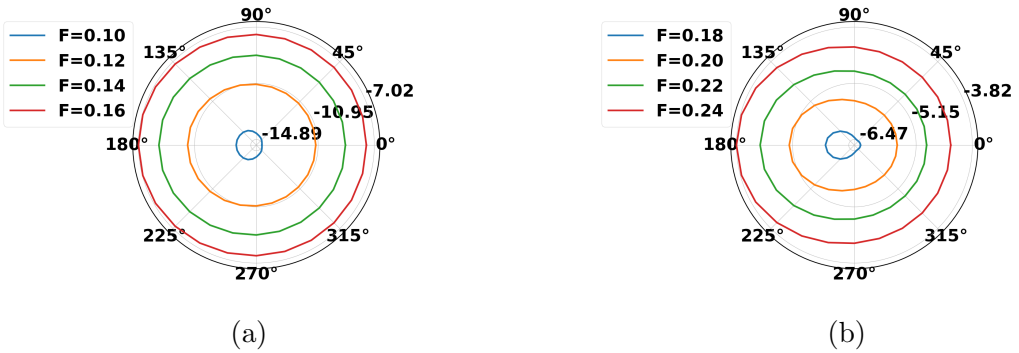

Figure 5.2: The static field ionization rate of (a) the lower field strength 0.10, 0.12, 0.14, and 0.16 a.u. and (b) the higher field strength 0.18, 0.20, 0.22, and 0.24 a.u. The numbers are represented in log10 scale and for more ionization rates with other intensities (refer to Table B.1 in Sec. B).

rate is higher when electron 1 tunnel-ionizes from H^+ side rather than He^{2+} side. For the maximum field strength we consider, i.e., 0.2 a.u., the ionization rate is roughly three times higher when electron 1 tunnel-ionizes from H^+ (8.52×10^{-6}) rather than from He^{2+} side (2.54×10^{-6}). The full quantum-mechanical calculation by haCC provides the reliable static field ionization rates as the foundation of CTMC calculation of HeH^+.

5.1.4 Conclusion

The static field ionization rates of HeH^+ are calculated by haCC with precise parameters from the convergence study. The ionization rate dramatically increases with a linearly increasing external field. With the ionization rates from haCC as inputs, one can use the CTMC method to calculate the electron dynamics of the FDI processes of HeH^+, where we find intertwined electron-nuclear interactions.

5.2 Freeman resonance enhanced spectra of helium

5.2.1 Background and motivation

Freeman resonance [182, 183] is a well-known mechanism in the photoionization spectrum that enhances the signal, and it is highly related to the Stark effect. The Stark effect is the shifting and splitting of spectral lines of atoms and molecules exposed to an external electric field. It consists of the DC Stark effect and AC Stark effect. The DC Stark effect describes the shifting and splitting of spectrum lines of atoms or molecules in a constant electric field, and the AC Stark effect shows the spectrum line of excited state up-shifts in an oscillating laser field while the ground eigenenergy remains stable (see Sec. 5.2.4). The Freeman resonance is triggered when the eigenenergy difference of a shifted excited state and the ground state is $N\omega$ as

$$-E_0 + E_x + U_p(I) = N\omega, E_0 = I_p(1), \tag{5.3}$$

where ω is photon energy of the pulse, E_0 and E_x are the ground and excited eigenenergies, and the shifted value of ponderomotive energy $U_p(I)$ for our specific case is used. The schematic illustration of AC Stark effect and Freeman resonance is shown in Fig. 5.3. A set of mixed states influence the detected spectra with Freeman resonance. In this section, we investigate Freeman resonance and its influence on single ionization photoelectron spectra of Helium as well as the underlying mechanism. We first present the laser field and methods, followed by the enhanced single ionization spectrum of He and the investigation of AC Stark shift using Floquet analysis to discover the potential excited states responsible for the enhancement. Subsequently, the underlying mechanism is discussed with a population analysis of the excited states. Finally, a collection of pulses that enhance the photoionization spectrum are given.

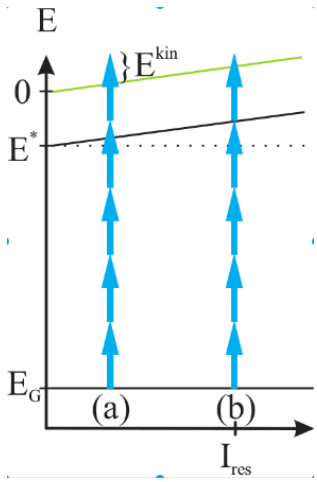

Figure 5.3: Freeman resonance criteria and AC Stark shift in a laser field. $I = I_{res}$ at (b) satisfies the Freeman resonance condition. E_g and E^* are the ground and excited eigenenergies. The solid lines show how the eigenenergies move with intensity.

5.2.2 Method and laser field

Laser field parameters

The dipole field of a laser pulse with peak intensity $I = \mathcal{E}_0^2$ (atomic units) and linear polarization in z-direction is defined as $E_z(t) = \partial_t A_z(t)$ with

$$A_z(t) = \frac{\mathcal{E}_0}{\omega} a(t) \sin(\omega t + \phi_{CEP}). \tag{5.4}$$

Two pulse envelopes $a(t)$ are used. First, a "flat-top" trapezoidal function with a linear rise and descent over a single optical cycle (τ=1 opt.cyc. $= 2\pi/\omega$) and n opt.cyc. constant amplitude in between, whose formula is

$$a(t) = f_{\frac{n}{2}\tau,(\frac{n}{2}+1)\tau}(-t) f_{\frac{n}{2}\tau,(\frac{n}{2}+1)\tau}(t), \quad -(1+\frac{n}{2})\tau \le t \le (1+\frac{n}{2})\tau, \tag{5.5}$$

where $f_{\alpha,\beta}(t)$ is the truncation function firstly defined in Eq. (2.16) of tSurff methods. The pulse is illustrated in Fig. 5.4a. The general formula of the pulse is defined in Sec. A.4. A flat-top pulse with full width half maximum (FWHM) $n = 5$ opt.cyc. is used for SI spectrum calculation unless specified differently. Although the envelope introduces artificial structures due the sidebands in its spectral decomposition [90], the flat-top shape pulse has advantages in the following two aspects. First, the flat-top pulse shape is a perfect choice for investigating the Stark shift (see below) and Freeman resonance with the help of the strictly time-periodic vector potential $A(t)$. Second, the photoionization of a long, Gaussian shape pulse which is close to experimental condition can be approximated by the flat-top pulse. Although the intensity of a Gaussian shape pulse evolves with time, the photoionization around the peak intensity ($t = 0$) dominates the whole photoionization process; the intensity varies slowly and can be treated as constant if the pulse is long enough.

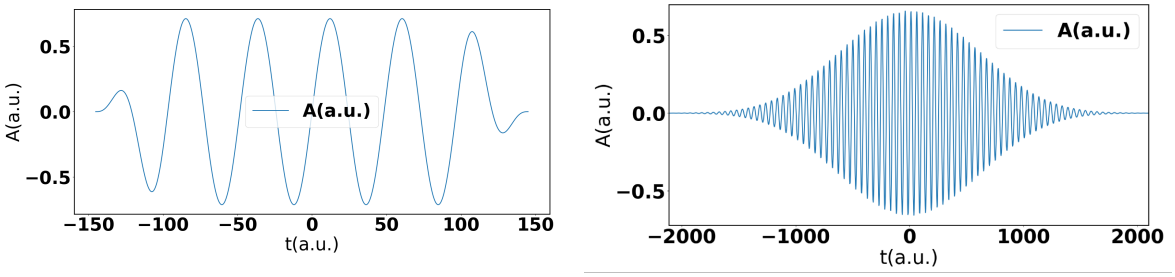

(a) (b)

Figure 5.4: The vector potential $A_z(t)$ of (a) a flat-top envelope, 351-nm, $3\times10^{14}\,\mathrm{W/cm^2}$ and FWHM=5 opt.cyc. pulse, and (b) a Gaussian envelope, 370-nm, $2.3\times10^{14}\,\mathrm{W/cm^2}$ and FWHM=20 opt.cyc. pulse.

$\cos^8$ envelope illustrated in Fig. 5.4b has been widely used in many calculations for its good approximation to the Gaussian envelope (see Sec. A.4.2). After the investigations with the flat-top pulse, calculations with n opt.cyc. $\cos^8$ shape pulses by formula

$$a(t) = \cos^8(\frac{\pi t}{4n\tau}), \quad -2n\tau \le t \le 2n\tau \tag{5.6}$$

will be presented to verify that mechanism exists in real pulses. This strategy will also be used in Sec. 6.4.4.

The atomic units ($\hbar = e^2 = m_e = 4\pi\epsilon_0 = 1$) are used in this section. For detailed information, refer to the appendix in Sec. A.1. In this section, we focus on the single ionization spectrum with the Hamiltonian

$$\mathrm{i}\partial_t\psi(\vec{r},t) = [-\frac{\Delta}{2} - \mathrm{i}\vec{A}(t)\cdot\vec{\nabla} - \frac{1+\exp(-2.135r)}{r}]\psi(\vec{r},t), \tag{5.7}$$

where $-\frac{1+\exp(-2.135r)}{r}$ is the effective Coulomb term of the single ionization. The ground state energy is -0.9029 a.u. by our calculation, in good agreement with the experimental data $I_p(1) = -0.903\,\mathrm{a.u.}$

Floquet states: Hamiltonian periodic in time

In solid state physics, the Hamiltonian is periodic in space, and the corresponding electronic eigenstates are Bloch states. Similarly, Floquet states are the eigenstates of the time-periodic Hamiltonian, which are essential to attosecond physics when a system is exposed an laser pulse with a considerable pulse duration. In this section, an introduction to the Floquet theory and derivation of the matrix elements is given.

When the Hamiltonian $H(t)$ is strictly periodic in time with a cycle T: $H(t+T) = H(t)$, a complete set of solutions of TDSE can be written in the form of Floquet states

$$\psi_{E,n} = e^{-\mathrm{i}E\cdot t}v_{E,n}(t), \quad n = -\infty,\cdots,-1,0,1,\cdots,\infty \tag{5.8}$$

where $v_{E,n}(t)$ is periodic with cycle T and $E \in [0, 2\pi]/T$. With the above equation taken into the TDSE $\mathrm{i}\partial_t \psi_{E,n} = H(t)\psi_{E,n}$, one has

$$i\frac{d}{dt}v_{E,n}(t) = (H(t) - E)v_{E,n}(t). \tag{5.9}$$

As $v_{E,n}$ is periodic in time with cycle T, it can be expanded in Fourier series as

$$v_E(\vec{r}, t) = \sum_m e^{\mathrm{i}m\omega t}\phi_m(\vec{r}), \quad \omega = \frac{2\pi}{T}. \tag{5.10}$$

We take the expansion into Eq. (5.9), multiply both sides with $e^{-\mathrm{i}n\omega t}$ and then average both sides on $t \in [0, T]$. After some algebraic calculations, one has

$$\sum_n E\delta_{mn}\phi_n(\vec{r}) = \sum_n [H_{m,n} + m\delta_{mn}\omega]\phi_n(\vec{r}), \tag{5.11}$$

where the element

$$H_{m,n} = \frac{1}{T}\int_0^T dt H(t)e^{\mathrm{i}(m-n)\omega t} \tag{5.12}$$

is independent of time. m, n are re-indexed to $\cdots, -2, -1, 0, 1, 2, \cdots$. Then the time-dependent Schrödinger equation is transformed into a linear algebra problem as

$$E\begin{bmatrix} \vdots \\ \phi_{-2} \\ \phi_{-1} \\ \phi_0 \\ \phi_1 \\ \phi_2 \\ \vdots \end{bmatrix} = \begin{bmatrix} \ddots & \vdots & & & & \vdots & \\ \cdots & H_{-2,-2} - 2\omega & H_{-2,-1} & H_{-2,0} & H_{-2,1} & H_{-2,2} & \cdots \\ \cdots & H_{-1,-2} & H_{-1,-1} - \omega & H_{-1,0} & H_{-1,1} & H_{-1,2} & \cdots \\ \cdots & H_{0,-2} & H_{0,-1} & H_{0,0} & H_{0,1} & H_{0,2} & \cdots \\ \cdots & H_{1,-2} & H_{1,-1} & H_{1,0} & H_{1,1} + \omega & H_{1,2} & \cdots \\ \cdots & H_{2,-2} & H_{2,-1} & H_{2,0} & H_{2,1} & H_{2,2} + 2\omega & \cdots \\ & \vdots & & & & \vdots & \ddots \end{bmatrix}\begin{bmatrix} \vdots \\ \phi_{-2} \\ \phi_{-1} \\ \phi_0 \\ \phi_1 \\ \phi_2 \\ \vdots \end{bmatrix}. \tag{5.13}$$

To simplify the notation, we define $H_{m,n} =: H_{m-n}$.

In this thesis, we only consider the ionization with a linearly polarized pulse along z-direction. We focus on single-frequency laser pulses here, where the time-dependent part of our Hamiltonian is proportional to $\cos(\omega t)$ or $\sin(\omega t)$. Thus, only the matrix element with a sub-index that satisfies $|m-n| = 0, 1$ is nonzero. Then, the Hamiltonian of Eq. (5.13) can be re-written as a band matrix

$$E\begin{bmatrix} \vdots \\ \phi_{-2} \\ \phi_{-1} \\ \phi_0 \\ \phi_1 \\ \phi_2 \\ \vdots \end{bmatrix} = \begin{bmatrix} \ddots & \vdots & & & & \vdots & \\ \cdots & H_0 - 2\omega & H_{-1} & 0 & 0 & 0 & \cdots \\ \cdots & H_1 & H_0 - \omega & H_{-1} & 0 & 0 & \cdots \\ \cdots & 0 & H_1 & H_0 & H_{-1} & 0 & \cdots \\ \cdots & 0 & 0 & H_1 & H_0 + \omega & H_{-1} & \cdots \\ \cdots & 0 & 0 & 0 & H_1 & H_0 + 2\omega & \cdots \\ & \vdots & & & & \vdots & \ddots \end{bmatrix}\begin{bmatrix} \vdots \\ \phi_{-2} \\ \phi_{-1} \\ \phi_0 \\ \phi_1 \\ \phi_2 \\ \vdots \end{bmatrix}. \tag{5.14}$$

In order to give the correct Floquet eigenenergies in velocity gauge, $|\vec{A(t)}|^2/2$ term that is always neglected for simplicity (see Sec. 1.3.1) is included back in Hamiltonian. This

operation does not change the eigenstate as the vector potential is independent of $\vec{r}$. With the Hamiltonian in velocity gauge

$$H(t) = -\frac{\Delta}{2} + V(\vec{r}) - \mathrm{i}\vec{A}_0 \sin(\omega t) \cdot \vec{\nabla} + |\vec{A}_0 \sin(\omega t)|^2/2, \tag{5.15}$$

and length gauge

$$H(t) = -\frac{\Delta}{2} + V(\vec{r}) + \vec{\mathcal{E}}_0 \cos(\omega t) \cdot \vec{r}, \tag{5.16}$$

we have

$$H_0 = \frac{1}{T}\int_0^T -\frac{\Delta}{2} + V(\vec{r}) + |\vec{A}_0 \sin(\omega t)|^2/2 dt = -\frac{\Delta}{2} + V(\vec{r}) + U_p, \tag{5.17}$$

$$H_1 = -H_{-1} = -\mathrm{i}\frac{1}{T}\int_0^T e^{\mathrm{i}\omega t}\vec{A}_0 \sin(\omega t) dt \cdot \vec{\nabla} = \frac{\vec{A}_0}{2} \cdot \vec{\nabla} \tag{5.18}$$

for velocity gauge and

$$H_0 = \frac{1}{T}\int_0^T -\frac{\Delta}{2} + V(\vec{r}) dt = -\frac{\Delta}{2} + V(\vec{r}), \tag{5.19}$$

$$H_1 = H_{-1} = \frac{1}{T}\int_0^T e^{\mathrm{i}\omega t}\vec{\mathcal{E}}_0 \cos(\omega t) dt \cdot \vec{r} = \frac{\vec{\mathcal{E}}_0}{2} \cdot \vec{r} \tag{5.20}$$

for length gauge, where ω is photon energy, A_0 is the maximum vector potential, $U_p = \frac{A_0^2}{4}$ is the ponderomotive energy and $\vec{\mathcal{E}}_0$ is the maximum electric field. For velocity gauge, as $\vec{\nabla}$ is anti-symmetric, the blocks appear with opposite sign to either side of the diagonal, and the total matrix is symmetric.

5.2.3 Enhanced SI Spectrum

The photoelectron spectra w.r.t photon numbers N_{photon} are

$$\sigma(N_{\mathrm{photon}}) = \int d\phi \int \sin\theta d\theta |b(k,\theta,\phi,T)|^2 k, \quad k = \sqrt{2(N_{\mathrm{photon}}\omega + U_p + I_p(1))}, \tag{5.21}$$

where $b(k,\theta,\phi,T)$ are the scattering amplitudes from tSurff computations.

Resonances appear with ground and $3p$ excited state (shown later) at wavelength $\lambda = 369$ nm, intensity $I = 3 \times 10^{14}\,\mathrm{W/cm^2}$, and wavelength $\lambda = 378$ nm, intensity $I = 2.3 \times 10^{14}\,\mathrm{W/cm^2}$. In the photoionization spectrum, each peak position corresponds to the number of absorbed photons, and its height represents the probability of an electron absorbing these photons ($N_{\mathrm{photon}}\omega$), which is favorable for low photon energy. But the peaks from the 369-nm and 378-nm calculations are the highest among those from their neighbored wavelengths at $I = 3 \times 10^{14}\,\mathrm{W/cm^2}$ and $I = 2.3 \times 10^{14}\,\mathrm{W/cm^2}$, respectively. In other words, the spectra are enhanced, as shown in Fig. 5.5.

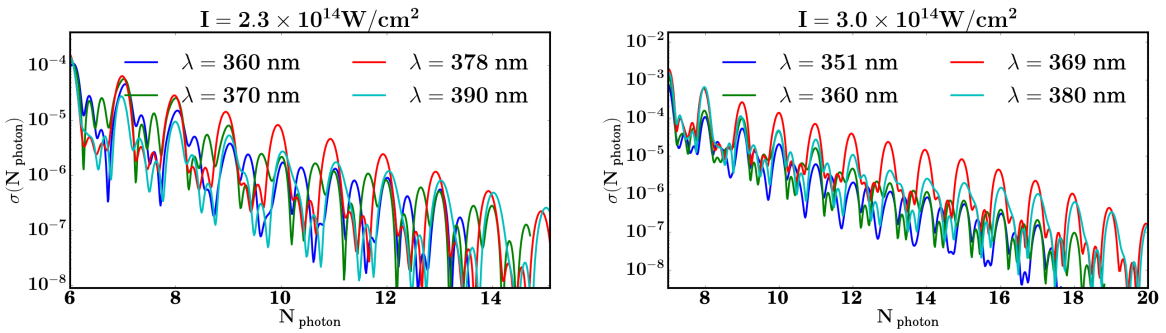

(a) (b)

Figure 5.5: Enhanced spectrum at intensity (a) I = 2.3×10^{14} W/cm^2 and (b) 3×10^{14} W/cm^2. The x values $N_{\text{photon}} = \frac{\frac{k^2}{2}+U_p-I_p(1)}{\omega}$ are the photon numbers. The y values are photoelectron spectra by Eq. (5.21). The pulses with flat-top envelope with 1 opt.cyc. cutoff and FWHM 5 opt.cyc. are used.

5.2.4 AC Stark shift by States Evolution

To investigate the underlying mechanism of the enhanced spectrum, verify the AC Stark shift, and find the excited state for the enhancement, one needs to know how the excited and ground states evolve with intensity, especially their eigenenergies. The evolution of Floquet eigenenergies of helium in a periodic external field with intensities are analyzed below by solving Eq. (5.14).

The schematic illustration of Floquet eigenenergies is shown in Fig. 5.6. Without the external field, the distribution of Floquet eigenenergies is composed by compact equidistant intervals with length ω, with each holding the eigenvalues of a field-free helium atom that are shifted leftwards or rightwards by $N\omega$. With the non-zero external electric field, each interval value moves right (increase) by a field-strength-dependent U_p. If a unit of eigenenergy moves to the position of the ground state eigenenergy of another block, the corresponding excited state is the one that satisfies the Freeman resonance condition.

Stable Floquet eigenenergies

Before presenting the results, we would like to show the our alternative notations for the eigenstates. We use "1s", "2p", "3s", "3p", and "3d" to denote the ground state of E_0 (eigenenergy -0.903 a.u.) and excited states $E_{1,l=1}$, $E_{2,l=0}$, $E_{2,l=1}$ and $E_{2,l=2}$, respectively.

To investigate the evolution of these eigenvalues, the Floquet eigenenergies are scanned through a set of intensities. The matrix of Eq. (5.14) is approximated by a block matrix where the default block number is 19 with the diagonal blocks $H_{-11,-11} - 11\omega, H_{-10,-10} - 10\omega, \cdots, H_{0,0}, H_{1,1} + \omega, \cdots, H_{6,6} + 6\omega, H_{7,7} + 7\omega$. As we are interested in the stable resonance states that contribute to the enhancement, the arbitrary and unstable eigenenergies need to be removed. This can be done by data analysis of results from various calculations

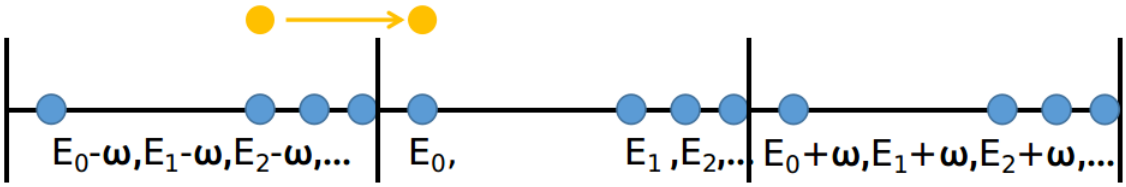

Figure 5.6: The Floquet states (lower blue circles) without and (upper orange circles) with the external field. The length of the three intervals are ω. The yellow circles and arrows represent an excited eigenenergy (left yellow circle) upshifts in the external field to the ground eigenenergy (right yellow circle) of the right hand side block.

with different complex scaling angles, as the eigenenergies of the stable states are invariant with the complex scaling angles. As shown in Fig. 5.7, various unstable states exist far from the real axis. The values in common for both the two irECS angles are the Floquet eigenenergies of our interest, which are plotted with increasing intensities below. As shown in Fig. 5.8, the ground energy eigenvalue is approximately invariant of the increasing intensity in our calculation (The small variances can be found in the next subsection, which do not show much in our intensities). But the eigenenergy of $3p$ state up-shifts by an intensity-dependent U_p, showing a linear relationship with the intensity. When the intensity dependent, up-shifting energy eigenvalue of $3p$ state equals that of a ground state energy with a shift by $N\omega$, the Freeman resonance criteria in Eq. (5.3) is satisfied. At $\lambda = 369$ nm, $I = 3.0 \times 10^{14}\,\mathrm{W/cm^2}$ and $\lambda = 378$ nm, $I = 2.3 \times 10^{14}\,\mathrm{W/cm^2}$, Freeman resonance is enhanced by the analysis of energy eigenvalues, where the photoionization spectra are also enhanced.

Tracing Floquet eigenenergies

The above behaviors of the eigenenergies are verified by tracing the corresponding Floquet eigenstates. If the overlap of n_1th eigenstate ψ_{I_1,n_1} at intensity $I_1 \neq 0$ and the n_0th ground eigenstate ψ_{I_0,n_0} is larger than a given criteria Ovr as $|\langle\psi_{I_1,n_1}|\psi_{I_0,n_0}\rangle| \geq$ Ovr, one may conclude that ψ_{I_1,n_1} is evolved from ψ_{I_0,n_0} with the increasing intensity. If no such $\langle\psi_{I_1,n_1}$ is obtained, the step size is reduced until the overlap can follow.

In practice, calculating all the eigenvectors and eigenvalues consumes a large amount of memory, and the tracing dies after a few recursive steps. To solve this problem, the eigenvalues and eigenvectors of each intensity are saved on disk and read back if needed. Thus, we can quickly restart the searching from the point where it crashed.

Another method to avoid such a huge computational task is inverse iteration (also known as the inverse power method), which solves the eigenvalue problem when the approximated eigenvalue is already known. To compute the eigenvalue near E'_x of the Hamiltonian H, we perform the iteration from a desired eigenvalue E'_x and a vector ψ_0 using the

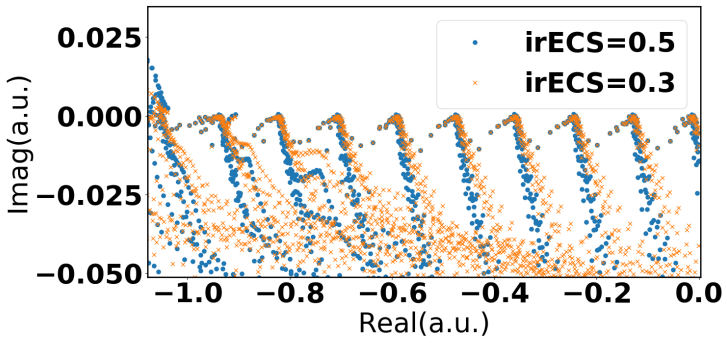

(a)

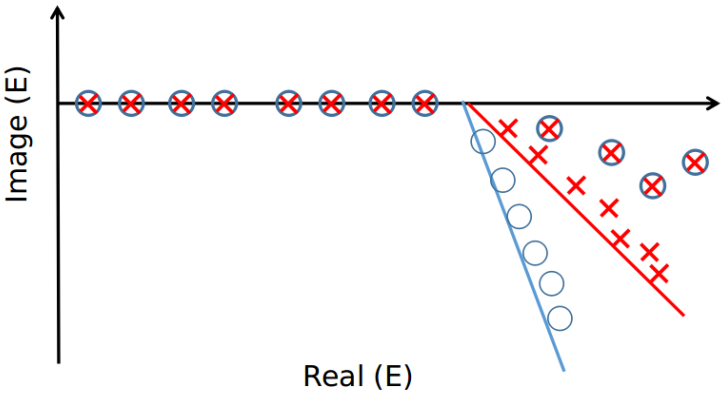

(b)

Figure 5.7: (a) Floquet states with λ = 394.5 nm,I = 9×10^{14} W/cm^2 at complex scaling angle 0.5 and 0.3. (b) Illustration of eigenstates from two different irECS angles depicted by red crosses and blue circles. The solid blue and red lines are the exact continuous spectra with twice the irECS angles $2\theta_{1/2}$. The overlap of blue circles and red crosses depict the resonance states.

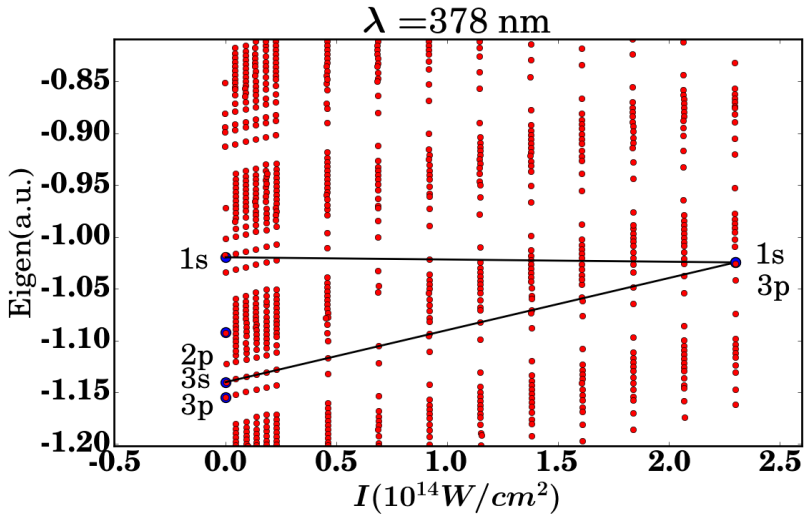

(a)

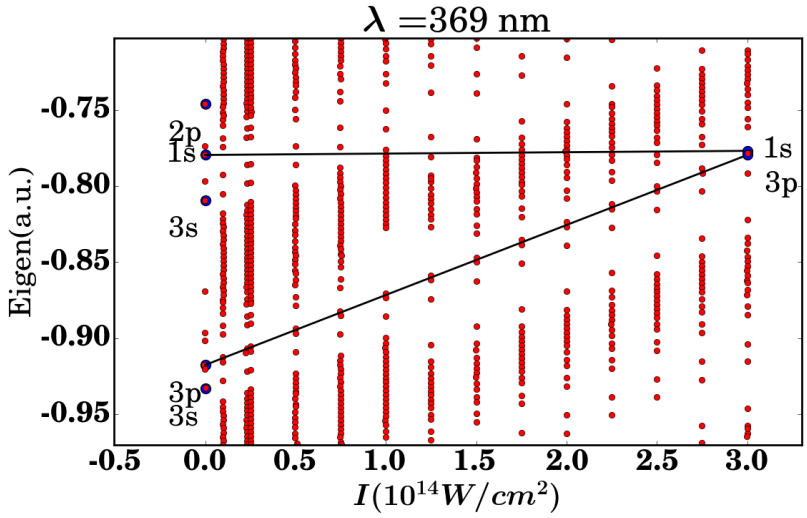

(b)

Figure 5.8: The evolution of Floquet states with respect to intensity based on calculations on wavelengths (a) 378 nm (maximum intensity $I = 2.3 \times 10^{14}\,\mathrm{W/cm^2}$) and (b) 369 nm (maximum intensity $I = 3.0 \times 10^{14}\,\mathrm{W/cm^2}$). One may find $E_{2,l=1} - E_0 = n\omega$ (n is integer) is satisfied at the maximum intensity of each sub-plot. The blocks of the eigenenergies are shifted by $m\omega$ (m is integer). In the plots, the labels "1s", "2p", "3s", "3p", and "3d" orbital depict E_0, $E_{1,l=1}$, $E_{2,l=0}$, $E_{2,l=1}$ and $E_{2,l=2}$, respectively, which are all highlighted by blue circles.

formula

$$\psi_{k+1} = \frac{(H - E'_x I)^{-1}\psi_k}{C_k}, \tag{5.22}$$

where C_k are some constants chosen

$$C_k = \|(H - E'_x I)^{-1}\psi_k\|. \tag{5.23}$$

In every iterative step, ψ_k is multiplied by $(H - E'_x I)^{-1}$. Similar to the power method, by iteratively calculating $H\psi, H\psi^2, H\psi^3\cdots$, the result converges to an eigenvector that corresponds to the dominant eigenvalue. In the inverse power method, ψ_k converges at the eigenvector that corresponds to the dominant eigenvalue of $(H - E'_x I)^{-1}$. The eigenvalues of this matrix are $(\lambda_0 - E'_x)^{-1}, (\lambda_1 - E'_x)^{-1}, (\lambda_2 - E'_x)^{-1}\cdots$, where λ_k are the eigenvalues of H. The largest number of these corresponds to the smallest of λ_k. And as we have

$$(H - E'_x I)^{-1}\psi = (\lambda - E'_x)^{-1}\psi \Leftrightarrow H\psi = \lambda\psi, \tag{5.24}$$

$(H - E'_x I)^{-1}$ and H have the same eigenvectors, ψ_k converges to the eigenvector of H corresponding to the approximated eigenenergy E'_x. The method converges fast if we choose a suitable E'_x and converges slowly for an incorrect E'_x.

With the inverse iteration method, one gets the eigenenergy E_x at intensity I with eigenenergy E'_x at intensity I' as the approximation eigenenergy, when I' closely approaches I from the left. Choosing a relatively small intensity interval, we can trace the field free eigenstates evolution with the increasing intensity. In Fig. 5.9, we plot the eigenenergy of Floquet states $E_{3s}(E_{2,l=0})$ and $E_{3p}(E_{2,l=1})$ at different intensities. The ground eigenenergy E_0 does not move with the increasing intensity, but the eigenenergy of excited p state linearly up-shifts with intensity, and the shifted value is U_p. The evolution of $s(l = 0)$ eigenenergy deviates the linearity within an error at maximum $0.3\times10^{14}\,\mathrm{W/cm^2}$, especially in high intensity region. The behavior of eigenenergy E_{3p} shows the particle acquires ponderomotive energy, like a free electron in the pulse, and feels little interaction from the nucleus. According to the one-level analysis model from Delone et.al. [184], the shifted energy by AC Stark effect is linear with $\sqrt{I}$ and I in high-intensity region ($n^6\mathcal{E}_0^2 \gg \omega$, n is energy level). The high-intensity region depicted by the dotted red line in Fig. 5.9 are fit with the green curve, where we find the fitting matches E_{3s} well with maximum error below 5%. As the one-level model only applies if the state does not mix with other principle quantum numbers, the good fitting of E_{3s} shows orbital $3s$ does not mix with other states well like $3p$, which is consistent with the higher population of $3p$ in the population analysis below (in Fig. 5.14). Thus, a particle in the $3p$ orbital behaves like a free electron, fully couples with the external field, and mixes with other states, but the $3s$ orbital does not. The cross from the eigenenergies of excited states and the ground state indicates enhancements of $2.3\times10^{14}\,\mathrm{W/cm^2}$ for 378 nm and $3\times10^{14}\,\mathrm{W/cm^2}$ for 369 nm, which is consistent with the photoelectron spectrum and the analysis of populations (shown later).

Gauges

The consistency of the eigenenergies calculated with different gauges also needs to be checked. A detailed structure of traces of the eigenenergies of E_0 can be found in Fig. 5.10a.

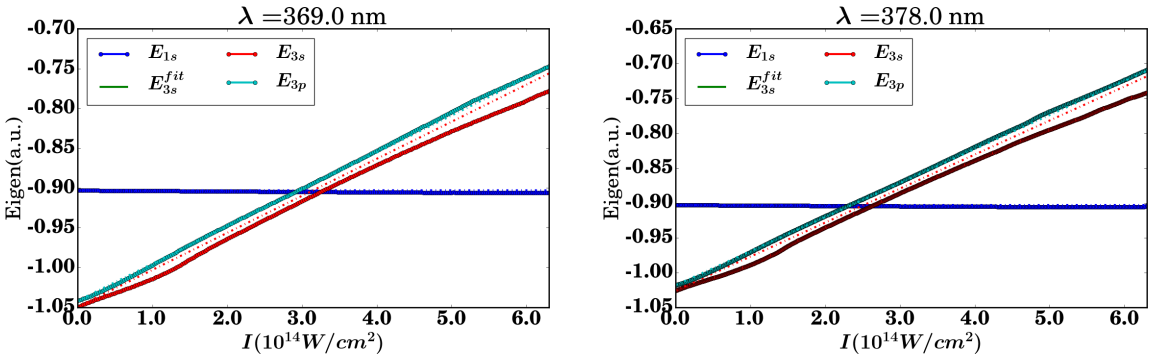

(a) (b)

Figure 5.9: The scanning of eigenenergies of Floquet states $E_{1s}(E_{0,l=0})$, $E_{3s}(E_{2,l=0})$ and $E_{3p}(E_{2,l=1})$ with different intensities at (a) λ = 369 nm and (b) λ = 378 nm. The dash-doted lines of near the solid lines with the same color show theoretical lines $E_x + Up$ or E_0. The green lines (coincide with and can be hardly distinguished from the red line-dots) with label E_{3s}^{fit} are fittings of E_{3s} with formula $E(I) = a + b\sqrt{I} + cI$ when $I \geq 1 \times 10^{14}\,\mathrm{W/cm^2}$.

It is found that for both gauges E_0 drops linearly with intensities before the intensity approaches $4 \times 10^{14}\,\mathrm{W/cm^2}$. After that, the trend continues for the length gauge, but the curve goes up with intensity for the velocity gauge, introducing an error for predicted resonance intensity at around $0.1 \times 10^{14}\,\mathrm{W/cm^2}$ for $I = 6 \times 10^{14}\,\mathrm{W/cm^2}$. A calculation with more blocks of the Floquet matrix shows that the curve of E_0 from the velocity gauge converges with that of the length gauge. The eigenenergies for excited states are also checked for convergence. The reason for the ground eigenenergy slightly reducing is explained in Ref. [184]; the shift of the ground eigenenergy is similar to the static polarization of an atom, which is negative, because the frequency of the photon is small compared to the ground energy.

The results of state searching confirmed the linear relationship between Floquet eigenenergy and intensity, consistent with Fig. 5.8. Therefore, we can confirm that the excited states with the expected resonance evolve from $3p$ states.

5.2.5 Population of excited states

To investigate the mechanism of the enhanced photoionization spectra, the population of the excited states are investigated as they are paramount to the spectrum. In this section, we scan the populations of the excited states with wavelengths at fixed intensities and consider the peaks of the populations as indicators of the resonance. For the analysis of population, we switch to solving the time-dependent Schrödinger equation. After spectral

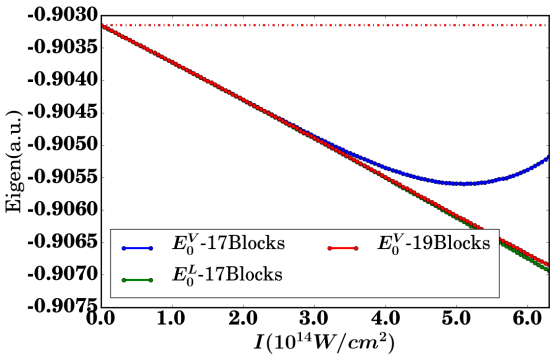

(a)

Figure 5.10: Floquet energy eigenvalues E_0 scanning with intensity calculated from velocity gauge (blue and red) and length gauge (green). There are 17 blocks for the blue and green curves, with the diagonal blocks $H_{-11,-11} - 11\omega, H_{-10,-10} - 10\omega, \cdots, H_{0,0}, H_{1,1} + \omega, \cdots, H_{4,4} + 4\omega, H_{5,5} + 5\omega$, and 19 blocks for the red curve with diagonal blocks $H_{-11,-11} - 11\omega, H_{-10,-10} - 10\omega, \cdots, H_{0,0}, H_{1,1} + \omega, \cdots, H_{6,6} + 6\omega, H_{7,7} + 7\omega$.

decomposition with

$$\psi(\vec{r},t) = \sum_{i=0}^{N} C_i(t)\varphi_i(\vec{r}), C_i(t) = \langle\varphi_i(\vec{r})|\psi(\vec{r},t)\rangle, \tag{5.25}$$

the norm square of the coefficient

$$P_i(t) = \langle\psi(\vec{r},t)|\varphi_i(\vec{r})\rangle\langle\varphi_i(\vec{r})|\psi(\vec{r},t)\rangle \tag{5.26}$$

serves as the population value, where $\varphi_i(\vec{r})$ represents the eigenstate of the field free Hamiltonian. We take $t = T$ ($T = t_{\text{end}}$ (see previous chapters), where the population values are calculated at the end of the pulse unless specified differently. Then, we have the wavelength scan of population values for $I = 3 \times 10^{14}\,\text{W/cm}^2$ and $I = 2.3 \times 10^{14}\,\text{W/cm}^2$ in Fig. 5.11. As can be seen in the figures, populations of s and d states (l = 0 and l = 2) are enhanced at $\lambda = 378$ nm for $I = 2.3 \times 10^{14}\,\text{W/cm}^2$ and $\lambda = 369$ nm for $I = 3 \times 10^{14}\,\text{W/cm}^2$. Note that at conditions $\lambda = 378$ nm, $I = 2.3 \times 10^{14}\,\text{W/cm}^2$ and $\lambda = 369$ nm, $I = 3 \times 10^{14}\,\text{W/cm}^2$, the spectra are also enhanced (see Fig. 5.5). When the Freeman resonance condition is satisfied, there exists a strong states mixing. As the eigenenergies of 3p (-0.54 a.u.) and 3d (-0.53 a.u.) are close, there remains possibility that the 3s and 3d orbitals are involved in the states mixing. This also gives an indication of Freeman resonance.

5.2.6 Application to general cases

As shown in Fig. 5.12a, the crossing (labeled with circles) of a ground-state eigenenergy ($E_0 + N\omega$) and an excited-state eigenenergy ($E_2 + M\omega$) satisfies Eq. (5.3) and enhances

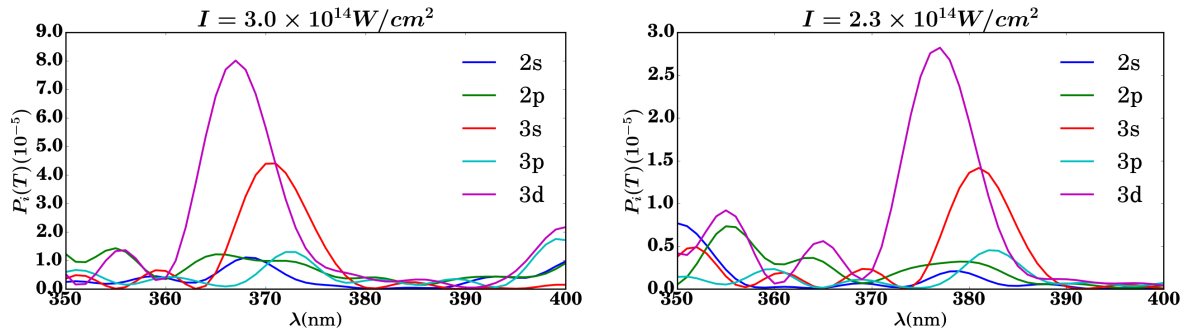

(a) (b)

Figure 5.11: The populations of $E_{2,l=0,l=2}$ (depicted by 3s and 3d) are enhanced at (a) 378 nm, $I = 2.3 \times 10^{14}$ W/cm^2, and at (b) 369 nm, $I = 3 \times 10^{14}$ W/cm^2. The pulses with the 1 opt.cyc. cut-off, flat-top envelope and FWHM=5 opt.cyc. are used.

Freeman resonance. By solving the following equation

$$\begin{aligned} E_0^{I=0} + m\omega \approx E_0^{I=I_0} + m\omega \\ = E_2^{I=I_0} + n\omega \approx E_2^{I=0} + U_p + n\omega \end{aligned}, \tag{5.27}$$

the Freeman resonance conditions for various wavelength-intensity pairs can be obtained, and their values are plotted in Fig. 5.12. The performance of the enhancement is presented in Fig. 5.13, with laser parameters selected from Fig. 5.12, and the spectra suggest that despite the weaker enhancement at lower intensities, the solvers do produce enhanced spectra, where at constant intensity, the photoelectron spectra with respect to the absorbed number of photons produced at the wavelength λ that satisfy the resonance condition is higher than those produced from $\lambda \pm 10$ nm.

As is mentioned in Sec. 5.2.2, flat-top envelop introduces artificial effects and the $\cos^8$ envelop approximates the real pulse shape well. To examine the extension of the Freeman resonance to pulses with experimental envelopes, spectra are calculated at 20 opt.cyc. pulses with $\cos^2$ or $\cos^8$ envelop in Fig. 5.14. The SI spectra are also enhanced when the resonance criteria is satisfied, indicating Freeman resonance enhancement is an universal mechanism.

5.2.7 Conclusion

The AC Stark shift of the eigenenergies of excited states are calculated using the Floquet states in the single ionization of Helium. It is observed that the excited eigenenergies of $3p$ orbitals in the pulse can be well described by $E_x + U_p$ and $3s$ eigenenergy also shifts linearly but with an acceptable error to $E_x + U_p$. When the eigenenergy of an excited state differs from that of the ground state by $-E_0 + E_{2,l=1} + U_p = N\omega$, the SI spectrum is enhanced by Freeman resonance, and the populations of the exited states reach the maximum. The

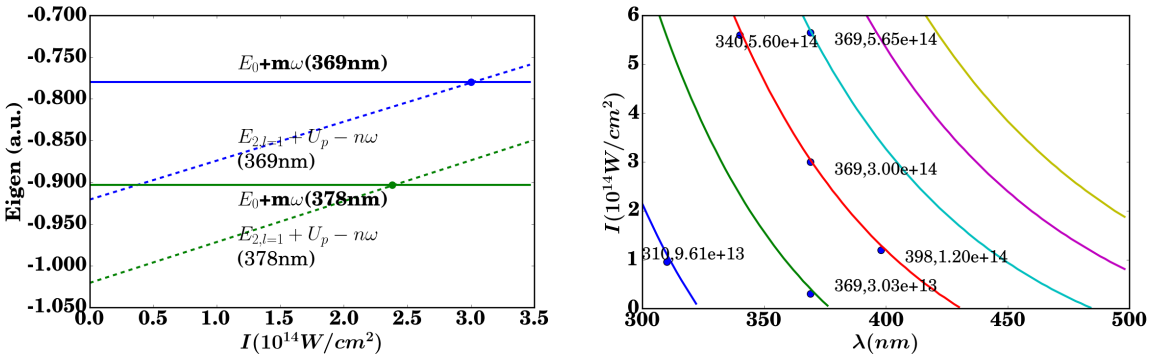

(a) (b)

Figure 5.12: (a) The evolution of E_0 and E_2 eigenstates of λ = 378 nm and λ = 369 nm. The cross of the dashed tilt and horizontal lines depicted by the circles are corresponding resonance conditions. (b) The (λ, I) values that satisfy the Freeman resonance conditions solved from Eq. (5.27).

enhanced excited l = 1 state with p orbital fully couples with the external field. The population of its neighbored $l = 0, 2$ states with $3s$ and $3d$ orbitals increases when the atom is exposed to the external laser field, and survives for a long time after the laser pulse. The SI spectrum is not only enhanced when the system is exposed to a flat-top envelope pulse but also when it's exposed to long, Gaussian-like envelope pulses.

5.3 Experimental photoionization spectrum fitting

5.3.1 Background

Understanding relevant experimental details and methods paves the way for better interpretations. This subsection mainly demonstrates the experimental details for measuring intensity and smooth range as well as their influences on the observables. We produce the SI and DI photoionization spectra using theoretical calculations to fit those from the experimental data at $I = 3.5 \times 10^{14}\,\mathrm{W/cm^2}$, $I = 4.6 \times 10^{14}\,\mathrm{W/cm^2}$ and $I = 5.7 \times 10^{14}\,\mathrm{W/cm^2}$ from Ref. [46]. The main result is given in the next chapter.

5.3.2 Laser field

For the comparison with experimental data, a 394.5-nm and $\cos^8$ pulse that's linear-polarized along the z-direction is used for the single ionization spectrum calculations of a Helium atom. The calculated spectra are the sources for fitting the experimental data. The Hamiltonian of the single ionization process is shown in Eq. (5.7).

The following numerical treatments and approximations are applied for the fitting.

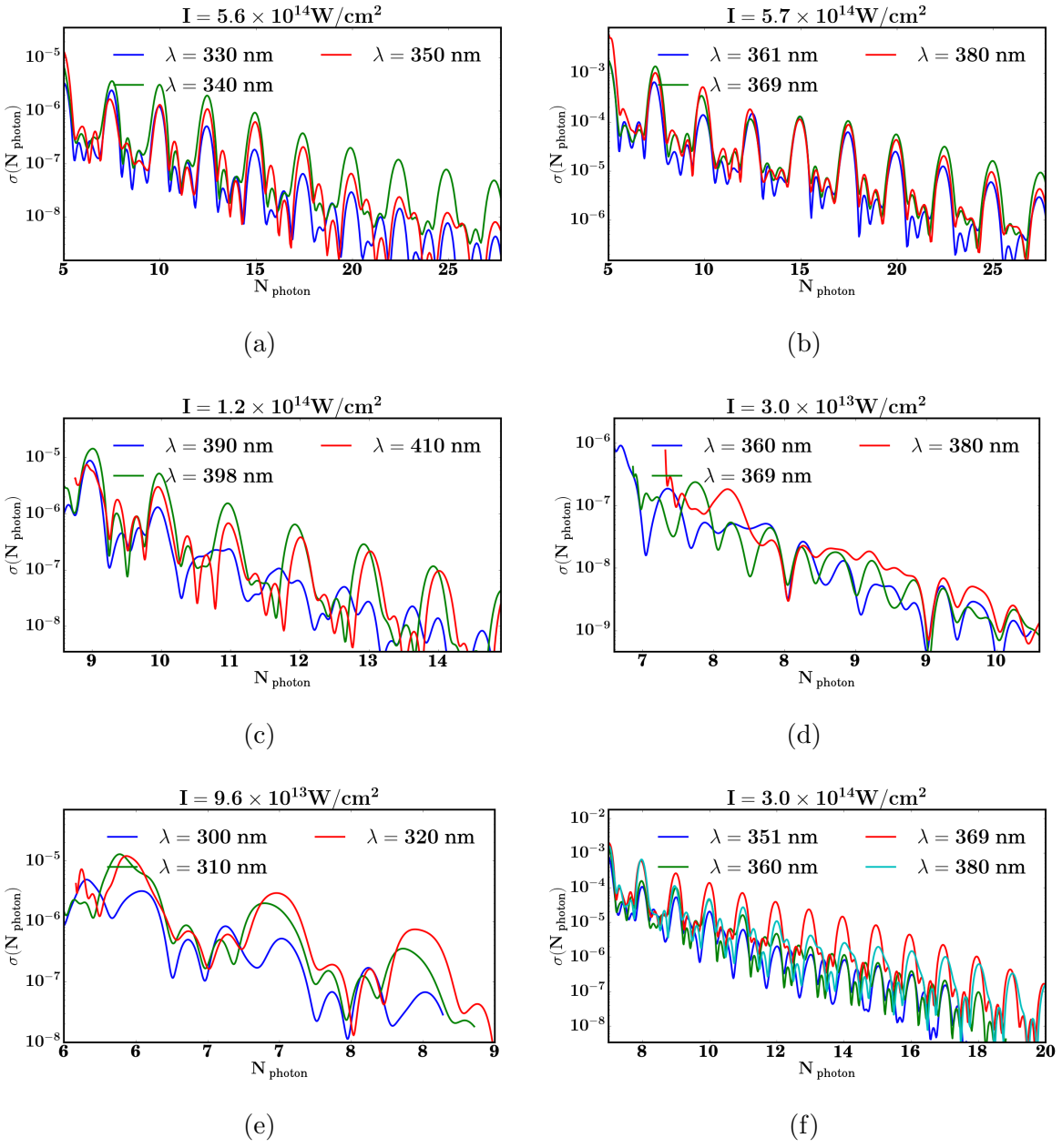

Figure 5.13: SI spectra by (a) $\lambda = 340$ nm, $I = 5.60 \times 10^{14}$ W/cm^2, (b) $\lambda = 369$ nm, $I = 5.65 \times 10^{14}$ W/cm^2, (c) $\lambda = 398$ nm, $I = 1.12 \times 10^{14}$ W/cm^2, (d) $\lambda = 369$ nm, $I = 3.03 \times 10^{13}$ W/cm^2, (e) $\lambda = 310$ nm, $I = 9.61 \times 10^{13}$ W/cm^2 and (f) $\lambda = 369$ nm, $I = 3 \times 10^{14}$ W/cm^2 labeled in Fig. 5.12b.The x values $N_{\text{photon}} = \frac{\frac{k^2}{2} + U_p - I_p(1)}{\omega}$ are the photon numbers. The y values are the photoelectron spectra from Eq. (5.21).

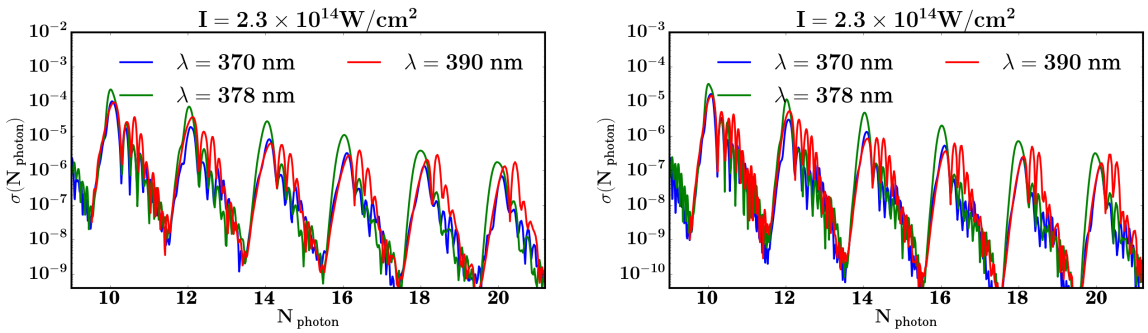

(a) (b)

Figure 5.14: The spectra with (a) $\cos^2(\frac{t}{2T})$ and (b) $\cos^8(\frac{t}{2T})$ envelopes for various wavelengths. FWHM is 20 opt. cyc., and intensity is $2.3{\times}10^{14}$ W/cm^2. 378 nm, $2.3{\times}10^{14}$ W/cm^2; this condition satisfies the Freeman resonance criteria. The definition of the pulse shape can be found in the appendix in Sec. A.4.The x values $N_{\text{photon}} = \frac{\frac{k^2}{2}+U_p-I_p(1)}{\omega}$ are the photon numbers. The y values are photoelectron spectra obtained by Eq. (5.21).

5.3.3 Experimental details

Data smoothing

Theoretically, the smoothing $\overline{\sigma(E,I)}$ of the yield in the SI spectrum $\sigma(E)$ with the smooth range E_s is given by

$$\overline{\sigma(E,I)} = \frac{\int_{E-E_s}^{E+E_s} \sigma(E',I)dE'}{2E_s}, \tag{5.28}$$

where E_s is the smooth range. Usually, E_0 does not change the overall shape of the spectrum. Data smoothing is always required for comparing theoretical calculations with experimental results, which helps dampen artificial signals with numerical approximations as well as highlight the physical properties.

Intensity

The experimental laser pulse beam pulse beam travels in the $\vec{e_z}$ direction with peak intensity I_0, which satisfies the standard Gaussian distribution by formula

$$I(r,z) = I_0 \frac{I_0}{1+(\frac{z}{\rho_0})^2} \exp(-\frac{2r^2}{\omega_0^2(1+(\frac{z}{\rho_0})^2)}), \tag{5.29}$$

where ω_0 is the focal radius and ρ_0 is the Rayleigh length. The parameters of laser in Ref. [46] are $\omega_0 = 2\,\mu$m, $\rho_0 = 30\,\mu$m, $(\frac{\omega_0}{\rho_0})^2 \ll 1$; thus, the distribution can be approximated by a Gaussian distribution as

$$I(r,z) \approx I_0 \exp(-\frac{2r^2}{\omega_0^2}), \tag{5.30}$$

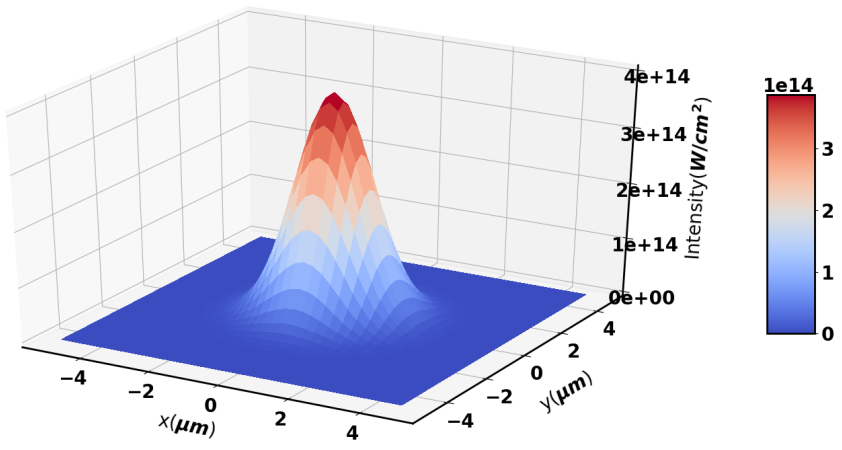

Figure 5.15: The illustration of the Gaussian distribution of the intensity. The intensity distribution satisfies $I(r,z) = I_0 \exp(-2\frac{r^2}{\omega_0^2})$, where $I_0 = 4\times10^{14}\,\mathrm{W/cm^2}$ and $\omega = 2\,\mu\mathrm{m}$.

whose shape is schematically illustrated in Fig. 5.15.

Thus, the measured photoionization spectrum in these experiments is a weighted average of those from a distribution of intensities in the pulse beam and is calculated using the focal volume average:

$$\overline{\sigma(E)} = \frac{\int_{I_0}^{0}\sigma(E,I)S(I)dI}{\int_{I_0}^{0}S(I)dI} \tag{5.31}$$

where $S(I)$ is the weight of the intensity on xy plane. According to Eq. (5.30), the volume element is

$$S(I)dI \propto 2\pi r dr = -\frac{\pi\omega_0}{\sqrt{2I}}dI. \tag{5.32}$$

The directly computed SI photoionization spectrum at $5.7\times10^{14}\,\mathrm{W/cm^2}$ and the focal volume averaged computation from a Gaussian distribution laser field with peak intensity $5.7\times10^{14}\,\mathrm{W/cm^2}$ are illustrated in Fig. 5.16. As shown in the above-mentioned figure, with the focal volume average operation, spectra at the high-energy regime ($E > 30eV$ where it differs most between $5.7\times10^{14}\,\mathrm{W/cm^2}$ and $5.3\times10^{14}\,\mathrm{W/cm^2}$) are weakened and shifted to those from the lower intensity calculation, but they are still higher than $5.3\times10^{14}\,\mathrm{W/cm^2}$. One may conclude that the error from focal volume averaging to predict the intensity by SI photoelectron spectra comparison is within $0.4\times10^{14}\,\mathrm{W/cm^2}$, which is below the error from counting the wrong photon number, as shown below.

Due to experimental limitations, a direct observation of the intensity is not possible. The values are derived from the peak positions in the SI or DI (double ionization) energy

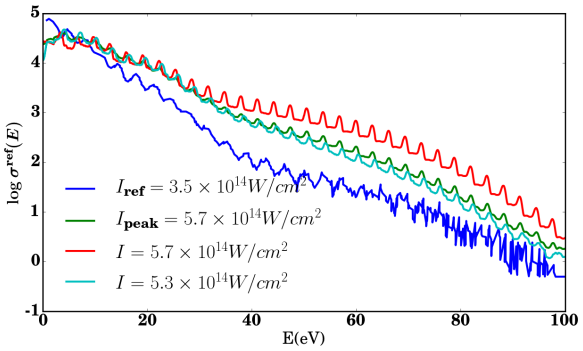

Figure 5.16: The SI spectra at 5.7×10^{14} W/cm^2 (green line) with focal volume averaging operation compared with those without averaging operation at (red line) 5.7×10^{14} W/cm^2 and (cyan line) 5.3×10^{14} W/cm^2. The blue line is from experiments by Ref. [46] at 3.5×10^{14} W/cm^2. Here FWHM=7 opt.cyc. and the pulse shape is cos^8. The smooth range is 2 eV.

photoionization spectra with formula

$$E_n^{(1)} = n\Omega - I_p^{(1)} - U_p \tag{5.33}$$

for SI photoionization spectra and

$$E_n^{(2)} = n\Omega - I_p^{(2)} - 2U_p, \tag{5.34}$$

for DI photoionization spectra, respectively, where Ω is frequency, $I_p^{(1)}$ and $I_p^{(2)}$ are the ionization potentials for single and double ionization, $U_p = \mathcal{E}_0^2/(4\Omega^2)$ is the ponderomotive energy, and n is the number of absorbed photons. It should be noted that for the pulse parameters used here, U_p reaches up to several photon energies and the error for predicting the intensities approximates $\delta n \times 2.1 \times 10^{14}$ W/cm^2, where δn is the error of the photon numbers. The extraction of intensity from the spectra only needs to be performed once, as the size of the focus can be adjusted with high accuracy. If I_0 is the first intensity derived from the peak positions using either of the two equations above, the other intensities can be calculated by

$$I_i = I_0 \frac{S_0}{S_i}, \tag{5.35}$$

where I_i is the intensity of interest and S_0, S_i are the areas of the focus. $\frac{S_0}{S_i}$ can be easily and precisely controlled in the experiments. This is called the "spot size measurement" and is applied in Ref. [46] and [45]. According to Ref. [46], using peaks of joint energy spectra from DI calculations (Eq. (6.12)) results in more accurate values than that with SI positions (Eq. (6.11)).

5.3.4 Conclusion

This section introduces the methods for fitting the experimental data, including the smooth range, distribution of intensity, and the method for deriving the intensities in experiments. We have found that the focal volume averaging method moves the photoionization spectrum to a lower intensity with an error of approximately $0.4 \times 10^{14}\,\mathrm{W/cm^2}$, which is small compared to the wrong photon number situation.

Chapter 6

Double ionization at 400nm

This section mainly taken from my paper Ref [185].

6.1 Introduction

Double-ionization of noble gas atoms has been and still is being investigated for studying the effects of elementary correlation and for gauging computational methods. Notably the measurement of enhanced double-ionization by strong laser pulses [44] has triggered a large number of theoretical studies and consensus has emerged that "recollision", where the first emitted electron collides with the still-bound one, is the primary mechanism of double ionization. Variants of this basic mechanism have been used to explain in increasing detail spectra using short, intense pulses that were obtained by cold target recoil ion momentum spectroscopy (COLTRIMS) [34].

The assignment of the observed spectral features to specific mechanisms remains a challenge for theory. The Helium atom is, in principle, accessible to a complete numerical solution of its time-dependent Schrödinger equation (TDSE) and the computation of fully differential spectra, even if the parameter range where this can be achieved remains narrow. However, an accurate time-dependent wave function by itself does not provide physical insight or intuitive mechanisms. For that, the use of classical and semi-classical models is of interest. Such models have been very successful in strong field physics [55, 130, 171].

The recollision model for non-sequential double ionization (NSDI) consists of three steps: (1) electron e_1 leaves the atom, typically by tunnel ionization; (2) e_1 picks up energy in the laser field; (3) it returns to the vicinity of the nucleus and the second electron e_2 is detached by collision. The scenarios for the interaction in step (3) are often phrased in terms of classical mechanics. Energetic recollsions predominantly occur near nodes of the field. The energy of e_1, the energy imparted to e_2, and e_2's ultimate detachment time are the main parameters to distinguish various classical mechanisms. At large energy, e_1 can knock out e_2 in an $e - 2e$ collision and the two leave nearly at the same time. When the energy imparted to e_2 is below the ionization threshold, the simultaneous presence of the laser field can still allow detachment by suppressing the potential barrier. The

mechanisms where the release occurs within a narrow time-window of the recollision we call "double-ionization upon recollision" (DUR), which subsumes direct knock-out and release by suppression of the binding barrier as well as tunneling [186–188]. If e_1 looses much of its energy in the process, the field will accelerate both electrons into the same direction, which we denote as side-by-side (SBS) emission. At non-equal energy sharing e_1 continues its path, while e_2 is emitted into the opposite direction, which we call back-to-back (B2B) emission. When studying the momenta, one has to also include scattering of the electrons by the nucleus. Such a process is the "slingshot-NSDI" [171], which leads to B2B emission of the two electrons, even when both electrons have comparably low momenta upon recollision.

When an actual excited state is formed with a decay time that is not locked to the recollision event, one speaks of "recollision induced excitation with subsequent ionization" (RESI) [76, 77], which allows both, SBS and B2B emission. A similar pattern, where, however, SBS emission favored, is the formation of a quasi-bound state of both electrons which can survive for at least one-quarter cycle and gets ionized with the electrons moving into the same direction ("double delayed ejection", [73]).

In this paper we present *ab initio* quantum mechanical calculations of double-ionization of the He atom by short and intense laser pulses at a carrier wavelength of 394.5 nm and relate these to recent measurements and some of the mechanisms listed above. Dependence of SBS and B2B emission on pulse intensity and pulse duration is used as the main observable.

We present joint energy and momentum distributions at various intensities and pulse durations and find generally good agreement with measurement. Our simulations also show enhanced B2B emission at non-equal energy sharing, as predicted by the classical models. B2B emission is further enhanced by Freeman resonances, a genuinely quantum phenomenon. Finally, we will point to another manifestation of quantum mechanics, namely the modulation by $2\hbar\omega$ of the joint energy distribution along lines of constant sum energy — the "checkerboard pattern" of Ref. [46]. In classical language this translates into repeated electron collisions. We also present calculations with ultrashort pulses (2 fs FWHM, parameters of Ref. [171]), that generally support the slingshot mechanism of Ref. [171], although the match is found at lower than predicted intensity.

6.2 Methods and laser parameters

6.2.1 Two-electron calculations

The Hamiltonian of the He-atom with infinite nuclear mass is (using atomic units $\hbar = e^2 = m_e = 4\pi\epsilon_0 = 1$)

$$H(\vec{r}_1, \vec{r}_2, t) = H_I(\vec{r}_1, t) + H_I(\vec{r}_2, t) + \frac{1}{|\vec{r}_1 - \vec{r}_2|}, \tag{6.1}$$

with the ionic Hamiltonian

$$H_I(\vec{r}, t) = -\frac{\Delta}{2} - \mathrm{i}\vec{A}(t) \cdot \vec{\nabla} - \frac{2}{r}. \tag{6.2}$$

Interaction with the laser is described in dipole approximation and velocity gauge, where $\vec{A}$ is defined below.

For numerically solving the TDSE and for computing spectra we use the time-dependent recursive indexing (tRecX) code [96]. tRecX implements the time-dependent surface flux (tSurff) method [93, 139] (see also Refs. [54, 94, 95, 109, 119, 189, 190]), infinite range exterior complex scaling (irECS) [84, 150], and FE-DVR methods [145]. In brief, the full two-electron calculation is restricted to within a surface radius $|\vec{r}_1|, |\vec{r}_2| \leq R_s$ with irECS absorption beyond R_s. tSurff is based on the idea that beyond R_s all interactions can be neglected and spectra are reconstructed from the time-evolution of values and derivatives on a four-dimensional hypersurface $|\vec{r}_1| = |\vec{r}_2| = R_s$. Expansions into single-particle angular momenta and FE-DVR radial functions are used. The most critical convergence parameter is R_s and, to a lesser degree, the number of angular momenta. All convergence parameters were varied systematically to ensure sufficient accuracy. In the majority of calculations angular momentum quantum numbers $l_i = 0, \ldots, 19$ and $|m_i| \leq 1$ were used for each electron. The convergence with R_s was studied using values up to 80 arb. units For the bulk of calculations we found $R_s = 40$ to suffice, except for joint angular distributions, where full convergence requires simultaneous increase of angular and radial discretization to unreasonable sizes. With that we obtain a He ground state energy of −2.902 with $|m_i| \leq 1$ and the three decimal digits exact value of −2.903 with $|m_i| \leq 2$. In the FE-DVR an 18 point Lobatto quadrature rule for was used with an average grid spacing of 0.6 arb. units. up to R_s, followed by a 15 point rule for exponentially damped polynomials with complex scaling for absorption. We ensured that for a given R_s the discretization error is negligible on the accuracy level discussed here. Except for the replacement of the exact FE-basis with the computationally more efficient FE-DVR grid, mathematical and numerical background of tRecX as well as procedures employed to assess convergence are described in full detail in Ref. [54].

Alternative to extracting single emission spectra from the full two-electron calculation, we also used a single-active-electron model with the Hamiltonian

$$H_M(t) = -\frac{\Delta}{2} - \mathrm{i}\vec{A}(t) \cdot \vec{\nabla} - \frac{1 + e^{-2.135r}}{r}, \tag{6.3}$$

where the screening factor is chosen as -2.135 to obtain the ionization potential $I_p = 0.903$ arb. units. This simple model largely reproduces results from the full calculation, see below.

6.2.2 Differential spectra

Starting from the fully differential momentum spectrum $\sigma(\vec{p}_1, \vec{p}_2)$ we compute various partially differential spectra.

The co-planar joint angular distributions (JADs) at given energy sharing $\eta = (E_1, E_2)$, $E_i = p_i^2/2m_e$ are defined by choosing the first electron at θ_1 and taking into account cylindrical symmetry, i.e.

$$JAD(\theta_2) = \sigma(p_1, \theta_1, 0, p_2, \theta_2, \varphi_2) \tag{6.4}$$

with $\varphi_2 = 0$ for $\theta_2 \in [0, \pi]$ and $\varphi_2 = \pi$ for $2\pi - \theta_2 \in [0, \pi]$. For experimentally realistic JADs we average over a small energy region ±0.3 eV, which is comparable to the spectral width of the pulses used here.

Joint distributions of momentum in polarization- (z-) direction and joint energy distributions are defined as

$$\sigma(p_{1z}, p_{2z}) = \int dp_{1x} dp_{2x} dp_{1y} dp_{1y} \sigma(\vec{p}_1, \vec{p}_2) \tag{6.5}$$

$$\sigma(E_1, E_2) = p_1 p_2 \int d\Omega_1 d\Omega_2 \sigma(\vec{p}_1, \vec{p}_2), \tag{6.6}$$

where $d\Omega_i$ is the integration over the solid angle of $\vec{p}_i$. B2B emission is the the part of $\sigma(p_{z1}, p_{z2})$ with opposite signs of the p_{zi}, and SBS with equal signs.

For studying correlation in double electron emission we introduce the correlation ratio Γ of B2B to SBS emission

$$\Gamma := Y_-/Y_+, \tag{6.7}$$

$$Y_\pm = \iint_0^\infty dp_{z1} dp_{z2} [\sigma(p_{z1}, \pm p_{z2}) + \sigma(-p_{z1}, \mp p_{z2})], \tag{6.8}$$

where larger Γ indicates more B2B emission. We would like to mention that, numerically, values of Γ here is from Eq. 4.9, see Sec. 4.1.2 and Eq. 6.7 here is for an easy interpretation.

We will further study the correlation at individual energy sharing points $\eta = (E_1, E_2)$ using the ratio Γ_η where the integration for $Y_\pm$ is restricted to a small region surrounding $p_{iz} = \sqrt{2 m_e E_i}, i = 1, 2$.

6.2.3 Laser pulses

The dipole field of a laser pulse with peak intensity $I = \mathcal{E}_0^2$ (atomic units) and linear polarization in z-direction is defined as $\mathcal{E}_z(t) = \partial_t A_z(t)$ with

$$A_z(t) = \frac{\mathcal{E}_0}{\omega} a(t) \sin(\omega t + \varphi_{CEP}). \tag{6.9}$$

The wave-length was chosen as exactly $\lambda = 394.5$ nm to match the experimental wave length used in Ref. [46], with the corresponding photon energy of $\hbar\omega \approx 3.14$ eV. For the pulse envelope $a(t)$ we used two different shapes: a "flat top" trapezoidal function with a linear rise and descent over a single optical cycle (1 opt.cyc. = $2\pi/\omega$) and constant amplitude in between. This somewhat unrealistic pulse shape is chosen to better isolate the intensity dependent effects of Freeman resonances. For examining the robustness and experimental observability of effects we chose $a(t) = [\cos(t/T)]^8$ as a more realistic envelope. Pulse durations are specified by the FWHM w.r.t. intensity. The carrier-envelope phase φ_{CEP}, in general, affects all non-linear processes. Highly differential observables such as the JADs show CEP-dependence for pulses as long as 14 optical cycles. However, yields and energy spectra vary only weakly with φ_{CEP}, reaching observable level only for single- or two-cycle pulses. We compare our results to an experiment with long pulses of FWHM > 7 Opt.Cyc, for which we demonstrate the absence of relevant CEP-dependence in selected cases. Unless indicated otherwise, calculations are for $\varphi_{CEP} = 0$.

6.2.4 Ponderomotive shifts and Freeman resonances

The ac-Stark shifts of ground and excited states differ, leading to intensity-dependent resonance conditions known as Freeman resonances [183]. In good approximation, the shift of excited states energies relative to the ground state is equal to the ponderomotive potential $U_p = \mathcal{E}_0^2/(4\omega^2)$, leading to the n-photon Freeman resonance condition

$$-E^{(g)} + E^{(x)} + U_p = n\omega, \tag{6.10}$$

where $E^{(g)}$ and $E^{(x)}$ are field-free ground and excited state energies of the He-atom. The validity of this formula for the present purposes was verified by Floquet calculations with the single-electron Hamiltonian Eq. (6.3).

Similarly, photo-electron peaks are shifted to lower energies by U_p as the ponderomotive potential of the continuum electron is not converted into kinetic energy due to the rapid passage of the pulse. The n-photon peaks in single- and double-emission appear at energies

$$S_n = n\omega - I_p^{(s)} - U_p \tag{6.11}$$

and

$$D_n = n\omega - I_p^{(d)} - 2U_p, \tag{6.12}$$

respectively, where $I_p^{(s)}$ and $I_p^{(d)}$ are the ionization potentials for single and double ionization. Note that for the pulse parameters used here, U_p reaches up to several photon energies.

6.3 Single electron emission

In the He atom, single-ionization at longer wave length is little affected by multi-electron effects. At 800 nm this had been observed for photoemission with linear [54] as well as elliptical polarization [119]. We find the same to hold at the present shorter wavelength. The difference in total yields obtained from model and full two-electron calculation is about 20%. After normalization, the shapes of the spectra agree within a few % in the energy range up to 100 eV. As the single ionization calculation can easily be pushed to complete convergence this also supports the correctness of the full calculation.

In Fig 6.1 we compare the spectral shapes at two sets of intensities, $3.5, 4.6, 5.7 \times 10^{14}$ and $5.7, 7.4, 9.2 \times 10^{14}\,\mathrm{W/cm^2}$, respectively, to three measured spectra from Ref. [46]. We verified that on the level of the comparison the exact pulse duration does not matter. The two sets of intensities are chosen w.r.t. the lowest intensity of $3.5 \times 10^{14}\,\mathrm{W/cm^2}$ of Ref. [46]: the difference of ponderomotive shifts at 3.5 and $5.7 \times 10^{14}\,\mathrm{W/cm^2}$ is approximately one photon energy. Photo-electron peaks at the two intensities are located at the same energies, just differing by one photon number. Choosing these two sets of intensities separated by a ponderomotive shift of $\hbar\omega$ is motivated by the procedure for determining intensities in Ref. [46], where at $3.5 \times 10^{14}\,\mathrm{W/cm^2}$ shape and peak positions of single-electron spectra were used to infer the on-target intensity. For such a procedure, given the incertainty of

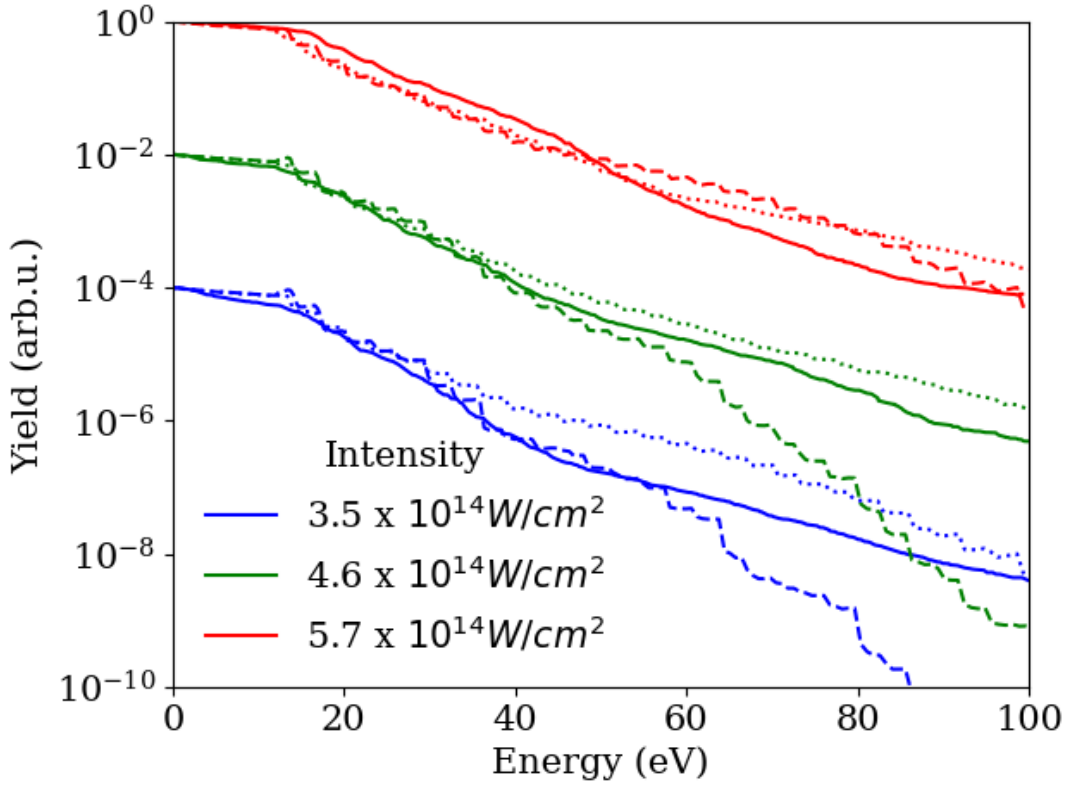

Figure 6.1: Single-electron energy spectra. Solid lines: experiment [46], dashed: TDSE, dotted: TDSE at intensities 5.7, 7.4 and $9.2 \times 10^{14}\,\mathrm{W/cm^2}$. Curves were smoothed over 4 photo-electron peaks, normalized, and offset artificially for visibility. The TDSE was solved for a $\cos^8$-pulse with duration 20 fs FWHM. The computed spectra are smoothed over 12 eV for easier comparison with experimental data.

the shapes, peak-positions remain ambiguous w.r.t. to ponderomotive shift. Both triplets of intensities will be used in further comparison with experimental data.

Somewhat surprisingly, for this rather simple observable the agreement is not satisfactory for either set of intensities. Strikingly, at 3.5 and $4.6 \times 10^{14}\,\mathrm{W/cm^2}$ the predicted pronounced cutoff is not found in the experimental data. The calculations at the higher set of intensities bear more similarity to the experimental data but agreement at the high photo-electron energies remains off by nearly an order of magnitude.

The difficulty in using single-electron spectra for intensity calibration is that the photoionization threshold shifts with intensity by one or several photon energies ($\hbar\omega$ = 3.14 eV) and channel closure occurs. For example, at intensity $4.6 \times 10^{14}\,\mathrm{W/cm^2}$ the 10-photon transition falls right onto the ionization threshold and at higher intensity a minimum of 11 photons is needed for ionization. If the signal is averaged over individual photo-electron peaks, the low-energy photo-electron spectrum appears to change shape rather erratically. If individual photoelectron peaks were resolved one should be able to reliably gauge the intensity with an ambiguity of multiples of $\hbar\omega$. For resolving that ambiguity one needs additional information: the checkerboard pattern observed in double emission (sec. 6.4.3) allows distinguishing even and odd photon counts, reducing ambiguity to multiples of two photon energies, $2\hbar\omega = 6.3$ eV.

The ambiguous comparison of the single-electron spectra precludes the use of these spectra for gauging the experimental intensity. The double emission calculations below suggest that the actual experimental intensities were higher than quoted in [46].

6.4 Double electron emission

6.4.1 Joint momentum distributions

In Fig. 6.2 we show the joint momentum distributions obtained at our two intensity sets and the corresponding data digitized from Ref. [46]. At the lower intensities from 3.5 to $5.7 \times 10^{14}\,\mathrm{W/cm^2}$ "back-to-back"(B2B) emission into the quadrants with opposite sign of the p_z-momentum is more prominent. This changes markedly at $9.3 \times 10^{14}\,\mathrm{W/cm^2}$, where the "side-by-side" (SBS) emission dominates. The same transition appears in experiment, although at a nominal intensity near $5 \times 10^{14}\,\mathrm{W/cm^2}$.

We note that the transition to dominantly SBS emission occurs at the intensities in the simulation where the energy of the recolliding electron approaches the threshold for excitation of He^+, cf. Ref. [45], see also Sec. 6.4.4. An inelastic collision at that threshold leaves both electrons at comparatively low momentum and unbounded or loosely bound, respectively. From such a state, acceleration by the laser into similar directions is favored.

6.4.2 Ratio of $He^{2+}$to He^+ yields

The question of experimental intensities also arises, when we consider the ratio He^{2+}/He^+ of the yields of total double to single ionization. Fig. 6.3 compares our simulations with the

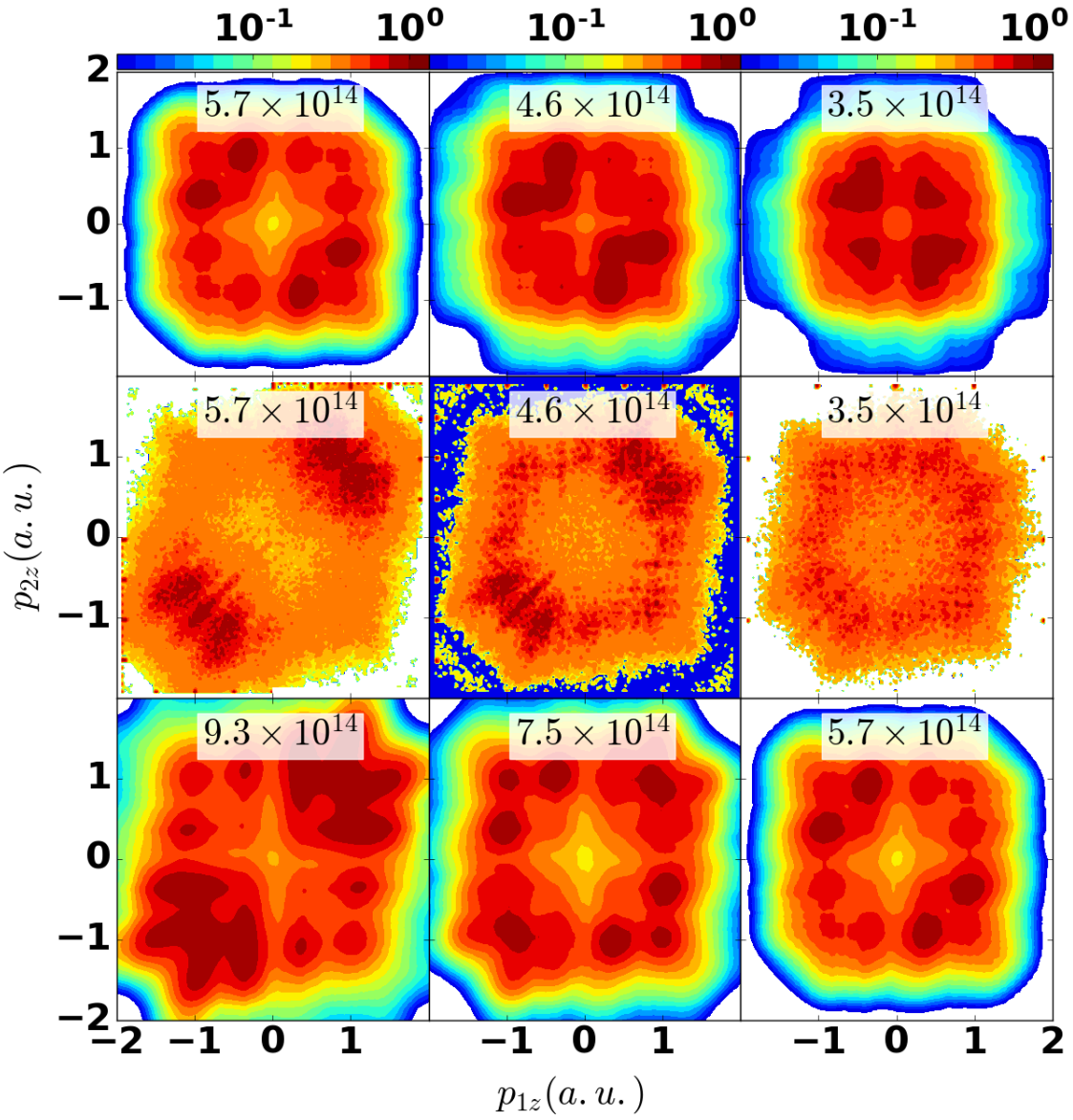

Figure 6.2: First row: computed spectrum with a 394.5-nm, $\cos^8$ pulse. Second row: measured spectra from Ref. [46] at nominally the same intensities as first row. Third row: computed spectra at a higher set of intensities. Computed data were smoothed for better visibility.

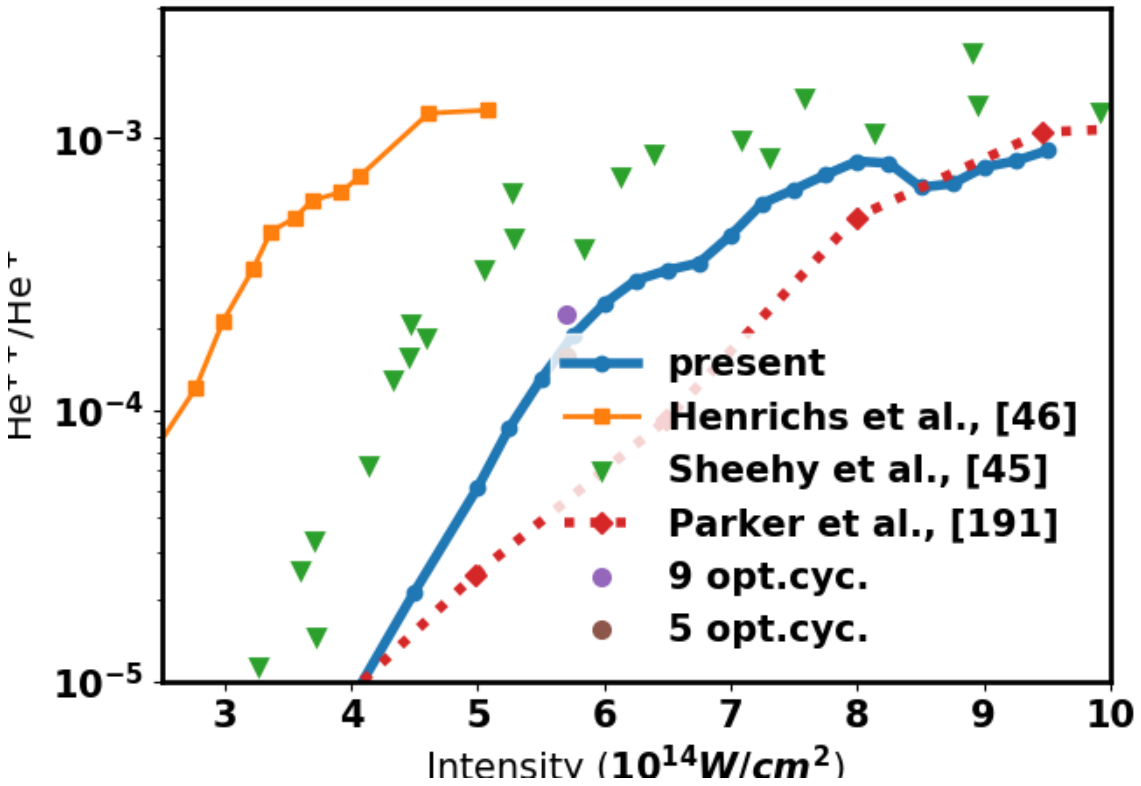

Figure 6.3: Ratios He^{2+}/He^{+} for $\lambda = 390$ nm from present calculation and literature values. Dotted blue line: 7 opt.cyc. FWHM, dots: (lower) 5 and (upper) 9 opt.cyc. FWHM.

experimental results from references [45] and [46]. In Ref. [45] intensities were calibrated using spot size measurements and Xe ionizaiton yields, with a reported uncertainty of approximately 25%. Our results suggest that the peak intensities in both experiments should be scaled to higher values, with about a factor two for Ref. [46]. The discrepancy to Ref. [45] was discussed in Ref. [46] considering in particular the shorter pulse duration used in[46]. For the bulk of our simulations we use short pulses of ~ 9 fs (7 opt.cyc. FWHM), even shorter than in Ref. [46]. As recollision occurs within one or at most two optical cycles, pulse-duration effects are expected to be small and mostly due to the wider spectrum of shorter pulses. Crosschecks at intensity $5.7 \times 10^{14}\,\mathrm{W/cm^2}$ show variations of ~ 20% as we change pulse duration from 5 to 9 opt.cyc., see Fig. 6.3.

Fig. 6.3 also includes results from the *ab initio* calculation [191], which are close to our results at most intensities. In Ref. [191] yields are accumulated outside a finite radius, which is in spirit comparable to the present tSurff calculation, but it differs by the use of flat-top pulses and by the actual extraction method, which plausibly accounts for the observed differences.

6.4.3 The checkerboard pattern

An interesting observation reported in Ref. [46] is the appearance of a "checkerboard" pattern in the energy distributions. In Fig. 6.4 we show joint energy spectra at two different intensities and line-outs of the spectrum along the 40 and 48-photon peaks according to Eq. (6.12) for B2B and SBS events separately. The line-outs highlight the modulation of the yield at energy differences $|E_1 - E_2| = 2n\hbar\omega$. In the line-out for the higher intensity of $5.7 \times 10^{14}\,\mathrm{W/cm^2}$ and 48 photons, modulation becomes weaker in the SBS events, but remains pronounced in B2B. These observations are consistent with Ref. [46], where the pattern was only observed in B2B and became washed out with intensity, although at nominally lower intensities.

In absence of interaction a trivial checkerboard pattern would appear in the emission of two electrons whenever there are photon-peaks in the emission of the individual electrons. This cannot be the primary cause for the pattern observed here, as independent ("sequential") emission of the electrons is several orders of magnitude less intense than the recollision induced double emission. In general, periodicity of emission modulates energy patterns at multiples of the photon energy, which is interpreted as photon counts and energy conservation, Eq. (6.12). In double emission this leads to distinct photon peaks in total energy, when contributions from subsequent optical cycles add constructively. The checkerboard pattern shows that the energy *difference* favors multiples of *twice* the photon energy, $E_1 - E_2 = 2n\hbar\omega$. This is the signature of a process that occurs repeatedly at 1/2 of the optical period. As it appears in the two electrons' relative energy, it suggests repeated exchanges of energy between at a time separation of 1/2 optical period. With recollision as main mechanism for double ionization at the given parameters, we interprete the modulation as a signature of multiple collisions of the electrons during the ionization process. Such multiple recollisions were suggested for double-ionization [186–188], being more dominant at lower energies and favoring B2B emission. The energy modulation shown in Fig. 6.4 supports these classical predictions. The fact that the pattern appears in experiment in B2B but non in SBS emission [46] also fits the picture. The checkerboard pattern is not qualitatively affected by the exact of $\phi_{CEP} = 0$, see Fig. 6.4.

6.4.4 Correlation and Freeman resonances

Fig. 6.5 shows the correlation ratio Γ, Eq. (6.7), and the total double-ionization yields for intensities from 2.5 to $7 \times 10^{14}\,\mathrm{W/cm^2}$. In both curves we see peaks when lowest excited energies $E^{(x)}$ shift into Freeman resonance, Eq. 6.10. The curves are calculated with a 9 opt.cyc. $\sim 12\,fs$ flat top pulse. A few additional points were calculated with a pulse duration of 15 opt.cyc.: Γ is further enhanced and while it drops slightly off-resonance, as to be expected.

An overview of the dependence of Γ_η on the photo-electron energies for 4 different intensities is shown in Fig. 6.6. We see that in general points of non-equal energy sharing are more B2B, $\Gamma_\eta > 1$. This TDSE result supports the prediction of preferred B2B emission at non-equal energy sharing [187, 188] based on the analysis of classical trajectories. The clas-

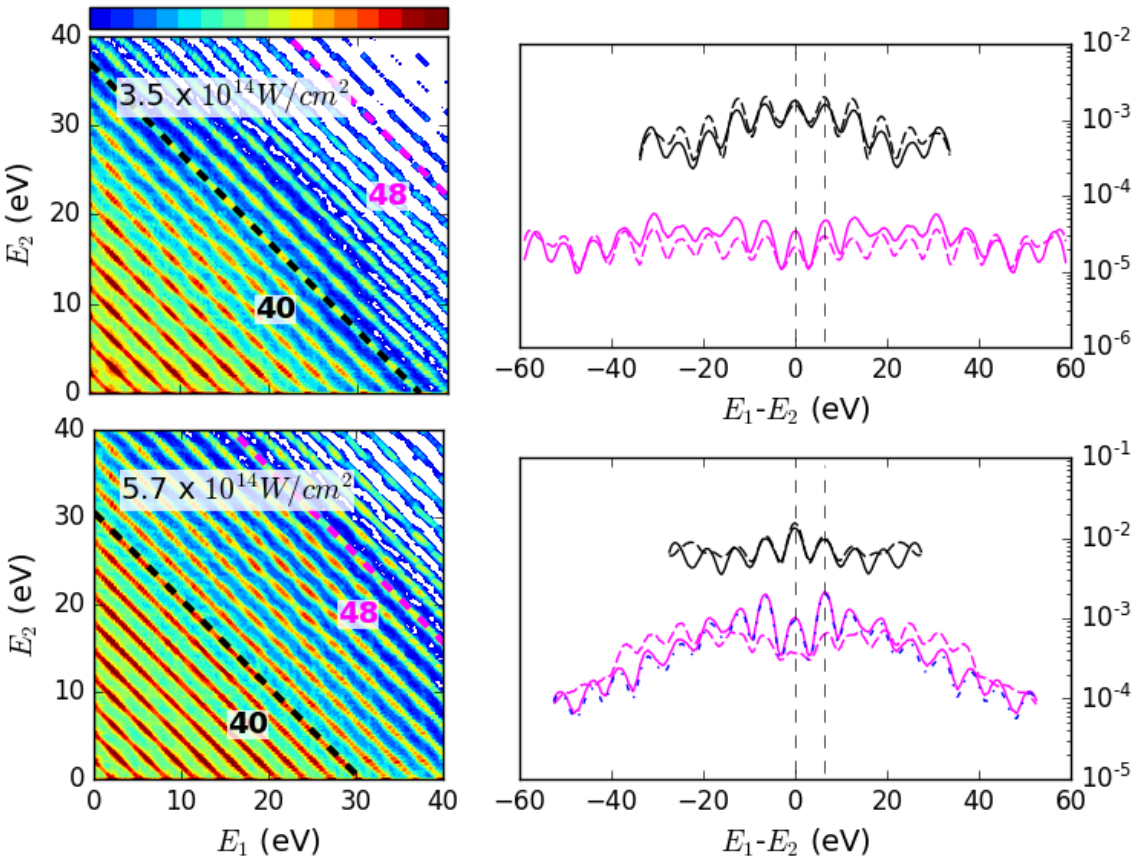

Figure 6.4: Modulation of two-electron emission by the photon-energy. Left column: $\sigma(E_1, E_2)$ for intensities 3.5 and 5.7×10^{14} W/cm^2 for a flat-top pulse with FWHM=14 opt.cyc.. Right column: line-outs at 40 (upper, black in each figure) and 48 (lower, magenta in each figure) absorbed photons. Solid line is for B2B, dashed is SBS, vertical dashed lines indicate two-photon spacing, the $\sigma(E_1, E_2)$ are normalized to maximum = 1. The lower right panel also includes the modulation for $\phi_{CEP} = \pi/2$ (dashed dotted blue line), which nearly coincides with the result for $\phi_{CEP} = 0$ (solid magenta line).

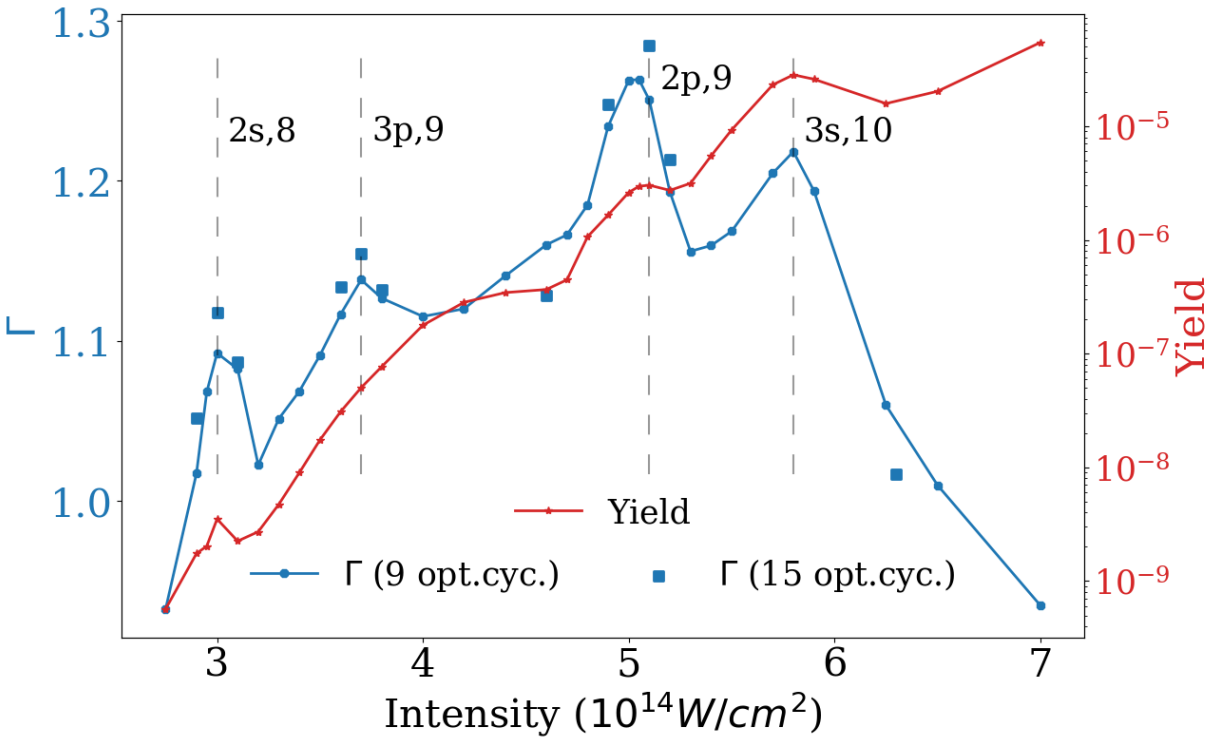

Figure 6.5: Correlation ratio Γ and total DI yield as a function of laser intensity. Dotted blue line: Γ for 9 opt.cyc., dots: 15 opt.cyc., squared red line: DI yield. The dashed lines labeled by nl, N indicate the N-photon Freeman resonance positions with the nl state. A flat-top pulse was used.

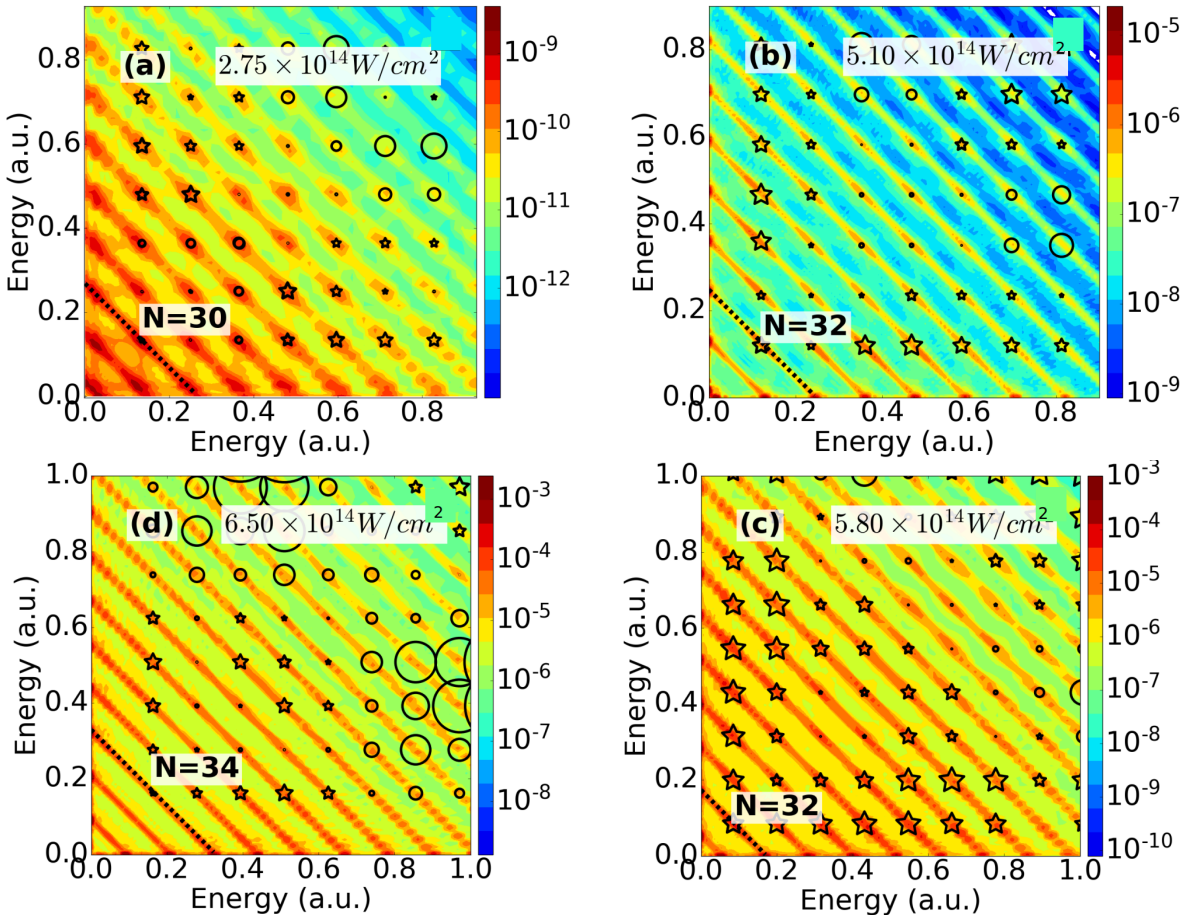

Figure 6.6: Joint energy distributions for four different intensities. Circles indicate more SBS emission, $\Gamma_\eta < 1$, stars indicate more B2B, $\Gamma_\eta > 1$ at $\eta = (E_1, E_2)$ and the size of the symbols indicates pronouncement of the effect. (a) and (d) without Freeman resonance, (b) and (c) on resonance, see also Fig. 6.5. The black lines labeled by N indicate N-photon energy peaks in $E_1 + E_2$.

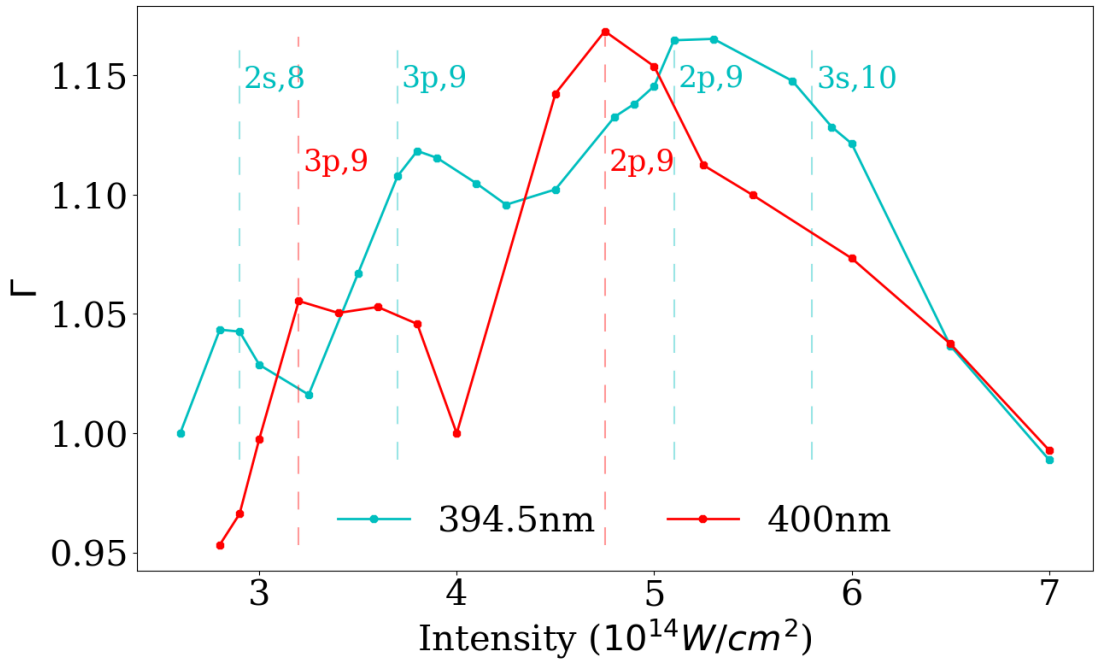

Figure 6.7: Correlation ratio Γ as a function of laser intensity with a $\cos^8$ pulse, FWHM=7 opt.cyc. pulse with λ at 394.5 nm and 400 nm. The dashed lines labeled by nl, N indicate the N-photon Freeman resonance positions with the given excited state at the respective wave length.

sical simulations were interpreted by taking into account the modification of the classical potential by the simultaneous action of the re-approaching electron and the laser field. In more quantum mechanical language this is excitation simultaneous with tunneling and/or over barrier ionization. The mechanisms are distinguished from the conventional idea of RESI (resonant excitation with subsequent ionization) in that excitation and ionization happen within the time-frame of a given recollision. In contrast, in RESI the two single ionizations would ultimately occur without narrow correlation in time and leave emission directions largely independent.

A more precise mapping of the mechanisms onto quantum mechanics is difficult: both, the presence of a rather strong field and the brevity of the interaction deprives individual states of their identity. Wavefunctions can, with great success, be associated with trajectories at larger distances from the nucleus, but the mapping breaks down as one approaches to within the range of the electrons' de-Broglie wave lengths. Still, the behavior of B2B emission corroborates the essence of Refs. [187, 188]: the contribution from "double-emission upon recollsion" (DUR) is important, in addition to a possible RESI background.

Fig. 6.5 was computed with flat-top pulses for better exposure of the mechanism, but Freeman peaks in B2B emission also appear with the more realistic $\cos^8$ pulse envelope, as shown in Fig. 6.7.

Freeman resonances do not appear in classical simulation, as they depend on the quan-

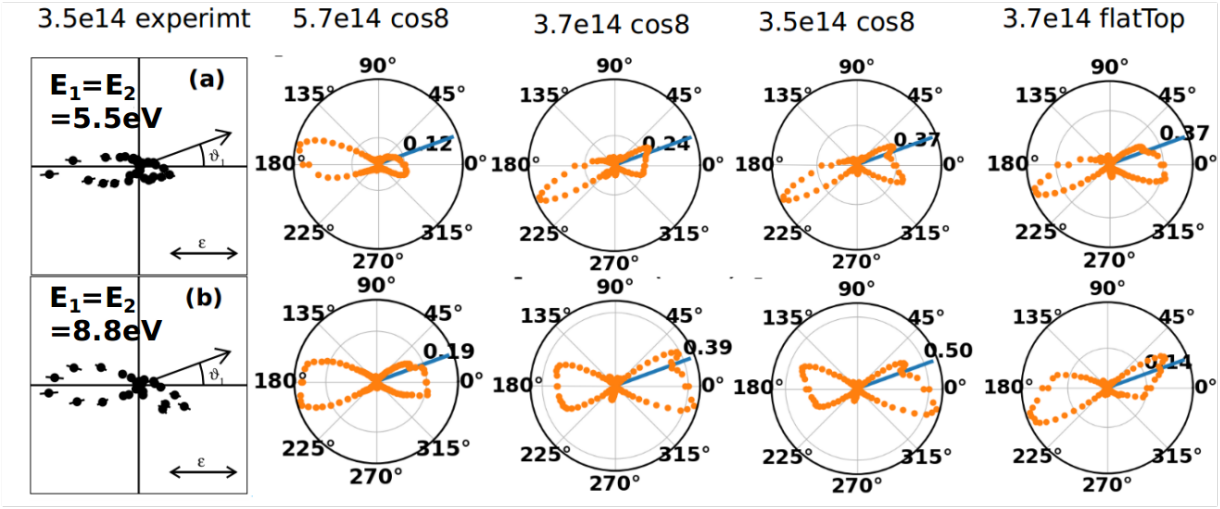

Figure 6.8: JADs from Ref. [46] (leftmost) and present simulations at energies $E_1 = E_2 = 5.5$ eV (upper row) and = 8.8 eV (lower row). Direction of the first electron (blue lines) is fixed at $\theta_1 = \pi/6$ relative to the polarization axis. Intensities and pulse shapes are indicated above the respective columns. The distributions are averaged over ±4° and normalized to maximal emission 1. A flat-top pulse (last column) does significantly, but not qualitatively change the JAD.

tization of excitation energies. Resonance implies in particular that there is a well-defined photon energy and that the process spans several optical periods. In such a mechanism, standard multi-photon type excitation is followed double-ionization from the excited state. The fact that Freeman resonances enhance B2B emission indicates that that mechanism is of DUR-type.

6.4.5 Joint angular distributions

JADs strongly depend on the total energy, the energy sharing between the two electrons, and on the laser parameters. Fig. 6.8 reproduces two JADs from Ref. [46] together with our results. For illustration we have chosen two points with equal energy sharing $E_1 = E_2$ at 5.5 and 8.8 eV, respectively. Experiment and simulation agree in showing clear angular anti-correlation. Near intensity 3.5×10^{14} W/cm^2, the JAD bends into the lower half plane, away from the first emitted electron. At the higher intensity of 5.7×10^{14} W/cm^2 anti-correlation is less pronounced and shapes are more similar to the experimental ones. Apart from that general qualitative behavior, the spectra vary significantly with the exact pulse shape and intensity. Because of the high sensitivity to intensities, e.g. comparing 3.5 and 3.7×10^{14} W/cm^2, a more detailed comparison of computed JADs with experiment is not possible at this point.

By studying the convergence with increasing R_s we see that the bulk of correlation effects originates at distances $\lesssim 30\,au$ from the nucleus. Fig.6.9 shows the convergence of

the correlation ratio Γ and the maximal relative error of the energy-integrated angular distributions

$$\epsilon_{JAD} = \max_{\theta_1,\theta_2} \frac{|\sigma(\theta_1,\theta_2) - \sigma^n(\theta_1,\theta_2)|}{\sigma(\theta_1,\theta_2)}, \tag{6.13}$$

where σ^n refers to results obtained with the next smaller box size. While Γ is converged for the purpose of the present argument, convergence of the JADs remains delicate, but qualitatively correct results may be expected at interaction ranges $R_s \gtrsim 40$.

6.4.6 Double-emission by short pulses

We also investigated double emission by extremely short pulses of 2 fs FWHM with the purpose of identifying a signature of the "slingshot" mechanism for B2B emission which was proposed in [171]. In that mechanism, the first electron reverts momentum in a close encounter ("slingshot"), while the second electron is emitted with some delay that results in B2B emission. Ref. [171] reports pronounced B2B emission at the pulse duration of 2 fs and intensity $5 \times 10^{14}\,\mathrm{W/cm^2}$ as a signature of the mechanism. Fig. 6.10 compares that classical finding with our TDSE simulations. The result for $5 \times 10^{14}\,\mathrm{W/cm^2}$ favors unequal energy sharing, which is characteristic of a DUR process. In contrast, the $3 \times 10^{14}\,\mathrm{W/cm^2}$ result bears great similarity with the classical simulation with more weight on equal energy sharing.

While our finding does not rule out the slingshot mechanism at $5 \times 10^{14}\,\mathrm{W/cm^2}$, it indicates important double ionization through alternative pathways with unequal energy sharing. Note that we use the exact same pulse as in Ref. [171].

The slingshot mechanism may be dominating at the lower intensity. However, attempts to trace the classical motion of the two electrons studying time-dependent spatial correlations in the quantum wave function failed due to the general difficulty of such a mapping. In addition, we remark that the very large band width of the 2 fs pulse admits lower order multi-photon ionization, which erodes the quasi-static tunneling picture employed for initial ionization in the classical model. Also, by their very construction, classical calculations do not account for effects of the quantum mechanical structure of the atom, as for example, the Freeman resonances discussed above.

6.5 Conclusions

The *ab initio* quantum mechanical calculations of single- and double-emission confirm the generally important role of DUR-type double-ionization, where the second ionization is simultaneous with the recollision, if we accept the enhancement of B2B emission as a signature of the process. This is supported also by the relatively stronger B2B emission at spectral points with large differences between electron energies. Further differentiation of the classical mechanisms is hampered by the fact that Freeman resonances add a genuine quantum aspect to the discussion and that the individual classical mechanisms involve

concepts such as classification of individual trajectories or exact release times, for which at present no quantum correspondence exists.

Comparing with recent experimental results on double emission spectra [46], we find good qualitative agreement, if we allow for an increase of experimental intensities by a factor ~ 2. Such an adjustment is suggested by three different and largely independent observables: the He^{2+}/He^{+} ratio, the dependence of B2B emission on intensity, and the intensity where the checkerboard pattern in joint-energy distributions fades.

Unfortunately, the ambiguity of intensity could not be resolved using the single-electron spectra published in [46]: this observable can be computed easily and with great reliability, but we were unable to establish convincing agreement at any set of intensities. Again higher than the experimental intensities appear to be favored.

We have not considered volume averaging over intensities when comparing to the experimental results. One reason is that the experimental arrangement of Ref. [46] managed to strongly reduce the effect by collimating the atomic beam, which makes contributions from half of the peak intensity appear unlikely. Also, averaging effects would exacerbate the disagreement with experiment, as even higher peak-intensities would be needed achieve a given yield. In general, considering the near-exponential drop of yields at our lower intensities, e.g. in Fig. 6.3, we expect only minor effects from volume averaging, mostly by Stark-induced broadening and displacement of the peaks. Such effects should be re-examined when comparing to experimental data exhibiting sufficient detail.

For JADs we can clearly identify the effect of electron repulsion, analogous to what was reported in [46]. Comparison with experiment beyond that general level is made difficult by the sensitivity of the JADs to intensity, carrier-envelope phase, pulse-duration, and exact pulse shape. On the computational side, for reliable convergence of JADs one needs to take into account the interaction between electrons over large spatial regions, which inflates tSurff computations to large scale.

Finally we offer a simple explanation for the checkerboard pattern noted in [46], which also appeared in earlier simulations at 800 nm [54]: the modulation at energy-differences of $2\hbar\omega$ means that the underlying process involves periodic re-encounters of the two electrons at one-half of the optical period, i.e. multiple recollisions.

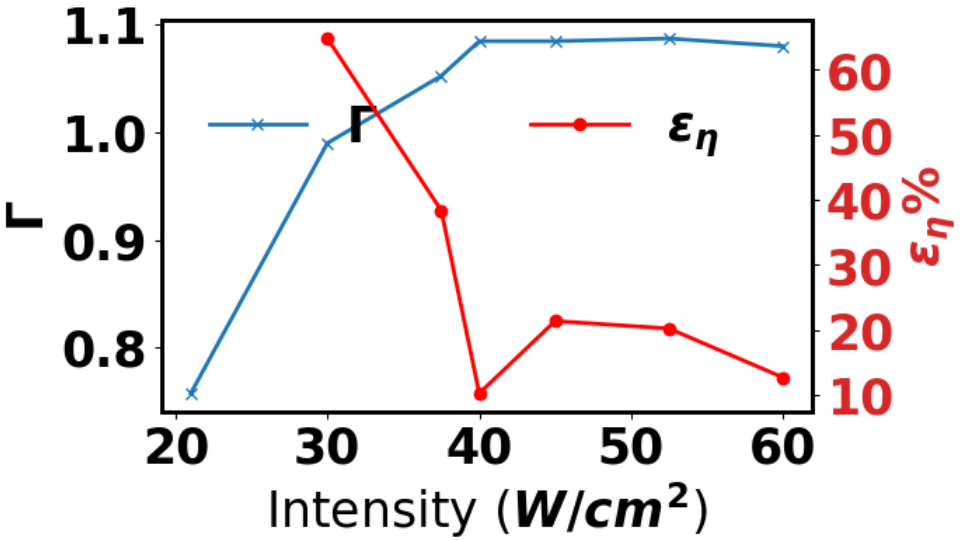

Figure 6.9: Convergence of Γ and JADs with the radius R_s of the interaction region. Calculations at 5×10^{14} W/cm^2 and FWHM of 2 fs. ϵ_{JAD} is the maximal relative error of the JADs, Eq. (6.13).

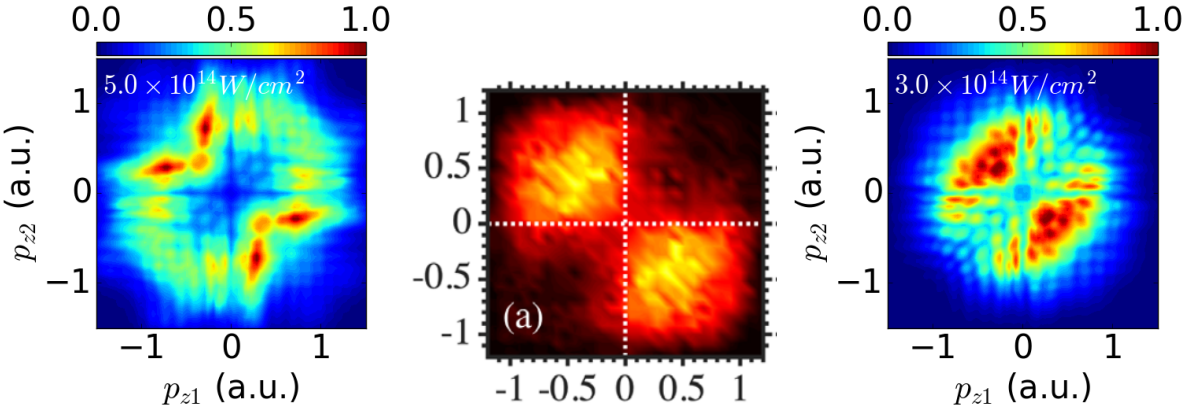

Figure 6.10: Joint momentum distributions in p_z-direction at FWHM 2fs and intensity averaged over carrier-envelope phase. Center: classical trajectory calculation at 5×10^{14} W/cm^2, reproduced from Ref. [171], Fig.1(a). Left: TDSE result for 5×10^{14} W/cm^2, right: TDSE for 3×10^{14} W/cm^2. Densities are normalized to a maximal value of 1.

Chapter 7

Conclusion and outlook

7.1 Methods

With the tSurff method, one can simulate the electron dynamics in an intense laser field by solving the TDSE with a limited radial extension. The tSurff method not only is available for computing photoelectron spectra of single-electron system, but also is extended to the double ionization of a Helium atom and single ionization of polyelectron molecules. Our new tRecX code numerically implements FE-DVR for radial discretization which creates a diagonal overlap matrix that speeds up the computation. The armchair constraints on angular momenta for two-electron basis functions, irECS for the absorber and 4th order Runge-Kutta for time propagation are also introduced. A general procedure for parallelization of the time propagation of any dimensions is presented, and the computation for double-emission photoelectron spectrum with 128 momentum grid points is scaled at maximum by a factor of 6.

Convergence behavior of double-emission photoelectron spectra highly depends on the type of observables; we can get a convergent correlation ratio from the overall B2B to SBS emissions, but the quantitative convergent JAD spectra at different electron energies are yet not possible.

7.2 Single ionization

The static field ionization of helium hydride ion by haCC shows the expected exponential increase of the ionization rate with the linearly increasing field strength, and ionization from helium side is favorable.

We also do computations on single ionization of helium atoms. First, the single-ionization photoelectron spectra of a helium atom exposed to flat-top envelope laser pulses are computed. The photoelectron spectra are enhanced at certain intensity-and-wavelength pairs. Second, the AC Stark shift of the eigenenergies are investigated by Floquet analysis. The stable eigenenergies with intensities are obtained by irECS and plotted for an overview. Evolution of the target excited eigenenergies are computed using inverse itera-

tion method. The above-mentioned analysis shows that the excited eigenenergies up-shift U_p and the ground eigenenergy is invariant with the intensity of the laser. The eigenenergies of s orbitals slightly violate this behavior. The resonance condition is satisfied when the eigenenergy difference of an excited state E_{3p} ($E_{2,\,l=1}$) and the ground state E_{1s} (E_0) is $N\Omega$. The population analysis shows the adjacent orbitals $3s$ and $3d$ have the largest population after time-propagation when the resoannce condition is satisfied. Finally, the resonance criteria $E_{3p} - E_{1s} + U_p = N\Omega$ is ensured by spectra calculation with many other wavelengths and intensities, as well as different pulse shapes.

7.3 Double ionization

We did computations on double ionization of helium atom using a 400 nm laser pulse. The DUR-type double emission is confirmed by the single and double ionization computation by solving TDSE, if we accept that the enhancement of B2B emission at spectra points where large differences between electron energies is a signature of DUR. Qualitative good agreement with the experimental results of double emission spectra [46] is obtained if the intensities from their experimental observations are increased by a factor ~ 2. This adjustment is supported by three different largely independent observables: the He^{++}/He^{+} ratio, the dependence of B2B emission on intensity, and the intensity where the checkerboard pattern in joint-energy distributions fades. However, the ambiguity of intensity could not be resolved using the single-electron spectra in Ref. [46]. We can clearly identify the effect of electron repulsion by computed JADs, analogous to what was reported in Ref. [46].

We find that the given pulse parameters Freeman resonances affect the double emission in general and that they disproportionally enhance B2B emission. Taking B2B emission as an indicator for a DUR mechanism, this suggests that DI through a Freeman resonance is primarily DUR. A simple explanation of checkerboard pattern noted in Ref. [46] is given: the modulation at energy-differences of $2\hbar\omega$ indicates periodic re-encounters with two electrons at one-half of the optical period, i.e. multiple recollisions. The is consistent with DUR if multiple contributions to double-ionization originate only from close approaches.

7.4 Outlook

The effort in theory by numerical simulations paves way for understanding attosecond process, offering supplementary information to the experimental observation, bringing us a step closer to the underlying physics. With the development of the computers and new computational methods, the simulation of the behaviors of electrons in molecules or even solids are available, and the gap between the theory and experiments are filled.

Appendix A

Methods

A.1 Atomic Units

The atomic units are critical for the notational brevity in quantum mechanics. By forcing $\hbar = e^2 = m_e = 4\pi\epsilon_0 \equiv 1$, the units of the physical variables are

Unit	Definition	Numerical Value
Length	$\alpha_0 = \frac{(4\pi\epsilon_0)\hbar^2}{m_e e^2}$	0.052917 nm
Velocity	$v_0 = \frac{e^2}{(4\pi\epsilon_0)\hbar c}$	$c/137.035$
Time	$\tau_0 = \frac{\alpha_0}{v_0}$	$24.188 \times 10^{-18} s$
Energy	$E_h = 2\mathrm{Ry} = \frac{e^2}{(4\pi\epsilon_0)\alpha_0}$	27.211 eV
Field Strength	$\varepsilon_0 = \frac{E_h}{e\alpha_0}$	$5.1422 \times 10^{11} V/m$
Intensity	$I_0 = \frac{\varepsilon_0^2 \epsilon_0 c}{2}$	$3.50944 \times 10^{16}\,\mathrm{W/cm^2}$

Table A.1: Relevant physical variables for describing electron dynamics in the laser field represented by atomic units. Vacuum permittivity and speed of light are denoted by ϵ_0 and c, respectively.

A.2 Typical energies

This section demonstrates three typical energies of electrons in a classical model. Suppose the external field is a continuous wave (cw) field with $E(t) = E_0 \cos\omega t$ and vector potential $A_0 = \frac{E_0}{\omega}$. The vector potential $A(t)$ and the electric field $E(t)$ satisfies

$$A(t) = -\int_{-\infty}^{t} E(t')dt' \tag{A.1}$$

where $A(-\infty) = A(\infty) = 0$. The integration of the electric field is

$$A(t) - A(t_0) = \int_{t_0}^{t_1} E(t')dt'. \tag{A.2}$$

Thus, the momenta satisfies

$$v(t) - v(-\infty) = \int_{-\infty}^{t} E(t')dt' = A(t). \tag{A.3}$$

ponderomotive energy U_p

The ponderomotive energy represents the averaged energy a particle acquires from the external field. The maximum acceleration of an particle from times when $\varepsilon(t) = 0$ contributes the maximum momenta

$$p_{\max} := \frac{\epsilon_0}{\omega} = A_0, \tag{A.4}$$

and the maximum energy is

$$\frac{p_{\max}^2}{2} = \frac{\varepsilon_0^2}{2\omega_0^2} = \frac{A_0^2}{2} = 2U_p, \tag{A.5}$$

with

$$U_p = \frac{A_0^2}{4}. \tag{A.6}$$

the recollision energy

The re-collision condition

$$0 = z(t_0) - z(t_1) = \int_{t_0}^{t_1} v(t)dt = \int_{t_0}^{t_1} dt \int_{t_0}^{t} E(t')dt' \tag{A.7}$$

with the initial state $\dot{z}(t_0) = 0$, we have the re-collision condition

$$A(t_0)(t_1 - t_0) = \int_{t_0}^{t_1} A(t)dt, \tag{A.8}$$

where Eq. (A.2) is used. Thus, the re-collision energy is

$$\frac{\dot{z}^2}{2} = \frac{|A(t_1) - A(t_0)|^2}{2}. \tag{A.9}$$

With the constraint by Eq. (A.8), $A(t_1)$ and $A(t_0)$ can not get the maximum A_0 at the same time. With the numerical calculation, the maximum recollision energy exists with $\omega t_0 \approx -0.45 \times 2\pi$ and $\omega t_1 \approx 0.2 \times 2\pi$, and the maximum re-collision energy is $3.17U_p$.

the $10U_p$ cutoff

Assuming the particle ionizes at t_0 with initial momenta 0 and re-collides at t_1, where the re-collision condition Eq. (A.8) is satisfied. The acceleration from t_0 to t_1 is

$$p(t_0, t_1) = A(t_1) - A(t_0) \tag{A.10}$$

and the acceleration from t_1 to ∞ is

$$p(t_1, \infty) = A(\infty) - A(t_1) = -A(t_1). \tag{A.11}$$

If the particle does not scatter with the system at t_1, the final momenta is simply

$$p_{\text{final}} = p(t_0, t_1) + p(t_1, \infty) = -A(t_0). \tag{A.12}$$

And if the particle elastically scatters at t_1 to the opposite direction, we have the final momenta

$$p_{\text{final}} = -p(t_0, t_1) + p(t_1, \infty) = -2A(t_1) + A(t_0). \tag{A.13}$$

With the constraint in Eq. (A.8), the numerical solution for the maximum energy gives

$$E_{\max} = \frac{p_{\text{final}}^2}{2} \approx 10U_p, \tag{A.14}$$

which serves as a cutoff energy in many spectra.

A.3 Polynomials

A.3.1 Associated Legendre functions

The associated Legendre polynomials in this thesis are written as

$$P_l^m(x) = (-1)^m (1 - x^2)^{m/2} \frac{d^m}{dx^m}(P_l(x)), \tag{A.15}$$

which satisfies

$$P_l^{-m}(x) = (-1)^m \frac{(l-m)!}{(l+m)!} P_l^m(x). \tag{A.16}$$

The associated Legendre polynomials that are also used in literatures $P_{l,m}$ can be written as

$$P_{lm}(x) = (-1)^m P_l^m(x). \tag{A.17}$$

$P_l(x)$ are Legendre polynomials.

A.3.2 Spherical harmonics

In this thesis, the spherical harmonics are written as

$$Y_l^m(\theta, \phi) = \sqrt{\frac{2l+1}{4\pi} \frac{(l-m)!}{(l+m)!}} P_l^m(\cos\theta) e^{\mathrm{i}m\phi}, \tag{A.18}$$

where $P_l^m(\cos\theta)e^{\mathrm{i}m\phi}$ are associated Legendre polynomials, and orthogonality is satisfied

$$\int d\phi \int d\theta \sin\theta Y_l^m(\theta, \phi) Y_{l'}^{m'*}(\theta, \phi) = \delta_{l,l'}\delta_{m,m'}. \tag{A.19}$$

The complex conjugate form of spherical harmonics satisfy

$$Y_l^{m*}(\theta, \phi) = (-1)^m Y_l^{-m}(\theta, \phi), \tag{A.20}$$

where Eq. (A.17) is used.

A.4 Pulse envelope

A.4.1 Formula

The laser pulse has no direct current component and we can write the electric in the vector potential form as

$$\vec{A(t)} = -\int_{-\infty}^{t} d\tau \varepsilon(\tau), \tag{A.21}$$

where

$$A(-\infty) = A(\infty) = 0 \tag{A.22}$$

is satisfied.

In the linear, z direction polarized case, the vector potential can be written as

$$\vec{A(t)} = A_0(t)\sin(\omega t + \phi_{CEP})\hat{z}, \tag{A.23}$$

where ω is the photon energy, ϕ_{CEP} is the phase and $A_0(t)$ represents the shape of the envelope.

The frequently used envelopes in this thesis are Gaussian like envelope $\cos^8$

$$A_0^{(\cos^8)}(t) = A_{\max}\cos^8(\frac{\omega t}{8n}) = A_{\max}\cos^8(\frac{\pi t}{4n\tau}), \quad -2n\tau \le t \le 2n\tau \tag{A.24}$$

with smooth ramp-up and ramp-down and flat-top envelope with constant intensity for n optical cycles

$$A_0^{(\text{flat-top})}(t) = A_{\max} f_{\frac{n}{2}\tau,(\frac{n}{2}+n_r)\tau}(-t) f_{\frac{n}{2}\tau,(\frac{n}{2}+n_r)\tau}(t), \quad -(n_r+\frac{n}{2})\tau \le t \le (n_r+\frac{n}{2})\tau, \tag{A.25}$$

and n_r optical cycle cycle ramp-up and ramp-down, where τ is the optical period, $A_{\max}$ is the maximum vector potential solved from peak intensity, and $f_{\frac{n}{2}\tau,(\frac{n}{2}+n_r)\tau}$ is the truncation function defined in Sec. 2.2. The full widths at half maximum (FWHM) are $0.744n\tau$ for $\cos^8$ envelope with $t \in [-0.372n\tau, 0.372n\tau]$ and $(n+n_r)\tau$ for flat-top envelope with $t \in [-\frac{n_r+n}{2}\tau, \frac{n_r+n}{2}\tau]$. In this thesis, we use n to represent the FWHM of $\cos^8$ pulse for simplicity of inputs and set $n = 1$ with one optical cycle ramp-up and ramp-down for flat-top pulse.

For completeness, we also listed the commonly used envelope $\cos^2$ pulse

$$A_0^{(\cos^2)}(t) = A_{\max}\cos^2(\frac{\omega t}{2n}), \quad -\frac{n}{2}\tau \le t \le \frac{n}{2}\tau \tag{A.26}$$

with the same FWHM $n\tau$ as $\cos^8$ for $t \in [-\frac{n\tau}{4}, \frac{n\tau}{4}]$ with larger spectra width than $\cos^8$ and ideal Gaussian pulse

$$A_0^{(\text{Gaussian})}(t) = A_{\max}\exp(-2\ln 2(\frac{t}{\tau_0})^2), \quad -\infty \le t \le \infty, \tag{A.27}$$

where τ_0 is the FWHM of the pulse.

Although Gaussian pulse envelope well approximates the pulses in experiments, it is difficult to be applied in numerical calculations as it is hard to determine the start of the time propagation. Usually we use $\cos^8$ pulse shape for an approximation to Gaussian pulse shape which well approximates the Gaussian envelope even for short pulses, see Fig. A.1.

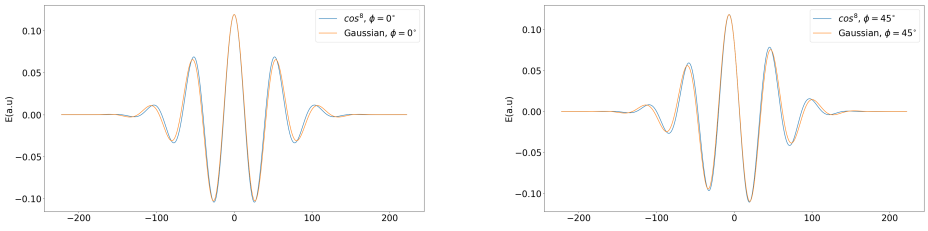

(a) $\phi = 0°$

(b) $\phi = 45°$

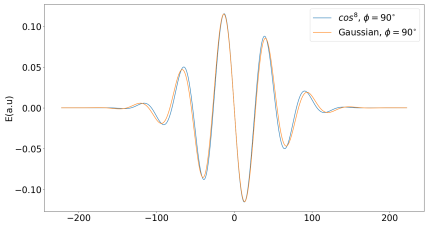

(c) $\phi = 90°$

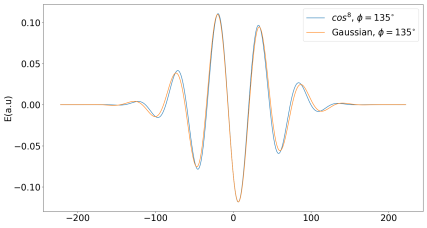

(d) $\phi = 135°$

Figure A.1: The $\cos^8$ envelope and Gaussian envelope comparison at different ϕs.

A.4.2 Comparison

In this section, we will use a short pulse for the comparison of $\cos^8$ and Gaussian type pulses, where one may easily find the difference. In Ref. [171], a 2 fs long, 400 nm, 5×10^{14} W/cm^2 Gaussian envelope with formula

$$E = E_0 \exp(-2 \ln 2 (t/\tau_0)^2) \cos(\omega t + \phi). \tag{A.28}$$

is used for calculation. The $\cos^8$ type cap is used to approximate the Gaussian type pulse for simplicity with the electric field

$$E = E_0 \cos^8(\pi t/(4n\tau)) \cos(\omega t + \phi) \tag{A.29}$$

where the E_0 is the maximum electric field, τ_0 is the pulse duration and where τ is the optical period and $n = 2$ for maximum numerical performance. The $\cos^8$ envelope approximates the Gaussian envelope well, see in Fig. A.1.

A.5 tSurff

A.5.1 Commutator expectation for 3D

With the wavefunction representation in spherical coordinate,

$$
\begin{aligned}
&\langle\chi_{\vec{k}}(t)|\left[H_V(t),\Theta(R_c)\right]|\psi(t)\rangle e^{-\mathrm{i}\Phi(\vec{k},t)}\sqrt{\frac{\pi}{2}}\frac{1}{R_c^2}\\
&=\sum_{l,m}(-\mathrm{i})^l Y_l^m(\Omega_k)\langle Y_l^m(\Omega_r)j_l(kr)|\left[H_V(t),\Theta(R_c)\right]|\sum_{l',m'}C_{l',m'}Y_{l'}^{m'}(\Omega_r)R_{l',m'}(r)\rangle\\
&=\sum_{l,m,l',m'}(-\mathrm{i})^l Y_l^m(\Omega_k)[\frac{1}{R_c^2}\langle Y_l^m(\Omega_r)|Y_{l'}^{m'}(\Omega_r)\rangle\\
&\quad\langle j_l(kr)|-\frac{1}{2}\frac{1}{r^2}\partial_r r^2\delta(r-R_c)-\frac{1}{2}\delta(r-R_c)\partial_r|R_{l',m'}(r)\rangle\\
&-(\mathrm{i}A_x\langle Y_l^m|\sqrt{1-\eta^2}\cos\phi|Y_{l'}^{m'}\rangle+\mathrm{i}A_z\langle Y_l^m|\eta|Y_{l'}^{m'}\rangle)j_l(kR_c)R_{l',m'}(R_c)]C_{l'.m'}(t)\\
&=\sum_{l,m}(-\mathrm{i})^l Y_l^m(\Omega_k)[-\frac{1}{2}(-\partial_r j_l(kr)|_{R_c}c_{l,m}(t)+j_l(kR_c)d_{l,m}))\\
&-\mathrm{i}A_x j_l(kR_c)\langle Y_l^m|\sqrt{1-\eta^2}\cos\phi\sum_{s_l=\pm1,s_m=\pm1}|Y_{l+s_l}^{m+s_m}\rangle C_{l+s_l,m+s_m}(t)\\
&-\mathrm{i}A_z j_l(kR_c)\langle Y_l^m|\eta\sum_{s_l=\pm1}|Y_{l+s_l}^m\rangle C_{l+s_l,m}(t)]
\end{aligned}
\tag{A.30}
$$

where $c_{l,m}\coloneqq R_{l,m}(R_c)C_{l,m}(t)$ and $d_{l,m}\coloneqq\partial_r R_{l,m}(R_c)C_{l,m}(t)$ are used for notational brevity. And we let $A_y=0$, assuming the laser propagate in y direction. For the linear polarization, Eq. (A.30) transforms to

$$
\begin{aligned}
&\langle\chi_{\vec{k}}(t)|\left[H_V(t),\Theta(R_c)\right]|\psi(t)\rangle e^{-\mathrm{i}\Phi(\vec{k},t)}\sqrt{\frac{\pi}{2}}\frac{1}{R_c^2}\\
&=\sum_{l,m}(-\mathrm{i})^l Y_l^m(\Omega_k)[\frac{1}{2}j_l'(kR_c)c_{l,m}(t)-\frac{1}{2}j_l(kR_c)d_{l,m}\\
&-\mathrm{i}A_z\sum_{s=\pm1}j_l(kR_c)\langle Y_l^m|\eta|Y_{l+s}^m\rangle C_{l+s,m}(t)].
\end{aligned}
\tag{A.31}
$$

With some algegra operation, we have

$$
\langle\chi_{\vec{k}}(t)\,|[H_V(t),\Theta(R_c)]|\,\psi(t)\rangle=\frac{e^{\mathrm{i}\Phi(\vec{k},t)}}{\sqrt{\pi/2}}R_c^2\sum_{l,m}(-\mathrm{i})^l Y_l^m(\Omega_k)(J_{lm}-\mathrm{i}A_z K_{lm}),
\tag{A.32}
$$

where

$$
J_{lm}\coloneqq\frac{1}{2}j_l'(kR_c)R_{lm}(R_c,t)-\frac{1}{2}j_l(kR_c)R_{lm}'(R_c,t)
\tag{A.33}
$$

and

$$
K_{lm}\coloneqq\sum_{s=\pm1}\langle Y_l^m(\theta,\phi)|\cos\theta|Y_{l+s}^m(\theta,\phi)\rangle j_l(kR_c)R_{l+s,m}(R_c,t)
\tag{A.34}
$$

.

A.6 Double ionization p_z spectra

In our code, the p_z spectrum is computed from $\sigma(\vec{k}_1, \vec{k}_2)$ from the square norm of the scattering amplitudes. The p_z spectra are used in chapter 4 and chapter 6. The code produces the norm square of scattering amplitudes for SI $\sigma(k, \theta, \phi) = |b(k, \theta, \phi)|^2$ and DI spectra $\sigma(k_1, k_2, \theta_1, \theta_2, \phi_1, \phi_2) = |b(k_1, k_2, \theta_1, \theta_2, \phi_1, \phi_2)|^2$, where k, k_1, k_2 are the momenta and $b(k, \theta, \phi)$, $b(k_1, k_2, \theta_1, \theta_2, \phi_1, \phi_2)$ are the scattering amplitudes. In this section we will show the method to produce the $\sigma^{Z,DI}(p_{1z}, p_{2z})$ in this thesis. Before showing the formula for $\sigma^{Z,DI}(p_{1z}, p_{2z})$ of the double ionization, we firstly show the transformation from the SI $\sigma(k, \theta, \phi)$ to the single $\sigma^{Z,SI}(p_z)$. Firstly we do the integration of the spectra as

$$\begin{aligned}
&\int_{-\infty}^{+\infty} dp_z \sigma^{Z,SI}(p_z) \\
&= \int_0^{2\pi} d\phi \int_0^{+\infty} dk k^2 \int_0^{\pi} d\theta \sin\theta \sigma(k, \theta, \phi) \\
&= \int_0^{2\pi} d\phi \int_0^{+\infty} dk \int_0^{\pi} d(-k\cos\theta) k \sigma(k, \theta, \phi) \\
&= \int_0^{2\pi} d\phi \int_0^{+\infty} dk \int_{-k}^{+k} dp_z k \sigma(k, \arccos\frac{p_z}{k}, \phi) \\
&= \int_{-\infty}^{+\infty} dp_z \int_0^{2\pi} d\phi \int_{|p_z|}^{+\infty} dk k \sigma(k, \arccos\frac{p_z}{k}, \phi),
\end{aligned} \tag{A.35}$$

Thus, we have

$$\sigma^{Z,SI}(p_z) = \int_0^{2\pi} d\phi \int_{|p_z|}^{+\infty} dk k \sigma(k, \arccos\frac{p_z}{k}, \phi). \tag{A.36}$$

It is easy to get that

$$\sigma^{Z,DI}(p_{1z}, p_{2z}) = \int_0^{2\pi} d\phi_1 \int_0^{2\pi} d\phi_2 \int_{|p_{1z}|}^{+\infty} dk_1 \int_{|p_{2z}|}^{+\infty} dk_2 k_1 k_2 \sigma(k_1, k_2, \arccos\frac{p_{1z}}{k_1}, \arccos\frac{p_{2z}}{k_2}, \phi_1, \phi_2). \tag{A.37}$$

Appendix B

Static field ionization rates of HeH^+

The static filed ionization rates of HeH^+ by haCC calculations are shown in table B.1.

Angle	0.10	0.11	0.12	0.13	0.14	0.15	0.16	0.17	0.18	0.19
Angle	0.10	0.11	0.12	0.13	0.14	0.15	0.16	0.17	0.18	0.19
0	1.28E-15	2.56E-13	7.59E-12	1.05E-10	9.11E-10	5.63E-09	2.69E-08	1.05E-07	3.45E-07	9.92E-07
15	1.32E-15	2.56E-13	7.57E-12	1.05E-10	9.07E-10	5.60E-09	2.67E-08	1.04E-07	3.43E-07	9.88E-07
30	1.45E-15	2.58E-13	7.56E-12	1.04E-10	8.98E-10	5.54E-09	2.64E-08	1.03E-07	3.39E-07	9.76E-07
45	1.71E-15	2.67E-13	7.63E-12	1.04E-10	8.92E-10	5.48E-09	2.61E-08	1.02E-07	3.35E-07	9.64E-07
60	2.05E-15	2.83E-13	7.86E-12	1.06E-10	9.00E-10	5.51E-09	2.62E-08	1.02E-07	3.35E-07	9.63E-07
75	2.52E-15	3.11E-13	8.35E-12	1.11E-10	9.36E-10	5.70E-09	2.70E-08	1.05E-07	3.45E-07	9.93E-07
90	3.51E-15	3.69E-13	9.47E-12	1.23E-10	1.03E-09	6.24E-09	2.95E-08	1.14E-07	3.75E-07	1.08E-06
105	5.27E-15	4.76E-13	1.17E-11	1.49E-10	1.23E-09	7.37E-09	3.46E-08	1.34E-07	4.38E-07	1.26E-06
120	7.72E-15	6.40E-13	1.53E-11	1.91E-10	1.57E-09	9.36E-09	4.38E-08	1.68E-07	5.51E-07	1.58E-06
135	9.94E-15	8.48E-13	2.03E-11	2.54E-10	2.08E-09	1.24E-08	5.76E-08	2.21E-07	7.21E-07	2.06E-06
150	1.16E-14	1.08E-12	2.64E-11	3.32E-10	2.71E-09	1.61E-08	7.49E-08	2.86E-07	9.30E-07	2.65E-06
165	1.29E-14	1.29E-12	3.18E-11	4.02E-10	3.28E-09	1.95E-08	9.02E-08	3.43E-07	1.11E-06	3.16E-06
180	1.34E-14	1.37E-12	3.41E-11	4.31E-10	3.52E-09	2.08E-08	9.64E-08	3.67E-07	1.19E-06	3.37E-06
Angle	0.20	0.21	0.22	0.23	0.24	0.25	0.26	0.27	0.28	0.29
0	2.54E-06	5.91E-06	1.26E-05	2.51E-05	4.68E-05	8.27E-05	1.39E-04	2.24E-04	3.46E-04	5.16E-04
15	2.53E-06	5.89E-06	1.26E-05	2.50E-05	4.67E-05	8.24E-05	1.39E-04	2.23E-04	3.45E-04	5.15E-04
30	2.50E-06	5.82E-06	1.25E-05	2.48E-05	4.63E-05	8.17E-05	1.38E-04	2.21E-04	3.43E-04	5.12E-04
45	2.47E-06	5.76E-06	1.23E-05	2.45E-05	4.58E-05	8.11E-05	1.37E-04	2.20E-04	3.41E-04	5.09E-04
60	2.47E-06	5.76E-06	1.23E-05	2.46E-05	4.59E-05	8.13E-05	1.37E-04	2.21E-04	3.42E-04	5.12E-04
75	2.55E-06	5.93E-06	1.27E-05	2.53E-05	4.74E-05	8.38E-05	1.41E-04	2.28E-04	3.53E-04	5.29E-04
90	2.76E-06	6.43E-06	1.38E-05	2.75E-05	5.14E-05	9.09E-05	1.53E-04	2.47E-04	3.83E-04	5.74E-04
105	3.22E-06	7.49E-06	1.60E-05	3.19E-05	5.97E-05	1.06E-04	1.77E-04	2.86E-04	4.44E-04	6.64E-04
120	4.03E-06	9.36E-06	2.00E-05	3.98E-05	7.43E-05	1.31E-04	2.20E-04	3.54E-04	5.49E-04	8.20E-04
135	5.25E-06	1.22E-05	2.59E-05	5.14E-05	9.57E-05	1.69E-04	2.82E-04	4.53E-04	6.99E-04	1.04E-03
150	6.73E-06	1.55E-05	3.30E-05	6.52E-05	1.21E-04	2.12E-04	3.55E-04	5.67E-04	8.72E-04	1.29E-03
165	8.01E-06	1.84E-05	3.91E-05	7.70E-05	1.42E-04	2.49E-04	4.15E-04	6.62E-04	1.01E-03	1.50E-03
180	8.52E-06	1.96E-05	4.15E-05	8.16E-05	1.51E-04	2.64E-04	4.39E-04	6.99E-04	1.07E-03	1.58E-03

Table B.1: Ionization rate at field strengths 0.10 to 0.29 a.u of Helium hydride ion at different angles (step size 0.01). Parameters are chose as Interval=4, decay factor=2, Laguerre=16, Legendre=24, Lmax=8 and Mmax=6.

References

[1]L. Plaja, "Attosecond physics", J. Phys. B **1**, R1–R37 (2006).

[2]A. H. Zewail, "Femtochemistry: Atomic-scale dynamics of the chemical bond", J. Phys. Chem. A **104**, 5660–5694 (2000).

[3]M. Hentschel, R. Kienberger, C. Spielmann, G. A. Reider, N. Milosevic, T. Brabec, P. Corkum, U. Heinzmann, M. Drescher, and F. Krausz, "Attosecond metrology", Nature **414**, 509–513 (2001).

[4]A. Baltuška, T. Udem, M. Uiberacker, M. Hentschel, E. Goulielmakis, C. Gohle, R. Holzwarth, V. S. Yakovlev, A. Scrinzi, T. W. Hänscht, and F. Krausz, "Attosecond control of electronic processes by intense light fields", Nature **421**, 611–615 (2003).

[5]R. Kienberger, E. Goulielmakis, M. Uiberacker, A. Baltuska, V. Yakovlev, F. Bammer, A. Scrinzi, T. Westerwalbesioh, U. Kleineberg, U. Heinzmann, M. Drescher, and F. Krausz, "Atomic transient recorder", Nature **427**, 817–821 (2004).

[6]E. Goulielmakis, M. Uiberacker, R. Kienberger, A. Baltuska, V. Yakovlev, A. Scrinzi, T. Westerwalbesloh, U. Kleineberg, U. Heinzmann, M. Drescher, and F. Krausz, "Direct measurement of light waves", Science (80-.). **305**, 1267–9 (2004).

[7]S. Neppl, R. Ernstorfer, A. L. Cavalieri, C. Lemell, G. Wachter, E. Magerl, E. M. Bothschafter, M. Jobst, M. Hofstetter, U. Kleineberg, J. V. Barth, D. Menzel, J. Burgdörfer, P. Feulner, F. Krausz, and R. Kienberger, "Direct observation of electron propagation and dielectric screening on the atomic length scale", Nature **517**, 342–346 (2015).

[8]A. L. Cavalieri, N. Müller, T. Uphues, V. S. Yakovlev, A. Baltuška, B. Horvath, B. Schmidt, L. Blümel, R. Holzwarth, S. Hendel, M. Drescher, U. Kleineberg, P. M. Echenique, R. Kienberger, F. Krausz, and U. Heinzmann, "Attosecond spectroscopy in condensed matter", Nature **449**, 1029–1032 (2007).

[9]M. Schultze, M. Fieß, N. Karpowicz, J. Gagnon, M. Korbman, M. Hofstetter, S. Neppl, A. L. Cavalieri, Y. Komninos, T. Mercouris, C. A. Nicolaides, R. Pazourek, S. Nagele, J. Feist, J. Burgdörfer, A. M. Azzeer, R. Ernstorfer, R. Kienberger, U. Kleineberg, E. Goulielmakis, F. Krausz, and V. S. Yakovlev, "Delay in photoemission", Science (80-.). **328**, 1658–1662 (2010).

[10]H. Nilkura, F. Légaré, R. Hashani, A. D. Bandrauk, M. Y. Ivanov, D. M. Villeneuve, and P. B. Corkum, *Sub-laser-cycle electron pulses for probing molecular dynamics*, June 2002.

[11]M. Lein, N. Hay, R. Velotta, J. P. Marangos, and P. L. Knight, "Role of the Intramolecular Phase in High-Harmonic Generation", Phys. Rev. Lett. **88**, 4 (2002).

[12]J. Itatani, J. Lavesque, D. Zeidler, H. Niikura, H. Pépin, J. C. Kieffer, P. B. Corkum, and D. M. Villeneuve, "Tomographic imaging of molecular orbitals", Nature **432**, 867–871 (2004).

[13]M. Meckel, D. Comtois, D. Zeidler, A. Staudte, D. Pavičić, H. C. Bandulet, H. Pépin, J. C. Kieffer, R. Dörner, D. M. Villeneuve, and P. B. Corkum, "Laser-induced electron tunneling and diffraction", Science (80-.). **320**, 1478–1482 (2008).

[14]M. Uiberacker, T. Uphues, M. Schultze, A. J. Verhoef, V. Yakovlev, M. F. Kling, J. Rauschenberger, N. M. Kabachnik, H. Schröder, M. Lezius, K. L. Kompa, H. G. Muller, M. J. Vrakking, S. Hendel, U. Kleineberg, U. Heinzmann, M. Drescher, and F. Krausz, "Attosecond real-time observation of electron tunnelling in atoms", Nature **446**, 627–632 (2007).

[15]E. Goulielmakis, Z. H. Loh, A. Wirth, R. Santra, N. Rohringer, V. S. Yakovlev, S. Zherebtsov, T. Pfeifer, A. M. Azzeer, M. F. Kling, S. R. Leone, and F. Krausz, "Real-time observation of valence electron motion", Nature **466**, 739–743 (2010).

[16]A. Wirth, M. T. Hassan, I. Grguraš, J. Gagnon, A. Moulet, T. T. Luu, S. Pabst, R. Santra, Z. A. Alahmed, A. M. Azzeer, V. S. Yakovlev, V. Pervak, F. Krausz, and E. Goulielmakis, "Synthesized light transients", Science (80-.). **334**, 195–200 (2011).

[17]M. Schultze, E. M. Bothschafter, A. Sommer, S. Holzner, W. Schweinberger, M. Fiess, M. Hofstetter, R. Kienberger, V. Apalkov, V. S. Yakovlev, M. I. Stockman, and F. Krausz, "Controlling dielectrics with the electric field of light", Nature **493**, 75–78 (2013).

[18]A. Schiffrin, T. Paasch-Colberg, N. Karpowicz, V. Apalkov, D. Gerster, S. Mühlbrandt, M. Korbman, J. Reichert, M. Schultze, S. Holzner, J. V. Barth, R. Kienberger, R. Ernstorfer, V. S. Yakovlev, M. I. Stockman, and F. Krausz, "Optical-field-induced current in dielectrics", Nature **493**, 70–74 (2013).

[19]E. Goulielmakis, V. S. Yakovlev, A. L. Cavalieri, M. Uiberacker, V. Pervak, A. Apolonski, R. Kienberger, U. Kleineberg, and F. Krausz, "Attosecond control and measurement: Lightwave electronics", Science (80-.). **317**, 769–775 (2007).

[20]M. Y. Shverdin, D. R. Walker, D. D. Yavuz, G. Y. Yin, and S. E. Harris, "Generation of a single-cycle optical pulse", Phys. Rev. Lett. **94**, 033904 (2005).

[21]T. Fuji, N. Ishii, C. Y. Teisset, X. Gu, T. Metzger, A. Baltuska, N. Forget, D. Kaplan, A. Galvanauskas, and F. Krausz, "Parametric amplification of few-cycle carrier-envelope phase-stable pulses at 21 μm", Opt. Lett. **31**, 1103 (2006).

[22]J. Duris, S. Li, T. Driver, E. G. Champenois, J. P. MacArthur, A. A. Lutman, Z. Zhang, P. Rosenberger, J. W. Aldrich, R. Coffee, G. Coslovich, F. J. Decker, J. M. Glownia, G. Hartmann, W. Helml, A. Kamalov, J. Knurr, J. Krzywinski, M. F. Lin, J. P. Marangos, M. Nantel, A. Natan, J. T. O'Neal, N. Shivaram, P. Walter, A. L. Wang, J. J. Welch, T. J. Wolf, J. Z. Xu, M. F. Kling, P. H. Bucksbaum, A. Zholents, Z. Huang, J. P. Cryan, and A. Marinelli, "Tunable isolated attosecond X-ray pulses with gigawatt peak power from a free-electron laser", Nat. Photonics **14**, 30–36 (2020).

[23]J. Itatani, F. Quéré, G. L. Yudin, M. Y. Ivanov, F. Krausz, and P. B. Corkum, "Attosecond Streak Camera", Phys. Rev. Lett. **88**, 173903 (2002).

[24]A. S. Landsman, M. Weger, J. Maurer, R. Boge, A. Ludwig, S. Heuser, C. Cirelli, L. Gallmann, and U. Keller, "Ultrafast resolution of tunneling delay time", Optica **1**, 343 (2014).

[25]A. N. Pfeiffer, C. Cirelli, M. Smolarski, D. Dimitrovski, M. Abu-Samha, L. B. Madsen, and U. Keller, "Attoclock reveals natural coordinates of the laser-induced tunnelling current flow in atoms", Nat. Phys. **8**, 76–80 (2012).

[26]C. I. Blaga, J. Xu, A. D. Dichiara, E. Sistrunk, K. Zhang, P. Agostini, T. A. Miller, L. F. Dimauro, and C. D. Lin, "Imaging ultrafast molecular dynamics with laser-induced electron diffraction", Nature **483**, 194–197 (2012).

[27]M. Drescher, M. Hentschel, R. Kienberger, M. Uiberacker, V. Yakovlev, A. Scrinzi, T. Westerwalbesloh, U. Kleineberg, U. Heinzmann, and F. Krausz, "Time-resolved atomic inner-shell spectroscopy", Nature **419**, 803–807 (2002).

[28]L. Seiffert, Q. Liu, S. Zherebtsov, A. Trabattoni, P. Rupp, M. C. Castrovilli, M. Galli, F. Submann, K. Wintersperger, J. Stierle, G. Sansone, L. Poletto, F. Frassetto, I. Halfpap, V. Mondes, C. Graf, E. Ruhl, F. Krausz, M. Nisoli, T. Fennel, F. Calegari, and M. F. Kling, "Attosecond chronoscopy of electron scattering in dielectric nanoparticles", Nat. Phys. **13**, 766–770 (2017).

[29]D. Shafir, H. Soifer, B. D. Bruner, M. Dagan, Y. Mairesse, S. Patchkovskii, M. Y. Ivanov, O. Smirnova, and N. Dudovich, "Resolving the time when an electron exits a tunnelling barrier", Nature **485**, 343–346 (2012).

[30]F. Calegari, D. Ayuso, A. Trabattoni, L. Belshaw, S. De Camillis, S. Anumula, F. Frassetto, L. Poletto, A. Palacios, P. Decleva, J. B. Greenwood, F. Martín, and M. Nisoli, "Ultrafast electron dynamics in phenylalanine initiated by attosecond pulses", Science (80-.). **346**, 336–339 (2014).

[31]R. Kienberger, M. Hentschel, M. Uiberacker, C. Spielmann, M. Kitzler, A. Scrinzi, M. Wieland, T. Westerwalbesloh, U. Kleineberg, U. Heinzmann, M. Drescher, and F. Krausz, "Steering attosecond electron wave packets with light", Science (80-.). **297**, 1144–1148 (2002).

[32]F. Krausz, "The birth of attosecond physics and its coming of age", Phys. Scr. **91**, 1–12 (2016).

[33]M. Ossiander, F. Siegrist, V. Shirvanyan, R. Pazourek, A. Sommer, T. Latka, A. Guggenmos, S. Nagele, J. Feist, J. Burgdörfer, R. Kienberger, and M. Schultze, "Attosecond correlation dynamics", Nat. Phys. **13**, 280 (2017).

[34]J. Ullrich, R. Moshammer, A. Dorn, R. Dörner, L. P. H. Schmidt, and H. Schmidt-Böcking, "Recoil-ion and electron momentum spectroscopy: Reaction-microscopes", Reports Prog. Phys. **66**, 1463–1545 (2003).

[35]R. Dörner, V. Mergel, O. Jagutzki, L. Spielberger, J. Ullrich, R. Moshammer, and H. Schmidt-Böcking, "Cold Target Recoil Ion Momentum Spectroscopy: A 'momentum microscope' to view atomic collision dynamics", Phys. Rep. **330**, 95–192 (2000).

[36]M. Kircher, F. Trinter, S. Grundmann, I. Vela-Perez, S. Brennecke, N. Eicke, J. Rist, S. Eckart, S. Houamer, O. Chuluunbaatar, Y. V. Popov, I. P. Volobuev, K. Bagschik, M. N. Piancastelli, M. Lein, T. Jahnke, M. S. Schöffler, and R. Dörner, "Kinematically complete experimental study of Compton scattering at helium atoms near the threshold", Nat. Phys., 1–5 (2020).

[37]A. Hartung, S. Eckart, S. Brennecke, J. Rist, D. Trabert, K. Fehre, M. Richter, H. Sann, S. Zeller, K. Henrichs, G. Kastirke, J. Hoehl, A. Kalinin, M. S. Schöffler, T. Jahnke, L. P. H. Schmidt, M. Lein, M. Kunitski, and R. Dörner, "Magnetic fields alter strong-field ionization", Nat. Phys. **15**, 1222–1226 (2019).

[38]M. Weckenbrock, M. Hattass, A. Czasch, O. Jagutzki, L. Schmidt, T. Weber, H. Roskos, T. Lffler, M. Thomson, and R. Drner, *Experimental evidence for electron repulsion in multiphoton double ionization*, 2001.

[39]N. Camus, B. Fischer, M. Kremer, V. Sharma, A. Rudenko, B. Bergues, M. Kübel, N. G. Johnson, M. F. Kling, T. Pfeifer, J. Ullrich, and R. Moshammer, "Attosecond correlated dynamics of two electrons passing through a transition state", Phys. Rev. Lett. **108**, 073003 (2012).

[40]M. Kübel, K. J. Betsch, N. G. Kling, A. S. Alnaser, J. Schmidt, U. Kleineberg, Y. Deng, I. Ben-Itzhak, G. G. Paulus, T. Pfeifer, J. Ullrich, R. Moshammer, M. F. Kling, and B. Bergues, "Non-sequential double ionization of Ar: From the single- to the many-cycle regime", New J. Phys. **16**, 1367 (2014).

[41]B. Bergues, M. Kübel, N. G. Johnson, B. Fischer, N. Camus, K. J. Betsch, O. Herrwerth, A. Senftleben, A. M. Sayler, T. Rathje, T. Pfeifer, I. Ben-Itzhak, R. R. Jones, G. G. Paulus, F. Krausz, R. Moshammer, J. Ullrich, and M. F. Kling, "Attosecond tracing of correlated electron-emission in non-sequential double ionization", Nat. Commun. **3**, 1 (2012).

[42]B. Bergues, M. Kubel, N. G. Kling, C. Burger, and M. F. Kling, "Single-Cycle Non-Sequential Double Ionization", IEEE J. Sel. Top. Quantum Electron. **21**, 8701009 (2015).

[43]M. Kübel, C. Burger, N. G. Kling, T. Pischke, L. Beaufore, I. Ben-Itzhak, G. G. Paulus, J. Ullrich, T. Pfeifer, R. Moshammer, M. F. Kling, and B. Bergues, "Complete characterization of single-cycle double ionization of argon from the nonsequential to the sequential ionization regime", Phys. Rev. A **93**, 053422 (2016).

[44]B. Walker, B. Sheehy, L. F. Dimauro, P. Agostini, K. J. Schafer, and K. C. Kulander, "Precision measurement of strong field double ionization of helium", Phys. Rev. Lett. **73**, 1227–1230 (1994).

[45]B. Sheehy, R. Lafon, M. Widmer, B. Walker, L. F. DiMauro, P. A. Agostini, and K. C. Kulander, "Single- and multiple-electron dynamics in the strong-field tunneling limit", Phys. Rev. A **58**, 3942–3952 (1998).

[46]K. Henrichs, S. Eckart, A. Hartung, D. Trabert, K. Fehre, J. Rist, H. Sann, M. Pitzer, M. Richter, H. Kang, M. S. Schöffler, M. Kunitski, T. Jahnke, and R. Dörner, "Multiphoton Double Ionization of Helium at 394nm - a Fully Differential Experiment", Phys. Rev. A **98**, 1–10 (2018).

[47]M. Spanner, O. Smirnova, P. B. Corkum, and M. Y. Ivanov, "Reading diffraction images in strong field ionization of diatomic molecules", J. Phys. B **37**, 243 (2004).

[48]M. Lein, N. Hay, R. Velotta, J. P. Marangos, and P. L. Knight, "Interference effects in high-order harmonic generation with molecules", Phys. Rev. A **66**, 1–6 (2002).

[49]J. Feist, S. Nagele, R. Pazourek, E. Persson, B. I. Schneider, L. A. Collins, and J. Burgdörfer, "Nonsequential two-photon double ionization of helium", Phys. Rev. A **77**, 043420 (2008).

[50]J. S. Parker, B. J. Doherty, K. J. Meharg, and K. T. Taylor, "Time delay between singly and doubly ionizing wavepackets in laser-driven helium", J. Phys. B **36**, L393–L400 (2003).

[51]J. S. Parker, B. J. Doherty, K. T. Taylor, K. D. Schultz, C. I. Blaga, and L. F. Dimauro, "High-energy cutoff in the spectrum of strong-field nonsequential double ionization", Phys. Rev. Lett. **96**, 13001 (2006).

[52]A. Emmanouilidou, J. S. Parker, L. R. Moore, and K. T. Taylor, "Direct versus delayed pathways in strong-field non-sequential double ionization", New J. Phys. **13**, 043001 (2011).

[53]S. X. Hu, "Boosting photoabsorption by attosecond control of electron correlation", Phys. Rev. Lett. **111**, 123003 (2013).

[54]A. Zielinski, V. P. Majety, and A. Scrinzi, "Double photoelectron momentum spectra of helium at infrared wavelength", Phys. Rev. A **93**, 023406 (2016).

[55]H. Price, C. Lazarou, and A. Emmanouilidou, "Toolkit for semiclassical computations for strongly driven molecules: Frustrated ionization of H2 driven by elliptical laser fields", Phys. Rev. A **90**, 053419 (2014).

[56]S. Palaniyappan, A. Dichiara, E. Chowdhury, A. Falkowski, G. Ongadi, E. L. Huskins, and B. C. Walker, "Ultrastrong field ionization of Nen+ (n8): Rescattering and the role of the magnetic field", Phys. Rev. Lett. **94**, 243003 (2005).

[57]C. J. (J. Joachain, *Quantum collision theory* (North-Holland, 1983), p. 710.

[58]J. Su, H. Ni, A. Jaroń-Becker, and A. Becker, "Time delays in two-photon ionization", Phys. Rev. Lett. **113**, 263002 (2014).

[59]E. A. Pronin, A. F. Starace, M. V. Frolov, and N. L. Manakov, "Perturbation theory analysis of attosecond photoionization", Phys. Rev. A - At. Mol. Opt. Phys. **80** (2009) 10.1103/PhysRevA.80.063403.

[60]Y. Gontier, and M. Trahin, "Energetic electron generation by multiphoton absorption", J. Phys. B At. Mol. Phys. **13**, 4383–4390 (1980).

[61]P. Agostini, F. Fabre, G. Mainfray, G. Petite, and N. K. Rahman, "Free-free transitions following six-photon ionization of xenon atoms", Phys. Rev. Lett. **42**, 1127–1130 (1979).

[62]M. V. Ammosov, N. 8. Delone, and V. P. Krainov, "Tunnel ionization of complex atoms and of atomic ions in an alternating electromagnetic field", Sov. Phys. - JETP **64**, 938695 (1986).

[63]A. Perelomov, V. Popov, and M. Terent'ev, "Ionization of Atoms in an Alternating Electric Field", Sov. J. Exp. Theor. Phys. **23**, 924 (1966).

[64]X. M. Tong, Z. X. Zhao, and C. D. Lin, "Theory of molecular tunneling ionization", Phys. Rev. A **66**, 11 (2002).

[65]D. Pavičić, K. F. Lee, D. M. Rayner, P. B. Corkum, and D. M. Villeneuve, "Direct measurement of the angular dependence of ionization for N 2, O2, and CO2 in intense laser fields", Phys. Rev. Lett. **98**, 1–4 (2007).

[66]V. P. Majety, and A. Scrinzi, "Dynamic Exchange in the Strong Field Ionization of Molecules", Phys. Rev. Lett. **115**, 103002 (2015).

[67]M. Smits, C. A. De Lange, A. Stolow, and D. M. Rayner, "Absolute lonization rates of multielectron transition metal atoms in strong infrared laser fields", Phys. Rev. Lett. **93**, 19–22 (2004).

[68] L.V. Keldysh, "Ionization in the Field of a Strong Electromagnetic Wave", J. Exp. Theor. Phys. **20**, 1307 (1965).

[69]P. Eckle, A. N. Pfeiffer, C. Cirelli, A. Staudte, R. Dörner, H. G. Muller, M. Büttiker, and U. Keller, "Attosecond ionization and tunneling delay time measurements in helium", Science (80-.). **322**, 1525–1529 (2008).

[70]M. Bttiker, and R. Landauer, "Traversal time for tunneling", Phys. Rev. Lett. **49**, 1739–1742 (1982).

[71]K. Midorikawa, "Ultrafast dynamic imaging", Nat. Photonics **5**, 640–641 (2011).

[72]P. B. Corkum, "Plasma perspective on strong field multiphoton ionization", Phys. Rev. Lett. **71**, 1994–1997 (1993).

[73]A. Emmanouilidou, "Prevalence of different double ionization pathways and traces of three-body interactions in strongly driven helium", Phys. Rev. A **83**, 023403 (2011).

[74]P. A. Franken, A. E. Hill, C. W. Peters, and G. Weinreich, "Generation of optical harmonics", Phys. Rev. Lett. **7**, 118–119 (1961).

[75]E. Haug, and W. Nakel, *The elementary process of bremsstrahlung*, Scientific Lecture Notes in Physics (World Scientific, River Edge, NJ, 2004), p. 272.

[76]T. Shaaran, M. T. Nygren, and C. Figueira De Morisson Faria, "Laser-induced nonsequential double ionization at and above the recollision-excitation-tunneling threshold", Phys. Rev. A **81**, 063413 (2010).

[77]S. L. Haan, L. Breen, A. Karim, and J. H. Eberly, "Variable Time Lag and Backward Ejection in Full-Dimensional Analysis of Strong-Field Double Ionization", Phys. Rev. Lett. **97**, 103008 (2006).

[78]T. Ishikawa, X. M. Tong, and N. Toshima, "Double ionization of He in an intense laser field via a rescattering process", Phys. Rev. A **82**, 033411 (2010).

[79]Z. Chen, Y. Liang, and C. D. Lin, "Quantum theory of recollisional (e, 2e) process in strong field nonsequential double ionization of Helium", Phys. Rev. Lett. **104**, 253201 (2010).

[80]S. Chen, C. Ruiz, and A. Becker, "Double ionization of helium by intense near-infrared and VUV laser pulses", Phys. Rev. A **82**, 033426 (2010).

[81]F. Mauger, C. Chandre, and T. Uzer, "From recollisions to the knee: A road map for double ionization in intense laser fields", Phys. Rev. Lett. **104**, 043005 (2010).

[82]A. Zielinski, "Fully Differential Photo-Electron Spectra of Hydrogen and Helium Atoms", PhD thesis (ludwig-maximilians-universität münchen, 2015), p. 1.

[83]M. S. Pindzola, F. Robicheaux, S. D. Loch, J. C. Berengut, T. Topcu, J. Colgan, M. Foster, D. C. Griffin, C. P. Ballance, D. R. Schultz, T. Minami, N. R. Badnell, M. C. Witthoeft, D. R. Plante, D. M. Mitnik, J. A. Ludlow, and U. Kleiman, "The time-dependent close-coupling method for atomic and molecular collision processes", J. Phys. B **40**, 39 (2007).

[84]C. W. McCurdy, M. Baertschy, and T. N. Rescigno, "Solving the three-body Coulomb breakup problem using exterior complex scaling", J. Phys. B **37**, R137–R187 (2004).

[85]T. Schneider, P. L. Chocian, and J. M. Rost, "Separation and Identification of Dominant Mechanisms in Double Photoionization", Phys. Rev. Lett. **89**, 073022 (2002).

[86]R. Pazourek, J. Feist, S. Nagele, E. Persson, B. I. Schneider, L. A. Collins, and J. Burgdörfer, "Universal features in sequential and nonsequential two-photon double ionization of helium", Phys. Rev. A **83**, 053418 (2011).

[87]Z. Zhang, L. Y. Peng, M. H. Xu, A. F. Starace, T. Morishita, and Q. Gong, "Two-photon double ionization of helium: Evolution of the joint angular distribution with photon energy and two-electron energy sharing", Phys. Rev. A **84**, 043409 (2011).

[88]W. C. Jiang, L. Y. Peng, W. H. Xiong, and Q. Gong, "Comparison study of electron correlation in one-photon and two-photon double ionization of helium", Phys. Rev. A **88**, 023410 (2013).

[89]A. Liu, and U. Thumm, "Laser-assisted XUV few-photon double ionization of helium: Joint angular distributions", Phys. Rev. A **89**, 1–15 (2014).

[90]R. Nepstad, T. Birkeland, and M. Førre, "Numerical study of two-photon ionization of helium using an ab initio numerical framework", Phys. Rev. A **81**, 063402 (2010).

[91]A. Palacios, D. A. Horner, T. N. Rescigno, and C. W. McCurdy, "Two-photon double ionization of the helium atom by ultrashort pulses", J. Phys. B **43**, 194003 (2010).

[92]F. Lackner, I. Březinová, T. Sato, K. L. Ishikawa, and J. Burgdörfer, "Propagating two-particle reduced density matrices without wave functions", Phys. Rev. A **91**, 023412 (2015).

[93]L. Tao, and A. Scrinzi, "Photo-electron momentum spectra from minimal volumes: The time-dependent surface flux method", New J. Phys. **14**, 013021 (2012).

[94]L. Torlina, F. Morales, J. Kaushal, I. Ivanov, A. Kheifets, A. Zielinski, A. Scrinzi, H. G. Muller, S. Sukiasyan, M. Ivanov, and O. Smirnova, "Interpreting attoclock measurements of tunnelling times", Nat. Phys. **11**, 503–508 (2015).

[95]C. Hofmann, A. S. Landsman, A. Zielinski, C. Cirelli, T. Zimmermann, A. Scrinzi, and U. Keller, "Interpreting electron-momentum distributions and nonadiabaticity in strong-field ionization", Phys. Rev. A **90**, 043406 (2014).

[96]*tRecX Code*.

[97]F. Morales, T. Bredtmann, and S. Patchkovskii, "ISURF: A family of infinite-time surface flux methods", J. Phys. B At. Mol. Opt. Phys. **49**, 245001 (2016).

[98]V. P. Majety, "Strong field single ionization of atoms and small molecules: a hybrid antisymmetrized coupled channels approach", PhD thesis (ludwig-maximilians-universität münchen, 2015), p. 1.

[99]S. B. R. Scott, *The Mathematical Theory of Finite Element Methods* (Springer, 2007).

[100]K. C. Kulander, "Time-dependent Hartree-Fock theory of multiphoton ionization: Helium", Phys. Rev. A **36**, 2726–2738 (1987).

[101]J. C. Slater, "The self consistent field and the structure of atoms", Phys. Rev. **32**, 339–348 (1928).

[102]D. Hochstuhl, S. Bauch, and M. Bonitz, "Multiconfigurational time-dependent Hartree-Fock calculations for photoionization of one-dimensional Helium", J. Phys. Conf. Ser. **220**, 12019 (2010).

[103]T. Sato, and K. L. Ishikawa, "Time-dependent complete-active-space self-consistent-field method for multielectron dynamics in intense laser fields", Phys. Rev. A **88**, 023402 (2013).

[104]D. Hochstuhl, and M. Bonitz, "Time-dependent restricted-active-space configuration-interaction method for the photoionization of many-electron atoms", Phys. Rev. A **86**, 053424 (2012).

[105]H. Miyagi, and L. B. Madsen, "Time-dependent restricted-active-space self-consistent-field theory for laser-driven many-electron dynamics", Phys. Rev. A **87**, 062511 (2013).

[106]L. Greenman, P. J. Ho, S. Pabst, E. Kamarchik, D. A. Mazziotti, and R. Santra, "Implementation of the time-dependent configuration-interaction singles method for atomic strong-field processes", Phys. Rev. A **82**, 023406 (2010).

[107]Y. V. Vanne, and A. Saenz, "Numerical treatment of diatomic two-electron molecules using a B-spline based CI method Numerical treatment of diatomic two-electron molecules using a B -spline based CI method", J. Phys. B **37**, 4101–4118 (2004).

[108]M. Spanner, and S. Patchkovskii, "One-electron ionization of multielectron systems in strong nonresonant laser fields", Phys. Rev. A **80**, 063411 (2009).

[109]V. P. Majety, A. Zielinski, and A. Scrinzi, "Photoionization of few electron systems: A hybrid coupled channels approach", New J. Phys. **17**, 63002 (2015).

[110]C. Marante, M. Klinker, I. Corral, J. González-Vázquez, L. Argenti, and F. Martín, "Hybrid-Basis Close-Coupling Interface to Quantum Chemistry Packages for the Treatment of Ionization Problems", J. Chem. Theory Comput. **13**, 499–514 (2017).

[111]C. Marante, M. Klinker, T. Kjellsson, E. Lindroth, J. González-Vázquez, L. Argenti, and F. Martín, "Photoionization using the xchem approach: Total and partial cross sections of Ne and resonance parameters above the 2s22p5 threshold", Phys. Rev. A **96**, 756–762 (2017).

[112]M. Klinker, C. Marante, L. Argenti, J. González-Vázquez, and F. Martín, "Electron Correlation in the Ionization Continuum of Molecules: Photoionization of N2in the Vicinity of the Hopfield Series of Autoionizing States", J. Phys. Chem. Lett. **9**, 756–762 (2018).

[113]M. Klinker, C. Marante, L. Argenti, J. González-Vázquez, and F. Martín, "Partial cross sections and interfering resonances in photoionization of molecular nitrogen", Phys. Rev. A **98**, 1–9 (2018).

[114]S. Marggi Poullain, M. Klinker, J. González-Vázquez, and F. Martín, "Resonant photoionization of O2 up to the fourth ionization threshold", Phys. Chem. Chem. Phys. **21**, 16497–16504 (2019).

[115]N. Douguet, B. I. Schneider, and L. Argenti, "Application of the complex Kohn variational method to attosecond spectroscopy", Phys. Rev. A **98**, 023403 (2018).

[116]V. P. Majety, and A. Scrinzi, "Static field ionization rates for multi-electron atoms and small molecules", J. Phys. B **48**, 245603 (2015).

[117]V. Majety, and A. Scrinzi, "Photo-Ionization of Noble Gases: A Demonstration of Hybrid Coupled Channels Approach", Photonics **2**, 93–103 (2015).

[118]H. Lischka, T. Müller, P. G. Szalay, I. Shavitt, R. M. Pitzer, and R. Shepard, "Columbus-a program system for advanced multireference theory calculations", Wiley Interdiscip. Rev. Comput. Mol. Sci. **1**, 191–199 (2011).

[119]V. P. Majety, A. Zielinski, and A. Scrinzi, "Mixed gauge in strong laser-matter interaction", J. Phys. B **48**, 025601 (2015).

[120]M. Woodbury, *Inverting modified matrices*, tech. rep. 42 (Memorandum 42, Statistical Research Group, Princeton University, 1950), p. 106.

[121]O. Smirnova, Y. Mairesse, S. Patchkovskii, N. Dudovich, D. Villeneuve, P. Corkum, and M. Y. Ivanov, "High harmonic interferometry of multi-electron dynamics in molecules", Nature **460**, 972–977 (2009).

[122]J. Xu, C. I. Blaga, K. Zhang, Y. H. Lai, C. D. Lin, T. A. Miller, P. Agostini, and L. F. Dimauro, "Diffraction using laser-driven broadband electron wave packets", Nat. Commun. **5**, 1–6 (2014).

[123]R. B. Dingle, *Asymptotic expansions: their derivation and interpretation* (Academic Press, 1973), p. 521.

[124]X. M. Tong, and C. D. Lin, "Empirical formula for static field ionization rates of atoms and molecules by lasers in the barrier-suppression regime", J. Phys. B **38**, 2593–2600 (2005).

[125]A. Scrinzi, "Ionization of multielectron atoms by strong static electric fields", Phys. Rev. A **61**, 4 (2000).

[126]J. S. Parker, G. S. Armstrong, M. Boca, and K. T. Taylor, "From the UV to the static-field limit: Rates and scaling laws of intense-field ionization of helium", J. Phys. B **42**, 134011 (2009).

[127]I. I. Fabrikant, and L. B. Zhao, "Green-function approach to the theory of tunneling ionization", Phys. Rev. A **91**, 053412 (2015).

[128]A. Scrinzi, and N. Elander, "A finite element implementation of exterior complex scaling for the accurate determination of resonance energies", J. Chem. Phys. **98**, 3866–3875 (1993).

[129]R. Olson, "Classical Trajectory and Monte Carlo Techniques", in *Springer handb. at. mol. opt. phys.* (Springer New York, 2006), pp. 869–874.

[130]A. Vila, J. Zhu, A. Scrinzi, and A. Emmanouilidou, "Intertwined electron-nuclear motion in frustrated double ionization in driven heteronuclear molecules", J. Phys. B **51**, 1361 (2018).

[131]L. Malegat, H. Bachau, A. Hamido, and B. Piraux, "Analysing a two-electron wavepacket by semiclassically propagating its Fourier components in space", J. Phys. B **43**, 45601 (2010).

[132]L. Argenti, R. Pazourek, J. Feist, S. Nagele, M. Liertzer, E. Persson, J. Burgdörfer, and E. Lindroth, "Photoionization of helium by attosecond pulses: Extraction of spectra from correlated wave functions", Phys. Rev. A **87**, 053405 (2013).

[133]J. Feist, S. Nagele, R. Pazourek, E. Persson, B. I. Schneider, L. A. Collins, and J. Burgdörfer, "Probing electron correlation via attosecond XUV pulses in the two-photon double ionization of helium", Phys. Rev. Lett. **103**, 063002 (2009).

[134]B. I. Schneider, L. A. Collins, and S. X. Hu, "Parallel solver for the time-dependent linear and nonlinear Schrödinger equation", Phys. Rev. E - Stat. Nonlinear, Soft Matter Phys. **73**, 036708 (2006).

[135]A. S. Kheifets, and I. A. Ivanov, "Convergent close-coupling calculations of two-photon double ionization of helium", J. Phys. B **39**, 1731–1742 (2006).

[136]D. A. Horner, F. Morales, T. N. Rescigno, F. Martín, and C. W. McCurdy, "Two-photon double ionization of helium above and below the threshold for sequential ionization", Phys. Rev. A **76**, 030701 (2007).

[137]L. Feng, and H. W. Van Der Hart, "Two-photon double ionization of He", J. Phys. B **36**, 1 (2003).

[138]P. G. Burke, P. Francken, and C. J. Joachain, "R-matrix-floquet theory of multiphoton processes", Epl **13**, 617–622 (1990).

[139]A. Scrinzi, "t -SURFF: fully differential two-electron photo-emission spectra", New J. Phys. **14**, 085008 (2012).

[140]J. R. Hiskes, "Dissociation of molecular ions by electric and magnetic fields", Phys. Rev. **122**, 1207–1217 (1961).

[141]S. Hamdi, W. E. Schiesser, and G. W. Griffiths, "Method of Lines", Scholarpedia **2**, 2859 (2009).

[142]K. Varga, "Solution of the time-dependent Schrödinger equation using time-dependent basis functions", Phys. Rev. E - Stat. Nonlinear, Soft Matter Phys. **85**, 016705 (2012).

[143]L. Tao, C. W. McCurdy, and T. N. Rescigno, "Grid-based methods for diatomic quantum scattering problems: A finite-element discrete-variable representation in prolate spheroidal coordinates", Phys. Rev. A **79**, 012719 (2009).

[144]M. Weinmüller, M. Weinmüller, J. Rohland, and A. Scrinzi, "Perfect absorption in Schrödinger-like problems using non-equidistant complex grids", J. Comput. Phys. **333**, 199–211 (2017).

[145]T. N. Rescigno, and C. W. Mccurdy, "Numerical grid methods for quantum-mechanical scattering problems", Phys. Rev. A **62**, 032706 (2000).

[146]J. Feist, S. Nagele, R. Pazourek, E. Persson, B. I. Schneider, L. A. Collins, and J. Burgdörfer, "Nonsequential two-photon double ionization of helium", Phys. Rev. A - At. Mol. Opt. Phys. **77**, 043420 (2008).

[147]E. Gamma, *Design Patterns: Elements of Reusable Object-Oriented Software. Addison-Wesley,* (1994).

[148]R. a. Horn, and C. R. Johnson, *Matrix Analysis 2nd Ed* (2012), p. 662.

[149]B. R. Junker, and C. L. Huang, *Complex-coordinate method. Structure of the wave function*, tech. rep. 2 (1978), p. 313.

[150]A. Scrinzi, "Infinite-range exterior complex scaling as a perfect absorber in time-dependent problems", Phys. Rev. A **81**, 053845 (2010).

[151]F. He, C. Ruiz, and A. Becker, "Absorbing boundaries in numerical solutions of the time-dependent Schrödinger equation on a grid using exterior complex scaling", Phys. Rev. A **75**, 053407 (2007).

[152]E. Cormier, and P. Lambropoulos, "Optimal gauge and gauge invariance in non-perturbative time-dependent calculation of above-threshold ionization", J. Phys. B **29**, 1667–1680 (1996).

[153]L. A. Collins, J. D. Kress, and R. B. Walker, "Excitation and ionization of molecules by a single-mode laser field using a time-dependent approach", Comput. Phys. Commun. **114**, 15–26 (1998).

[154]E. S. Smyth, J. S. Parker, and K. T. Taylor, "Numerical integration of the time-dependent Schrödinger equation for laser-driven helium", Comput. Phys. Commun. **114**, 1–14 (1998).

[155]H. Ni, S. Chen, C. Ruiz, and A. Becker, "Selection rules in the few-photon double ionization of the helium atom Erratum: Selection rules in the few-photon double ionization of the helium atom Selection rules in the few-photon double ionization of the helium atom", J. Phys. B **44**, 175601–175609 (2012).

[156]A. Staudte, C. Ruiz, M. Schöffler, S. Schössler, D. Zeidler, T. Weber, M. Meckel, D. M. Villeneuve, P. B. Corkum, A. Becker, and R. Dörner, "Binary and recoil collisions in strong field double ionization of helium", Phys. Rev. Lett. **99**, 263002 (2007).

[157]H. Ni, S. Chen, C. Ruiz, and A. Becker, "Selection rules in the few-photon double ionization of the helium atom", J. Phys. B **44**, 175601 (2011).

[158]B. Feuerstein, T. Ergler, A. Rudenko, K. Zrost, C. D. Schröter, R. Moshammer, J. Ullrich, T. Niederhausen, and U. Thumm, "Complete characterization of molecular dynamics in ultrashort laser fields", Phys. Rev. Lett. **99**, 1–58 (2007).

[159]R. E. Silva, P. Rivière, F. Morales, O. Smirnova, M. Ivanov, and F. Martín, "Even harmonic generation in isotropic media of dissociating homonuclear molecules", Sci. Rep. **6**, 1–9 (2016).

[160]M. Lara-Astiaso, R. E. Silva, A. Gubaydullin, P. Rivière, C. Meier, and F. Martín, "Enhancing High-Order Harmonic Generation in Light Molecules by Using Chirped Pulses", Phys. Rev. Lett. **117**, 1–5 (2016).

[161]W. Joppich, and S. Mijalković, *Multigrid Methods for Process Simulation*, Computational Microelectronics (Springer Vienna, Vienna, 1993).

[162]N. Moiseyev, "Quantum theory of resonances: Calculating energies, widths and cross-sections by complex scaling", Phys. Rep. **302**, 212–293 (1998).

[163]W. P. Reinhardt, "Complex Coordinates in the Theory of Atomic and Molecular Structure and Dynamics", Annu. Rev. Phys. Chem. **33**, 223–255 (1982).

[164]M. Lupetti, M. F. Kling, and A. Scrinzi, "Plasmon-enhanced-attosecond-extreme ultraviolet source", Phys. Rev. Lett. **110**, 223903 (2013).

[165]M. Lupetti, J. Hengster, T. Uphues, and A. Scrinzi, "Attosecond photoscopy of plasmonic excitations", Phys. Rev. Lett. **113**, 113903 (2014).

[166]"Eigen library", http://eigen.tuxfamily.org/.

[167]"Alglib library", http://www.alglib.net/.

[168]"Arpack library", http://www.caam.rice.edu/software/ARPACK/.

[169]Y. Saad, A. Stathopoulos, J. Chelikowsky, K. Wu, and S. Öğüt, "Solution of large eigenvalue problems in electronic structure calculations", BIT Numer. Math. **36**, 563–578 (1996).

[170]"MPI library", http://www.open-mpi.org/.

[171]G. P. Katsoulis, A. Hadjipittas, B. Bergues, M. F. Kling, and A. Emmanouilidou, "Slingshot Nonsequential Double Ionization as a Gate to Anticorrelated Two-Electron Escape", Phys. Rev. Lett. **121**, 263203 (2018).

[172]O. Smirnova, M. Spanner, and M. Ivanov, "Analytical solutions for strong field-driven atomic and molecular one- and two-electron continua and applications to strong-field problems", Phys. Rev. A **77**, 033407 (2008).

[173]T. Nubbemeyer, K. Gorling, A. Saenz, U. Eichmann, and W. Sandner, "Strong-field tunneling without ionization", Phys. Rev. Lett. **101**, 233001 (2008).

[174]J. Yao, B. Zeng, H. Xu, G. Li, W. Chu, J. Ni, H. Zhang, S. L. Chin, Y. Cheng, and Z. Xu, "High-brightness switchable multiwavelength remote laser in air", Phys. Rev. A **84**, 51802 (2011).

[175]B. Manschwetus, T. Nubbemeyer, K. Gorling, G. Steinmeyer, U. Eichmann, H. Rottke, and W. Sandner, "Strong laser field fragmentation of H2: Coulomb explosion without double ionization", Phys. Rev. Lett. **102**, 113002 (2009).

[176]T. Nubbemeyer, U. Eichmann, and W. Sandner, "Excited neutral atomic fragments in the strong-field dissociation of N 2 molecules", J. Phys. B **42**, 134010 (2009).

[177]A. Chen, H. Price, A. Staudte, and A. Emmanouilidou, "Frustrated double ionization in two-electron triatomic molecules", Phys. Rev. A **94**, 043408 (2016).

[178]A. Emmanouilidou, C. Lazarou, A. Staudte, and U. Eichmann, "Routes to formation of highly excited neutral atoms in the breakup of strongly driven H2", Phys. Rev. A **85**, 011402 (2012).

[179]L. Wolniewicz, "Variational treatment of the HeH+ ion and the 0-decay in HT", J. Chem. Phys. **43**, 1087–1091 (1965).

[180]H. H. Michels, "Molecular Orbital Studies of the Ground and Low-Lying Excited States of the HeH + Molecular Ion *", J. Chem. Phys. **44**, 3834 (1966).

[181]I. Shavitt, "The Method of Configuration Interaction", Methods Electron. Struct. Theory **978**, 189–275 (1977).

[182]R. M. Potvliege, "STRFLO: a program for time-independent calculations of multiphoton processes in one-electron atomic systems I. Quasienergy spectra and angular distributions", Comput. Phys. Commun. **114**, 42–93 (1998).

[183]R. R. Freeman, P. H. Bucksbaum, H. Milchberg, S. Darack, D. Schumacher, and M. E. Geusic, "Above-Threshold Ionization with Subpicosecond Laser Pulses", Phys. Rev. Lett. **59**, 1092–1095 (1987).

[184]N. B. Delone, and V. P. Krainov, "Reviews of topical problems: AC stark shift of atomic energy levels", Phys.-Uspekhi **42**, 669–687 (1999).

[185]J. Zhu, and A. Scrinzi, "Electron double-emission spectra for helium atoms in intense 400-nm laser pulses", Phys. Rev. A **101**, 063407 (2020).

[186]Y. Liu, S. Tschuch, A. Rudenko, M. Dürr, M. Siegel, U. Morgner, R. Moshammer, and J. Ullrich, "Strong-field double ionization of Ar below the recollision threshold", Phys. Rev. Lett. **101**, 5–8 (2008).

[187]S. L. Haan, Z. S. Smith, K. N. Shomsky, and P. W. Plantinga, "Anticorrelated electrons from weak recollisions in nonsequential double ionization", J. Phys. B **41**, 211002 (2008).

[188]D. F. Ye, and J. Liu, "Strong-field double ionization at the transition to below the recollision threshold", Phys. Rev. A **81**, 43402 (2010).

[189]A. Karamatskou, S. Pabst, Y. J. Chen, and R. Santra, "Calculation of photoelectron spectra within the time-dependent configuration-interaction singles scheme", Phys. Rev. A **89**, 069907 (2014).

[190]L. Yue, and L. B. Madsen, "Dissociative ionization of H2+ using intense femtosecond XUV laser pulses", Phys. Rev. A **90**, 063408 (2014).

[191]J. S. Parker, L. R. Moore, D. Dundas, and K. T. Taylor, "Double ionization of helium at 390 nm", J. Phys. B **33**, L691–L698 (2000).

Acknowledgement

First, I am in heavy debt to my advisor Prof. Dr. Armin Scrinzi who gave me the opportunity for the Ph. D study and is willing to help even with the details that guided me when I was struggling with the coding and researches. He also helped me a lot in the writting of the paper and my thesis.

I am very grateful for the funding from the DFG project and Qutif that gives me the financial support in the Ph.D. study for 3 years and gave me the opportunities to communicate with the scientists in this field.

I am grateful to Dr. Vinay Pramod Majety for teaching me the haCC methods and introducing the old version of the double ionization problem.

I am very thankful for the co-operation with the group of Dr. Agapi Emmanouilidou from University College London. They did the calculations with CTMC methods on FDI in the thesis, and the communication with Georgios Petros Katsoulis inspires me the connection with the quantum and classical simulations.

I am grateful for our co-operators Prof. Reinhard Dörner and Dr. Kevin Henrichs from Frankfurt University who offered the experimental data and explained the relevant details of from the experiments side. I should also give my special thanks to Dr. Qingcao Liu who showed me the detailed experimental methods such as the spot size measurement. His information inspired me when I was comparing our computations with the experimental data.

I am grateful for Dr. Lun Yue, Dr. Honchen Ni and Dr. Xiaochun Gong for the fruitful discussions in my research.

I would like to thank Ms. Ute Tobiash, the secretary of our department, for helping me with many bureaucratic things.

Finally, I would like to give my thanks to my friends in Munich especially Dr. Chan Ka Lok, Dr. Bin Liu, Sheng Ye and Dr. XinKe Wang who make my life here more enjoyable.

Declaration

I hereby declare that this thesis is my own work, and that I have not used any sources and aids other than those stated in the thesis.

Munich, Sept 19, 2020

Jinzhen Zhu